On the Mesoscale Plasticity of Nickel-Base Superalloy Single Crystals

Siqi Ying

St Cross College

Department of Engineering Science

University of Oxford

A thesis submitted for the degree of

Doctor of Philosophy

Trinity 2017

Abstract

Experimental micromechanics of materials is a branch of science that seeks to build tight connections between composition, structure, processing and performance of materials under specific operating conditions required for particular technology applications. The present project is focused on the development of techniques that use the combination of electron, ion and X-ray microscopies to study the deformation behaviour of a particularly important class of metallic alloys used in the manufacture of aeroengines, namely, the so-called Ni-base superalloys. The complex hierarchical structure of these materials means that their macroscopic response is controlled to a great extent by the phenomena that play out on very fine scales, from angstroms (lattice spacing dimension) to nanometres (precipitates, phase boundaries, dislocations, chemical inhomogeneities) to microns (grains and their boundaries, defects and their clusters, dislocation pileups) to millimetres (component scale). Understanding the fine structure and deformation behaviour requires the development of specially configured experimental setup that allow the observation and quantification of deformation to external loading.

In this study, FIB-SEM methods for sample characterization and fabrication were combined with synchrotron-based X-ray diffraction and imaging techniques, and backed up by theoretical analysis and numerical simulation, to elucidate the origins of the strength of these alloys. Micropillar compression tests using in-SEM nanoindentation were used to reveal the size dependence of the apparent strength, and connection was made with the dislocation-mediated crystal slip to provide an explanation of the observed Hall-Petch type dependence with a modified Hall-Petch equation considering both intrinsic and extrinsic characteristic lengths introduced. X-ray scattering was used in the polychromatic micro-Laue mode and using Bragg coherent diffractive imaging to reveal the crystal distortion arising due to plastic deformation. A Discrete dislocation dynamics in the 2.5D formulation was used to obtain a model description of the observed phenomena. The key outcome of the work presented in this thesis lies in the successful development of advanced observational tools and relevant theoretical or computational models for mesoscale plasticity problems for crystal with complex microstructure.

Acknowledgements

My deepest appreciation goes to my parents, **Mr Rulang Ying** and **Mrs Aihua Yao**, for their firm and persistent belief in me and selfless love devoted to me.

I would like to express my gratitude to **Professor Alexander M. Korsunsky** for the opportunity he has offered me for the unforgettable once-in-a-lifetime living and researching experience in Oxford.

My dearest colleagues and friends are kindly acknowledged for their academic support and company throughout this important period of my life. In particular, Professor Jin-Chong Tan, Professor Lifeng Ma, Dr Tan Sui, Dr Alexander J G Lunt, Dr Gaurav Mohanty, Dr Enrico Salvati, Dr Bohang Song, Dr Igor Dolbnya, Dr Kalin Dragnevski, Dr Jiří Dluhoš, Dr Mahdi E Mahmoud, León R Brandt, Hongjia Zhang, Yuewen Sheng, Chrysanthi Papadaki, Kirill Titov, for the academic guidance, collaboration and sleepless nights spent together on synchrotron and microscopy experiments. Additionally, to Haoyang Mao, Yichen Li, Xiaochen Wang, Rui Jia, Xianghui Ye, Wenxiang Wang, Chenyang Xue for your kindest company, emotional support and/or pleasant business collaboration. And to many family and friends not listed here, who I am glad to have shared my honesty with.

Gratitude must go to my tutors and teachers who have inspired and encouraged me to meet higher expectations and, in general, affected my life monumentally. In particular, to Dr Kuan Yoong Chan, Dr Hengan Ou, Linlin Shan, Anping Cheng, Chonger Wang, Guozhong Wei, Qiujuan Ma, Qing Ye, Jin Du.

Finally, a big thank-you to everyone in my life who has helped me directly or indirectly achieve my position today.

Common abbreviations

BCC	Body Centred Cubic crystal structure
BCDI	Bragg Coherent X-ray Diffractive Imaging
CCD	Charge-coupled Device
CRSS	Critical Resolved Shear Stress
DCM	Double Crystal Monochromator
DDD	Discrete Dislocation Dynamics (models)
DIC	Digital Image Correlation (algorithm)
DLS	Diamond Light Source (Synchrotron X-ray Source, UK)
EBSD	Electron Backscattered Diffraction
EDS	Energy Dispersive X-ray Spectroscopy
FCC	Face Centred Cubic crystal structure
FE	Finite Element (method or analysis)
FESEM	Field Emission Scanning Electron Microscopy
FIB	Focused Ion Beam (microscopy)
FWHM	Full Width at Half Maximum
GNB	Geometrically Necessary (dislocation) Boundary
GND	Geometrically Necessary Dislocation
IDB	Incidental Dislocation Boundaries
KB	Kirkpatrick-Baez (X-ray focusing mirror pair)
MBLEM	Multi-Beam Laboratory for Engineering Microscopy
MCF	Mutual Coherence Function
MCP	Multi-Channel Plate (ion imaging detector)
MOI	Mutual Optical Intensity
RVE	Representative Volume Element
SEM	Scanning Electron Microscopy
SSD	Statistically Stored Dislocations
TEM	Transmission Electron Microscopy

Table of contents

Abstract ..... **I**

Acknowledgements ..... **II**

Common abbreviations ..... **III**

Table of contents **1**

List of Figures **5**

List of Tables **14**

Chapter 1 Why do we care about scale anyway? an introduction **15**

Chapter 2 Scientific background and methods **19**

2.1 Ni-base superalloys 19

2.1.1 Introduction and applications 19

2.1.2 Composition, structure and phases 20

2.1.3 Mechanical properties and modes of failure 24

2.2 Microstructure and mechanical characterization techniques 27

2.2.1 Electron microscopy techniques 27

2.2.2 Focused ion beam technique 34

2.2.3 Micropillar compression technique 38

2.3 Crystal size effect: phenomena, theories and models 41

2.3.1 Hall & Petch and power law 42

2.3.2 Discrete dislocation dynamics models 43

2.4 X-ray Diffraction Microscopy 45

2.4.1 Fundamentals of X-ray diffraction 45

2.4.2 The Laue method 48

2.4.3 Scanning micro-Laue X-ray microscopy and reciprocal space mapping 51

2.4.4 Dual-mode micro-focus full-field imaging and reflective Laue diffraction during *in situ* pillar compression 62

2.4.5 Bragg Coherent X-ray diffraction imaging of strain in single crystal 63

Chapter 3 On the nanostructural origins of the size effect in the compression response of single crystal Ni-base superalloy micropillars 65

3.1 Introduction and motivation 66

3.2 Experimental method 70

3.3 Micropillar compression test results 76

3.4 Models for flow stress of two-phase single crystal 87

3.4.1 An approximate model based on the intrinsic length scale d and external dimension D 87

3.4.2 A model explicitly incorporating the finite size effect 91

3.5 Discussion 94

3.6 Conclusion 96

Chapter 4 *In situ* micro-Laue diffraction studies on the three-point bending of a notched single crystal 97

4.1 Introduction and motivation 98

4.2 Material and specimen preparation 100

4.3 Experimental setup 102

4.4 Experimental Procedures 105

4.5 Data interpretation 108

4.5.1 X-ray Intensity 108

4.5.2 Elastic strain and stress 113

4.5.3 Misorientation 115

4.5.4 Bragg peak streaking analysis 117

4.5.5 Peak splitting 121

4.6 Reciprocal space mapping 126

4.7 Discussion 130

4.8 Conclusion 133

Chapter 5 Development of dual mode X-ray microscopy technique for *in situ* micropillar compression test 134

5.1 Introduction, motivation and background 135

5.2 Material, specimen and experimental set-up 140

5.3 Experimental procedures and methods 146

5.3.1 Triangulation calibration 147

5.3.2 Full-field imaging and Laue diffraction 148

5.3.3 Peak fitting and indexation 150

5.4 Experiment results 154

5.4.1 Laue pattern and peak study 154

5.4.2 Laue spot sequence and mechanical annealing 160

5.4.3 Loading response and size effect 164

5.5 Discussion and conclusion 167

Chapter 6 Dislocation-based modelling for mesoscale plasticity and the development of advanced X-ray diffractive imaging techniques 169

6.1 Dislocation Dynamics and Modelling 170

6.1.1 Dislocation properties, force and dynamics 171

6.1.2 Discrete dislocation simulations 177

6.1.3 A versatile 2.5-D discrete dislocation dynamics model 179

6.1.4 Conclusions 188

6.2 Bragg coherent X-ray diffractive imaging of dual-phase Ni-base superalloy single crystals 189

6.2.1 Fundamentals of the coherent diffractive method 189

6.2.2 Experimental practices and solutions 196

6.2.3 Experiment design and performance 198

6.2.4 Results and discussion 202

6.2.5 Discussion and future work 205

Chapter 7 Conclusions and future work 207

Publications by the Author 211

References 215

List of Figures

Figure 2.1 Schematic of a typical gas turbine engine [5]. 20

Figure 2.2 Crystal structure of $L1_2$ type: (a) unit cell (b) atomic arrangement in the (111) plane, with the stacking sequence indicated 21

Figure 2.3 Secondary electron image and Energy-Dispersive X-ray Spectroscopy maps of single crystal CMSX-4 alloy, collected on the (0 0 1) plane 23

Figure 2.4 Illustration of the {1 1 1} ⟨1 1 0⟩ slip system in FCC structured crystals 26

Figure 2.5 Electron microscopic images (a) SE imaging of etched nickel superalloy ABD1 with weak phase contrast (b) SE and BSE imaging of a cracked nano-multilayer coating on a polymer substrate 30

Figure 2.6 Inelastic interaction of the electrons which produce (a) characteristic X-rays; (b) Auger electrons..... 31

Figure 2.7 EDS elemental mappings of a pristine hexagonal monolayer WS_2 domain, before (a, b, c, d) and after (h, i, j, k) being degraded by high-power laser exposure. [31]..... 33

Figure 2.8 The ion-solid interaction for FIB (a) imaging; (b) milling; (c) deposition. 35

Figure 2.9 Focused ion beam examples of (a) 3D tomography of Li battery electrodes at various cyclic charge/discharge stages; [21] (b) “Parallel” FIB-DIC milling arrangement (‘chocolate block’ geometry) with ion-beam deposited platinum ‘sunflower’ patterns; [35] (c) micropillar fabrication for compression test; (d)TEM lamella fabrication and lifting (taken in the MBLEM lab @ Oxford)..... 36

Figure 2.10 (a) An illustration of X-ray diffraction from a lattice row of atoms; (b) the incident and diffracted beam by vector notation. 46
Figure 2.11 Bragg's Law diagram.....47
Figure 2.12 The Ewald reflecting sphere (2D diagram) for the hkl reciprocal lattice section probed by a polychromatic beam with the maximum wavelength λ_{max} and minimum wavelength λ_{min}. 49
Figure 2.13 Schematic diagram of the Kirkpatrick Baez mirror focusing system. 51
Figure 2.14 Cartesian coordinates attached to the real-space unit cell 52
Figure 2.15 Reciprocal space illustration for broadened Bragg peak (shaded in blue), with $\mathbf{q}_{||}$//Q and transverse plane directions $q_{\perp}$ shown in parallelogram. ...58
Figure 3.1 An illustration of the experimental setup: (a) pre-tilted frame of the ALEMNIS in-chamber nanoindenter; (b) SEM image from a 70˚ tilt angle showing the single crystal diamond flat punch hovering over a FIB-fabricated pillar. 72
Figure 3.2 A typical experimental result set: (a) a sequence of 70◦ tilt SEM imaging video recorded during the compression test of a micropillar; (b) High resolution SEM image (taken at 30˚ title angle) of a micropillar after compression; (c) True stress and strain curve of the pillar, with individual stress drops associated with the corresponding distinct slip bands.....76
Figure 3.3 (a) Variation of Schmid factor of the six active slip system as a function of the azimuthal angle of misalignment between the loading direction and the crystal axis [001] in the range 0˚ to 180˚. (b) Maximum Schmid factor variation as a function of azimuthal angle in the range 0˚ to 180˚.....78

Figure 3.4 Comparison of two similar sized pillars (a)SEM image of a 30◦ tilt 1.5μm pillar dominated by cross slips during compression; (b) SEM image of a 30◦ tilt 1.41μm pillar dominated by large slipping during compression. 80
Figure 3.5 FIB-SEM tomography and EDS results. (a) A FIB milled vertical section of a pillar after compression in both SE and BSE detectors (55˚ tilt), featured by one slip burst; (b) EDS results shows phase contrast by Al, Co, Ni and Cr mapping, on a selected area indicated on the SE image; (c) Comparison of EDS spectrum of the typical γand γ' phase, indicated on the BSE image.....82
Figure 3.6 (a) Typical stress-strain curves for pillars of different diameters. (b) Plot of true flow stress at 5% true compressive strain for all tested pillars, and fitting of the data. 84
Figure 3.7 Flow stress of a micropillar is under uniaxial compression: boundary and inclusion effect (a) Perfect pillar with surface effect. (b) Equivalent damaged pillar with surface effect, considering the weak phase.....87
Figure 3.8 Flow model incorporating the effects of amorphous surface layer and varying internal friction (critical shear stress).....88
Figure 3.9 Centre crack in a strip [143].....91
Figure 4.1 Beamline Schematic for B16 [152] 102
Figure 4.2 DEBEN in situ tensile testing stage with max loading of (a)200 N; and (b)5000 N [153] 103
Figure 4.3 Experimental setup on the beamline. The gold colour box contains the KB mirror pair, with associated controls. 104
Figure 4.4 Schematic diagrams of sample preparation and experimental setup. 105

Figure 4.5 Laue diffraction pattern of Silicon {001} of sample-detector distance 110 mm, and energy band of 6-26 KeV.....106
Figure 4.6 Laue diffraction pattern from ABD sample, collected (a) in the elastic region on the sample; (b) from a plastically deformed region that shows “streaking” of Bragg spots 107
Figure 4.7 ABD alloy: Diffraction intensity map over the notch crack at different loading stages: (a) diffraction intensity map over the crack tip when loaded up to 100 N; (b) intensity map when initially loaded to 5 N; (c) SEM image of the crack tip when unloaded and dismounted; (d) normalized dislocation density map of the region loaded to 100 N; (e) dislocation density map initially loaded to 5 N; (f) Symmetric 3D finite element modelling on the stress concentration of the specimen geometry. 111
Figure 4.8 CMSX4 alloy: diffraction intensity map over the notch crack at different loading stages: (a) diffraction intensity map over the crack tip when loaded up to 1000 N; (b) intensity map when loaded to 2000 N, with map zone indicated in dashed frame; (c) comparison image between frame a and b, showing the intensity difference; (d) dislocation density map of the region loaded to 1000 N; (e) normalized dislocation density map initially loaded to 2000 N; (f) density difference of different loading stage, based on mapping data shown in d and e. 112
Figure 4.9 Maps of elastic strain and stress tensor components based on the indexed lattice parameters on CMSX-4 alloy when loaded up to 1KN (a) local elastic strain tensor mapping in experimental axes XYZ; (b) local elastic stress tensor mapping in experimental axes XYZ.....114

Figure 4.10 Illustration for misorientation vector **m**, showing difference between any reciprocal space point to the nearest Bragg spot.....116
Figure 4.11 Misorientation variation of the sample surface normal vector for CMSX-4 alloy under loading of 2KN and 1KN respectively. 116
Figure 4.12 Illustration of the normal axes of a (0 0 L) reflection Laue spot which streak as a result of slip activity of geometrically necessary dislocations on the slip systems defined by b = [-1 1 0]/2, τ= [1 1 -2]/6 resulting ξ= [1 1 0]/ 2. The diffraction pattern is taken from Fig. 4.8e for CMSX-4 sample loaded to 2000N. 118
Figure 4.13 Laue diffraction patterns for CMSX-4 alloy, (a) elastic region with Bragg peaks indexed by hkl indices; (b) Peak separation due to SSDs; (c) pattern streaking due to geometrically necessary slip system with b=[110]; and (d) streaking due to GN slip system b=[-110].....119
Figure 4.14 Bragg peak (00L) consisting of two local cell blocks with misorientation between them.....122
Figure 4.15 Illustration of lattice cell orientation relative to XYZ(system) coordinates derived from two fitted peaks P1 and P2 (Fig 4.13) 122
Figure 4.16 3D visualization of the stress tensor for two cell blocks indexed by P_1 and P_2, (a) P_1 stress tensor in lattice coordinates; (b) P_2 stress tensor in lattice coordinates; (c) P_1 stress tensor in experiment coordinates; (d) P_2 stress tensor in experiment coordinates. 123
Figure 4.17 Monochromatic incident beam energy scan spanning 8 KeV to 20 KeV, with respect to the maximum Laue spot intensity collected on the area detector 127
Figure 4.18 3D intensity map in reciprocal space of (1 -1 7) peak.....128

Figure 4.19 The 3D reconstruction of intensity map of a Laue spot (1 -1 7) streaks in reciprocal space.....129
Figure 5.1 (a) TESCAN LYRA3 dual beam FE-SEM and FIB system at MBLEM, University of Oxford; (b) ALEMNIS in-chamber nanoindenter with high resolution optical microscope attached, mounted on rotation-enabled stage.....143
Figure 5.2 (a) Focused ion beam milled free standing micropillars on the edge of prism-shaped bulk crystal with the direction of the [001] axis indicated; (b) experimental setup schematic. 144
Figure 5.3 Multi-detector arrangement on the beam with CCD area detector, diode, side-view and top-view optical microscopes. 145
Figure 5.4 (a) 55° tilted SEM image of FIB fabricated micropillar on the surface of silicon wafer; (b) Diffraction pattern of the silicon micropillar collected by the CCD area detector. 146
Figure 5.5 Schematic for triangulation distance calibration 147
Figure 5.6 Schematic of full-field magnification imaging with images collected on X-ray EYE detector at various sample-detector distances.....149
Figure 5.7 (a) contour map of the intensity of a [0 0 L] reflection spot of silicon; (b) fitted peak of the same reflection.....151
Figure 5.8 Comparison of strain tensor visualizations of indexed Laue pattern of Silicon pillar before (transparent mesh) and after (coloured surface) strain refinement process, where (b) is a zoom-in of frame (a). 152
Figure 5.9 Indexed Laue pattern from (a) silicon pillar as calibration sample, and (b) CMSX-4 pillars with *hkl* peaks labelled. 153
Figure 5.10 Laue pattern of the studied CMSX-4 alloy micropillar on the nanoindenter; (a) full frame collected on CCD detector; (b) zoom in of the [066]

reflection of CMSX-4; (b) zoom in of the [-1,5,3] peak of the diamond indenter tip. 155
Figure 5.11 Plots of X-ray transmission through (a) 2-micron thick CMSX-4 alloy and (b) 20-micron diamond crystal across different photon energy (eV); 3D morphology of the intensity map of (c) [0 6 6] reflection of CMSX-4 and (d) [-1 5 3] reflection of the diamond. 156
Figure 5.12 SEM image of the tested pillar (a) at 55° tilt angle before the experiment; and (b) at 30° tilt angle after the compression test.....157
Figure 5.13 Comparison of two sets of split peaks in (a) strain tensor; (b) stress tensor; where the transparent mesh stands for primary peak and the solid coloured surface stands for secondary peaks. 158
Figure 5.14 (a) 2D Gaussian fit of the peak intensity of [006] reflection; (b) 3D Gaussian surface fit of the peak intensity; 159
Figure 5.15 Bragg peak [006] of the CMSX-4 pillar under various loadings 160
Figure 5.16 Peak intensity distribution map of the [-1 5 5] reflection of CMSX-4 alloy at (a) before compression; (b) 0.73 GPa loading; (c) 1.40 GPa loading; and (d) 1.18 GPa (softening stage); 162
Figure 5.17 (a) Illustration of the indexed lattice orientation comparison, where the black cube represents the initial status and the blue and red represent the upper and lower part of the slipped pillar; (b) visualization of the strain tensor of the upper(solid colour) and the lower part(transparent mesh) of the pillar.....164
Figure 5.18 (a) The true stress and strain response curve of the pillar for the compression test, where pauses for Laue pattern collection is marked by true displacements; (b) true flow stress at 5% with various top diameters, with the tested pillar in the present work marked as red square. 166

Figure 6.1 (a) Illustration of an edge dislocation with line direction along z-axis (perpendicular to the plane of paper), where b is the Burgers vector; (b) illustration of a screw type dislocation on the plane indexed P. 172
Figure 6.2 simulation plane of the model (a) close boundary grain at 300 MPa compressive external stress with simulation plane at an angle off the [001] direction; (b) periodic two boundary two-phase single crystal with simulation plane at [001] direction. 179
Figure 6.3 visualization of the stress field by an edge dislocation in an infinite plane.....181
Figure 6.4 Illustration of a single dislocation at (ξ,0) near a half-plane with an arbitrary point P described by r_1 and r_2. 183
Figure 6.5 Visualization of the stress field by an edge dislocation near free surface (to the left). 183
Figure 6.6 (a) Model setup for the Ni-base superalloy unit cell RVE. (b) The simulation plane snapshot of the discrete dislocation distribution within the ductile γ-phase under the maximum compressive stress of 300MPa, in the second fatigue half-loop; (c) The cyclic stress-strain curves for the RVE under cyclic loading. (d) The monotonic tensile loading curves for the RVE with different crystallographic orientations (α values). 185
Figure 6.7 The graphic user interface (GUI) of the model code for dual-phase crystal micropillar compression tests 187
Figure 6.8 Coherence length defined by half width at half maximum (HWFM) (a) Spectral bandwidth; (b) coherence length defined as destructive interference due to finite spectral bandwidth for radiation of wavelength λ and spectral bandwidth $\Delta\lambda$. 192

Figure 6.9 the general outline of the reconstructing algorithm.....196
Figure 6.10 Beamline schematic for I13-1 (coloured) at Diamond Light Source [194] 200
Figure 6.11 Illustration of the experimental setup of BCDI on beamline I13 at DLS. 201
Figure 6.12 Coherent Bragg peak for <111> planes collected by rocking χ at 0.04-degree steps.....202
Figure 6.13 Coherent Bragg peak for <0 0 2> planes collected by rocking θ at 0.04-degree steps.....203
Figure 6.14 3D visualisation of the treated data. Cross sectional intensity view for (a) reflection <111> (b) reflection <002> and (c) and (d) isosurfaces, respectively. 204

List of Tables

Table 2.1 Nominal Composition of Studied Superalloys.....21

Table 3.1 CMSX-4 Alloy Nominal Composition 69

Table 4.1 Grinding and polishing procedure for Ni-base superalloy 101

Table 5.1 The composition and etching condition for Kalling's No. 2 etchant..141

Table 5.2 Focused ion beam settings for micropillar fabrication.....142

Table 6.1 The terms and scales used to describe mechanics [197] 170

Chapter 1

Why do we care about scale anyway?

an introduction

The properties of materials have come into the focus of human attention ever since the very first tool was adopted in the stone age for productive purposes of supporting human existence. The techniques for developing or obtaining the best properties of materials to serve particular functions were discovered and used by the human race since several thousand years ago, first with stone and wood, and then with metallic armaments, such as swords. Mechanics-based, or mechanistic approaches for explaining the observed material behaviour dominated scientific research, until the development of physics progressively made it possible to begin looking inside materials towards the end of the nineteenth century. Such studies were greatly accelerated by the discovery of X-rays by Konrad Röntgen in 1895, and the development of the methods of using them for imaging and crystal structure analysis, such as X-ray diffraction by Max von Laue and the Braggs. The development of particle accelerators prepared the ground for the creation of advanced synchrotron sources, which made it possible to use X-rays for the characterization of material structure, defects such as vacancies and dislocations, etc. However, instead of the convergence towards one unified physical theory, significant differences in approaches and methods arise when we try to understand the material properties at different scales. The lack of unification in physics remains obvious in the fact that different descriptors and principles are applied depending on the certain length scale of consideration. It is nevertheless

encouraging to see that recent developments in advanced X-ray and electron microscopy techniques and the associated micro- and nano-mechanical materials testing techniques, linked to the corresponding theories of electronic structure, atomic and molecular interactions, and dynamics of dislocations, allow the understanding of crystal structure and defects to be related (through large computational frameworks) to the bulk material properties manifested in the macro-scale (continuum) behaviour.

With the required properties of the engineered and natural materials can be evaluated and understood on ever finer length scales, exquisite control over the nano- and microstructure can be achieved accordingly. An outstanding example is provided by the family of high-temperature materials known as Ni-base superalloys that develop complex multi-phase microstructure which makes them the principal choice of material to perform specific mechanical, thermal and chemical tasks under extreme working conditions. The results reported in this thesis are mainly devoted to the development and application of advanced material characterization techniques that emerged within the last decade(s), aiming to explore most feasible experimental approaches in combination with dislocation modelling, to achieve better understanding of mesoscale plasticity and its contribution to bulk material behaviour.

This thesis consists of the following chapters:

Chapter 2 provides a review of the materials studied. Ni-base superalloys are discussed from the point of view of their composition, structure, mechanical properties, and the modes of failure. In addition, this chapter also reviews the fundamentals and state-of-art of several advanced material characterization

techniques, including electron/ion microscopy techniques, X-ray diffraction methods (Laue and Bragg diffractive imaging), and micromechanical testing.

Chapter 3 reports on the fabrication of Ni-base superalloy micropillars using Focused Ion Beam (FIB), and in-chamber micropillar compression experiments performed in the MBLEM lab at Oxford. The results of these experiments show the so-called ‘size effect’ of the flow stress response. The deformation of the micropillars is then examined closely using a FIB-SEM microscope, and the correlation between the observations and the stress-strain deformation response is discussed. A dislocation-based flow stress model for finite size crystal with intrinsic length scale is proposed, and good agreement with the experimental data is recorded.

Chapter 4 presents the results of *in situ* micro-Laue diffraction study of three-point bending of two types of Ni-base superalloy samples. Two different types of superalloy specimens with different stress-strain behaviour were loaded and examined by sub-micron focused synchrotron X-ray beam. The feasibility of using the micro-Laue method to study Ni-base superalloy single crystals is discussed, together with the reciprocal space diffractive imaging experiments performed carried out.

Chapter 5 reports on the development of variable magnification full-field X-ray microscopy to enable *in situ* single-crystal micropillar compression test using micro-Laue diffraction method. The approaches developed for the preparation, microscopic observation and dislocation structure analysis during micropillar compression are presented and discussed. The resulting insights into dislocation plasticity of micropillars are presented and discussed.

Chapter 6 presents the results of the synchrotron experiment using Bragg coherent X-ray diffraction imaging (BCDI) technique applied to Ni-base superalloy single crystal micropillars, a first-ever trial of such technique for single crystals with complex microstructure and strain distribution. A detailed explanation is presented of a versatile 2.5D discrete dislocation dynamics model, with multiple applications to simulating the bulk and micro-mechanical response of FCC crystals given.

Chapter 7 draws conclusions from the results presented in this thesis and proposes some ideas for future work.

Chapter 2

Scientific background and methods

This chapter contains a literature review of the materials studied in the present project, namely, Ni-base superalloys: their composition, microstructure, and mechanical properties which are key to their application in the aerospace industry. An introduction is also provided to several principal material characterization techniques employed in this study, including micro-mechanics experimentation, electron microscopy, and X-ray diffraction techniques. Finally, a brief review of the size dependence of the mechanical properties of crystalline materials is given, along with an overview of the modelling techniques developed for the relevant problems.

2.1 Ni-base superalloys

2.1.1 Introduction and applications

The turbine plays a key role in the aeroengine: it extracts energy from the hot gas stream and converts it to mechanical power to drive the compressor, and to generate electricity supply for the aircraft [1–4]. As shown in Figure 2.1, in a typical gas turbine aeroengine, the air is taken in through the inlet, compressed by a series of compressor discs and blades (stages), gets mixed with the fuel, before getting ignited and burned within the combustion chamber.

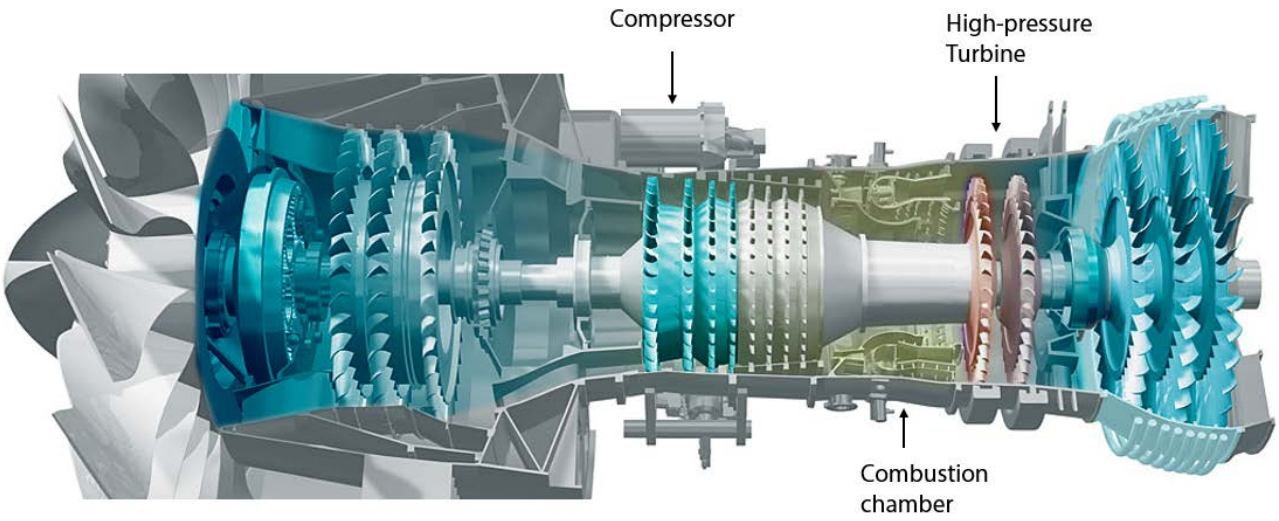

Figure 2.1 Schematic of a typical gas turbine engine [5].

Combustion product gases rotate the successive sets of turbine blades (stages), and finally get released by expanding to the outside pressure. Generally speaking, higher operating temperatures improve the efficiency of a gas turbine and lower the emission levels of CO_2 and NO_x. Following this reasoning, superior high temperature materials have been progressively sought. The outstanding high temperature properties of nickel-based superalloys make them an attractive choice for gas turbines.

2.1.2 Composition, structure and phases

Superalloys, as a family of metallic materials based on either Ni, Fe or Co, show very good mechanical and chemical properties even at absolute temperatures that amount to a high fraction (over 0.6) of the absolute temperature of their melting point [1,6,7].

Alongside the Ni base, a superalloy contains typically more than 10 alloying elements in total. Ni base defines the face-centred cubic (FCC) crystal lattice

structure, low thermal activation, and the absence of phase transformations from room temperature to the upper operating temperatures reached in service. Table 2.1 gives the nominal composition of the two Ni-base superalloys studied in this project [1,6,8].

Table 2.1 Nominal Composition of Studied Superalloys

Alloy	Composition WT%													
	Ni	Cr	Co	Mo	Fe	Al	Ti	Ta	W	Zr	C	B	Re	Hf
CMSX-4	bal.	6.5	9.6	0.6	-	5.6	1	6.5	6.4	-	-	-	3	0.1
ABD1	bal.	8	10	-	-	5.8	-	8.5	8.5	-	-	-	1.6	-

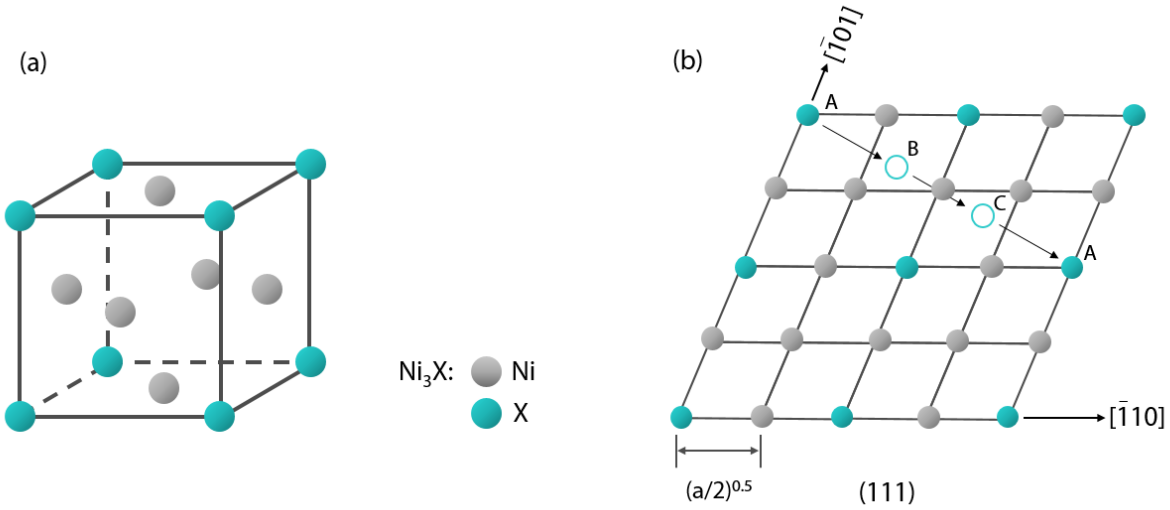

Figure 2.2 Crystal structure of $L1_2$ type: (a) unit cell (b) atomic arrangement in the (111) plane, with the stacking sequence indicated

Each of the alloying elements is added due to its ability to enhance certain specific property. For instance, aluminium is added to form Ni_3Al precipitates, an ordered cubic type compound ($L1_2$ - γ' phase). Such ordered compound precipitates coherently with the nickel-rich matrix (γ phase).

Figure 2.2(a) shows the unit cell of the $L1_2$ crystal structure, where Ni atoms occupy face centres of the cubic unit cell, while solute elements reside at cube corners. Such structure is very similar to that of FCC nickel, as can be seen in Figure 2.2(b), which shows the atomic arrangement of the close-packed (1 1 1) plane. It is evident that solute atoms follow a typical triangular ordering, and occupy alternate positions in rows along the [1 1 0]-type directions. The ABC stacking sequence is also indicated by the position of the solute atom in A, B and C layers. Similar arrangement of atoms can be found in the (1 1 1) plane of FCC nickel and in the planes of many other structures, including $D0_{24}$ (0 0 1), $D0_{19}$ (0 0 1), Cu_3Ti (0 1 0), etc. In contrast, in the disordered γ phase there is uniform probability of finding a Ni or a solute atom at any location within the structure. Coherence (lattice continuity) is maintained between different phases, whilst the structural difference between the γ' and γ phases leads to a small lattice parameter mismatch. This leads to misfit between phases, and lattice straining. Furthermore, dislocation glide is impeded by the interphase boundaries, where dislocation splitting leads to the creation of partial dislocations. Together, these effects lead to appreciable overall strengthening: increased yield strength and ultimate tensile strength(UTS), good high temperature performance, and asymmetric tensile/compressive properties.

Global and local variation in the solute concentration leads to the formation of different phases that are distinct in terms of structure and ordering: along with γ (the FCC matrix) and $\gamma'(L1_2)$ already mentioned, prominent phases present have the types $\gamma''(D0_{22})$, $\beta(Cu_3Ti)$, $\eta(D0_{24})$, topologically close-packed (TCP) phases, etc. In the alloys which are investigated here, γ and γ' phases are the two main phases present. They form a particular microstructure with the principal feature of

cuboidal precipitates, as can be seen in the SEM image Figure 2.3. The γ' phase appears dark in the image. The formation of cuboidal precipitates (with lateral dimensions from 200 nm to 600 nm) is related to the minimization of overall energy, including the contributions from strain energy and surface/interface energy terms. High volume fraction (up to 60-70%) of precipitates can be achieved with good coherence between the precipitates and the matrix being maintained. The size, spacing and conditioning of the precipitates can be optimized in order to enhance overall strength through preventing dislocations from bowing around obstacles, forcing them to cut through the precipitates, leading to the increase in the effective Critical Resolved Shear Stress (CRSS).

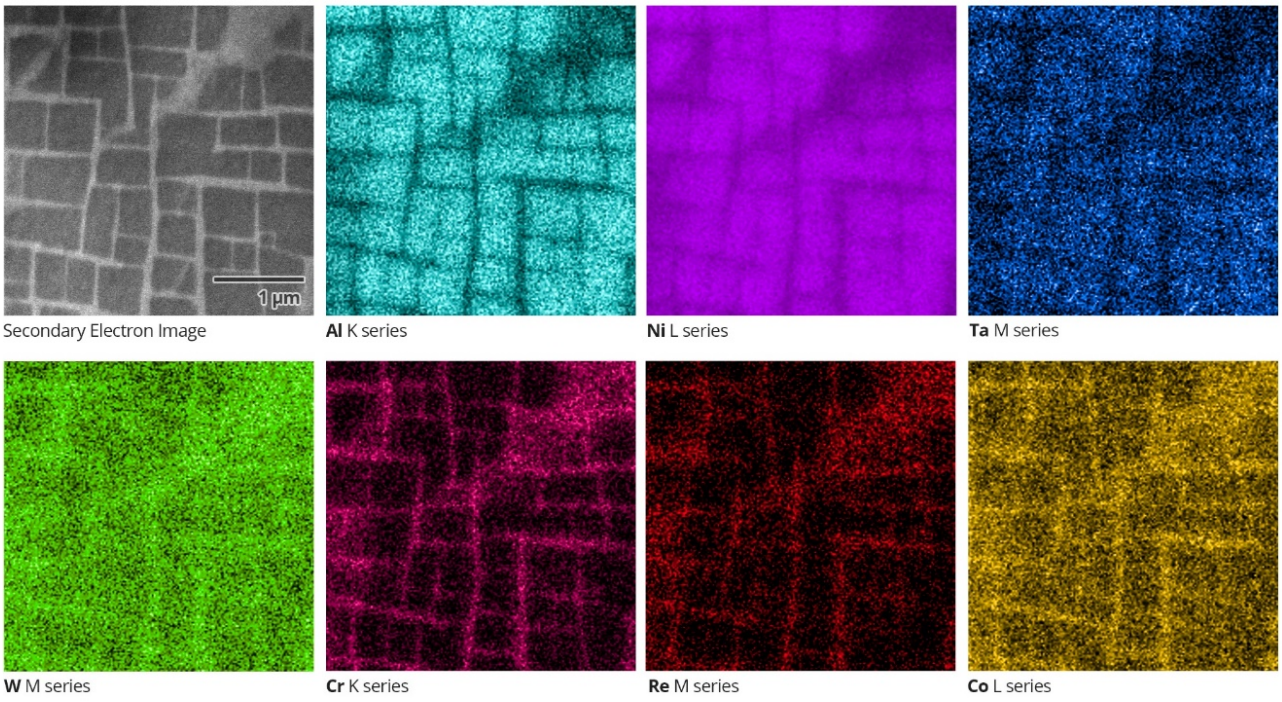

Figure 2.3 Secondary electron image and Energy-Dispersive X-ray Spectroscopy maps of single crystal CMSX-4 alloy, collected on the (0 0 1) plane

Further alloying elements are added to nickel-base superalloys for various purposes. These can be grouped into solid solution forming (W, Mo, Cr, Re, Co, etc.) and precipitate forming elements (Al, Ta, Ti) [2,3]. It has been found that Re confers significant improvement in creep resistance, and has been used widely in the 2nd generation of superalloys.

Apart from mechanical property control, some alloying elements also provide resistance to corrosion, oxidation and sulphidation (Cr, Al, Co), while some are added to control the lattice misfit (Ti, Mo, V, S), some of which were not present in the alloys discussed here [7].

2.1.3 Mechanical properties and modes of failure

Polycrystalline and single-crystal superalloys are used for different parts of the aeroengine [1,2,9–11]. Polycrystalline alloys are used in fabricating the combustor chamber and turbine disks, whilst single-crystal superalloys are used to manufacture turbine blades that experience the combination of the most arduous temperature and stress conditions in service. The blades mounted in successive stages downstream of the combustion chamber extract mechanical work from the hot gas stream. In order to maximise performance (thrust and energy efficiency), the blades are required to work close to their material limits of strength under hot straining. Achieving optimal creep resistance requires avoiding grain boundaries within the structure, so turbine blades are mostly manufactured in the form of single crystals.

The morphology of most commonly employed single crystal alloys (CMSX, Rene, TMS, Mar M, PW, ABD[8], etc) consists of coherent γ' precipitates embedded in the FCC γ matrix, indicating that the mechanical properties of these single crystals depend on the orientation. For instance, commonly the [0 0 1] axis is chosen to align with the blade's long axis since it possesses the lowest elastic modulus, so that elastic energy is kept to a minimum under constant strain conditions (given the strain energy density equation $\frac{1}{2}\ \sigma\varepsilon = \frac{1}{2}\ E\varepsilon^2 = \frac{1}{2}\ \sigma^2/E$). In practical manufacture, misorientations up to ~10º from the desired direction can be encountered, and have profound influence on key performance parameters, such as creep life [1,8,12–15].

The orientation-dependent response and performance of single-crystal superalloys is closely associated with the crystal slip system activity. When direct tensile or compressive stress is applied along the [0 0 1] axis, upon reaching the critical stress, octahedral slip is activated on slip systems of the $\{1\ 1\ 1\}\langle 1\ \bar{1}\ 0\rangle$ type. As illustrated in Figure 2.4, in this notation $\{1\ 1\ 1\}$ indicates the close packed slip plane, and $\langle 1\ \bar{1}\ 0\rangle$ the close packed slip direction. At elevated temperatures, cubic slip systems are thought to be activated, thus giving rise to changes in the deformation mechanism, with distinct features in the temperature-strength curve, and the tensile/compression strength asymmetry [10,16–19]. Literature reports indicate that deviations from the Schmid's law were observed for the $\{1\ 1\ 1\}\langle 1\ \bar{1}\ 0\rangle$ slip system, as shown in Figure 2.4, where glide can be blocked by cross-slip on the $\{0\ 0\ 1\}\langle 1\ \bar{1}\ 0\rangle$ system due to the presence of γ' precipitates with $L1_2$ structure, termed the Kear-Wilsdorf lock [1,20].

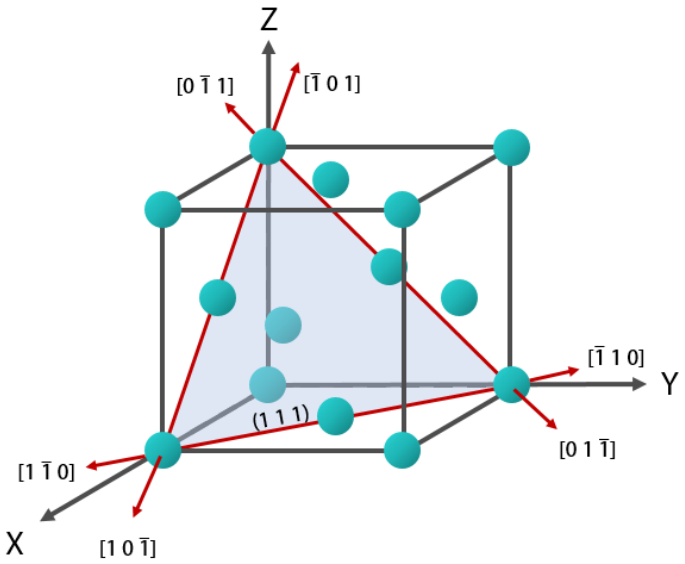

Figure 2.4 Illustration of the {1 1 1} ⟨1 $\bar{1}$ 0⟩ slip system in FCC structured crystals

Most studies of the orientation-dependent mechanical response of single crystals performed so far concern fatigue, creep, or monotonic tensile testing, given the fact that these are the working conditions of the most kinds of such crystals. There have been relatively few reports of the compression behaviour of superalloy single crystals, particularly accompanied by observation at finer scales. Therefore, micro- and nano-scale compression tests performed in the present study, coupled with *operando* deformation observation using electron microscopy and synchrotron X-ray techniques, are both timely and relevant for the characterization of single crystal alloy deformation behaviour. These experimental methodologies are reviewed in the following sections.

2.2 Microstructure and mechanical characterization techniques

Modern electron microscopy, focused ion beam milling and micro-mechanical testing techniques enable advancing materials research towards combined structure and deformation characterisation of condensed matter at the micro- to nano-scale. This chapter provides a review of the relevant techniques, identifying the procedures for sample preparation and miniature specimen fabrication, analysis of crystal deformation at fine scales, and the characterisation of material response at high spatial resolution. Each discussion is accompanied with a brief overview of the basic theory, applications, and the relevant published work, including references to the contributions made by the present author.

2.2.1 Electron microscopy techniques

Scanning electron microscopy (SEM) and transmission electron microscopy (TEM), along with various 'flavours', such as STEM (Scanning Transmission Electron Microscopy) provide a broad basis for a whole host of material characterization techniques based on various principles for the detection of signal from the beam-sample interaction volume, such as EDS, EBSD, etc. These methods have been developed to a stage whereby they are now being commonly used for microstructural studies of specimens for a wide range of applications, including 2D materials, bio-materials, natural fibre, aerospace materials, etc [15,17,21–27]. Scanning electron microscopy exploits the advantage of accelerating electrons through large voltage (normally in the range 0-30KeV), conferring on them the de Broglie wavelengths (as per equation 2.1 below) that

lie in the range 0.027 nm to 0.87 pm and are shorter than those in the visible light spectrum:

$$\lambda = h/[2m_0eU(1 + eU/2m_0C^2)]^{1/2} \quad (2.1)$$

Here λ, h, m_0, e, U, and c stand for the wave length, Planck constant, the rest mass of an electron, electron charge, the accelerating voltage, and the speed of light in vacuum, respectively. Due to the diffraction imaging limit, the use of short wavelengths allows achieving higher resolution [28].

The relativistic effects [29] for accelerated electrons are considered in the equation, including significant length contraction, time dilation and an increase in mass.

In electron microscopes, electrons are typically generated using one of two methods, thermionic emission or field emission. In thermionic emission, free electrons gain energy from external heating, overcome the attractive force of the atomic nucleus, and exit into vacuum (mostly seen in W or LaB_6 sources). In field emission, free electrons are emitted from the metal surface due to the strong electric field applied, which can take place at solid or liquid surfaces.

2.2.1.1 Scanning electron microscopy

Scanning electron microscopy is commonly used for observing the morphology of the specimen with high resolution (down to less than 1 nm per imaging pixel). In scanning electron microscopes, an electron beam is focused down to a nanometre-sized spot onto the sample surface. The beam rasters an area of the

surface defined by the magnification control, and imaging signals are recorded pixel by pixel. The two main types of imaging detectors in SEM are secondary electron (SE) detector and backscattered electron (BSE) detector.

Secondary electron detectors collect information from the electrons that are ejected from the sample atoms, which is mainly related to the morphology and surface topography. Secondary electrons are emitted from sample surface when it is struck by the electron beam. Significant contrast in secondary electron imaging is caused by edge effects, as electrons are preferentially attracted to and emitted from edges and peaks on the sample surface. The edge effect can be reduced with higher accelerating voltage of the beam.

Backscattered electron detectors collect the electrons that arrive in the illuminating beam and are scattered back after interaction with the sample, mainly through elastic collisions between the incident electron beam and the atomic electron clouds within the sample. In this process, only the trajectory of the electrons in the beam is changed, without loss in electron energy. To collected back-scattered electrons, the BSE detector is typically placed close to the sample surface, right below the ‘nose’ of the electron column that controls the incident beam. Contrast in BSE imaging is related to the mean atomic number of the sample element, as large atoms have greater scattering cross-section and hence stronger propensity to cause elastic scattering. Electron scattering is also sensitive to the underlying crystal structure of the sample, giving rise to grain contrast, which is widely used for microstructure imaging. The same mechanism leads to the formation of Kikuchi patterns that are used in for EBSD analysis.

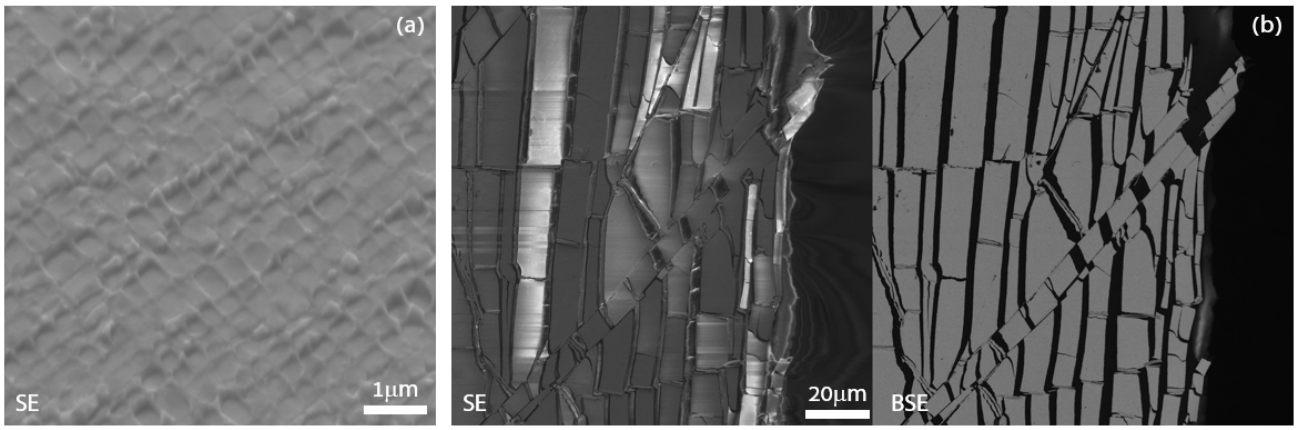

Figure 2.5 Electron microscopic images (a) SE imaging of etched nickel superalloy ABD1 with weak phase contrast (b) SE and BSE imaging of a cracked nano-multilayer coating on a polymer substrate

There are limitations to both SE and BSE imaging. Secondary electron imaging contrast depends strongly on the sample topography/morphology, so that little can be seen for very smooth surfaces (mostly polished for microscopic purpose such as EBSD). Therefore, surface roughness need to be introduced by etching.

Figure 2.5 (a) shows a SE image of the chemically etched surface of ABD1 alloy, where the precipitate/matrix contrast is hardly resolvable. Figure 2.5 (b) shows a comparison between imaging with SE and BSE for a nano-multiplayer metallic coating on a polymer substrate [24] that has developed a cracking pattern under tensile loading. The SE image is more sensitive to the surface topography, while the BSE image gives a much clear contrast between the metallic coating (appeared in grey) and polymer substrate (in black) due to atomic number difference. Both SE and BSE imaging modes only provide grey scale contrast, so that further information about sample composition and structure needs to be extracted by other detection techniques, such as EDS and EBSD, to perform elemental composition and crystal structure analysis and mapping.

2.2.1.2 Energy dispersive X-ray spectroscopy

Energy Dispersive X-ray Spectroscopy, often referred to as EDS or EDX, is a technique for the analysis of chemical elemental composition (qualitative and quantitative) widely used in conjunction with scanning electron microscopy (SEM). As one of EM analytical methods (along with Electron Energy Loss Spectroscopy - EELS), EDS detects the consequence of inelastic scattering between the incident electron beam and sample atoms. In inelastic interactions, secondary electrons, phonons, UV quanta or cathodoluminescence emission are produced due to energy being transferred from the incident electrons to the sample atoms. When inner shell electrons escape with energy gained from incident electrons, electrons from an outer shell fill the hole left in the inner shell, with the energy emitted in the form of characteristic X-ray photons, as shown in Figure 2.6 (a).

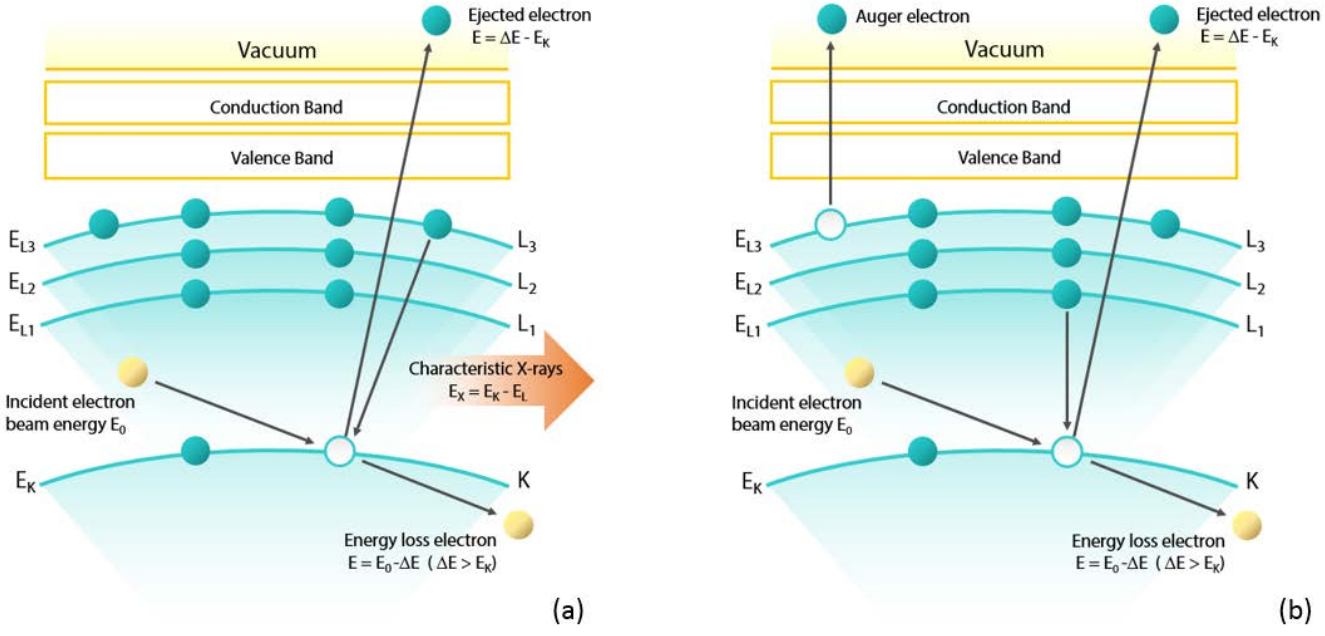

Figure 2.6 Inelastic interaction of the electrons which produce (a) characteristic X-rays; (b) Auger electrons

Another mechanism driven by inelastic interaction is the production of Auger electron by the ionization of the atom. When the hole in the inner shell is filled by an electron from an outer shell (such as L_1 shown in Figure 2.6 b), the energy released in the process is transferred to another electron (this case L_3) which is subsequently ejected as Auger electron. While X-ray production dominates in large atomic number elements, Auger electron production is favoured for elements of low atomic number.

The EDS X-ray detector, often solid-state device built around a lithium-drifted silicon crystal that measures the relative abundance of emitted characteristic X-ray as a function of their energy. According to Moseley's Law, the atomic number of the element producing the characteristic radiation can be determined by measuring the energy of a given K, L or M line, shown in the equation:

$$E = A_1(Z - A_2)^2 \qquad (2.2)$$

Here *E* stands for the energy of the emission line of a given X-ray series, *Z* is the atomic number of the emitter element, and A_1 and A_2 are two constants.

In the typical qualitative analysis that EDS technique can now provide, elements from beryllium to uranium can be determined. The spatial resolution of EDS, like other electron microscopic techniques, depends on the volume/depth of the material from which the corresponding information is collected, determined by the overvoltage (accelerating voltage minus the critical ionization energy of the examined element), and specimen density. Equation below [30] below gives a good estimate of the spatial resolution:

$$R = 0.064(E_0^{1.68} - E_C^{1.68})/\rho \quad (2.3)$$

Here R is spatial resolution (in microns); E_0 and E_C stand for accelerating voltage and the critical excitation energy respectively (in keV); and ρ is mean specimen density (in g/cc). X-ray emission and escape can occur from the greatest depth in the specimen, compared to (in descending order) back-scattered electrons, secondary electrons, and Auger electrons.

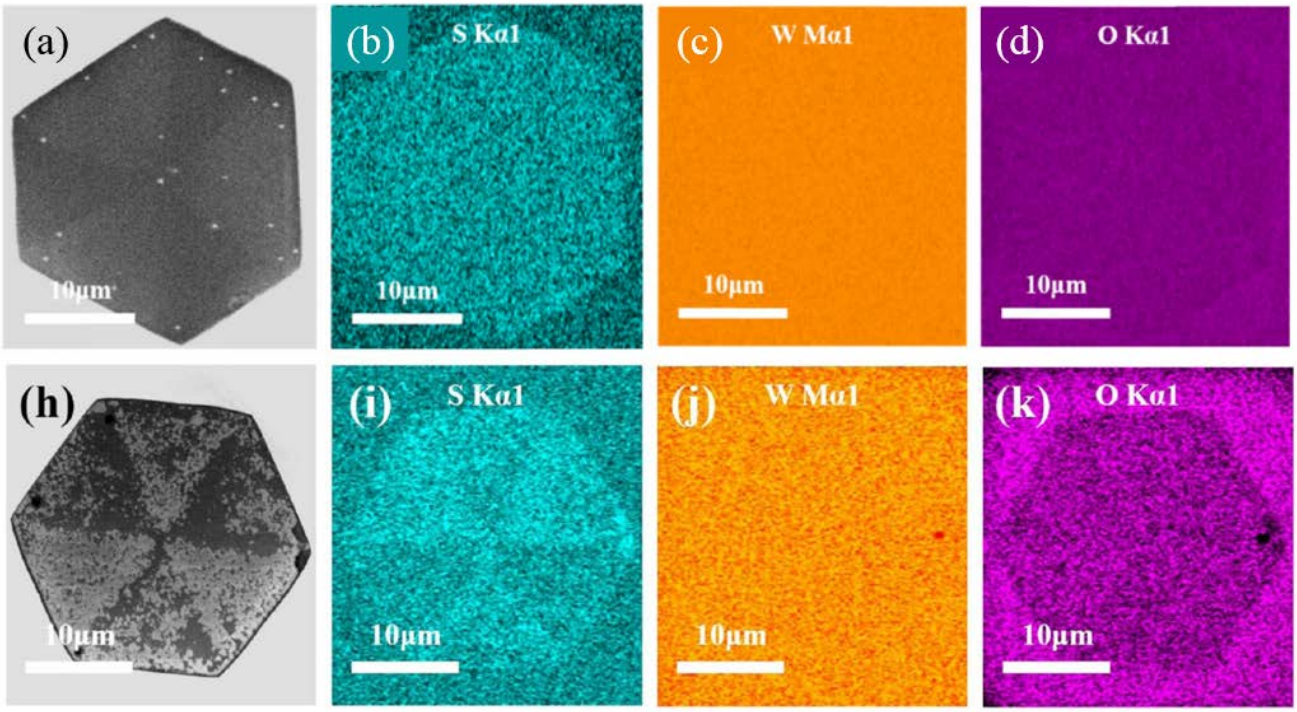

Figure 2.7 EDS elemental mappings of a pristine hexagonal monolayer WS_2 domain, before (a, b, c, d) and after (h, i, j, k) being degraded by high-power laser exposure. [31]

Figure 2.3 and Figure 2.7 provide illustration of the capabilities of energy dispersive X-ray spectroscopy technique for qualitative analysis of elemental

composition, which can underpin the studies probing the microstructure for alloys containing many elements.

2.2.2 Focused ion beam technique

Focused ion beam (FIB) is a technique developed during the 1970s and 80s that has now found wide application in various fields of research due to its ability to perform localized milling and deposition at the micro- to nano-resolution [15,21,32–39]. One application of FIB milling involves subsurface failure analysis performed by FIB technique, as well as sample fabrication for micro-mechanical testing (micropillars and cantilevers reviewed in section 2.2.3), and TEM lamella preparation.

The utilization of liquid metal ion sources for FIB microscopy has enabled the creation of small nano-probes possible. Gallium is the most commonly used liquid metal ion source for FIB instrument due to its low melting point, volatility, vapour pressure and excellent mechanical, electrical and vacuum properties, i.e. emission characteristics that enable high angular intensity with small energy spread.

The ability of the FIB instruments to mill, deposit and image depends critically on the nature of ion-solid interaction. During the imaging process (shown in Figure 2.8-a), secondary ions, neutral atoms and electrons which are generated by the focused ion beam rastering at relatively low ion current, are detected by a biased multichannel plate (MCP) detector. FIB milling is achieved, as schematically illustrated in Figure 2.8 (b), by blasting high current focused ion beam onto the sample surface in order to remove small volumes of substrate material. The system also typically allows localised deposition using the chemical vapour

deposition with the assistance of focused ion beam or electron beam, in a process that is similar to laser-induced deposition. As shown in Figure 2.8 (c), a precursor gas is injected at the surface through the nozzle, and is decomposed by the ion beam, with desired reaction products precipitating on the surface, whilst the volatile products are removed by the vacuum.

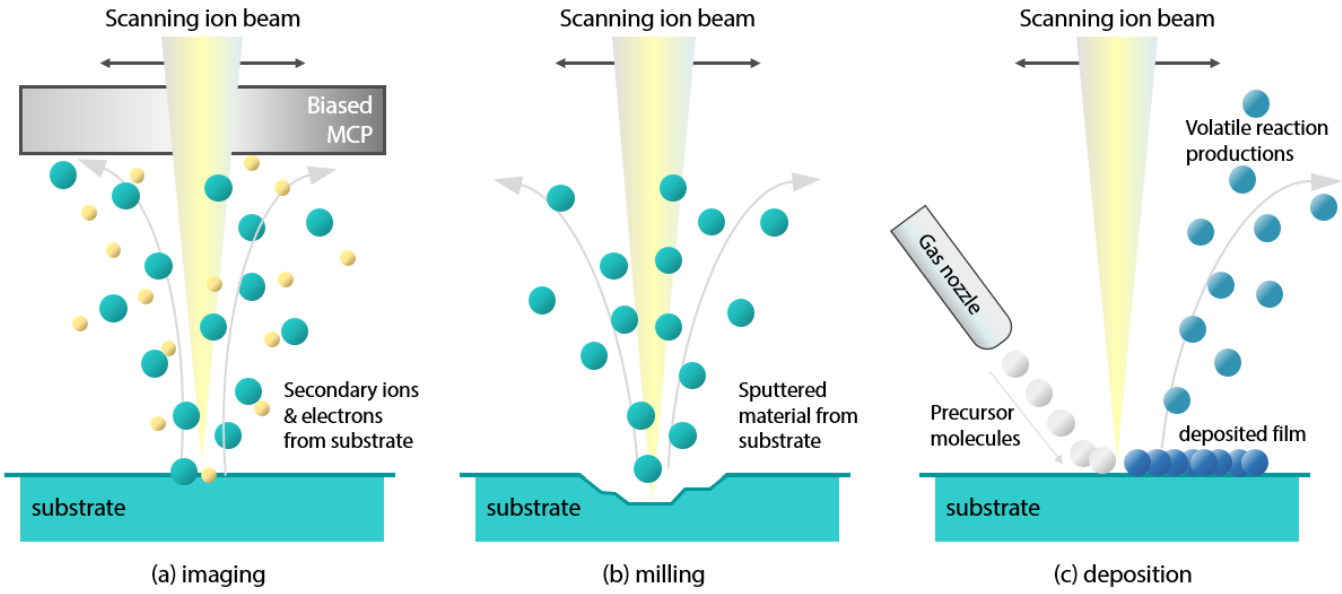

Figure 2.8 The ion-solid interaction for FIB (a) imaging; (b) milling; (c) deposition.

Modern focused ion beam instruments now come mostly in conjunction with scanning electron microscopes. The combination of high-resolution SEM imaging and FIB milling capabilities enables more versatile *in situ* studies of materials, such as metrology, 3D tomography [21], micropillar preparation, FIB-DIC ring-core milling [35] and TEM lamella fabrication and lifting out.

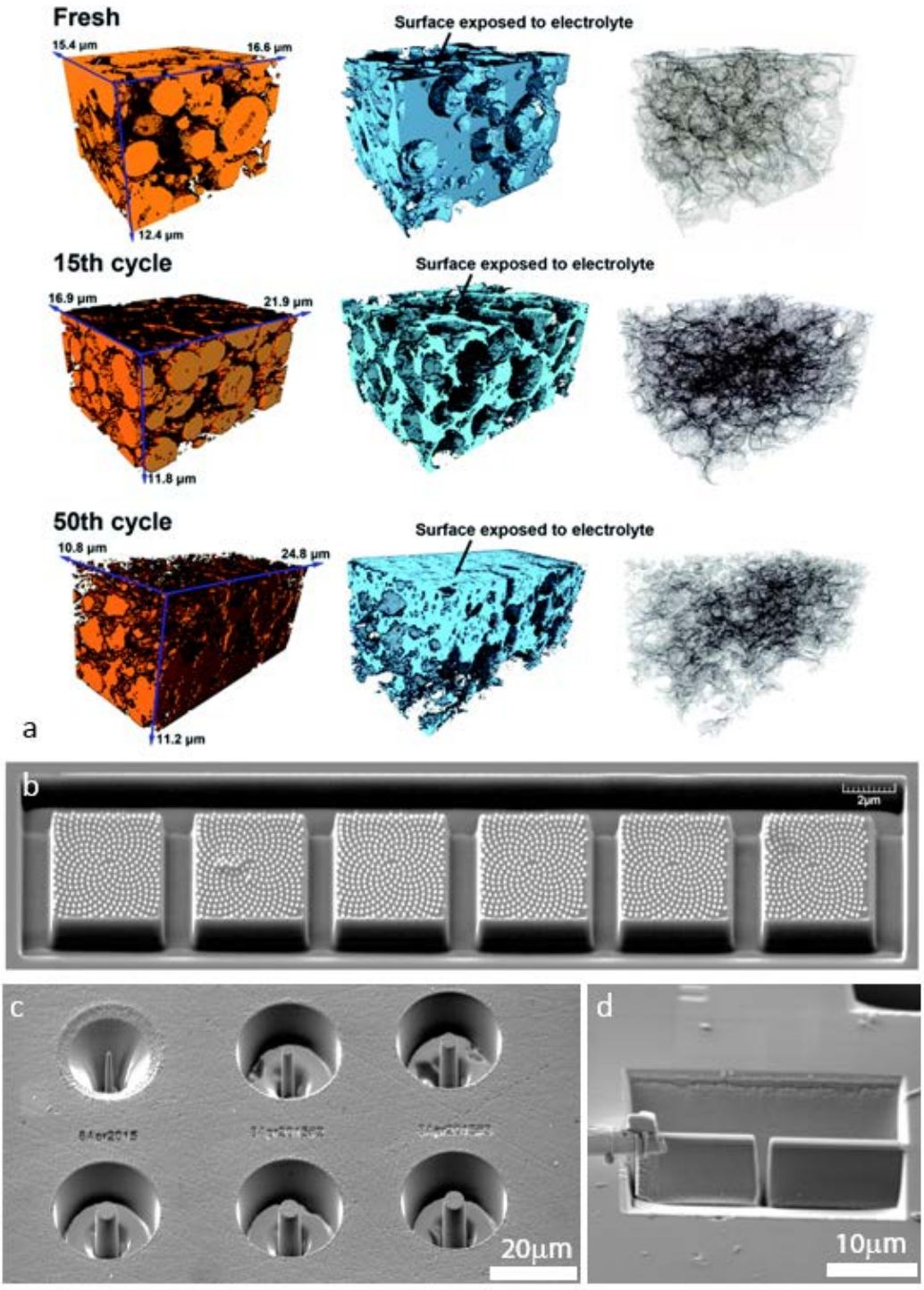

Figure 2.9 Focused ion beam examples of (a) 3D tomography of Li battery electrodes at various cyclic charge/discharge stages; [21] (b) "Parallel" FIB-DIC milling arrangement ('chocolate block' geometry) with ion-beam deposited platinum 'sunflower' patterns; [35] (c) micropillar fabrication for compression test; (d)TEM lamella fabrication and lifting (taken in the MBLEM lab @ Oxford).

Figure 2.9 illustrates the use of FIB in the author's research work devoted to various topics related to the present thesis. Individual techniques are introduced and reviewed in further detail in the following sections.

2.2.2.1 FIB-DIC ring-core milling

Focused Ion Beam offers generic capability for minimally destructive material removal at the nanoscale. In the context of material characterisation, this presents opportunities for residual stress evaluation using strain relief methods [15,37–42]. As a pre-requisite step for reliable design of engineering components to prevent failure, accurate residual stress evaluation at fine scales is crucial for both industrial and academic purposes. Compared to conventional non-destructive techniques (e.g. X-ray diffraction, reviewed in §2.4) and destructive analysis methods (sectioning or hole drilling), FIB based methods are relatively readily accessible, semi-destructive (considering e.g. ring-core milled features of several microns size at the sample surface), whilst capable of attaining high resolution.

This so-called FIB-DIC ring-core milling technique relies on inducing and measuring the strain relief in a well-defined gauge volume (ring-core pillar with a certain diameter), and using digital image correlation (DIC) on a sequence of SEM images which tracks the displacements of markers (deposited patterns or inherent surface roughness features) at the top surface of the ring-core, calculates the relief strain, and deduces the underlying residual stress state.

Publications [15,35] have presented examples of the application of FIB-DIC technique to aerospace alloys (including Ni-base superalloy polycrystals and single crystals) used in the manufacture of compressor and turbine blades.

2.2.3 Micropillar compression technique

To understand fully the mechanical properties of novel materials with advanced microstructure (such as Ni-base superalloys), multi-scale analysis is required that spans several orders of magnitude of dimensions. In order to predict and avoid failure associated with inelastic deformation, solid knowledge must be sought of plastic deformation mechanisms covering the range of phenomena from dislocation kinetics to grain level aggregation to bulk macroscopic response. In order to study the material properties at the smaller scales, many micro-mechanical testing techniques (mostly based on nano-indentation) are devised for concentrating the deformation either within localized volumes (e.g. under the sharp indentor tip), or geometrically isolated small specimens (micropillars for compression and splitting [43], micro-cantilevers for bending, etc.).

Compression offers a convenient way of investigating the mechanical properties of materials (e.g. elastic modulus, flow stress). The method has been applied widely in studies at the macro-scale, in various forms that include crushing, buckling, forging, and barrelling tests. In recent years, increasing amount of work has been directed at the micron or sub-micron scale compression studies [44–48]. This work was motivated by the desire to investigate the size effect (reviewed later in the section 2.3 of this thesis), a crucial phenomenon that needs to be brought into consideration in the context of connecting material scales.

The micropillar compression test mimics the conventional compression test applied for bulk materials. One distinction of micropillar compression testing is that the specimens remain integrally attached to the bulk substrate as a consequence of the sample fabrication, and with a view to reducing the amount of post-fabrication specimen manipulation.

Typical micropillar compression tests are carried out using commercial nanoindentation devices using diamond plat-punch indentation tips with the flat punch geometry. One example of such system that is distinguished by its portability is the in-chamber nanoindenter from ALEMNIS. Micropillar specimens for such micro- to nano-scale compression tests are mostly fabricated by FIB, to take advantage of the ability to mill pillars directly out of bulk crystals and the exquisite control of the size, geometry, location and orientation of the pillars [23,25,49,50]. Micropillars for compression studies reported in the present work were fabricated by FIB milling, as illustrated in Figure 3.2, Figure 3.4 and Figure 3.5.

As many pillars fabricated by FIB are created by ion beam milling perpendicular to the sample surface, the samples that are produced often have a small degree of taper: even careful low beam current polishing typically reduces it down to 2º to 5º. Therefore, extra care is needed to control the aspect ratio to lie within an optimised range required for the testing purpose (typically 2:1 to 3:1 for the compression experiments, to avoid buckling).

The micropillar compression testing has been applied to many face centred cubic (FCC) crystals, such as Ni, Au, Cu and Al [46,47,51–57]. The fundamental phenomenon that has been observed and reported in the literature is that when

sample diameter becomes smaller than some tens of microns, the flow stress shows a significant increase compared to the bulk material due to the high degree of strain hardening that takes place within the small material volume. As the sizes of the test pillars become even smaller, the flow stress observed can reach extraordinarily high values. Along with the flow stress anomalies, there are other phenomena that can be observed in size dependent strength studies based on the micropillar compression method. The details will be reviewed in the following section (section §2.3). Inspection of the stress-strain curves also reveal that the choice of the loading mode for the compression test exerts significant influence on the mechanical response. Displacement control mode (constant displacement rate) gives a serrated curve, while load control mode (constant loading rate) leads to strain bursts in the response curve.

2.3 Crystal size effect: phenomena, theories and models

The fundamental idea that the size of a microstructural feature or characteristic dimension in metals and alloys can play an important role in the manifested strength — or, more broadly, in the general mechanical properties — was firstly introduced by Hall and Petch in their early work in the 1950's [58,59]. The relationship between the macroscopic flow stress and the average grain size *d* was written in the form:

$$\sigma_y = \sigma_0 + kd^n \ , \qquad (2.4)$$

where σ_y denotes the yield stress, σ_0 the limiting yield stress for large-grained sample, the power exponent *n* was postulated to be equal to -0.5, and k an empirically adjusted constant. The studies of metallic whiskers by Brenner several years later [60,61] pointed out that specimens of smaller size (down to 1μm diameter) consistently show higher strength. Early work led by research on metal thin film properties emphasised the importance of dislocation interaction and dislocation pileup against boundaries or interfaces [62,63], until the work of micro-compression of single crystals (reviewed in §2.2.3) revealed that size effect exists even in single crystals without intrinsic boundaries or interfaces. Ever since, progressively more micro-mechanical testing methods were devised for the study of crystals at smaller scales, including pillars and cantilevers. With attention drawn to the dislocation-level plasticity inside small samples, the theory of dislocation starvation and discrete dislocation dynamics models were developed in an attempt to understand the underlying hardening mechanisms.

2.3.1 Hall & Petch and power law

As mentioned in §2.2.3, micromechanical testing of crystals of micron sizes revealed a range of strongly size-dependent phenomena, namely, the dependence of the flow stress, yield and hardening rate on the sample dimension, and the intermittent nature of plastic flow (discrete bursts). Reports have shown that compression test on crystals of tens of microns in diameter or smaller demonstrate a much higher strain-hardening rate and flow stress values compared to that of bulk samples (stage II hardening). However, following this high-rate hardening stage, the response curve tends to change, showing a constant flow stress or even softening behaviour (see Figure 3.4 b).

In order to describe the size-dependence of the flow stress and hardening response, researchers sought to establish a relationship between the flow stress (σ) and sample diameter (d, in the case of micropillars) empirically, via a power law written as:

$$\sigma = C d^n. \qquad (2.5)$$

Here n is the power law exponent, and C is a constant. Various values of n (-0.61 to -0.97 for FCC) have been deduced and proposed, even for crystals of the same structure, which differ from the typical Hall-Petch exponent (n=-0.5) for grain size dependence studies (where d stands for the average grain size). The application of the power law has also been extended to fit different stress values (flow stress at certain percentage of strain, or a saturation stress value at high strain), to suit the nature of the micropillar compression test.

The size effect in micropillar compression tests are observed in both single-slip and multiple-slip orientations. However, the question concerning the quantitative

relation between the orientation and size-dependent response remains unresolved to the present. Since many reports [47,57,64–67] show similar quantitative results for various orientations, the effect of this parameter on the size-dependent response is believed to be minor. Detailed review will be continued in the later chapters.

2.3.2 Discrete dislocation dynamics models

The size-dependent flow response (size effect) is most prominent in the regime between tens of nanometres and some micrometres. In this range, continuum mechanics approaches (classical analytical or finite element models) are not appropriate for investigating the plastic behaviour of the crystals, since the intrinsic length scales must be drawn into consideration. Other numerical models such as molecular dynamics turn out to be too computationally expensive for the simulation of realistic size specimens, and hence not efficient for the study of mesoscale mechanics problems. For these reasons, discrete dislocation dynamics (DDD) models have been introduced for intermediate scale analysis. These models take into account the time-dependent evolution (generation, movement and annihilation) of individual (discrete) dislocations [62,68–70]. Such models seek to capture the elastic interaction of dislocations, the rule of motion of the dislocations, and the prevailing mechanical boundary conditions. DDD models can yield insights into the dynamics of individual dislocations, as well as their collective properties as the overall response for crystals with a small finite volume.

Many two-dimensional and three-dimensional DDD models [53,68,71–78] have been developed to capture the plastic response of materials in confined specimens, and tend to establish the size effect relation in the form of the original Hall-Petch relation (2.4).

According to the literature, the value of *n* is mostly found to vary from -0.5 to -1, which is different from the classic Hall-Petch description. Some authors argue that there is likely to exist one underlying, universally applicable equation or law that describes these manifestations of the size effect. However, most researchers focus their attention on the specific dominant mechanisms in different materials and regimes, such as dislocation nucleation and escape, mode of dislocation motion (glide, climb, etc.), interaction and pileup, etc.

As micropillar compression tests became a popular tool for investigating the plastic behaviour of crystals of small volume, many DDD studies appeared devoted to the mechanism that are active in such scenario [79–85]. However, the predictions of DDD models vary due to the many different assumptions, such as the initial dislocation source density, the size and spatial frequency of Frank-Read sources, critical activation stress for sources, etc.

The present work establishes the connection between the classical Hall-Petch equation and the plastic behaviour of crystals at the mesoscopic scale. The relevant results and analysis are presented in Chapter 3 , Chapter 5 and Chapter 6 .

2.4 X-ray Diffraction Microscopy

X-rays, more specifically hard X-rays, have long been utilised for the characterization of crystalline materials due to their non-destructive and penetrating nature. Over a century of steady development in this field that took place since the interaction between X-rays and crystals was first discovered, and to date, it remains one of the most significant techniques for revealing the internal structure, magnetism, chemical bonding, orbital orientation, etc. With the advent of modern synchrotron facilities, X-ray microscopy techniques enabled versatile visualisation of material properties across nano and mesoscopic scales. This section reviews the fundamentals of X-ray diffraction, as well as the novel X-ray microscopy techniques developed in the recent decades, which are relevant to the present work.

2.4.1 Fundamentals of X-ray diffraction

Fundamentals of X-ray diffraction were first discovered and laid down in the early work by Laue (1913), Friedrich, Knipping, and Ewald, and developed by the father-son team of Braggs [86,87]. This was later summarised by Hammond [88]. The Laue model considers atoms in crystals as scattering centres positioned at lattice points. Figure 2.10 shows a row of atoms with spacing **a** along one of the crystal axes, and for constructive interference, the travel paths AB and CD must differ by an integer multiple of the wavelength of the incident beam.

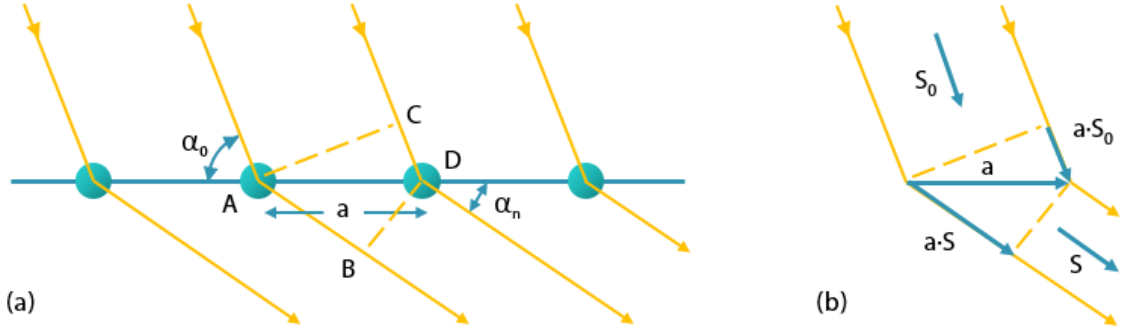

Figure 2.10 (a) An illustration of X-ray diffraction from a lattice row of atoms; (b) the incident and diffracted beam by vector notation.

Therefore, an equation showing this relationship can be written as (first Laue equation):

$$AB - CD = a(cos\alpha_n - cos\alpha_0) = n_x\lambda \ . \qquad (2.6)$$

Here, α_n is the angle between the diffracted beam and the lattice axis, and α_0 is the angle between the incident beam and the lattice axis, while n_x stands for an integer. Equation 2.6 can be rewritten in vector notation as:

$$a(cos\alpha_n - cos\alpha_0) = \mathbf{a} \cdot (\mathbf{s} - \mathbf{s_0}) = n_x\lambda \ . \qquad (2.7)$$

Here $\mathbf{s_0}$ and $\mathbf{s}$ stand for the unit vectors of the incident and diffracted beams, respectively. The second and third Laue equations can be written similarly for the other two lattice axes, as below:

$$b(cos\beta_n - cos\beta_0) = \mathbf{b} \cdot (\mathbf{s} - \mathbf{s_0}) = n_y\lambda \qquad (2.8)$$

$$c(cos\gamma_n - cos\gamma_0) = \mathbf{c} \cdot (\mathbf{s} - \mathbf{s_0}) = n_z\lambda \qquad (2.9)$$

With these three Laue equations (eq. 2.7, 2.8, and 2.9) it is clear that in order for constructive interference to occur, these relations need to be satisfied

simultaneously for all three axes, with each diffracted beam identified by the integers n_x, n_y, and n_z, or alternatively by the *h, k, l* Miller indices of the reflecting crystal plane.

The Braggs, however, interpreted X-ray diffraction in a simpler geometric way. Unlike Laue's equations which require six angles, three lattice parameters, and three integer numbers to be determined, the Braggs derived an equation based on the reflection of X-ray beam from layers of crystal planes. The Bragg's Law gives:

$$n\lambda = 2d_{hkl}sin\theta. \qquad (2.10)$$

Here n is an integer (the order of reflection or diffraction), and d_{hkl} stands for the spacing between the lattice planes from which the incident beam is reflected, as shown in Figure 2.11.

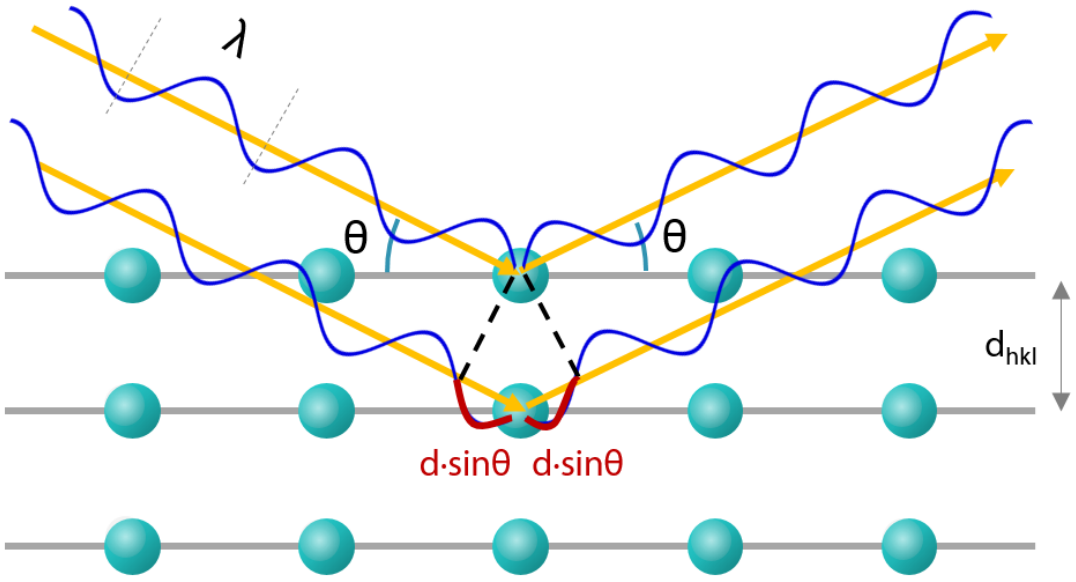

Figure 2.11 Bragg's Law diagram.

2.4.2 The Laue method

Modern X-ray diffraction techniques can be simply classified into two groups, depending on how Bragg's law is satisfied. In the context of powder diffraction, one mode is associated with fixed wavelength (angle dispersive), and the other with fixed incident angle (energy dispersive), The latter is also widely used for single crystal diffraction, and is named the Laue method. With the recent development of synchrotron-based X-ray facilities, Laue diffraction techniques have been enhanced due to the simultaneous availability of high flux, high energy, and high resolution (tightly focused beam spot) and modern detectors. These techniques contribute to the possibility of resolving long-standing fundamental issues in materials research, such as mesoscale structure analysis with particular emphasis on the study of defect organisation, plastic deformation, etc.

The practical setup for synchrotron-based Laue diffraction is either high energy transmission Laue mode (the original mode used by Laue and co-workers), or reflective mode Laue diffraction. The first mode aligns the incident beam, the crystal sample and centre of the detector on the same line; while the latter one collects the diffraction in the direction roughly perpendicular to the reflected beam (at an angle of $2\theta \sim 90°$). According to Ewald's analysis, the Ewald sphere for a wavelength λ always passes through the origin of reciprocal lattice point, and may intersect some lattice points depending on the orientation of the crystal. Each constructive interference collected represents a wavelength and set of parallel crystal planes.

Figure 2.13 shows a two-dimensional Ewald sphere diagram showing the reciprocal space volume which can be probed by a white beam (or polychromatic

beam) with a minimum and maximum wavelength range. The reciprocal lattice generated via x-ray diffraction (coloured red in the Figure 2.12) and the real space lattice (coloured green) can be seen as the Fourier transform of each other.

Since continuum range of wavelength is directed onto the crystal, multiple constructive interference conditions are satisfied (by Bragg's Law), which are shaded in light blue in the figure.

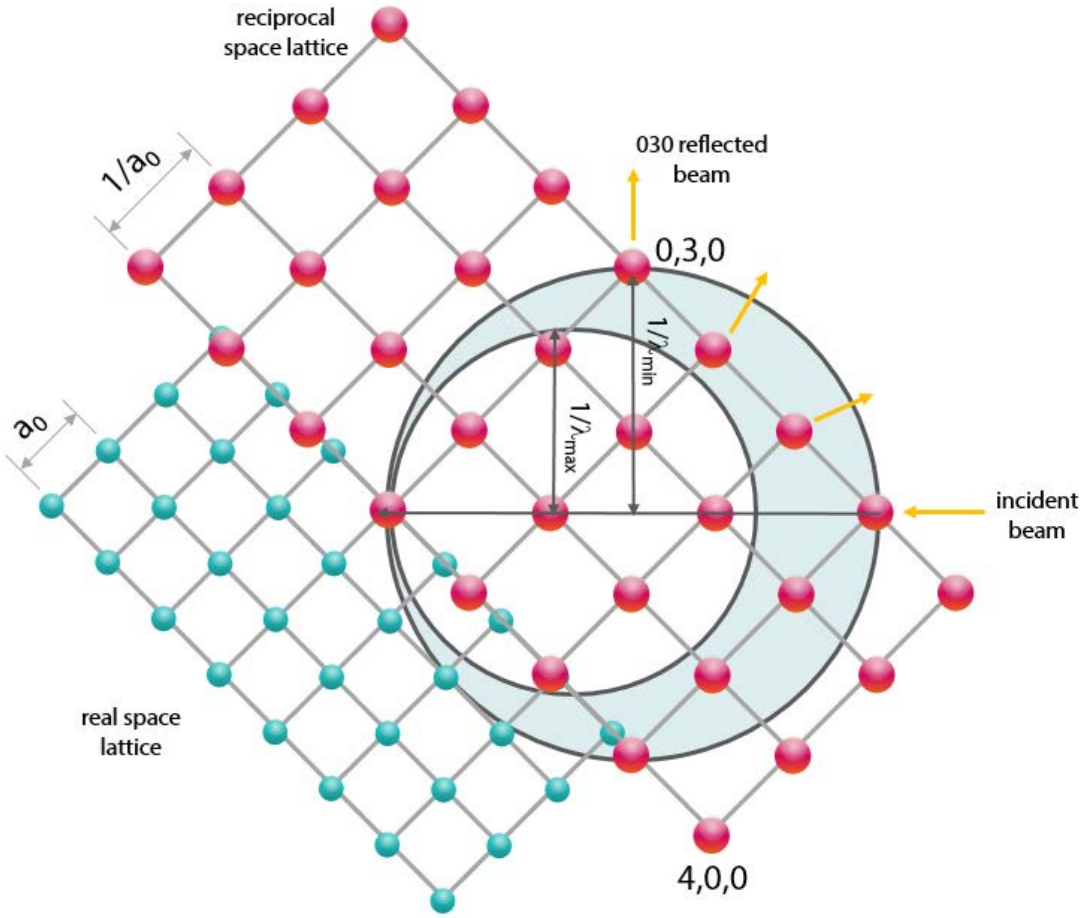

Figure 2.12 The Ewald reflecting sphere (2D diagram) for the hkl reciprocal lattice section probed by a polychromatic beam with the maximum wavelength λ_{max} and minimum wavelength λ_{min}.

All the qualified sets of crystal planes along with the corresponding energy (wavelength) will contribute to the Laue diffraction pattern. This makes the method particularly suitable for the study of the structure and mechanical properties of single crystals, which can be set into a certain orientation to obtain the desired reflections.

The so-called Miller hkl indices are used to define the crystal planes which contribute to each reflection, by specifying the intercept of the next parallel plane with the real-space lattice vectors (a_1/h, a_2/k, a_3/l). The plane normal for Laue refection, $\mathbf{n}_{hkl}$, is determined by the bisector of the directions of the incident beam and scattered beam in real space, as follows:

$$\boldsymbol{n}_{hkl} = \frac{\boldsymbol{r}_{hkl} - \boldsymbol{j}}{|\boldsymbol{r}_{hkl} - \boldsymbol{j}|} \tag{2.11}$$

Here **j** is the unit vector of the incident beam, $\mathbf{n}_{hkl}$ and $\mathbf{r}_{hkl}$ stand for the plane normal and the scattered beam in the real space.

For cubic lattices, crystal plane spacing can be written as:

$$d = a_0/\sqrt{h^2 + k^2 + l^2} \tag{2.12}$$

Understanding and indexing (hkl) the peak identity is a key step in identifying the crystal orientation for the analysis of structure and properties.

2.4.3 Scanning micro-Laue X-ray microscopy and reciprocal space mapping

Sub-micron resolution can now be achieved by micro-Laue diffraction techniques through achromatic focusing optics, most commonly Kirkpatrick-Baez mirror pairs (KB mirrors) illustrated in Figure 2.13.

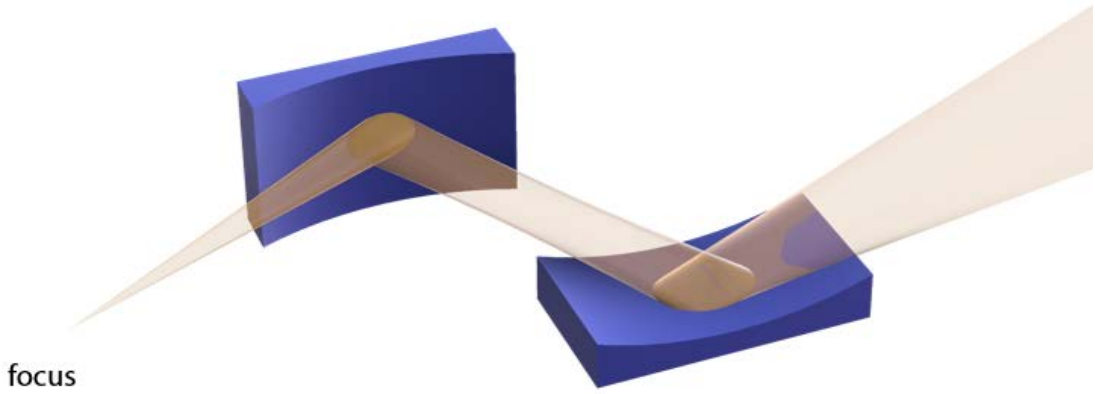

Figure 2.13 Schematic diagram of the Kirkpatrick Baez mirror focusing system.

With sub-micro focused X-ray beam produced, it is possible to target a volume of material defined by the beam spot on the sample (in the case of thin film), or a slightly extended volume with bulk material due to the penetration of the X-ray beam. With the highly focused beam scanning over a larger volume of the sample, it is possible to perform point-to-point comparison of Laue patterns, and hence reveal the structural differences. In addition, high-resolution X-ray imaging detectors can provide precise positioning and geometry information of the scattered beam spots, which can be interpreted to determine the deviatoric strain

tensors, the Nye Tensor, and hence obtain insights into mesoscopic plastic behaviour of crystals.

Key principles of determine the strain status which in interpreted from Laue diffraction pattern are derived by Busing and Levy [89], and later presented by Chung and Ice [90,91].

2.4.3.1 Elastic strain from unit-cell parameters

Elastic strain that is a quantity of principal interest for mesoscale mechanics can be locally determined by micro-Laue diffraction technique.

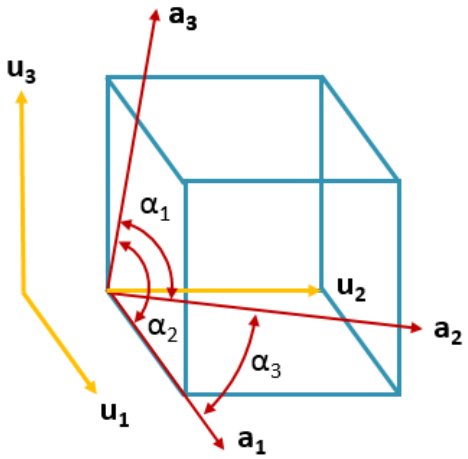

Figure 2.14 Cartesian coordinates attached to the real-space unit cell

Consider a unit-cell with lattice parameters a_i (length) and α_i (angle), with a Cartesian coordinate system $\mathbf{u_i}$ attached to it, and its reciprocal space lattice parameters described by b_i and β_i values. Let a_1 be aligned with u_1; thus, $\boldsymbol{u_1} = \frac{\boldsymbol{a_1}}{|\boldsymbol{a_1}|}$; $\boldsymbol{u_3} = \frac{\boldsymbol{a_1}\times\boldsymbol{a_2}}{|\boldsymbol{a_1}\times\boldsymbol{a_2}|}$; and $\boldsymbol{u_2} = \boldsymbol{u_3}\times\boldsymbol{u_1}$. Thus we have the equation for transforming a position from Cartesian coordinates to lattice units:

$$v_u = \begin{pmatrix} a_1 & a_1\cos(\alpha_3) & a_3\cos(\alpha_2) \\ 0 & a_2\sin(\alpha_3) & -a_3\sin(\alpha_2)\cos(\beta_1) \\ 0 & 0 & \frac{1}{b_3} \end{pmatrix} \cdot v \qquad (2.13)$$

The average elastic strain in the scattering volume can be determined by comparing the measured unit-cell parameters, $\mathbf{A_{meas}}$, to the undistorted values $\mathbf{A}_0$. The transform which performs the transition can be written as $\mathbf{A}_{meas}=\mathbf{T}\,\mathbf{A}_0$, where **T** contains both distortional and rotational terms. Taking the symmetric part of **T**, the strain tensor in the measured-crystal Cartesian-coordinate reference frame is given by:

$$\varepsilon_{ij} = \frac{\mathbf{T}_{ij}+\mathbf{T}_{ji}}{2} - \mathbf{I}_{ij} \qquad (2.14)$$

The strain tensor can be converted to the lab reference frame or sample frame using a rotation matrix **R**, using:

$$\varepsilon_{sample} = \mathbf{R}\varepsilon\mathbf{R}^{-1} \qquad (2.15)$$

Here ε can be presented as a combination of a distortional term (deviatoric strain) and a dilatation term (hydrostatic strain) as below:

$$\varepsilon = \begin{pmatrix} \varepsilon_{11}-\Delta/3 & \varepsilon_{12} & \varepsilon_{13} \\ \varepsilon_{12} & \varepsilon_{22}-\Delta/3 & \varepsilon_{23} \\ \varepsilon_{13} & \varepsilon_{23} & \varepsilon_{33}-\Delta/3 \end{pmatrix} + \begin{pmatrix} \Delta/3 & 0 & 0 \\ 0 & \Delta/3 & 0 \\ 0 & 0 & \Delta/3 \end{pmatrix} \qquad (2.16)$$

Here $\Delta = \varepsilon_{11} + \varepsilon_{22} + \varepsilon_{33}$, and finally the stress tensor can be determined as below:

$$\sigma_{ij} = \sum_{kl} C_{ijkl}\varepsilon_{kl}, \qquad (2.17)$$

where C_{ijkl} stands for the tensor of anisotropic single-crystal elastic constants, or the stiffness moduli.

Although elastic strain distorts the reflection angles, provided it is homogeneously distributed in the small gauge volume, the sharpness of the reflected spots will not be affected. The blurring effect on Bragg spots arises due to the strain gradients within the sampling volume, i.e. due to the elastic tensor changing within the volume of the crystal being probed. In addition to the “large scale” strain gradients, a significant contribution to spot “streaking” will come from the dislocations present inside the crystal gauge volume that arose due to prior plastic deformation.

2.4.3.2 Dislocations effects on X-ray diffraction

Qualitatively, the effect of defects inside the crystal gauge volume that manifest themselves in the reciprocal space can be classified into two types, Type I and Type II [92]. Type I redistributes the intensity of Bragg peaks, giving rise to secondary or diffuse scattering peaks. Defects of this type shift the position and weaken the intensity of Bragg peaks as the defect concentration increases, but they tend not to affect the sharpness of the Bragg peaks. Type II defects, on the other hand, broaden the Bragg peak with increasing defect concentration. Type I includes point defects, coherent precipitates (such as γ’ in Ni-base superalloys), and minor dislocation loops contained in the probing volume. Type II includes disclinations, planar defects such as twinning and grain boundaries, and dislocations, including large dislocation loops. Such classification is related to the static Debye-Waller Factor exponent, e^{-2W}, given by:

$$2W = ReT_{\infty} \cong c \lim_{\rho \to \infty} \sum_t (1 - \cos(\mathbf{Qu}_{ss't}))[1 + 1/f(\varphi_{st} - \varphi_{s't})] \qquad (2.18)$$

Here T_∞ stands for the correlation function for defects at a very large distance, *c* is the defect concentration value, ***f*** is the structure factor for the crystal, ***Q*** is the momentum transfer for a certain *hkl* reflection, $\boldsymbol{u_{ss't}}$ stands for two defect caused differing scattering cells with defect position ***t***, φ_{st} and $\varphi_{s't}$ stand for structure amplitude changes caused by the same defect at ***t***. The defects are thus classified by asymptotic behaviour of the displacement field which is generated by the defects. For Type I defects, displacement falls off more rapidly than $1/r^{3/2}$, the value of 2W is finite, and hence classified accordingly. With particular application on the dislocations stored in crystals, these can by thereby classified into paired (dipolar, or *statistically stored*) dislocations and unpaired (polar, *geometrically necessary*) dislocations, which cause "streaking" of the Laue peaks. It is claimed by many researchers [93–95] that unpaired dislocations (or geometrically necessary dislocations, GNDs) tend to be aggregated or grouped to minimize elastic energy. The equation for elastic energy of isolated or individual dislocation per unit length is given as:

$$\frac{E}{l} \sim \frac{\mu n b^2}{4\pi} \ln\left(\frac{L}{b}\right) . \qquad (2.19)$$

Here μ stands for the shear modulus, *n* stands for dislocation density, *b* is the modulus of the Burgers vector, and *L* is characteristic length of the material (referred to section 2.3). When *L* is smaller, or the dislocations become so-called correlated, the integrated elastic energy decreases. Hence dislocation wall or cell structures are arisen by the process of self-organised motion.

At initial stages of deformation, the probability for dislocations dipoles (pairs with opposite Burgers vectors) to form is high. However, when strain gradients occur in large plastic deformation (such as beam bending in Chapter 4), dislocations

with certain Burgers vector are nucleated preferentially, in order to sustain the required plastic strain distribution, to give rise to geometrical shape of the deformed crystal. In these cases, it is typical to find “streaking” of Laue patterns from severely plastically deformed crystals (those containing strain gradients), due to the contribution of unpaired dislocations (GNDs). Further illustrations of this observation can also be found in results in Chapter 4 . Long-range rotations are introduced by line defects which interrupt the periodic atomic arrangement inside crystals, with axes depending on the dislocation types, and rotation size depending on density of unpaired or geometrically necessary dislocations. Therefore, the slip systems can be determined by analysing the “streaking” Bragg spots [93,94,96,97]. In principle, according to the literature, total dislocation density information can be derived by analysing the longitudinal blurring of Bragg spots. However, this is based on assuming homogeneity of the sample, whilst it is apparent that other contributions to “streaking” exist, such as inhomogeneities (e.g. dual phase materials such as Ni-base superalloys), and elastic stresses. Micro-Laue diffraction analysis allows unambiguous determination of the local Nye distortion tensor resulting from the dislocations in the presence of strain gradients, as given:

$$\alpha_{ij} = \kappa_{ji} - (\kappa_{ii})I_{ij} - e_{ijk}\partial_k \varepsilon_{lj}. \qquad (2.20)$$

Here κ stands for the local lattice curvature, and local elastic strain gradients can be found by mapping the local crystallographic orientation with the full set of elastic strain tensors [98].

2.4.3.3 Paired dislocation effects on the Bragg peak

Bragg peaks with enlarged or broadened intensity profile can be found when crystal structures are affected by statistically stored dislocations, from which long-range distortion fields are generated in crystal lattices. By studying the peak intensity distribution and geometry, the type, structure and organisation of the contributing dislocations can be determined [99]. The scattered intensity around each reciprocal lattice point (corresponding reciprocal lattice vector $\mathbf{G}_{hkl}$) is a function of the diffraction vector **Q** or the deviation vector **q**, which are given as:

$$\boldsymbol{Q} = \boldsymbol{k_2} - \boldsymbol{k_1} = {}^{4\pi}\Big/_{\lambda\left(\widehat{\boldsymbol{k_2}} - \widehat{\boldsymbol{k_1}}\right)}; \boldsymbol{q} = \boldsymbol{Q} - \boldsymbol{G_{jkl}}. \qquad (2.21)$$

Here $\boldsymbol{k_2}, \boldsymbol{k_1}\widehat{\boldsymbol{k_2}}, \widehat{\boldsymbol{k_1}}$ are wave vectors of the scattered beam and incident beam, and their directional unit vectors. There are two distinct directions of **q**, radial direction (**q**□) and transverse plane (orientation space, $\mathbf{q}_{\perp}$ transverse to $\mathbf{G}_{hkl}$), with the presence of dislocations in reciprocal space. Each has distinct parameters associated with the dislocation structure, as shown in Figure 2.15.

The shape of the radial intensity distribution can be described by the equation, $I(\mathbf{q}_{\parallel}) \cong I(\theta/2\theta)$, which are mainly contributed to by the dilatation part of the displacement fields, given as **u**=**u**(**R**). Therefore, the elongation or broadening effect found in the radial direction can be seen as the dislocation strain field causing the *d* spacing (lattice spacing) variation. In contrast, $I(\mathbf{q}_{\perp})$ is mostly depending on the misorientation or lattice rotations due to the displacement fields. Broadening in the transverse plane can be seen as resulting from the variation of local lattice orientation, which can be used to characterize the local orientation distribution via Laue diffraction, or reciprocal space mapping (orientation mapping or rocking curve analysis).

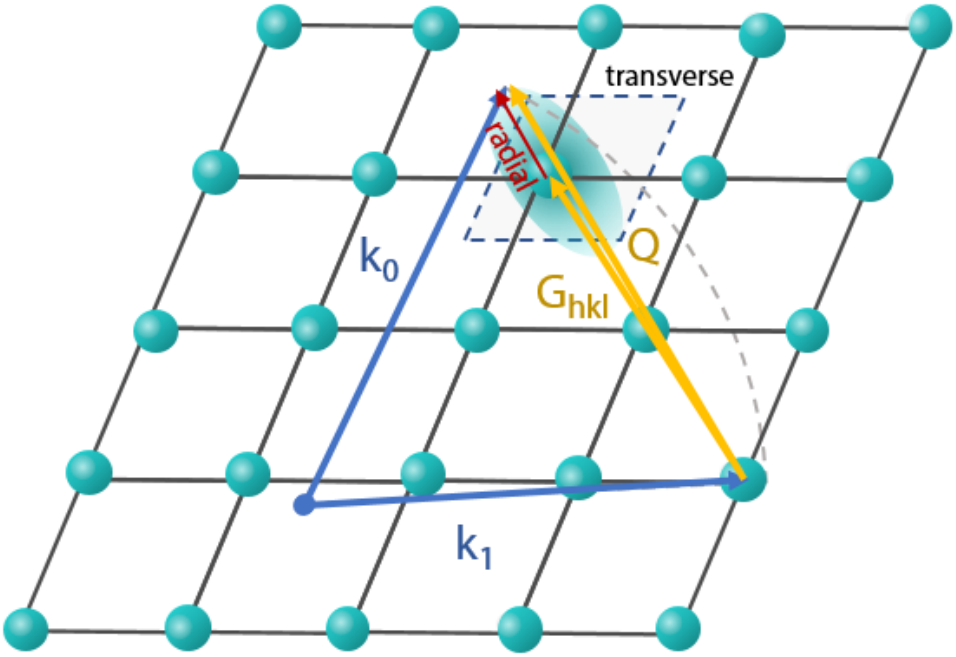

Figure 2.15 Reciprocal space illustration for broadened Bragg peak (shaded in blue), with $\mathbf{q}_{\parallel}$//Q and transverse plane directions $q_{\perp}$ shown in parallelogram.

The overall intensity distribution due to deviation vector **q** can be described as [92]:

$$\boldsymbol{I(q) = f^2 \sum_{i,j} e^{i\cdot \mathbf{q}\Delta e^{-T}}.} \qquad (2.22)$$

Here *f* is the average scattering factor, $\Delta = \mathbf{R}_i^0 - \mathbf{R}_j^0$ is the undistorted distance vector between lattice cells i and j, and **T** stands for correlation function given as,

$$\boldsymbol{T = nS_0 \sum_t 1 - e^{\left(i\mathbf{Q}(\mathbf{u}_{it}-\mathbf{u}_{jt})\right)} = c \sum_t 1 - e^{\left(i\mathbf{Q}(\mathbf{u}_{it}-\mathbf{u}_{jt})\right)}} \qquad (2.23)$$

Here $\boldsymbol{S_0}$ stands for the area related to dislocation position in the transverse plane, and ***n*** stands for the dislocation density, the product of which can be represented by ***c***, a dimensionless quantity indicating the fraction of lattice sites that are

intercepted by dislocations. Equation 2.23 represents the effect of the local dislocation structure and arrangement.

Paired and unpaired types of dislocations (also named statistically stored and geometrically necessary dislocations, SSD and GND) give rise to different broadening effects of the Bragg peaks. Therefore, they expand the correlation function in different ways, which in general have two parts, written as:

$$\boldsymbol{T_i = i\sum_t c_i(R_{ij}\nabla)(G_{hkl}u_{it})};\ \boldsymbol{T_R = -\sum_t c_i[1-\cos[(R_{ij}\nabla)(G_{hkl}u_{it})]]}. \qquad (2.24)$$

Here the T_i represents the imaginary part, mainly contributed to by the geometrically necessary dislocations (lattice rotation), while T_R represents the fluctuating strain fields from dislocations.

For statistically stored dislocations (paired), the correlation function has no imaginary part, and the real part can be expressed as,

$$\boldsymbol{T_R = C_2(\mathbf{Qb})^2 \ln L \sum_\lambda n_\lambda \varphi_\lambda} \qquad (2.25)$$

For edge dislocations, the displacement fields lie in the plane perpendicular to the dislocation line, τ; therefore, scattering is not affected in the direction along τ. The intensity distributed purely due to one set of edge dislocations can be expressed as, in a shape of an ellipsoid,

$$\boldsymbol{I(Q) = \frac{N}{v} f^2 \delta(q_z) \frac{(2\pi)^{\frac{3}{2}}}{\sqrt{|\alpha|}} \exp(-\frac{1}{2}\sum_{x,y}\beta_{xy}q_x q_y)}. \qquad (2.26)$$

Here $|\alpha|$ is the determinant of the matrix, which is the inverse of matrix β, $\alpha_{xy}=\beta_{xy}^{-1}$, where β stands for the contrast factor containing coefficients indicating the intensity distribution in each direction in reciprocal space. The form $\sum_{x,y}\boldsymbol{\beta_{xy}q_x q_y}$ describes the iso-intensity surface by the edge dislocation.

For screw type dislocation, along z direction, the intensity distribution can be expressed as,

$$I(\boldsymbol{Q}) = \frac{8\pi^2 N}{v}\boldsymbol{f^2}\boldsymbol{\delta}(\boldsymbol{q_z})\frac{1}{0.5n(\mathbf{Q}\cdot\mathbf{b})^2 l}\exp(-\frac{\pi(q_x^2+q_y^2)}{\sigma^2}), \qquad (2.27)$$

$$l \sim \ln\frac{\sqrt{\pi}\sigma L}{2\mathbf{Qb}} \approx \ln(\sqrt{nl}L). \qquad (2.28)$$

From the above it can be deduced that the full-width-at-half-maximum is proportional to the root of total dislocation density ($\sqrt{n}$), reciprocal lattice vector, **Q,** and **Qb**. Peak asymmetry can then be generated by the dislocation density variation in different slipping systems.

2.4.3.4 Unpaired dislocation affected Bragg peak

Geometrically necessary dislocations (GNDs) and incidental dislocation boundaries (IDBs) affect the scattering in various ways. IDBs are curved thick boundaries with certain distribution of dislocations within the region, formed by statistical mutual trapping of gliding dislocations. Another dislocation boundary type, namely geometrically necessary boundaries (GNBs), are defined as extended straight parallel boundaries separated by low dislocation density regions, which is usually formed when the crystal is under severe plastic deformation [100–102]. It is commonly assumed that GNBs are formed due to contrasting slip activity contributed by different active slip systems in neighbouring cells, or different partition of the total shear among the same set of systems. With that given, IDBs and GNBs show different misorientation and spacing sensitivity with strain. The effect of geometrically necessary dislocations can be classified

into three categories: randomly distributed GNDs, GNBs, and the combination of GNBs and IDBs.

The streaking of Bragg peaks is one of the main obvious effects caused by geometrically necessary dislocations, which is mainly due to the long-range lattice rotations. The orientation of streaking patterns depends on the orientation of GNDs slip system, and the scattering vector. From equations 2.23 and 2.24, the correlation terms for both real and imaginary parts can be written as,

$$T_i = -iC_1 \sum_\lambda \mathrm{n}_\lambda^+ (\boldsymbol{R}_i \mathbf{b}_\lambda)\big([\mathbf{Q} \times \mathbf{R}_{ij}]\boldsymbol{\tau}_\lambda\big);\ T_R = C_2(\mathbf{Q}\cdot\mathbf{b})^2 \ln L \sum_\lambda n_\lambda \varphi_\lambda. \qquad (2.29)$$

Here C_1 and C_2 are the contrast factors for radial and transverse directions respectively, L is the size of the interaction volume (smallest probe dimension), φ_λ stands for the orientation factor for each dislocation system, and T_i is linear with the polar dislocation density n^+. The scattering effect that GNDs have on the radial direction is similar to that for SSDs. The Gaussian intensity profile in the radial direction can be expressed as $FWHM = \delta 2\theta \propto n^{1/2}$. In the transverse direction, the broadening effect is much more severe, for randomly distributed dislocations $FWHM_\perp \equiv \delta\mathbf{q}_\perp \propto Ln^+$. Again, dislocations with the line parallel to the diffraction vector have no influence on the intensity redistribution in either direction.

2.4.4 Dual-mode micro-focus full-field imaging and reflective Laue diffraction during *in situ* pillar compression

Dual-mode micro-focus full-field imaging and micro-Laue diffraction techniques are frequently set up in separate experiments, rather than simultaneously, for reasons of the complexities associated with the configuration. However, in reflection mode Laue diffraction experiments locating the X-ray beam on a specific region of the sample represents a major challenge, especially with micro- and submicron- focused X-ray beams. Therefore, in order to apply micro-Laue diffraction method with tight focusing to study micrometre-sized features on the crystals (such as micropillars), simultaneous in-line imaging is needed to ensure spatial positioning with adequate accuracy. Dual-mode micro-focus full field imaging was implemented with reflective micro-Laue diffraction on the beamline B16 on the Diamond Light Source, UK. Full field imaging using divergent beam allows reaching much higher resolution, e.g. using 100x geometric magnification allows nominal resolution of ~50 nm/pixel.

Full field magnification is popularly used for the transmission x-ray imaging tomography which reveals materials internal structure by the difference in X-ray absorption due to the variation in thickness or composition. For the purpose of illuminating micrometre crystal features, such as free-standing micropillars, full-field X-ray imaging can take the transmitted flux from the incident beam, while the CCD area detector can collect the scattered beams in reflection mode, with the nominal angle of ~90° (Figure 5.2, b). Such combined setup improves the efficiency of locating the sought features, and makes it possible to achieve the

high accuracy required *in situ* micro-mechanical tests, such as micropillar compression by nanoindentation, and cantilever bending.

2.4.5 Bragg Coherent X-ray diffraction imaging of strain in single crystal

In the field of optical, electron microscopy and X-ray microscopy, technology has advanced fast towards the development and use of highly coherent sources of illumination [103,104]. Although with micro-Laue diffraction and full-field imaging technique, X-ray can how probe various types of material with tens of nanometres resolution [105–110], the most recent development of Bragg coherent diffraction imaging technique (BCDI) has opened up new opportunities and made a significant impact on the study of nano- and mesoscale materials science [107,111–115]. Most micro- and nano-scale X-ray techniques rely on beam focusing to achieve the finest resolution and to resolve the weak interference patterns arising from local ordering, coherent methods probe crystals nano-scale structure beyond the ensemble approximation [116–118]. This section reviews the fundamental concepts of the coherent X-ray methods and their application to crystal plasticity.

The first example of the use of coherent X-ray source [119] used small angle diffraction from a non-crystalline material to achieve the resolution of 75 nm. This was followed by similar studies [120–122] which employ 3D construction of the sample density map from several projections, that gain benefits from CDI's sensitivity to electron density. With the nano-focused X-ray beams widely used, recent advances in scanning X-ray microscopic techniques span the range from CDI to Bragg coherent diffraction imaging (BCDI) [123]. The technique of

‘ptychography’ has been proposed to remove the real-space positional ambiguity of phase features, and to recreate a 2d image. The combination of these images can then be used to reconstruct, via certain algorithms, the 3D volume of the sample at a resolution much beyond the probe size [124]. Since 2003, publications [125–129] report the measurement of lattice shape, distortion, strain, and crystallographic phase contrast in crystals such as gold, lead and ZnO, with some performed *in situ*. The technique of BCDI continues to advance in terms of higher resolution and wider range of applications.

In order to produce a 3D reconstruction of the probed crystal via BCDI with the full vector information of lattice distortion or strain, three separate reciprocal lattice points or Bragg peaks on different lines need to be measured. In the previously referred work on ZnO [126], for instance, six different Bragg peaks were measured fully in the reciprocal space of one micro-size probed zinc oxide nanorod, with each was inverted individually into phase and density isosurface sections. The combination of the two methods was used to deduce the six independent components of the strain tensor with resolution down to 40 nm. The data analysis and post-processing is arguably the most important part of the coherent imaging methods, with data taken with high-NA optics [123].

In general, the hard X-ray coherent diffraction method has extended the range of applications and pushed the limits of X-ray microscopic analysis further towards even higher resolution, and greater depth of information extracted. A more extensive introduction to BCDI given in Chapter 6 , along with the theories, methodology, and application to Ni-base superalloy single crystals.

Chapter 3

On the nanostructural origins of the size effect in the compression response of single crystal Ni-base superalloy micropillars

This chapter contains studies on size-dependent strengthening effect on Ni-base superalloy single crystal micropillars. Micropillars are fabricated by focus-ion-beam microscopy technique and tested by uni-axial compression, utilizing an in-chamber nanoindenter under true displacement control mode. The flow stress responses of the tested pillars are observed as variable depending on the pillar size (diameter).

Origins of the size effect is discussed with review of relevant work and theories given. A model considering flow stress in dual-phase crystals is proposed, which provides a mathematical fit that has good agreement with the experimental data.

3.1 Introduction and motivation

Nickel superalloys play a pivotal role in enabling power generation devices on land, sea, and in the air. They derive their strength from coherent cuboidal precipitates of the ordered γ' phase that is distinct from the γ matrix in composition, structure, and properties. In order to reveal the connections between elemental distribution, dislocation glide and the plastic deformation of micro- and nano-sized volumes of nickel superalloy, a combined *in situ* nanoindentation compression study was carried out within SEM on micro- and nano-pillars fabricated by FIB milling of Ni-base superalloy CMSX4. The observed mechanical response (hardening followed by softening) was correlated with the progression of crystal slip that was revealed using FIB nano-tomography and EDS elemental mapping. The size dependence of material strength was correlated with the characteristic dimension of the structural units (γ' precipitates) via dislocation modelling which allowed the results to be described by a parameter-free Hall-Petch equation.

The dependence of the mechanical properties of small material volumes on their size is an important theme in current research, both because it is required to make further progress in design and use of components and structures with ultra-small dimensions (nano-particles, nano-rods, nano-layers) for use in electronics, sensors, catalysis, and biomedicine; and because of the need to understand the macroscopic mechanical behaviour of nano-structured materials and composites incorporating these elements. One reason for the distinct nature of deformation response observed in nano-scale objects is due to the proximity of the free surface that can affect both elastic and plastic properties, whilst the other is the fact that the details of interaction between the externally applied load and the

internal structure (defects, inhomogeneities, second phase inclusion etc.) tend to become more prominent under those conditions, and manifest themselves clearly in the stress-strain relationship.

Size-dependent mechanical behaviour and properties of materials have been studied by various techniques, including micro-cantilever bending, wire torsion, micropillar compression [46,47,51,52,130], etc. It has often been observed that apparent material strength changes with the sample size, becoming either greater or smaller, thus manifesting the so-called size effect. The interpretation of such observations requires supported from some sort of numerical or conceptual modelling in order to ensure that experimental artefacts are avoided, and the conclusions drawn from the results are soundly justified by the physical mechanisms at work. One common theme in the various analytical approaches concerns the emergence of a characteristic length parameter that can be attributed to structural dimensions (grain size, inclusion size, characteristic length for plasticity, dislocation spacing, etc.). Characteristic lengths can be classified as intrinsic or extrinsic, depending on whether they are inherently present in the material structure, or emerge as a consequence of deformation, as e.g. in the case of strain gradient plasticity [47,131–133].

In the present study, our attention was placed on compression testing of micro- or nano-pillars fabricated by Focused Ion Beam (FIB) milling. This method has been applied to a wide variety of materials to reveal a correlation between the observed mechanical strength and the size of the studied material volume [130,134–136]. Various explanations have been proposed for the observations, including the widely quoted “dislocation starvation model” that claims that in small-sized objects, higher stress is required to achieve an appreciable density of

dislocations that mediate plastic deformation, since they are able to escape through the sample surface. Therefore, mechanical strength is higher in such objects, while mutual interactions are less likely to happen between dislocations, and the secondary strain hardening is absent [46,47,51,53].

This approach, however, may not apply for nanostructured materials such as nickel superalloys which contain second phase inclusions (cuboidal precipitates) even within nano-sized volumes; and in which a high density of dislocation sources is likely to be present at the γ/γ' interfaces, providing ample supply for the onset of slip. On the other hand, evidence has progressively emerged that FIB milling causes material damage to the depths of ~5-30 nm from the milled surface, producing an amorphous layer that may act as an obstacle to dislocation glide, causing additional strengthening [36,137]. In addition, little has been reported on studying the size effect with consideration given to both intrinsic and extrinsic characteristic lengths. These considerations provided the motivation for the present study, together with the obvious practical relevance of nickel superalloys for aerospace engineering, power generation, chemical and oil industries, etc.

In the present study, samples of a single crystal Ni-base superalloy (CMSX-4) were investigated. CMSX-4 is a second generation, Re-bearing nickel-base single crystal superalloy that has been successfully used in numerous aerospace and industrial gas turbine applications for quarter of a century, and has been the subject of a wide range of studies [1,14,138]. The nominal alloy composition is given in Table 3.1[6].

Table 3.1 CMSX-4 Alloy Nominal Composition

Element	Wt.%	Element	Wt.%
Cr	6.5	Al	5.6
Co	9.6	Ti	1.0
W	6.4	Ta	6.5
Re	3	Hf	0.1
Mo	0.6	Ni	Balance

The alloy possesses a two-phase microstructure that consists of cuboidal γ' precipitates with the ordered $L1_2$ structure embedded in the disordered FCC γ phase matrix. The two phases are coherent, in that atomic planes run continuously across the γ and γ' phases throughout the entire material volume [1]. However, the presence of a small lattice parameter mismatch between γ and γ' causes straining and distortion of the lattice, resulting in internal stresses that affect the mechanical response of the material, particularly under the conditions of plastic deformation. Dislocations travelling across the crystal meet additional resistance from internal stresses, and encounter obstacles in the form of interphase boundaries that lead to dislocation splitting and increased strength [139]. In addition, the two phases differ in the content of alloying elements (such as Cr) that are preferably segregated to the phase where these atoms can be more readily accommodated, depending on the relative size of the solute atom and the unit cell dimensions [1]. Micropillars of various diameters ranging from several microns down to sub-micron dimensions were prepared from single

crystals with the <0 0 1> crystallographic direction nominally aligned with the sample surface normal.

Figure 2.3 shows the secondary electron image of a region at the [001]-oriented surface of Ni-base superalloy (note the 1 μm scale bar), along with EDS elemental maps of individual elements over the same area. Cuboidal precipitates of the reinforcing γ' phase with the lateral length in the range ~200 nm to ~600 nm appear dark in the secondary electron map, while the matrix γ phase with the typical channel width of 50 nm appears bright. It is apparent from EDS images in Figure 2.3 that the γ' phase is rich in Ni, Al and Ta, whilst the γ phase contains increased concentrations of Cr, Co, W and Re.

The combination of the observed elemental and structural contrast between phases has important implications for the mechanical behaviour of the studied alloy. At room temperature, when dislocation climb is inhibited, the principal mode of deformation is crystal slip involving continuous travel of dislocations across multiple precipitates. The interphase boundaries, in this case, can be thought of as acting in a way similar to grain boundaries in polycrystals, leading to additional material strengthening. The implications of this hypothesis are tested in the study presented below through the combination of experimental tests and modelling.

3.2 Experimental method

Micropillars for the present study were fabricated using TESCAN LYRA3 FIB-SEM system with a Ga source Focused Ion Beam (FIB). A sample of CMSX-4 single crystal with the [001] direction nominally aligned perpendicularly to the surface was ground using a sequence of SiC grinding papers, followed by

polishing with 9 μm, 3 μm and 1 μm diamond suspension on polishing cloths. Using FIB ion energy of 30 keV and ion current ~1 nA, annular trenches with the outer diameter ~25 μm were milled around the central micropillars with the diameters in the range ~0.5-5 μm. Microscope pre-sets with lower ion current (200 pA and 50 pA) were then applied for slow finishing and polishing of the outside of the pillars. The aim of this operation was to control and reduce the degree of pillar tapering and barrelling, and to reduce the damaged "skin layer" of the micropillar samples. This layer arises as a consequence of ion beam damage due to Ga^+ ions penetrating the material surface, causing a cascade of atomic displacements, creating a population of defects and leading to material amorphisation. This effect has been the subject of a number of recent studies that have primarily focused on silicon, although other materials have also been considered [36,137]. It has been found that alongside the creation of up to ~30 nm thick amorphous layer (that presents an obvious obstacle to crystallographic dislocation glide), ion beam damage gives rise to eigenstrain (permanent inelastic strain) and residual stress that may exert additional influence on plastic deformation and strength of these micro-scale test samples. The smallest pillars had sub-micron diameters (down to ~250 nm). These were prepared to obtain sample size that is comparable or smaller than the typical γ' precipitate dimension (~200-500 nm). At the other end of the scale, the largest pillar diameters extended to ~8 μm to enable reaching the 'continuum' limit by studying the response of a material volume containing on average in excess of 250 precipitates.

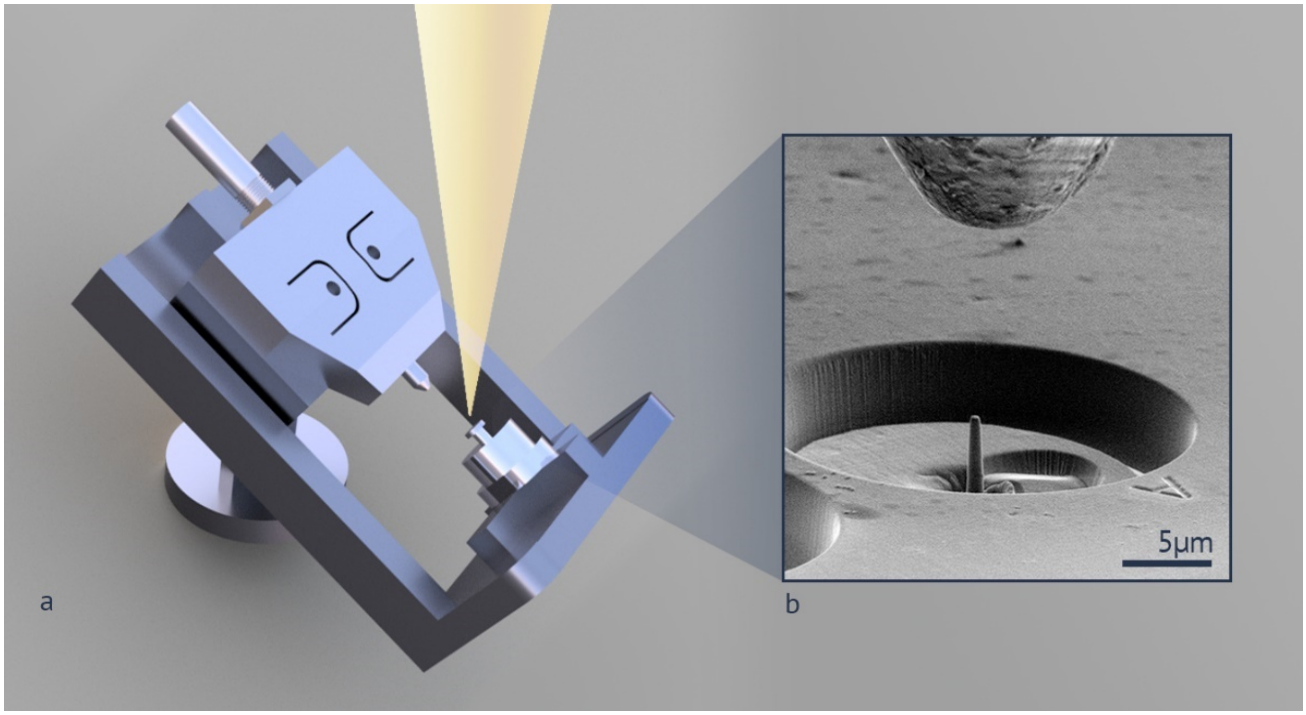

Figure 3.1 An illustration of the experimental setup: (a) pre-tilted frame of the ALEMNIS in-chamber nanoindenter; (b) SEM image from a 70˚ tilt angle showing the single crystal diamond flat punch hovering over a FIB-fabricated pillar.

Micropillar compression experiments were performed using an Alemnis nanoindenter that was placed inside the FIB-SEM microscope chamber. The overall geometry of the compact mechanical testing platform is illustrated in Figure 3.1 (a) The indenter is mounted on the sample stage using a pre-tilted support, allowing SEM image sequence recording during the experiment. The indenter was set to operate in a user-defined displacement-controlled mode that consisted of several experiment stages: alignment, approach, compression, hold, unload and finally the withdrawal of the indenter tip. Alignment and approach were performed either manually or choosing the programme tool provided by the manufacturer. Single crystal diamond flat tip punch with the end diameter of ~5µm was used. The end tip displacement in each experiment was set to achieve the

maximum compressive sample strain of ~30%. Micropillar compression stages of the test included a linear displacement ramp to the value corresponding to compressive strain ~0.3; a holding stage in which the indenter tip remained fixed at the maximum displacement for ~30 seconds; and the retraction stage, for which the same tip displacement ramp rate was used. The indenter tip speed was set to values in the range 10 nm/s to 50 nm/s depending on the diameter of the pillar.

Raw load-displacement data were post-processed to identify the point of initial contact with the sample that was assigned zero displacement. Indenter-sample contact was detected by the 20-40% increase of the load with respect to the noise floor that normally lies at the level of ~0.002-0.01 mN. The load drift was removed by a linear fit to the readings prior to sample contact and after unloading.

An accurate measure of engineering strain ε_{eng} was obtained by subtracting the elastic response of the indenter and of the bulk material that provides the elastic support below the pillars [46,140]:

$$\varepsilon_{eng} = (x_m - \frac{1-{\upsilon_i}^2}{E_i}\left(\frac{F_m}{D_t}\right) - \frac{1-{\upsilon_b}^2}{E_b}\left(\frac{F_m}{D_b}\right))/H \qquad (3.1)$$

Here E_i and υ_i denote Young's modulus and Poisson's ratio of the indenter (1050 GPa and 0.2 for diamond, respectively), and E_b and υ_b denote these parameters for the bulk material (207 GPa and 0.31 for Nickel, respectively). Notation x_m and F_m is used for the measured displacement and force, respectively, and the top and bottom diameters of the pillar are denoted by D_t and D_b, respectively. True strain and true stress were calculated using volume conservation law for the compression mode:

$$\varepsilon_{true} = -\ln(1 - \varepsilon_{eng}) \quad (3.2)$$

$$\sigma_{true} = \sigma_{eng}(1 - \varepsilon_{eng}) \quad (3.3)$$

It is clear that these calculations are approximate, as will become apparent from the consideration of the specific geometry of micropillar deformation that becomes evident from the image sequences recorded during indentation, as described below. In subsequent analysis, particular focus is placed on the flow stress values that corresponded to particular strain levels read from the stress-strain curves, typically around 3% to 10% compressive strain. Comparison of the flow stress values between pillars of different diameters was used to obtain insight into the strength size effect in single crystal superalloy micropillars.

A sequence of SEM images was recorded in the course of micropillar indentation, allowing to correlate distinct deformation phenomena with specific features in the stress-strain plot obtained by the interpretation of the simultaneously recorded load-displacement curve.

In order to reveal the internal structure of micropillars following compression testing, FIB-SEM dual beam system was used to perform serial sectioning tomography. This was combined with energy dispersive spectroscopy (EDS) analysis to make use of the additional contrast mode offered by this detection technique. For the purpose of tomographic analysis, the sample was mounted on a SEM stub and the stage was placed at 55˚ tilt, so that the focused ion beam was incident on the sample perpendicular to the overall sample surface and parallel to the longitudinal axis of the pillar prior to compression. Sample sections were prepared by FIB milling in the polishing regime, and high-resolution SEM images were collected using both secondary electron (SE) and backscattered

electron (BSE) detectors. The sample was then translated by 50 nm perpendicular to the ion beam, and another pair of images recorded. The resulting image stacks recorded in this way allowed volumetric rendering of the internal structure of deformed pillars.

To achieve a favourable compromise between the efficiency of material removal and the quality of section surfaces, FIB settings used were: accelerating voltage of 30 KeV, an ion beam current of 45 pA for section milling, and 1 pA for polishing to achieve the required finish. For the purpose of EDS mapping, the energy dispersive X-ray detector was inserted from top. The sample stage was tilted further to 70˚ in order to maximise the EDS signal recorded from the section of the pillar.

3.3 Micropillar compression test results

A typical set of experimental results is shown in Figure 3.2. The complete dataset consists of SEM image sequence (video) recording, high-resolution SEM images of the pillar before and after the compression test, and the true stress-strain curve interpreted from the raw load-displacement data captured by the nanoindenter system. The *in situ* nature of micropillar compression and SEM imaging allows direct correlation to be established between deformation phenomena observed in the images, and the features of the load-displacement curve.

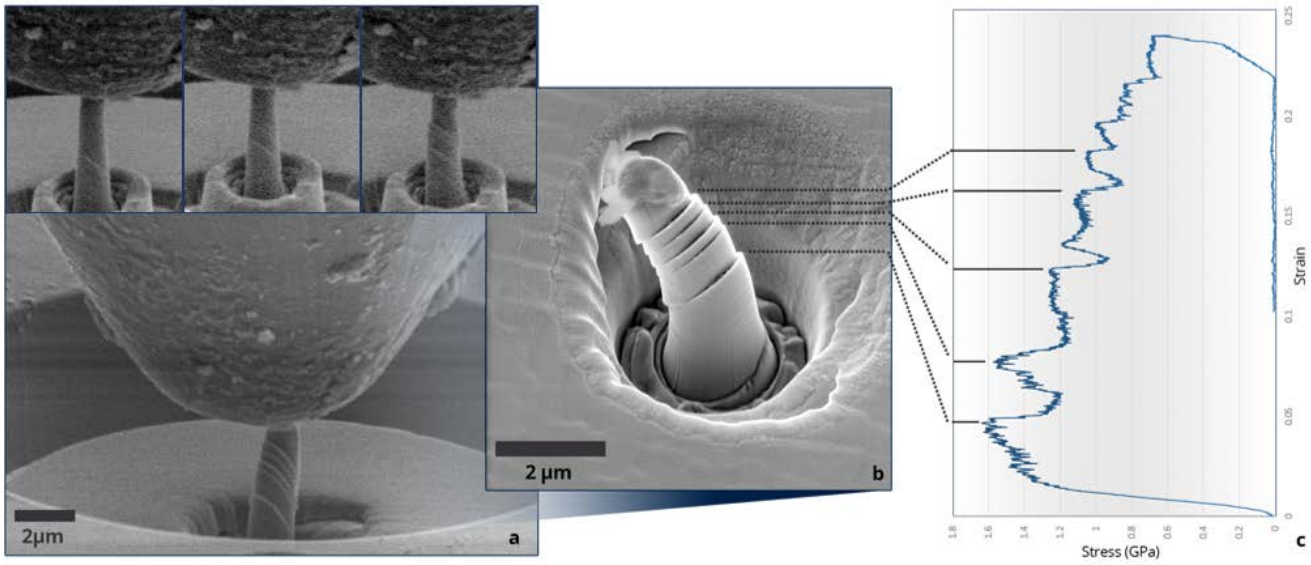

Figure 3.2 A typical experimental result set: (a) a sequence of 70◦ tilt SEM imaging video recorded during the compression test of a micropillar; (b) High resolution SEM image (taken at 30˚ title angle) of a micropillar after compression; (c) True stress and strain curve of the pillar, with individual stress drops associated with the corresponding distinct slip bands.

All recorded stress-strain curves display elastic response at strains below 1% (Figure 3.6 a), followed by hardening. At this stage slip traces on the pillar, side surface become apparent in the SEM image sequences. There are twelve {111} <$\bar{1}10$> slip systems that can be active in the face-centred cubic crystal structure. The close alignment of the compression axis with the [001] direction means that the normal of the four slip planes of {111} type are inclined to at approximately equal angle of $\phi \cong 54.74^{\circ}$. The same reasoning applies to the slip directions of (011) and (101) type on these slip planes that make the angle $\lambda \cong 35.26^{\circ}$ with the loading axis. It is worth noting that slip directions of type (110) are orthogonal to the loading axis, and therefore the critical resolved shear stress on these systems remains close to zero, meaning that no slip can occur.

The Schmid factor [46,47,51,141] for all eight active slip systems is computed as

$$m = \cos\phi \cos\lambda \cong 0.408 \qquad (3.4)$$

In real samples used in the experiments, the sample surface normal may not be perfectly aligned with the crystal axis. In accordance with the tolerances of sample preparation and experimental setup, the maximum possible misalignment between the loading direction and the [001] orientation of the crystal lattice was estimated not to exceed ~5°.

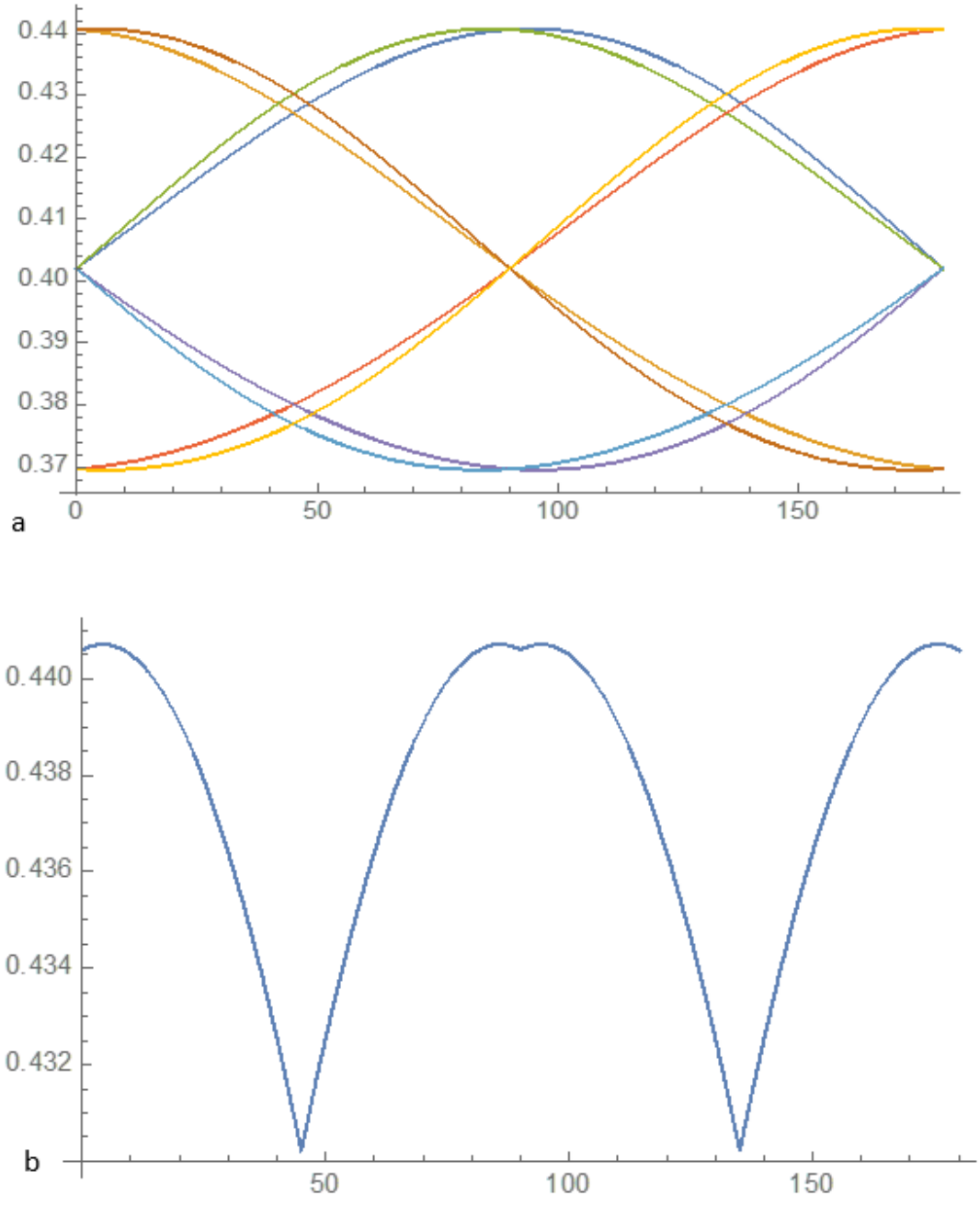

Figure 3.3 (a) Variation of Schmid factor of the six active slip system as a function of the azimuthal angle of misalignment between the loading direction and the crystal axis [001] in the range 0˚ to 180˚. (b) Maximum Schmid factor variation as a function of azimuthal angle in the range 0˚ to 180˚.

Figure 3.3 presents the plot of Schmid factor variation for the eight active slip systems as a function of the azimuthal angle α of the loading direction with

respect to the [001] crystal axis. Since the slip system with the largest Schmid factor value is always activated first, the maximum $\hat{m}$ and minimum $\check{m}$ values of the maximum Schmid factor in this range can be evaluated as:

$$\hat{m} \cong 0.441, \quad \check{m} = 0.430. \tag{3.5}$$

In comparison, Schmid factor for all eight potentially active slip systems in the case of perfect alignment corresponds to the value $\bar{m} \cong 0.408$. In other words, the deviation of Schmid factor due to 5˚ misalignment from the value that corresponds to perfect alignment between the loading direction and the [001] crystal axis lies in the range of ~8%. For the misalignment angle of only 1˚ this range reduces to less than 2%. Even small misalignment may lead to a significant change in the resolved shear stress on individual slip systems. This leads to one of the slip systems being strongly favoured at the initial stage of loading, which explains that in the experiments the appearance of deformed micropillars was dominated by parallel slip. In practical terms this finding means it is relatively unlikely that cross slip (multiple slip system activation) to occur at the beginning of loading, but it may be caused by subsequent slip system hardening.

Once plastic deformation begins, the passage of dislocations over parallel slip planes lying close to each other within a slip band leads to self-hardening, i.e. the increase in the shear stress required to cause further slip. Indeed, cross slip is observed in the latter stages of indentation experiments, signifying that the active slip system undergoes hardening of the order of ~10% sufficient to make an alternative slip system more favourable for further slip.

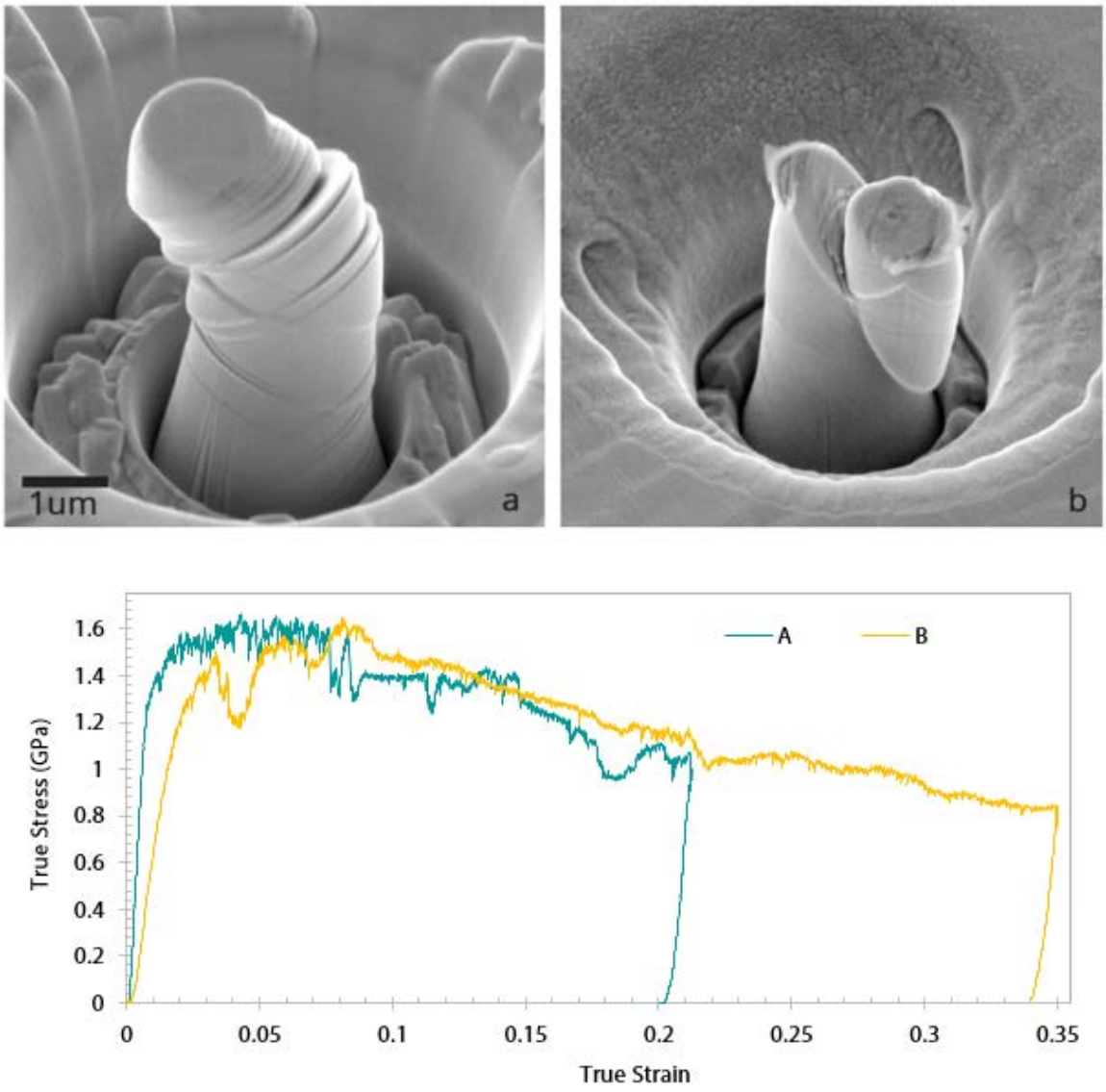

Figure 3.4 Comparison of two similar sized pillars (a)SEM image of a 30◦ tilt 1.5µm pillar dominated by cross slips during compression; (b) SEM image of a 30◦ tilt 1.41µm pillar dominated by large slipping during compression.

Consideration of the stress-strain plots shown in Figure 3.4 and Figure 3.6 reveals that initial Stage I hardening persists up to the strain values of ~10%. There is an important difference that can be noted between pillars that can be classified as large (~>5 µm) and small (~<2 µm) according to their diameter. For large diameter pillars the hardening process appears to be continuous and smooth (Figure 3.6

a). This is associated with multiple cross-slip caused by rapid hardening due to the large number of obstacles presented to their glide by interphase boundaries. In contrast, in small pillars the number of interphase boundaries in the dislocation glide path is small, leading to slower increase in the slip resistance within the slip bands. This hardening is insufficient to activate alternative slip systems. Instead, additional slip occurs in parallel slip bands belonging to the same slip system that was activated originally (Figure 3.2 and Figure 3.4 b).

In the current investigation, in contrast with some of the studies reported in the literature[72,142], displacement control was employed during indentation. In combination with suitably high stiffness and sampling rate of the measurement system, this mode allows efficient detection of load drop whenever additional slip band is initiated. Figure 3.4 provides a comparison between the slip geometries observed in two micropillars of similar size. The distinction between the two cases demonstrates that the plastic deformation pattern is not size dependent, but it is clearly strongly sensitive to small changes in the relative orientation of the crystal with respect to the load axis. What is interesting to note that at strains in the range 3-10% the flow stress required for further deformation is consistent between the two cases, suggesting that it may represent a useful parameter for further analysis. It is also apparent that further pillar deformation in Stage II is associated with apparent softening that requires further investigation and explanation.

Figure 3.5 (a) shows the high-resolution SEM image of a FIB polished section of a compressed pillar, on both the SE and BSE detectors. The microstructure reveals the arrangement of the γ' precipitates inside the pillar and how the slip cuts across the material. Large displacement bursts are illustrated by the shearing of the precipitates, and small multiple slips can be seen from the distortion of the

precipitate from rectangular (lower part of the pillar) into parallelogram shape appearing in the upper part of the pillar. EDS spectrum shown in Figure 3.5 (c) is taken to confirm the difference between γ and γ' phases.

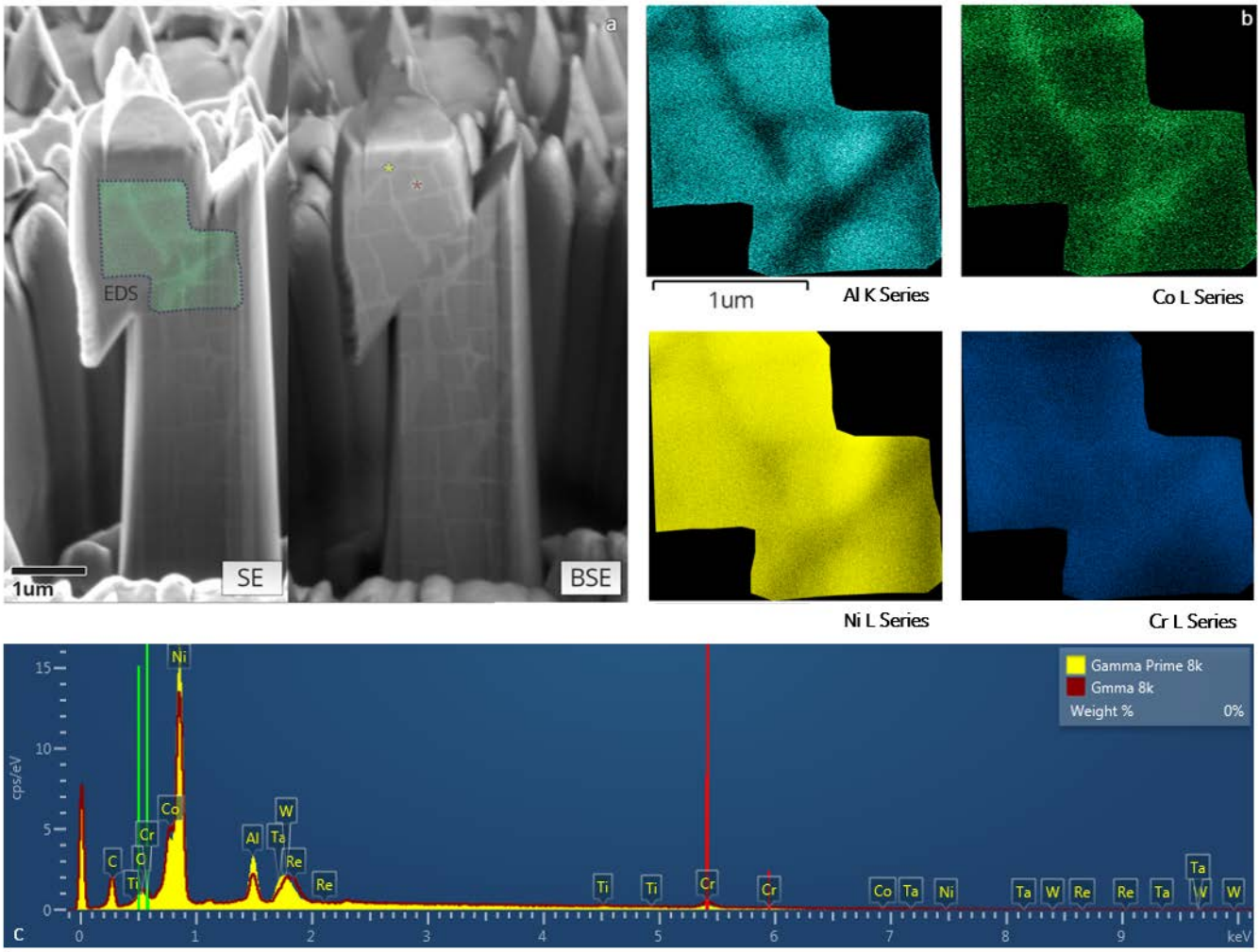

Figure 3.5 FIB-SEM tomography and EDS results. (a) A FIB milled vertical section of a pillar after compression in both SE and BSE detectors (55˚ tilt), featured by one slip burst; (b) EDS results shows phase contrast by Al, Co, Ni and Cr mapping, on a selected area indicated on the SE image; (c) Comparison of EDS spectrum of the typical γand γ' phase, indicated on the BSE image.

It agrees with previous results that γ phase has a higher concentration of Co, Cr and Re, and γ' phase contains more Ni and Al. An EDS elemental mapping of Al and Co over the slip area (indicated in Figure 3.5 a) shows agreement with the

same result revealed by the BSE image, the electron acceleration voltage was set to 8 KeV with pixel dwell time set to 5 μs for the EDS mapping process.

In the case shown in Figure 3.5, it can be seen that dislocations are freely gliding through the pillar, leaving the trace of sheared precipitates and steps on the side surface. It illustrates that dislocations escape before their interaction and multiplication (Stage II hardening) takes place, so that the dislocation density is, therefore, lower than for bulk samples. According to the popular “dislocation starvation” theory, such relatively dislocation-free status requires a higher shear stress to generate further dislocations, thus leading to materials strengthening.

Size effects of the strain hardening of the pillars arises in the present studies as expected. Figure 3.6 (a) shows representative true stress-strain curves for tested pillars with diameter of 0.39 μm, 0.92 μm, 1.35 μm and 7.88 μm. The smaller pillars (0.39 μm, 0.92 μm, 1.35 μm) clearly show a competition between softening and hardening in the stress-strain curve. After the almost linear hardening in Stage I, the flow stress becomes unstable, decreasing due to large dislocation bursts, and increasing again due to work hardening processes inside the pillar. Nonetheless, an obvious increase of the strength and work hardening of [001] pillars with the decreasing diameter is seen. This can be seen from the statistical representation of the results, in that the flow stress at a certain chosen strain value shows an increase with the decreasing pillar diameter. It is shown in Figure 3.6 (b) that the flow stress of the pillars at 5% strain varies from 0.95 GPa (which is somewhat larger, but close to the theoretical strength of the bulk crystal in the [001] orientation of ~0.8 GPa) up to 2.7 GPa, over three times the value for the bulk material.

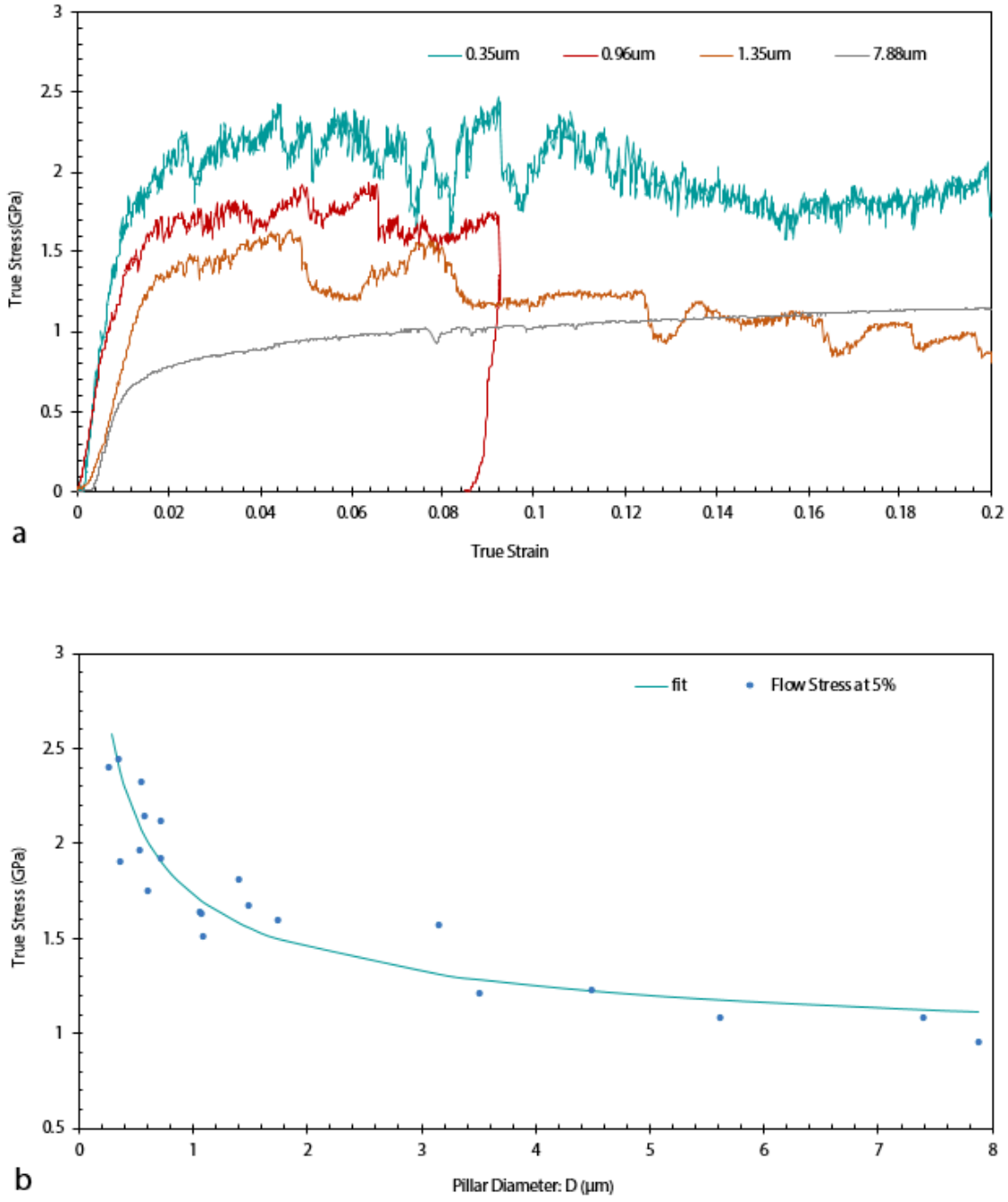

Figure 3.6 (a) Typical stress-strain curves for pillars of different diameters. (b) Plot of true flow stress at 5% true compressive strain for all tested pillars, and fitting of the data.

Top diameters of the pillars are mostly clear-defined and therefore identified as the correlation parameter for consistency. Due to the FIB fabrication process introduced previously, the pillars possess a 2-3˚ taper prior to compression, which is similar to the value reported in previous publications [47,51,130]. True stress at strain of 5% was chosen for the quantification of the size effect across the population of pillars. In this strain range, most pillars show a steady hardening stage towards a peak value before they undergo softening at a later stage of the compression test.

To describe the observed trend quantitatively, we introduce a modified Hall-Petch equation which incorporates both extrinsic and intrinsic length scales, namely

$$\sigma(D) = \sigma_0 \left[1 + c \left(\frac{d}{D}\right)^{\frac{1}{2}}\right] \tag{3.6}$$

Here σ_0 is the flow stress of the bulk material (σ_0=0.78GPa), *d* is the length of intrinsic microstructure feature (for example, it is possible to choose *d*=0.05 μm as the average width of the γ channels), *D* is the external length dimension (pillar diameter), and *c* stands for the fitting parameter that can be derived from the two-phase deformation model presented in the following section. According to this model,

$$\mathrm{c} = \frac{(\tau_1 - \tau_2)}{\tau_1 \cdot f(\lambda)} \tag{3.7}$$

where τ_1 and τ_2 respectively denote the high and low critical resolved shear stress in a two-phase structure, and $f(\lambda)$ is a geometric function with a value close to unity.

Figure 3.6 (b) shows a satisfactory quality fit of equation (3.6) to the experimental data with the quality coefficient of R^2=0.995 calculated as:

$$R^2 = 1 - \frac{SS_{res}}{SS_{tot}} = \frac{\sum_i e_i^2}{\sum_i (\sigma_i - \bar{\sigma})^2} \quad (3.8)$$

The value of c is found to be around 5.5 for the best agreement with the experimental results.

3.4 Models for flow stress of two-phase single crystal

3.4.1 An approximate model based on the intrinsic length scale d and external dimension D

Let us assume that on the micropillar surface a slip-resistant layer of amorphous material is present, whilst the inner crystalline volume has much lower resistance to slip. The distributed dislocation slip model is illustrated in Figure 3.7

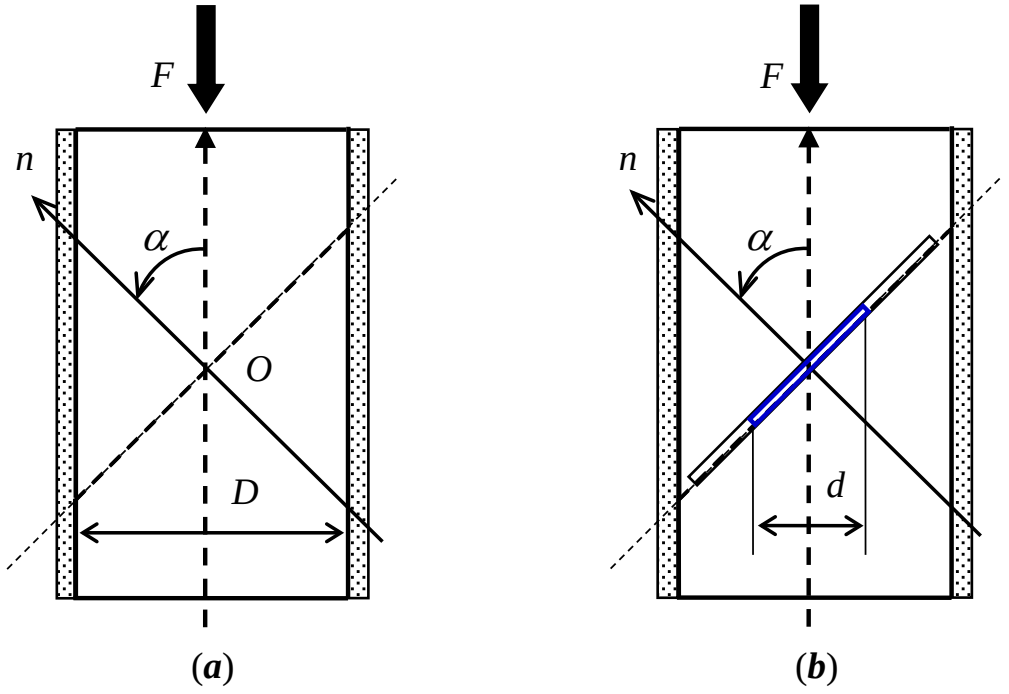

Figure 3.7 Flow stress of a micropillar is under uniaxial compression: boundary and inclusion effect (a) Perfect pillar with surface effect. (b) Equivalent damaged pillar with surface effect, considering the weak phase

This model is shown in greater detail in Figure 3.8.

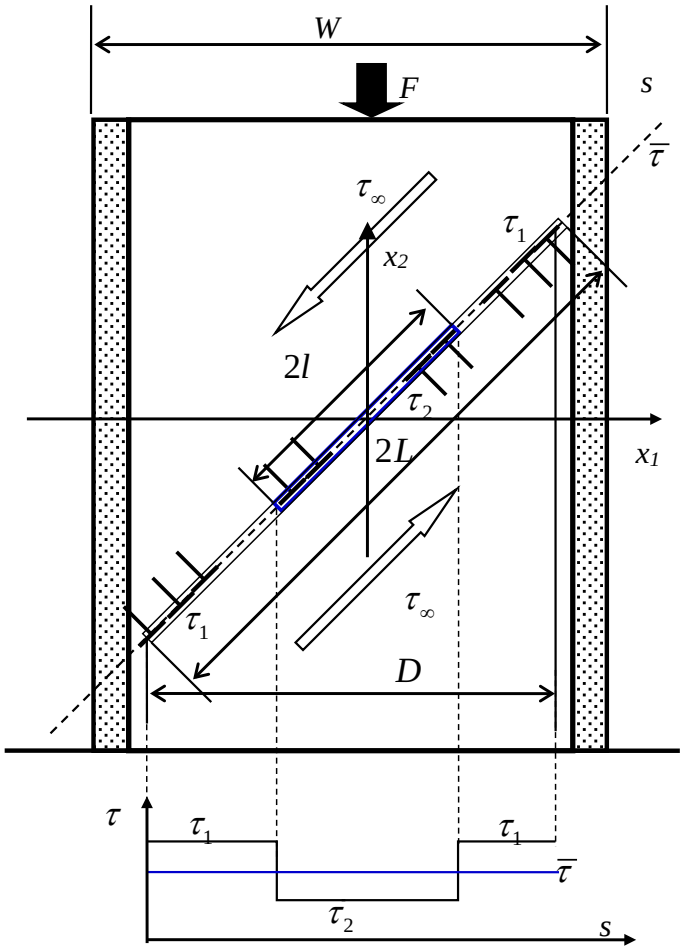

Figure 3.8 Flow model incorporating the effects of amorphous surface layer and varying internal friction (critical shear stress).

Under compressive load, a slip band is formed. The internal frictional shear stress for the strong phase is denoted by τ_1, whilst the weak phase (matrix) occupies an equivalent slip length 2*l* along the slip band has a lower friction shear stress denoted by τ_2 $\left(\tau_1 > \tau_2\right)$. The overall slip band length is denoted by *2L*, and its *average* friction shear stress is $\bar{\tau}$. When slip occurs, dislocations of opposite signs travel in opposite directions along the band towards the surface. The overall stress intensity factor due to the dislocation distribution and pile up against the amorphous surface layer is approximately given by:

$$K_{IIL} = \tau_{macr}\sqrt{\pi L} = \left(\tau_\infty - \overline{\tau}\right)\sqrt{\pi L}$$
$$\overline{\tau} = \frac{2l\tau_2 + \left(2L - 2l\right)\tau_1}{2L} = \frac{l\left(\tau_2 - \tau_1\right)}{L} + \tau_1 \qquad (3.9)$$

Now consider the stress intensity factor of the internal slip band that is shown in Figure 3.8 that arises due to internal dislocation pile up against interphase boundaries, which is given by

$$K_{III} = \tau_{micr}\sqrt{\pi l} = \left[\tau_\infty - \left(\tau_2 - \overline{\tau}\right)\right]\sqrt{\pi l} \qquad (3.10)$$

In order for the dislocation glide to occur along the entire slip band *and* to produce an extrusion/intrusion at pillar surface, we introduce the key assumption that this requires equality between slip resistances on the micro- and macro- scale:

$$K_{IIL} = K_{III} \qquad (3.11)$$

This means that

$$\left(\tau_\infty - \overline{\tau}\right)\sqrt{\pi L} = \left[\tau_\infty - \left(\tau_2 - \overline{\tau}\right)\right]\sqrt{\pi l} \qquad (3.12)$$

so that

$$\left(\tau_\infty - \overline{\tau}\right)\sqrt{L} = \left[\tau_\infty - \left(\tau_2 - \overline{\tau}\right)\right]\sqrt{l} = \left[\tau_\infty + \left(\overline{\tau} - \tau_2\right)\right]\sqrt{l} = \left(\tau_\infty + \tau_l\right)\sqrt{l}$$
$$\left(\overline{\tau} - \tau_2\right) = \frac{\left(L - l\right)\left(\tau_1 - \tau_2\right)}{L} = \tau_l > 0 \qquad (3.13)$$

From (equation 3.13), we can find

$$\tau_\infty = \frac{\sqrt{L}}{\left(\sqrt{L} - \sqrt{l}\right)}\overline{\tau}\left(1 + \frac{\tau_l}{\overline{\tau}}\frac{\sqrt{l}}{\sqrt{L}}\right) = \frac{\sqrt{L}}{\left(\sqrt{L} - \sqrt{l}\right)}\overline{\tau}\left(1 + \frac{\tau_l}{\overline{\tau}}\frac{\sqrt{l}}{\sqrt{L}}\right) \qquad (3.14)$$

or

$$\tau_\infty = \frac{\sqrt{L}}{\left(\sqrt{L}-\sqrt{l}\right)}\left(\left(\frac{l\left(\tau_2-\tau_1\right)}{L}+\tau_1\right)+\frac{\left(L-l\right)\left(\tau_1-\tau_2\right)}{L}\frac{\sqrt{l}}{\sqrt{L}}\right) \qquad (3.15)$$

Furthermore, for the case of moderate l/L ratio (e.g., $l/L<0.1$), equation (3.15) can be simplified as

$$\tau_\infty = \frac{\sqrt{L}}{\left(\sqrt{L}-\sqrt{l}\right)}\left(\left(\frac{l\left(\tau_2-\tau_1\right)}{L}+\tau_1\right)+\frac{\left(L-l\right)\left(\tau_1-\tau_2\right)}{L}\frac{\sqrt{l}}{\sqrt{L}}\right)=\tau_1\left(1+\frac{\left(\tau_1-\tau_2\right)}{\tau_1}\frac{\sqrt{l}}{\sqrt{L}}\right) \qquad (3.16)$$

Since the values of *l* and *L* are proportional to *d* and *D*, respectively, eq. (3.16) can be also expressed in terms of the micropillar diameter *D* and intrinsic length scale *d* as

$$\tau_\infty = \tau_1\left(1+\frac{\left(\tau_1-\tau_2\right)}{\tau_1}\sqrt{\frac{d}{D}}\right) \qquad (3.17)$$

We note that all parameters in (3.17) are material constants.

3.4.2 A model explicitly incorporating the finite size effect

We now present a more detailed model that is built on the previous approach, but incorporates a more complex dependence on the sample size by accounting for the presence of traction-free boundaries.

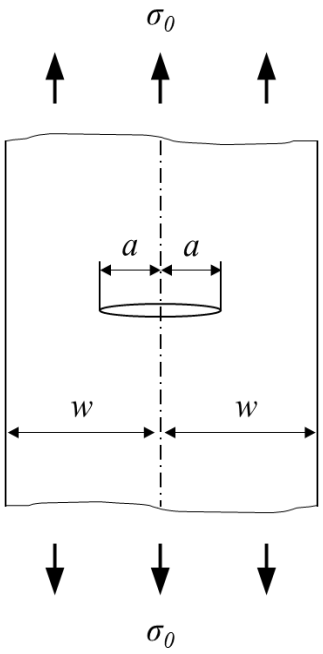

$$K_I = F(\lambda)\sigma_0\sqrt{\pi a}$$

$$F(\lambda) = (1 - 0.025\lambda^2 + 0.06\lambda^4)\sqrt{\sec(\pi\lambda/2)}$$

$$\lambda = a/W$$

Figure 3.9 Centre crack in a strip [143]

In Part I, the formula to calculate the stress intensity factor for a slip band (Mode II crack) used the expression for a dislocation distribution in an infinite plane. The finite geometry effect is expressed as follows

$$K_{IIL} = \tau_{macr} f(\lambda)\sqrt{\pi L} = (\tau_\infty - \overline{\tau}) f(\lambda)\sqrt{\pi L}$$
$$f(\lambda) = f\left(\frac{D}{W}\right) \qquad (3.18)$$

Here $f(\lambda)$ is a geometric function that has the form similar to that given by Tada [143] illustrated in Figure 3.9.

The stress intensity of the equivalent inner slip band in Figure 3.8 is still given by

$$K_{III} = \tau_{micr}\sqrt{\pi l} = \left[\tau_{\infty} - \left(\tau_2 - \overline{\tau}\right)\right]\sqrt{\pi l} \qquad (3.19)$$

where $\overline{\tau}$ is the average internal frictional stress, τ_1 and τ_2 are the internal frictional stresses along the friction line $\left(\tau_1 > \tau_2\right)$, Since

$$K_{IIL} = K_{III} \qquad (3.20)$$

then

$$\left(\tau_{\infty} - \overline{\tau}\right) f\left(\lambda\right)\sqrt{\pi L} = \left[\tau_{\infty} - \left(\tau_2 - \overline{\tau}\right)\right]\sqrt{\pi l} \qquad (3.21)$$

Thus

$$\begin{aligned} &\left(\tau_{\infty} - \overline{\tau}\right) f\left(\lambda\right)\sqrt{L} = \left[\tau_{\infty} - \left(\tau_2 - \overline{\tau}\right)\right]\sqrt{l} = \left[\tau_{\infty} + \left(\overline{\tau} - \tau_2\right)\right]\sqrt{l} = \left(\tau_{\infty} + \tau_l\right)\sqrt{l} \\ &\left(\overline{\tau} - \tau_2\right) = \frac{\left(L - l\right)\left(\tau_1 - \tau_2\right)}{L} = \tau_l > 0 \end{aligned} \qquad (3.22)$$

From (equation 3.22), it follows that

$$\tau_{\infty} = \frac{f\left(\lambda\right)\sqrt{L}}{\left(f\left(\lambda\right)\sqrt{L} - \sqrt{l}\right)}\overline{\tau}\left(1 + \frac{\tau_l}{\overline{\tau}}\frac{\sqrt{l}}{f\left(\lambda\right)\sqrt{L}}\right) \qquad (3.23)$$

or

$$\begin{aligned} \tau_{\infty} &= \frac{f\left(\lambda\right)\sqrt{L}}{\left(f\left(\lambda\right)\sqrt{L} - \sqrt{l}\right)}\left(\overline{\tau} + \tau_l\frac{\sqrt{l}}{f\left(\lambda\right)\sqrt{L}}\right) \\ &= \frac{f\left(\lambda\right)\sqrt{L}}{\left(f\left(\lambda\right)\sqrt{L} - \sqrt{l}\right)}\left(\frac{l\left(\tau_2 - \tau_1\right)}{L} + \tau_1 + \frac{\left(L - l\right)\left(\tau_1 - \tau_2\right)}{L}\frac{\sqrt{l}}{f\left(\lambda\right)\sqrt{L}}\right) \end{aligned} \qquad (3.24)$$

Furthermore, for small *l/L,* we simplify eq. (3.24) as

$$\tau_\infty = \tau_1\left(1+\frac{(\tau_1-\tau_2)}{\tau_1}\frac{\sqrt{l}}{f(\lambda)\sqrt{L}}\right) \tag{3.25}$$

Eq. (3.25) can be also expressed in terms of diameters as

$$\tau_\infty = \tau_1\left(1+\frac{(\tau_1-\tau_2)}{\tau_1}\frac{\sqrt{d}}{f(\lambda)\sqrt{D}}\right) \tag{3.26}$$

Where d and *D* can be found in Figure 3.7. Therefore, we may write eq. (3.26) in a generalized form as

$$\tau_\infty = \tau_1\left(1+c\frac{\sqrt{d}}{\sqrt{D}}\right) \tag{3.27}$$

Now *c* is a constant that needs to be determined by calibration of $f(\lambda)$, or from fitting the experimental data.

3.5 Discussion

Results of the current study show clear size-dependent behaviour of FIB-fabricated micropillars under compression testing. Stress-strain responses collected in the experiment illustrate that all pillars independently of the size show a clear elastic stage immediately the onset of loading, followed by a hardening stage that persists for the strains between 2-3% and up to ~5%, beyond which softening sets in. This softening behaviour is likely to be associated with the combination of inability of hardening to maintain the required load, and the failure of volume conservation due to large geometric changes. Softening is sought to be observed due to the low speed (10-50nm/s) displacement control mode employed. In contrast with some studies [46] where load control was used, the loading mode used in this study made it possible to capture the load fluctuation that accompanies the slipping behaviour.

The results displayed in Figure 3.6 reveal the size-dependent mechanical response of micro- and nanopillars under the uniaxial compression test. The observation assisted by FIB tomography and EDS mapping, have revealed the dislocation gliding behaviour inside the two-phase microstructure of Ni-base superalloys crystals. Ever since introduced in the 1950s, the Hall-Petch equation has been applied and modified in numeric ways [64,144–146] trying to capture the size-dependent variation of material's properties, known as *smaller is stronger*. Most recently, studies [46,47,130] tend to seek for an alternative exponent, other than ½, while fitting the size effect results. The mechanism behind which, however, has not been fully revealed. In the current study, exponent of ½ is kept in a modified equation based on Hall-Petch and the result manifests great correlation

(*R^2=0.995 for current study*) between the fitting and the experimental data points. it is also realized in some complex models [144,146] where proportion of dislocation mean free path length to characteristic size (λ) (along with dislocation source density) is considered in the fitting coefficient. However, it (λ) differs from the relationship between intrinsic and extrinsic characteristic lengths which is considered in the equation (3.6). Though more detailed discussion remains to be done while possibly carrying out comparison work, the application of this equation (3.6) shed light on dual characteristic length consideration on top of the original Hall-Petch equation format.

3.6 Conclusion

In situ micro- and nano- compression tests were carried out with an in-chamber Alemnis nanoindenter inside the LYRA dual beam FIB-SEM system, where EDS was also employed to assist in the observation of microstructure. Size effect was observed across Ni-base superalloy pillars with various sizes (from ~200 nm to several microns). Mechanical response was recorded, and the flow stress at the strain value of 5% was compared and discussed. A modified Hall-Petch equation incorporating both extrinsic and intrinsic characteristic lengths was introduced and led to a satisfactory fit with the experimental data.

The origins of the occurrence of such size effect on single crystals are widely discussed by many relevant works, with theories such as ‘dislocation starvation’ proposed. In later chapters (Chapter 5), experiments with advanced X-ray microscopic tools are designed and performed in order to directly reveal such effects.

Chapter 4

In situ micro-Laue diffraction studies on the three-point bending of a notched single crystal

This chapter contains the report of X-ray microscopy analysis of crystal plasticity of superalloys under different kinds of mechanical deformation. The principal technique used here is micro-Laue diffraction. Two types of nickel alloys with different pre-introduced residual stress states are tested *in situ*. The fundamentals of the micro-Laue method are discussed in the context of X-ray diffraction theory, and reviewed in the application to the class of problems studied. The methodology adopted for interpreting Laue diffraction patterns for plastically deformed crystals is presented, discussed and applied to the experimental results. The technique of energy scanning white X-ray beam reciprocal space mapping is also presented, and the data interpretation discussed.

4.1 Introduction and motivation

As reviewed in section 2.1, modern Ni-base superalloys contain ordered (γ', $L1_2$ structure) precipitates embedded in a disordered FCC solid solution matrix (γ phase). The coherent nature of the two phases, ordered vs disordered, gives rise to the strengthening effect in the material. Therefore, understanding the structure, defects and deformation mechanisms at the nano- to micro-scale is sought to enable purpose-driven alloy formulation, design, fabrication and processing to optimise performance.

Micro-Laue diffraction is well established as an effective technique for mapping grain orientation and structure, and more recently intra-granular strain [91,147–151]. The main emphasis of the present work is to utilize the micro-focus capabilities of synchrotron-based polychromatic X-ray beam to probe the relevant properties on Ni-base superalloy single crystals under elastoplastic deformation. The experiment was carried out for two types of Ni-base superalloys — one commonly used (CMSX-4), and one novel formulation (ABD-1) from the alloy-by-design paradigm (see section 2.1).

In situ loading of the samples was used to generate localised strain distributions. The samples were placed in a reflection mode arrangement, to allow micro-Laue mapping over the highly stressed notch tip region. Several loading increments were used to examine the influence of stress on both the intra-granular strain and the associated grain rotation. Two different methods were used to introduce notch/crack into the beam samples, namely, FIB milling, and fatigue crack initiation and growth. Different deformation patterns were observed for the two different cases.

The experiments were carried out on the beamline B16, Diamond Light Source, Harwell, UK. Beamline B16 offers the flexibility of using either white beam or monochromatic beam with KB focusing devices, hence providing the possibility to perform *in situ* micro-Laue diffraction experiments and reciprocal space mapping microscopy within the same setup. The experimental data presented this chapter was obtained in two separate beamtime allocations (5-8th May 2014 and 21-23rd May 2015). The experimental data is discussed below based on the underlying understanding of the Laue method provided, through area mapping over a raster array of beam positions on the sample, followed by automated data interpretation.

4.2 Material and specimen preparation

The ABD-1 specimen used for the present experiment was cut out of cast ABD-1 (alloy-by-design) bar provided by Roger Reed's group in the Department of Engineering Science, University of Oxford. The idea of the ABD alloy series allows, in the words of its developers [8], lies in designing the composition of single crystal superalloys to attain the numerically estimated targets in terms of creep resistance, microstructural stability, density, cost, and castability. In contrast, the CMSX-4 specimen used in the study represents a widely available commercial alloy type that has previously been the subject of significant research on structural and mechanical characterization.

A rectangular beam of ABD alloy was cut out of the cast crystal bar by utilizing a BUEHLER IsoMet diamond saw used at low speed, with the crystallographic orientation selected to be the [0 0 1] axis pointing perpendicular to the top surface of the specimen, over which the incident beam was scanned, as shown in Figure 4.4.

Once cut, the specimen was carefully polished to the quality required for EBSD examination. Since the interaction volumes for electron microscopy are typically much smaller (shallower) than for X-ray analysis, this suggested that good Laue patterns should be obtained at least from moderately deformed volumes. The procedure involved several polishing operations — performed on a rotational grinder with various grinding/polishing discs, lubricants/suspensions, etc. The sample was first ground to a flat surface using progressively finer grit SiC papers, then polished down in several steps using various diamond suspensions. Finally,

the sample was polished by colloidal silica suspension to achieve the final finish. The detailed procedures are listed in the Table 4.1 below.

Table 4.1 Grinding and polishing procedure for Ni-base superalloy

Grinder or Polishing Disc	Grit, Grain Size	Lubricant	Rotational Speed (rpm)	Force (N)	Time (min)
SiC paper	#1200	Water	150	15	Until plane
Woven acetate disc	3 μm diamond suspension	Water-base lubricant, green	150	10	20
Fibric disc for diamond	1 μm diamond suspension	Water-base lubricant, green	100	7.5	20
Fibric disc for diamond	0.3 μm diamond suspension	Water-base lubricant, green	100	7.5	25
Fibric disc for diamond	Colloidal silica	water	100	7.5	15

The ABD sample dimensions were 9.5 □ 1.55 □ 1.9 mm, with a 0.5 mm deep notch machined on one side. At the tip of the machined notch, a further notch of width less than 5μm was milled by focused ion beam, using a current of around 200 pA, as illustrated in Figure 4.4 a. The FIB machined notch had a length of 78μm, tip diameter of 3μm, and total depth of 300μm.

The CMSX-4 alloy beam was prepared under similar procedures. Firstly, the alloy beam was cut out utilizing a slow diamond saw, and polishing procedures listed

in Table 4.1 were performed. The finished dimensions for the specimen were 12 □ 1.5 □ 3.1 mm, with a 0.5 mm deep notch. A fatigue crack was introduced at the tip of the notch by cyclic three-point bending, carried out using Instron universal testing machine.

4.3 Experimental setup

The B16 beamline, Diamond Light Source, UK, offers several operational set-ups, including monochromatic and white beam modes combined with focusing of X-ray beams using Compound Refractive Lenses (CRL's), Fresnel Zone Plate (FZP), and KB mirrors. The schematic of the beamline set-up is shown in Figure 4.1.

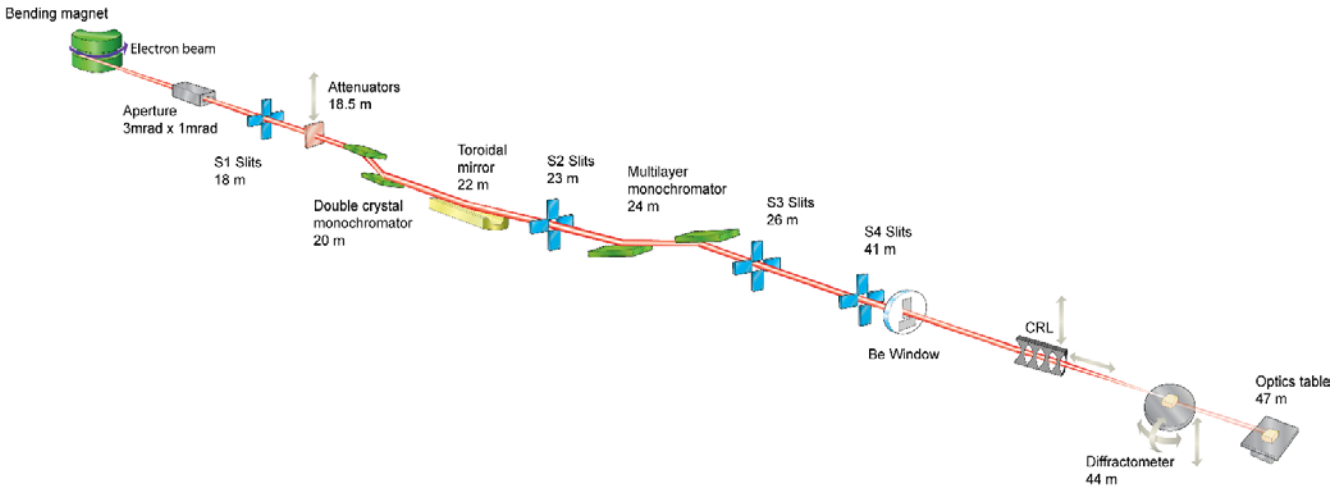

Figure 4.1 Beamline Schematic for B16 [152]

To perform *in situ* micro-Laue diffraction for the three-point bending experiment, micro-Laue diffraction in the 90° reflective configuration was designed and implemented, with the sample mounted at a 45° tilt to the incident white beam. Two DEBEN in situ tensile testing rigs/stages, with maximum loading of 200 N and 5000 N shown in Figure 4.2, were employed for the experimental purposes.

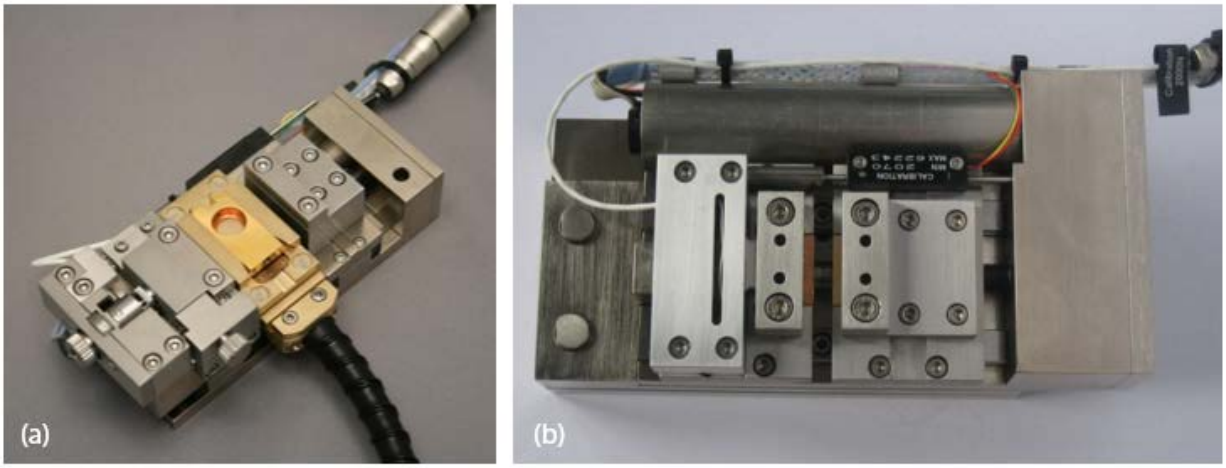

Figure 4.2 DEBEN in situ tensile testing stage with max loading of (a)200 N; and (b)5000 N [153]

The DEBEN rigs with the gripped crystal sample were mounted on the beamline sample stage driven by piezoelectric motors to allow movement across and along the beam in the working plane inclined at the 45° angle to the incident beam, as shown in Figure 4.3.

The X-ray beam spectrum spanned the energy band ~6-22keV, and was focused down to the spot size of 0.3×0.4μm^2 (in the plane normal to the incident beam) using a polished and bent Si Kirkpatrick-Baez (KB) mirror pair. The beam intensity profile was probed by scanning across the edges of vertically and horizontally mounted gold wires.

A CCD area detector (Photonic Science Full Frame 9-megapixel CCD camera) was mounted facing downwards to collect the diffraction pattern frames. This detector has 3056 x 3056 CCD array pixel with pixel size of 31μm. The pattern recording rate was 0.5 frame per second, with 16-bit extended dynamic range and GdOS/Tb scintillator suitable for operation in the range 5-55 KeV, with a minimum feature recognition of 101 p/mm (12 μm - 75 μm input size).

Figure 4.3 Experimental setup on the beamline. The gold colour box contains the KB mirror pair, with associated controls.

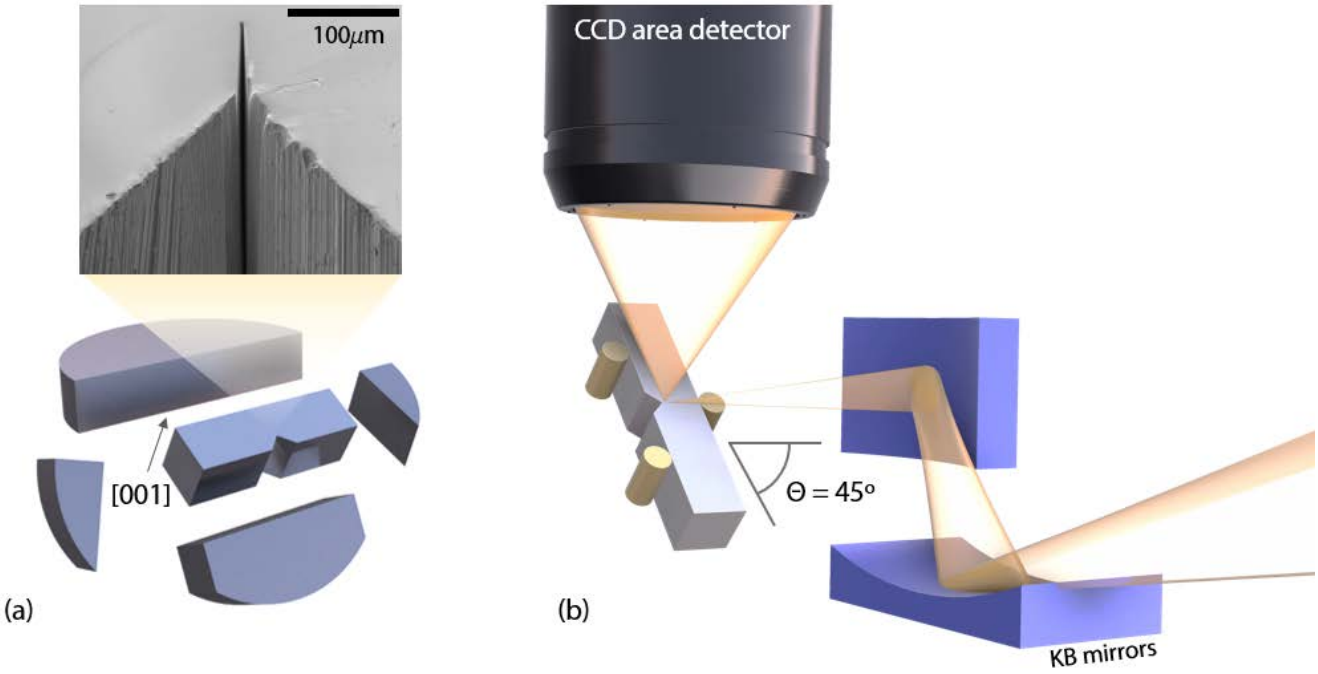

Figure 4.4 Schematic diagrams of sample preparation and experimental setup.

4.4 Experimental Procedures

Silicon wafer was used for the calibration of the geometrical parameters of the experimental setup, performed by placing the wafer at the sample position, and collecting Laue diffraction pattern from it. The diffraction patterns were collected at different detector-to-sample distances, *dd*. By applying triangulation to a particular tracked Bragg spot collected, precise values could be calculated for *dd* and the detector centre position (x and y) needed for pattern indexing. By refining the calculation for the silicon crystal with known lattice parameters and structure, small camera tilt angles could be accurately deduced. A typical frame of Laue pattern from the silicon crystal for calibration is shown in Figure 4.5.

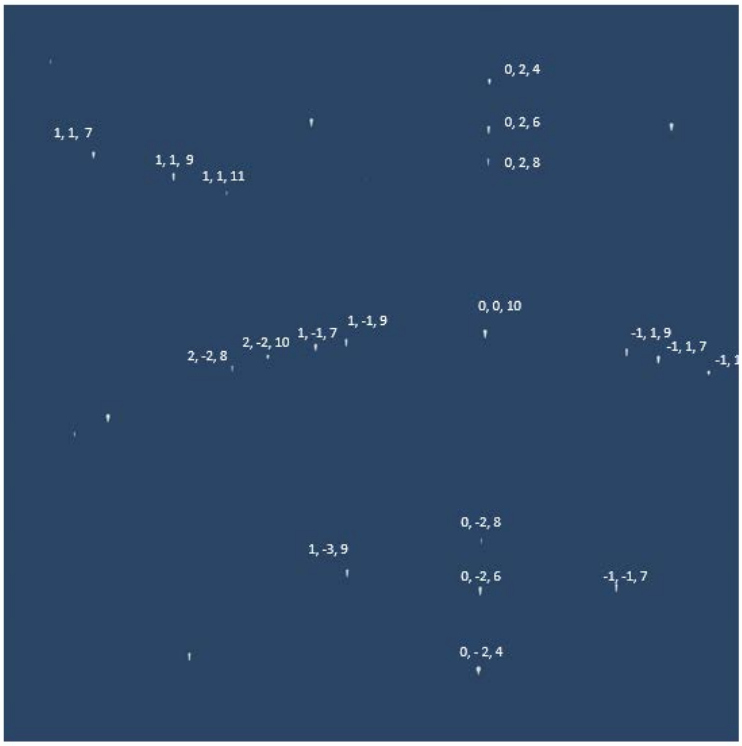

Figure 4.5 Laue diffraction pattern of Silicon {001} of sample-detector distance 110 mm, and energy band of 6-26 KeV

The DEBEN loading mounted on the sample stage with positioned using piezo motors that delivered the resolution of one micron. The zone of interest on the sample was found (around the notch and at the location of the crack tip). A diode sensor was used for rough scanning over an array of positions at the sample surface to align the incident beam with the zone of interest. Once aligned, the CCD detector will put in place for collecting Laue diffraction patterns, such as shown in Figure 4.6.

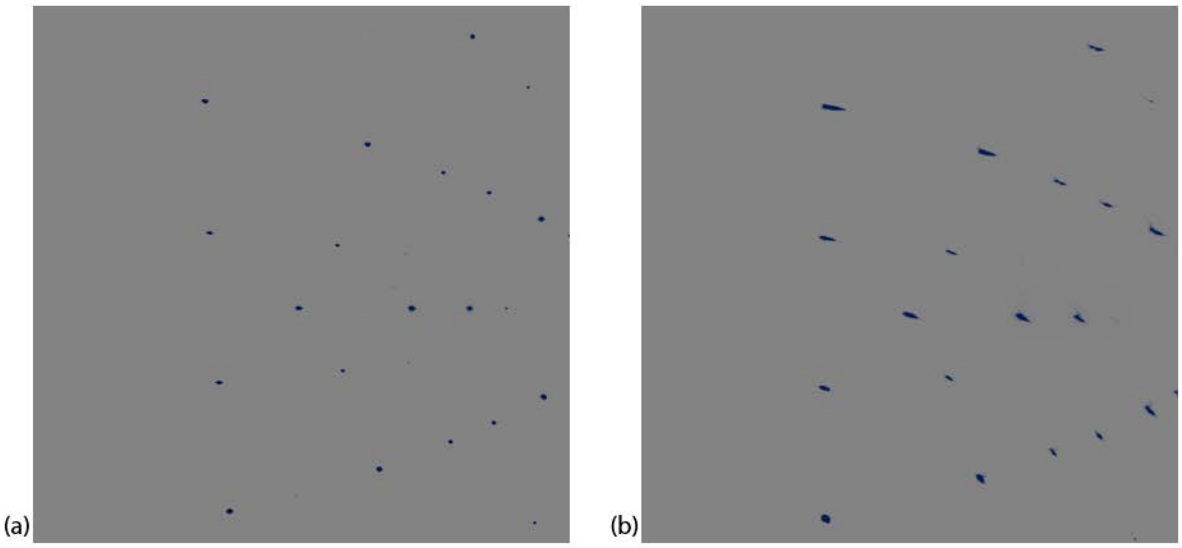

Figure 4.6 Laue diffraction pattern from ABD sample, collected (a) in the elastic region on the sample; (b) from a plastically deformed region that shows "streaking" of Bragg spots

By observing the diffraction pattern collected from different positions on the sample surface, the elastoplastic response of local crystal lattices (or averaged local plastic behaviour over the beam interactive volume) can be probed. Figure 4.6 (a) shows the micro-Laue diffraction pattern from ABD alloy bar where no obvious consequences of plastic strain can be noticed, whilst in Figure 4.6 (b), Bragg spots show "longitudinal blurring", or "streaking" effect, which arises as a consequence of the total dislocation population within the gauge volume [94,98].

At each loading step, mapping sequence for data acquisition was run, consisting of scanning the incident beam and collect the diffraction patterns of the region of interest). Once this was complete, the load was changed in accordance with the loading sequence, using remote control of the DEBEN miniature loading rig, and mapping was repeated.

4.5 Data interpretation

Diffraction patterns (one per probed volume) form the basic unit of experimental data acquired from the micro-Laue experiment. These can be interpreted in different ways. For instance, an intensity map over the scanned region provides a visual representation of the scattering strength of different gauge volumes, that is related to the degree of perfection (distortion) of the crystal lattice. More detailed analysis allows revealing how the change in the intensity distribution around the Bragg spot/peak relates to the plastic deformation sustained by the probed crystal gauge volume.

4.5.1 X-ray Intensity

The intensity of X-ray diffraction from a given source (at constant flux and energy) is sensitive to the degree of material crystallinity (lattice quality), which can be expressed by the following equation [154]:

$$I_{(hkl)\alpha} = \frac{K_e K_{(hkl)\alpha} \upsilon_\alpha}{\mu_s} \,. \qquad (4.1)$$

Here μ_s stands for the linear attenuation coefficient of the specimen, υ_α is the volume fraction of the certain phase/ structure/ crystal (α) in the sample that contributes to the chosen peak, and ***Ke*** is a constant multiplier for a given experimental setup or environment:

$$K_e = \frac{I_0 \lambda^3}{64\pi r} \left(\frac{e^2}{m_e c^2}\right)^2. \quad (4.2)$$

Here I_0 stands for the incident beam intensity, r is sample-detector distance, λ is the wavelength of the X-ray, $(e^2/m_e c^2)^2$ stands for the classical electron radius.

$K_{(hkl)\alpha}$ is a constant for the individual hkl reflection from phase α, given as:

$$K_{(hkl)\alpha} = \frac{M_{hkl}}{V_\alpha{}^2} \left|F_{(hkl)\alpha}\right|^2 \left(\frac{1+\cos^2(2\theta)\cos^2(2\theta_m)}{\sin^2\theta\cos\theta}\right)_{hkl}. \quad (4.3)$$

Here M_{hkl} is the multiplicity of a certain hkl reflection from phase α, V_α stands for the volume of unit cell of the diffracting structure (α), and $F\alpha$ stands for the structure factor of the corresponding reflection (hkl).

The volume fraction of the diffracting phase makes a significant contribution to determining the intensity of the Bragg peak. Hence, mapping the total diffraction intensity for a given experimental setup provides an indication on the mesoscale crystallographic quality within the sample.

Figure 4.7 (a), (b) and Figure 4.8 (a), (b) shows intensity maps over the studied region for the two specimens (ABD alloy and CMSX4 alloy, respectively), where the regions indicated by the dash box frames correspond to the accompanying zoomed in images. The ABD alloy beam was initially loaded up to 5 N to create a reference stress state (shown in frame b), and further loaded up to 100 N before being unloaded to 0 N for comparison. In the intensity map over the region, it can be observed that the intensity was not distributed evenly, with the upper part of

the crack tip showing average intensity compared to the lower part. This can be attributed to the fact that the crack was fabricated by focused-ion-beam with large ion beam current (200-400 pA). The ion beam scanning within the FIB-SEM is achieved by the combination of beam deflection using EM lenses and beam blanking, which occurs on the ms timescale. Small lack of synchronicity between operation results in ion beam hitting the sample surface, causing ion implantation and damage that affects the interaction with the X-ray beam.

Figure 4.8 (a), (b) and (c) show the diffracted beam intensity map over the notch and crack zone at a larger beam size of about 5 x 5μm. The sample was loaded up to 1000 N and 2000 N utilizing the larger capacity DEBEN rig. The specimen was subjected to cyclic fatigue loading under the same three-point bending condition using the INSTRON universal testing machine. Traces of slip lines which represent the active crystal deformation mode can be observed at the beam surface from the intensity map. Frame (c) in the figure reveals tip progress from right to left under increased load, obtained by the calculation of the difference map between frames (a) and (b).

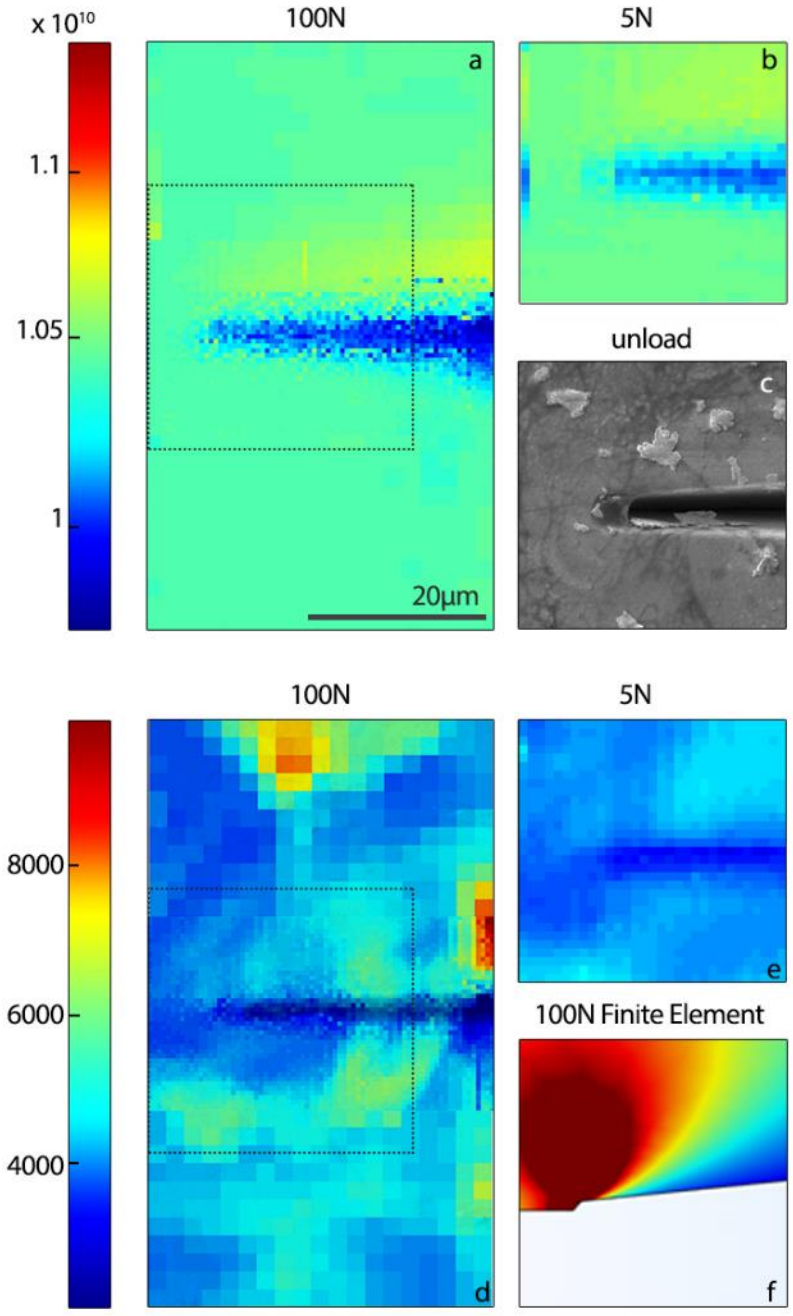

Figure 4.7 ABD alloy: Diffraction intensity map over the notch crack at different loading stages: (a) diffraction intensity map over the crack tip when loaded up to 100 N; (b) intensity map when initially loaded to 5 N; (c) SEM image of the crack tip when unloaded and dismounted; (d) normalized dislocation density map of the region loaded to 100 N; (e) dislocation density map initially loaded to 5 N; (f) Symmetric 3D finite element modelling on the stress concentration of the specimen geometry.

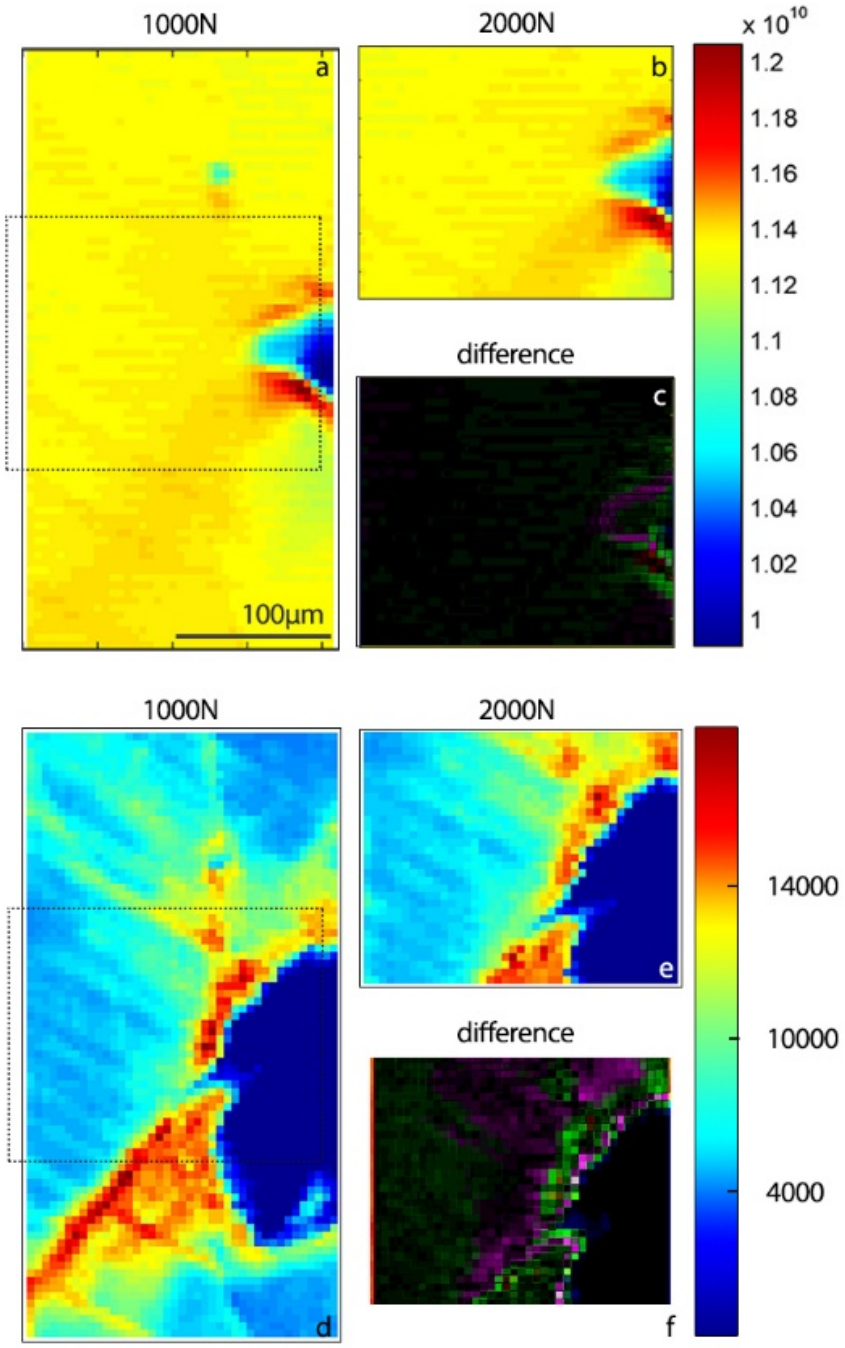

Figure 4.8 CMSX4 alloy: diffraction intensity map over the notch crack at different loading stages: (a) diffraction intensity map over the crack tip when loaded up to 1000 N; (b) intensity map when loaded to 2000 N, with map zone indicated in dashed frame; (c) comparison image between frame a and b, showing the intensity difference; (d) dislocation density map of the region loaded to 1000 N; (e) normalized dislocation density map initially loaded to 2000 N; (f) density difference of different loading stage, based on mapping data shown in d and e.

From the intensity mapping performed for the two different alloy crystals, significant differences can be noted. In the FIB-milled sample, the notch tip was formed without causing significant plasticity. Moreover, due to the lower loads applied no evidence of intensity change associated with the tip can be detected. In contrast, the sample containing a fatigue crack tip shows clear traces of plastic deformation activity becoming visible in the intensity maps. In Figure 4.8 (a), 45° slip lines can be seen, alongside some regions of modified intensity at the locations close to the crack tip that correspond to the plastic deformation zones, as defined by the classical Linear Elastic Fracture Mechanics (LEFM).

4.5.2 Elastic strain and stress

As reviewed in section 2.4.3.1, local elastic strain evaluation can be obtained from micro-Laue pattern indexation performed using nonlinear least-square fitting that provides information about crystal orientation and local lattice parameters. Probing the CMSX-4 alloy sample by point-by-point scanning and indexation, lattice distortion parameters were obtained. This allowed the map of local elastic strain to be constructed, as shown in Figure 4.9. Zero values in the maps indicate the failure of indexation due to severe streaking or splitting of the Laue diffraction spots. This is also indicated by the anomalously high values in the map shown in Figure 4.8 (d), where the results of indexing of elastic distortion (assuming low-level plasticity) were not valid. The possible approaches to the analysis of such highly distorted patterns are discussed in later sections. The stress calculation was performed by the computer programme XMaS based on the assumptions of zero stress in the out-of-plane direction on the sample, and the anisotropic elastic

stiffness matrix for the material obtained by rotating the reference matrix to the crystal axes in accordance with the determined orientation.

From the map, the strain and stress do not appear to show obvious directional trends or concentration for each term.

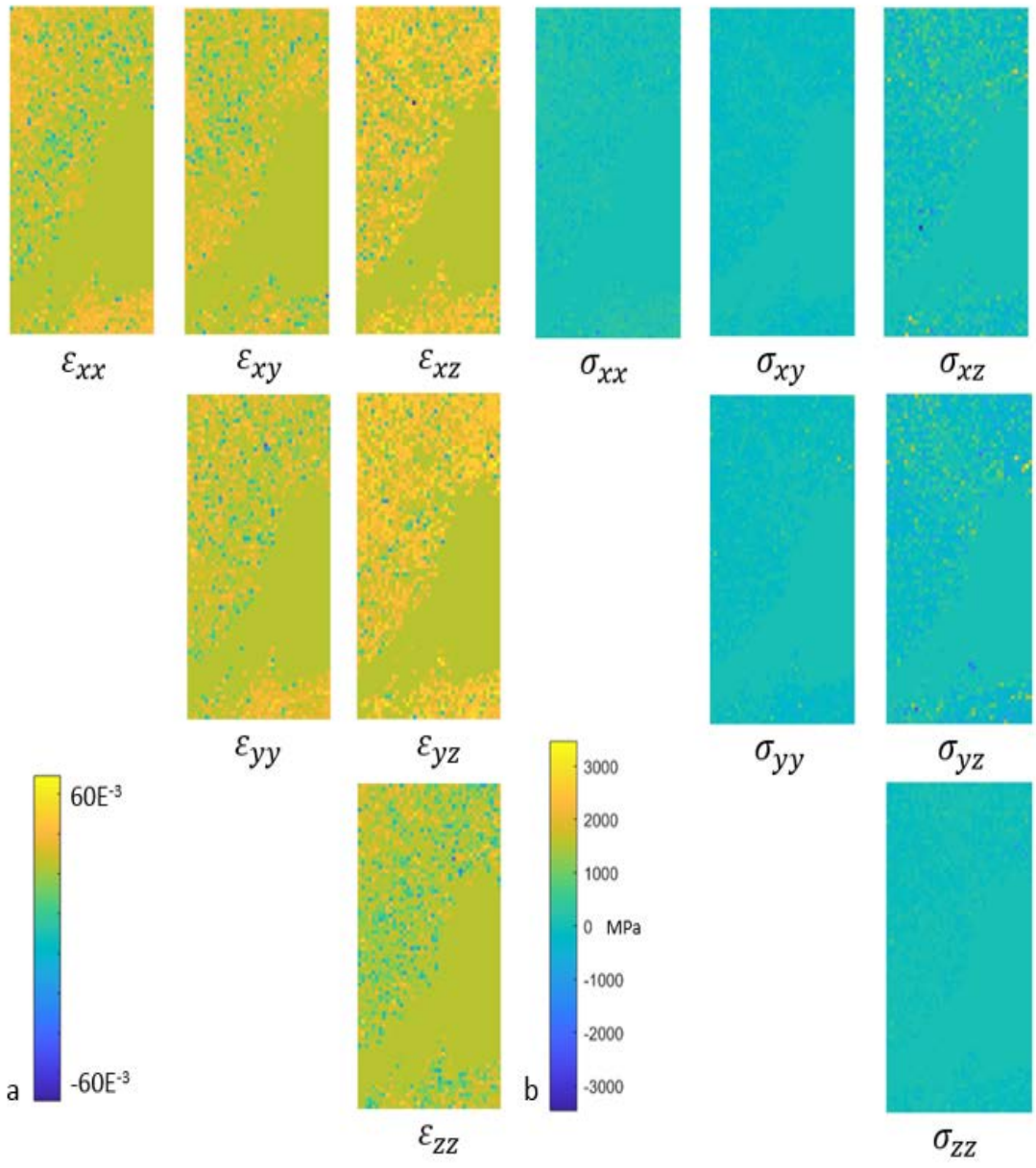

Figure 4.9 Maps of elastic strain and stress tensor components based on the indexed lattice parameters on CMSX-4 alloy when loaded up to 1KN (a) local elastic strain tensor mapping in experimental axes XYZ; (b) local elastic stress tensor mapping in experimental axes XYZ

4.5.3 Misorientation

Recalling the Ewald sphere construction for diffraction (Figure 2.12), some multiple reflection spots of type (0 0 *L*), (0 0 2*L*), (0 0 3*L*), etc., although they occupy different radial positions in reciprocal space, nevertheless share the same reflected beam orientation, and therefore are collected at the same pixel position in the area CCD detector. This multiple reflection phenomenon, although limited by the spectral range of incident beam, and the dependence of reflection intensity on the order of reflection, needs to be taken into account in the pattern interpretation and indexation.

To describe and analyse the crystal misorientation, consider the unit vector ($\widehat{\boldsymbol{k}}$) in the scattering direction, and the misorientation vector (**m**, illustrated in Figure 4.10) which are given as:

$$\widehat{\boldsymbol{k}} = \frac{\boldsymbol{k}}{|\boldsymbol{k}|}\ ; \boldsymbol{m} = \widehat{\boldsymbol{k}} - \widehat{\boldsymbol{k}}_{hkl} \tag{4.4}$$

Therefore, the region of distributed intensity in the vicinity of a Bragg reflection vector, $\widehat{\boldsymbol{k}}_{hkl}$, can be described as a function of misorientation vector **m**, which together lead to the beam intensity distribution expression:

$$I_L(\boldsymbol{m}) \cong A \int I_0(k) I(\boldsymbol{q}) dk; \tag{4.5}$$

$$\boldsymbol{q} = |\boldsymbol{k}_{hkl}|\boldsymbol{m}_{\perp} + (|\boldsymbol{k}_{hkl}|\boldsymbol{m}_{rad} + \Delta k \boldsymbol{G}/|\boldsymbol{k}_{hkl}|) \tag{4.6}$$

Where $\boldsymbol{m}_{\perp}$ and $\boldsymbol{m}_{rad}$ are the two components of vector **m** perpendicular to and along to the scattered beam vector $\widehat{\boldsymbol{k}}_{hkl}$, $\boldsymbol{k}_{hkl}$ stands for the radius of the Ewald sphere which passes through $\mathbf{G}_{hkl}$.

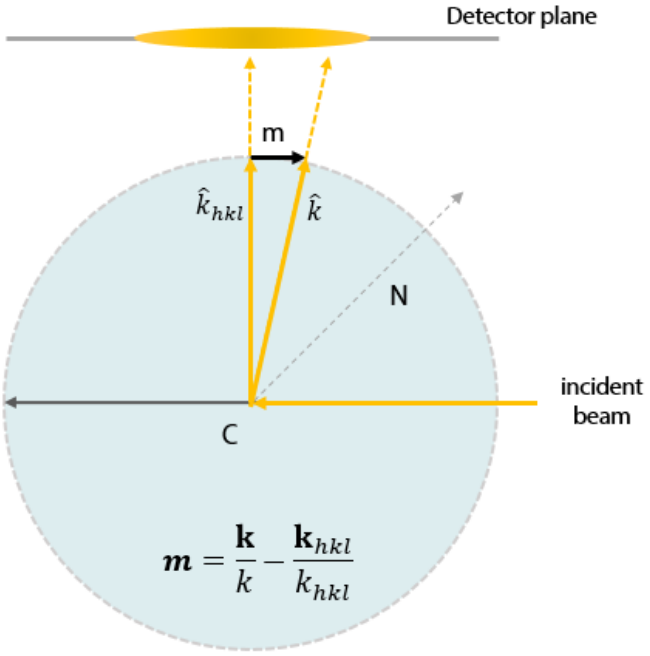

Figure 4.10 Illustration for misorientation vector **m**, showing difference between any reciprocal space point to the nearest Bragg spot

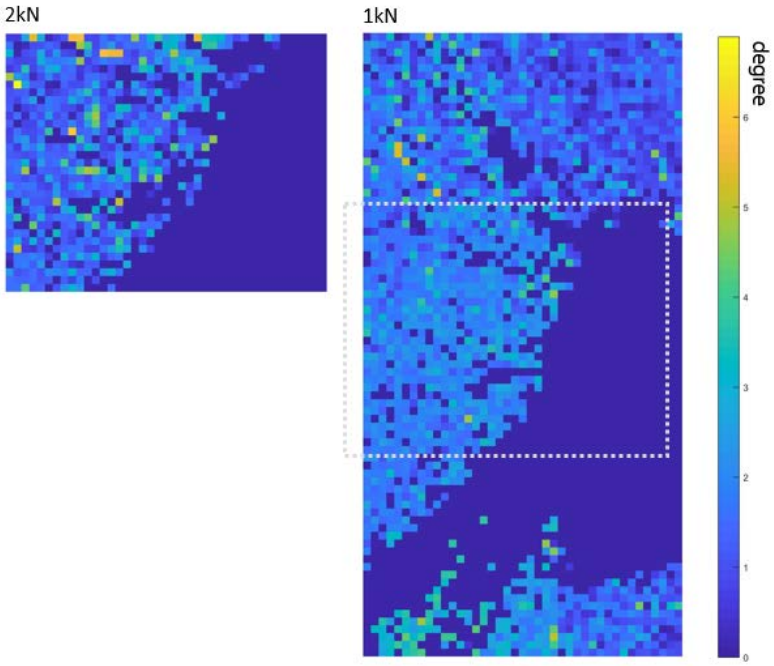

Figure 4.11 Misorientation variation of the sample surface normal vector for CMSX-4 alloy under loading of 2KN and 1KN respectively.

Figure 4.11 shows the degree of misorientation maps for the CMSX-4 alloy sample under the loading of 2KN (small square on the top left) and 1KN (rectangular region on the right), respectively. Overall, the misorientation is found to lie within 5° between the [001] direction and the out-of-surface normal). It can also be observed that overall magnitude of misorientation increases with higher loading.

4.5.4 Bragg peak streaking analysis

As briefly reviewed in Chapter 2, micro-Laue diffraction analysis reveals information about the elastic strain and dislocation population within the local volume of material probed by the X-ray beam. Dislocations stored within the crystal affect the X-ray diffraction pattern formation, and hence micro-Laue analysis reveals the density, type and distribution of the dislocations. To analyze Bragg peak broadening by dislocations, the mutual orientation of two planes for a particular set of dislocations is important, namely, the planes perpendicular to the dislocation line $\boldsymbol{\tau}$, and the direction of the reciprocal lattice vector $\mathbf{G}_{hkl}$ respectively. The intersection line between the two planes is the streaking axis of the corresponding Laue spot, which is given as,

$$\boldsymbol{\xi} = \frac{\boldsymbol{\tau} \times \boldsymbol{G_{hkl}}}{|\boldsymbol{\tau} \times \boldsymbol{G_{hkl}}|} \tag{4.7}$$

As shown in the Figure 4.2, the second normal axis is represented by $\boldsymbol{\nu}$, which is defined as being perpendicular to the ξ axis.

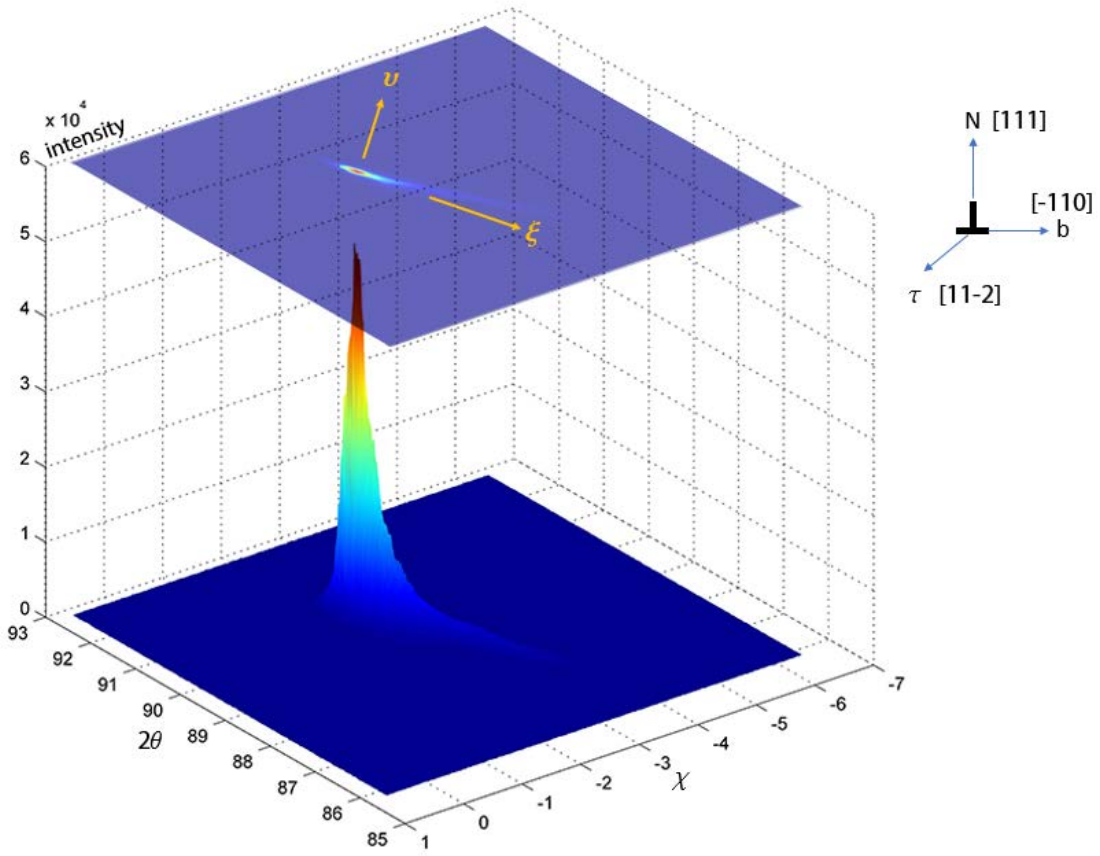

Figure 4.12 Illustration of the normal axes of a (0 0 L) reflection Laue spot which streak as a result of slip activity of geometrically necessary dislocations on the slip systems defined by b = [-1 1 0]/2, τ= [1 1 -2]/$\sqrt{6}$ resulting ξ= [1 1 0]/ $\sqrt{2}$. The diffraction pattern is taken from Fig. 4.8e for CMSX-4 sample loaded to 2000N.

In FCC crystals, each of the 12 slip systems results in different streaking axis (shown in Figure 4.13 c and d), and the length of streaking peaks is measured as the FWHM along the $\boldsymbol{\xi}$ axis ($FWHM_{\xi} \equiv \delta m_{\xi}$). It depends on the orientation and the population of geometrically necessary boundaries in the volume probed.

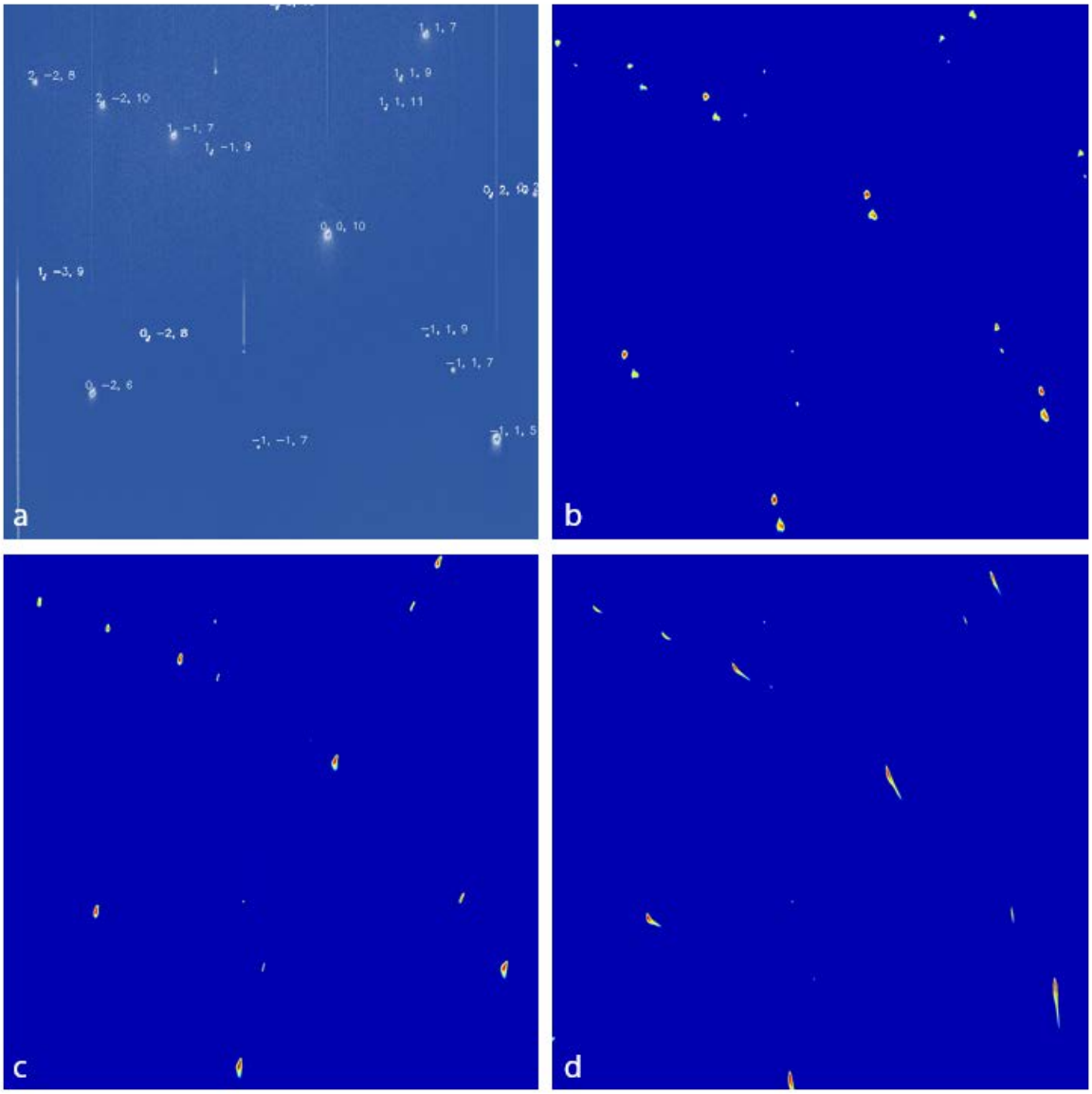

Figure 4.13 Laue diffraction patterns for CMSX-4 alloy, (a) elastic region with Bragg peaks indexed by hkl indices; (b) Peak separation due to SSDs; (c) pattern streaking due to geometrically necessary slip system with b=[110]; and (d) streaking due to GN slip system b=[-110].

It can also be observed that Bragg peaks arranged along a zone line tend to streak along directions closely aligned to each other, due to the fact that the ξ axis remains consistent along the line. However, when the contrast factor is low or close to zero for certain hkl peaks, streaking may weaken or disappear. The broadening in the transverse axis ν, depends on the total number of dislocation boundaries (GNBs and IDBs) per unit length 1/D. In general, the FWHM of a

Bragg peak can be thought of as a function of the misorientation vector $\boldsymbol{m}$, as mentioned previously. The characteristic dimensions of the peak along $\boldsymbol{\xi}$ and $\boldsymbol{\nu}$ axes depend on diffraction geometry and the number of geometrically necessary dislocation, and the total dislocation population. The two parameters σ_{ξ} and σ_{υ} can be described as,

$$\boldsymbol{\sigma_{\xi}} = n^{+}\boldsymbol{bG_{hkl}}L\sqrt{1-(\tau \boldsymbol{G_{hkl}}/\boldsymbol{G_{hkl}})};\ \boldsymbol{\sigma_{\upsilon}} = \frac{\boldsymbol{bG_{hkl}}}{8(1-\upsilon)}\sqrt{\frac{nl}{\pi}}\ . \quad (4.8)$$

Here n^{+} stands for the density of geometrically necessary dislocations, and n stands for the total dislocation density.

In severe streaking patterns ($\sigma_{\xi} >> \sigma_{\nu}$), such as in Figure 4.13 (c) and (d), the length along the ξ axis ($FWHM_{\xi} \equiv \delta m_{\xi} \sim \sigma_{\xi}/|k_0|$) provides the information on the GND population in the probed volume. In the frames where Laue spots are almost isotropic ($\sigma_{\xi} << \sigma_{\nu}$), the statistically stored dislocations make up most of the dislocation population, with the total dislocation density expressed by equation 4.8 for the FWHM in any in-plane direction.

When multiple slip systems are activated and contribute to streaking simultaneously, the correlation function should be expressed as the sum over all active slip systems, λ. The dislocation density tensor ρ_{ij} and effective strain gradient tensor η_{lmk} can be rewritten as,

$$\rho_{ik} = \tau_i \boldsymbol{b}_k \delta(r);\quad \varepsilon_{ilm}\eta_{lmk} = -\rho_{ik}. \quad (4.9)$$

Here the magnitude of τ is the net number of dislocations with the same Burgers vector, b, crossing a unit area normal to τ, and $\varepsilon_{\tau lm}$ is the Levi-Civita tensor. Therefore, the broadening of the intensity under multiple slip systems is related

to the dislocation tensor and strain gradient tensor. In order to obtain dislocation information, simulation of Laue peaks is performed using fitted lattice curvature tensor, and dislocation density tensor can be determined by seeking a least square fit to the streak profile.

4.5.5 Peak splitting

In the case of Laue spots that are split into several, as shown in Figure 4.13 (b), the pattern can be seen as the result of several independent crystal cells interacting with the X-ray beam along its penetration depth L. Naturally, each boundary between the cell blocks will contribute to the overall misorientation (Θ). Splitting of the peaks occurs when Θ exceeds the average $FWHM_a \equiv \delta m_a$ for each individual cell crystal along the ξ axis, which is given when dislocation boundaries or walls are unpaired:

$$K = \frac{\Theta}{\delta m_a}. \tag{4.10}$$

When K<1, the intensity of Bragg peak is considered to be mostly continuous, and when K>1, discontinuity occurs and discrete spikes appear.

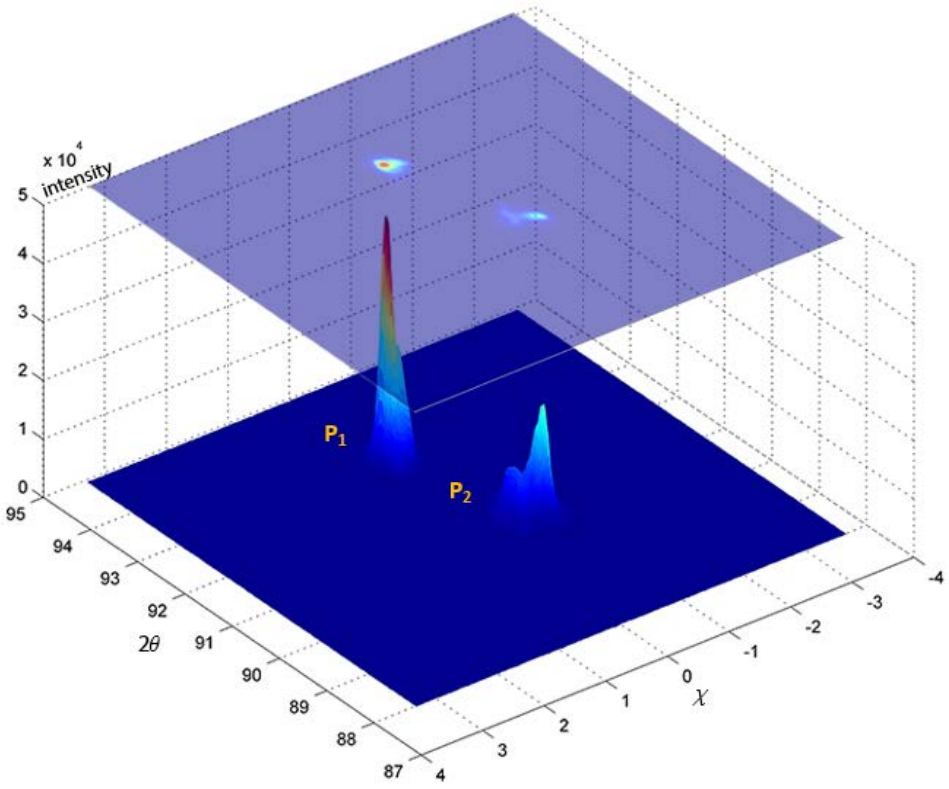

Figure 4.14 Bragg peak (00L) consisting of two local cell blocks with misorientation between them.

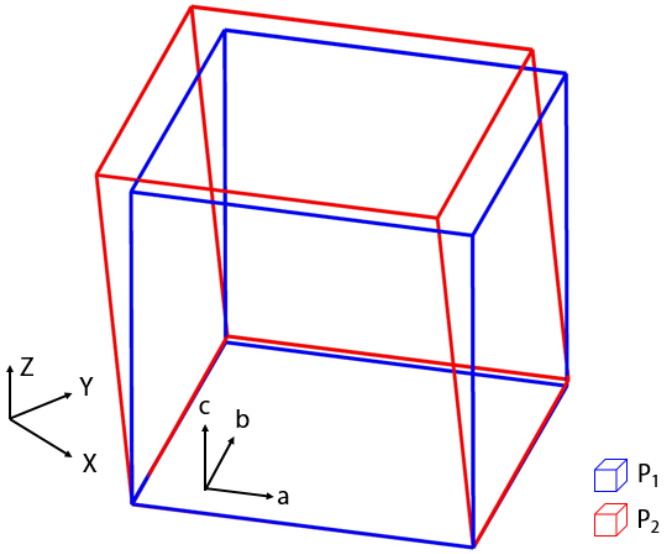

Figure 4.15 Illustration of lattice cell orientation relative to XYZ(system) coordinates derived from two fitted peaks P1 and P2 (Fig 4.13)

Figure 4.14 shows the intensity map of two split peaks of (0 0 L) Laue spot (also seen in Figure 4.13 b) due to local misorientation between different block cells under loading, named P_1 and P_2. Different intensities can be seen from the two peaks, and the indexing referring to each peak position gives two different lattice curvature matrices, corresponding to the sketch shown in Figure 4.15.

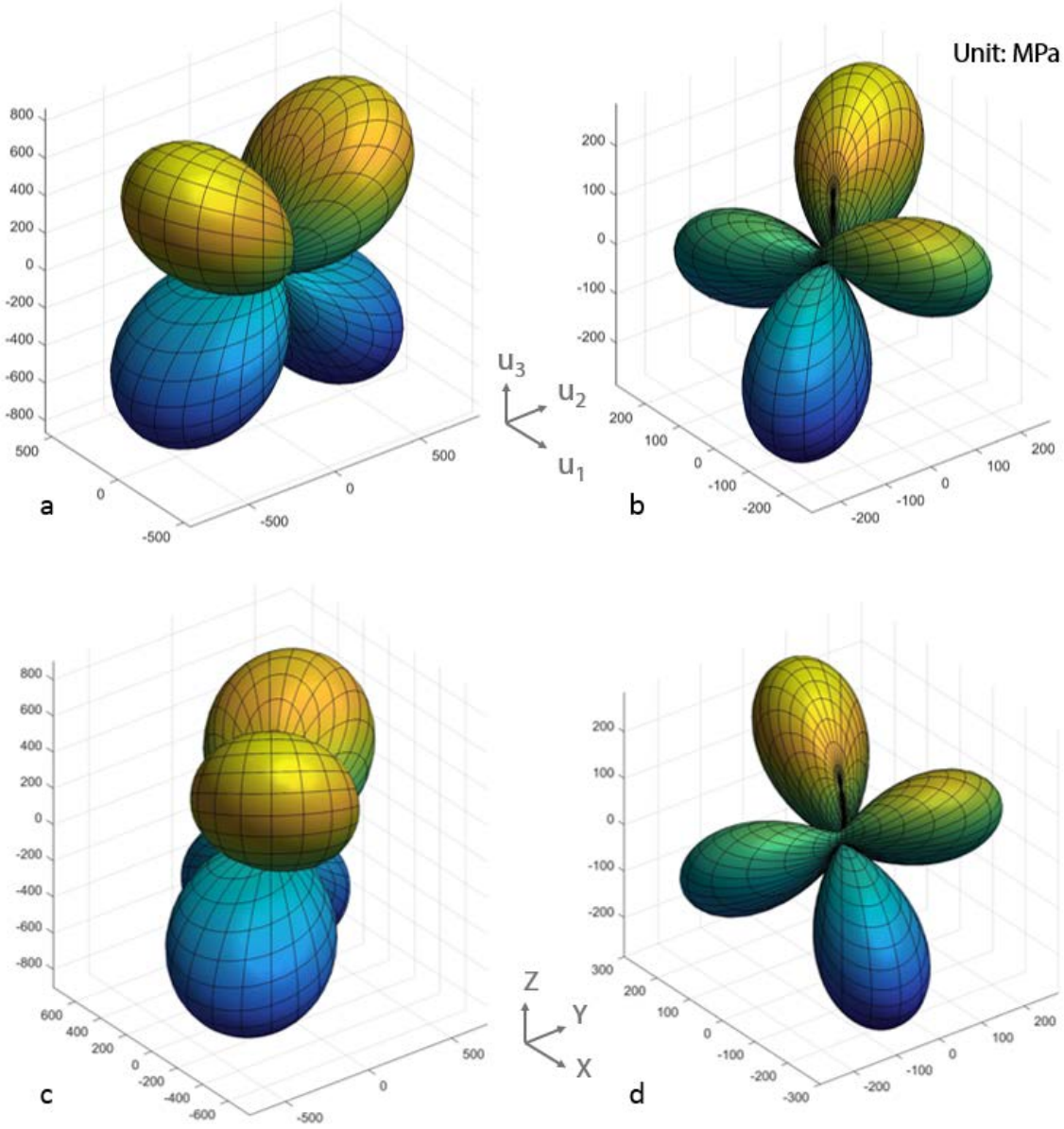

Figure 4.16 3D visualization of the stress tensor for two cell blocks indexed by P_1 and P_2, (a) P_1 stress tensor in lattice coordinates; (b) P_2 stress tensor in lattice coordinates; (c) P_1 stress tensor in experiment coordinates; (d) P_2 stress tensor in experiment coordinates.

Figure 4.16 illustrates the stress tensor for the two cell blocks obtained by indexing individual (0 0 L) sub-peaks on the detector, in crystal coordinates (u_1, u_2, u_3) and laboratory coordinates (X, Y, Z), respectively. The 3D elastic strain stress tensors (reviewed in §2.4.3.1) are given as:

$$\varepsilon_{u123}^{P1} = \begin{pmatrix} -0.0622 & -3.20793 & 18.08063 \\ -3.20793 & 1.69476 & 3.58195 \\ 18.08063 & 3.58195 & -1.62979 \end{pmatrix};$$

$$\sigma_{u123}^{P1} = \begin{pmatrix} -2.7 & -180.93 & 1019.75 \\ -180.93 & 78.3 & 202.02 \\ 1019.75 & 202.02 & -74.97 \end{pmatrix} MPa;$$

$$\varepsilon_{u123}^{P2} = \begin{pmatrix} -1.17888 & -3.49097 & -2.71005 \\ -3.49097 & 3.89083 & -3.08491 \\ -2.71005 & -3.08491 & -2.70006 \end{pmatrix};$$

$$\sigma_{u123}^{P2} = \begin{pmatrix} -53.62 & -196.89 & -152.85 \\ -196.89 & 180.09 & -173.99 \\ -152.85 & -173.99 & -123.75 \end{pmatrix} MPa.$$

Severe differences and variation across different active cell blocks are observed, both in lattice and lab coordinates. From comparing Figure 4.12 and Figure 4.14, the split peaks in the latter frame are arguably formed by distributing the intensity of single peak along the streaking axis, the ξ axis. Despite the local misorientation between the cell blocks, it is observed that both streaking and split peaks result from geometrically necessary dislocation networks of the same orientation (or slip system), yet show various distribution structure. Streaking is mainly the consequence of randomly distributed GNDs, which contribute to its continuous intensity; while split peaks or discontinuous intensity distributed along the streaking axis is mainly due to GNBs of the same type. Due to the existence of local strains, the streaking length is to a greater degree controlled by the

distributed individual GNDs, rather than those in GNBs. In addition, randomly distributed dislocations are also the main contributor to the FWHM in the normal axis to the streaking axis, (δm_{ν}). Further study can help distinguish the individual GNDs and GNBs contributions to the intensity distribution for a Laue spot, e.g. scanning white beam energy to provide differentiation with respect to $|\mathbf{k}_0|$. A detailed reciprocal space mapping study is presented in the following section. Simulation studies such as [94] reported that ~50-85% of the dislocations need to be grouped within the walls (cell boundaries) to create the discontinuity (splitting) in the streaked peaks.

Generally, the splitting of Laue spot can be determined and quantified by several parameters including the density of GNDs, misorientation angle between cell blocks due to dislocation boundaries, number of dislocation boundaries and walls in the probed volume, and the length ratio of the cell block to probed volume. When $n^{+}L>>0.1\sqrt{n}l$, the intensity of Laue spot is influenced by the unpaired dislocations (GNDs and GNBs), and $\delta m_{\xi} >> \delta m_{\nu}$. Otherwise, the Laue spot is almost isotropic, and $\delta m_{\xi} \sim \delta m_{\nu}$. When splitting is observed (K>1), unpaired dislocations (GNDs) are distributed into cells delimited by walls, thus forming a GNB structure.

4.6 Reciprocal space mapping

The average deviatoric strain tensor of a crystalline grain can be determined by the four non-planar Bragg reflections, as shown in the previous section. At least one wavelength is needed to be determined in order to measure the true absolute strain tensor. There are two schemes which provide the ability for this, namely, a wavelength dispersive diffracted beam analyser, or monochromator tuning of the incident beam (see Figure 4.1). Between the two schemes, the latter using a monochromatic incident beam has the benefit of high energy resolution and higher stability.

Recalling Figure 2.12, the Ewald sphere ($r=1/\lambda$) may intersect a lattice point in reciprocal space. Therefore, by scanning the energy (hence wavelength) of the incident beam, the intensity distribution of a Laue spot in reciprocal space can be directly mapped, as a function of the 3D momentum transfer vector.

The setup employed for reciprocal space mapping remains the same as shown in Figure 4.4, except for the monochromator being in working position to scan the energy of the monochromatic incident beam to perform steps across a Laue *hkl* spot. Figure 4.17 shows the maximum intensity collected by the area detector while monochromatic incident beam was scanned from 8 KeV to 20 KeV. Several peaks occur when the energy of the incident beam is close to the principal value for diffraction. And as the energy is scanned across the principal value for the reflection, the corresponding Bragg peak appears on the detector, increases in the size and intensity, and then diminishes and disappears again. The procedure corresponds to scanning the end of the scattering vector $\boldsymbol{q}$ through reciprocal space in the direction associated with its $\boldsymbol{z}$ component corresponding to the

normal to the family of scattering lattice planes that give rise to the reflection. The extent of the reflection in the two directions defined by the pixel rows and columns on the detector and corresponds to the reciprocal space directions x and y, respectively. The data collected in this configuration allows the complete high-resolution 3D reciprocal space map of a single reflection to be compiled in the form shown in Figure 4.19.

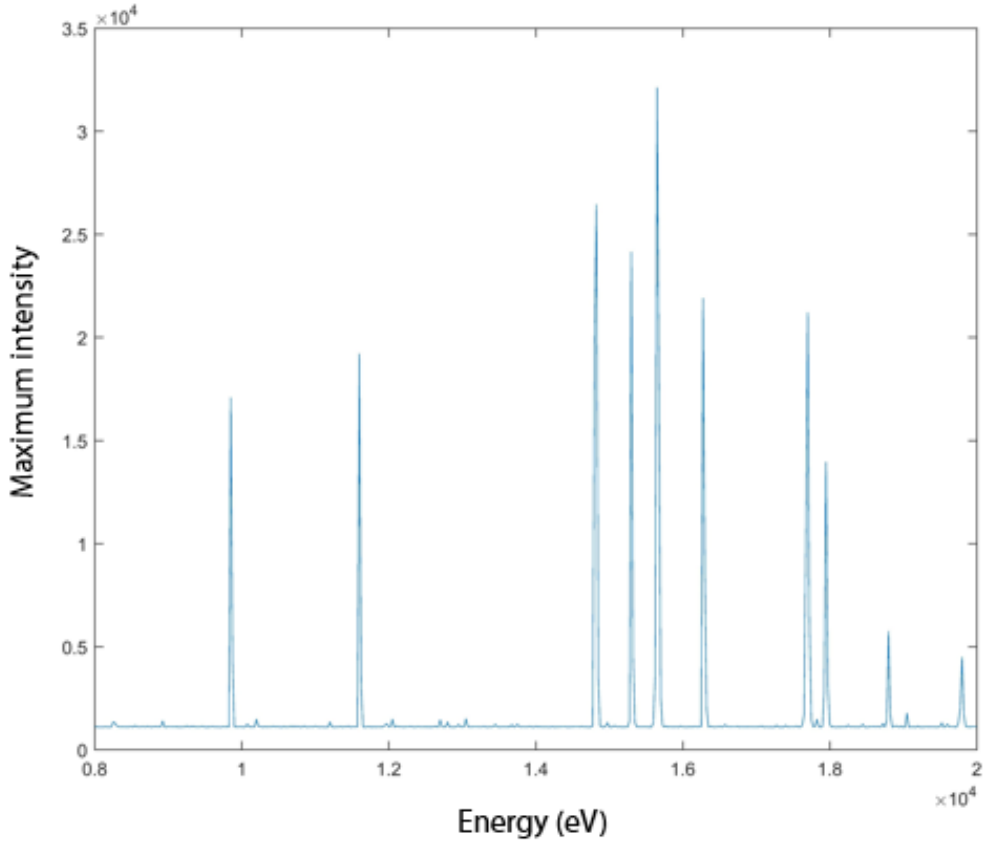

Figure 4.17 Monochromatic incident beam energy scan spanning 8 KeV to 20 KeV, with respect to the maximum Laue spot intensity collected on the area detector

Plastic deformation causes the reciprocal space peak to spread out in a way that is associated with specific crystallographic directions that relate to the slip systems and lattice distortions caused by the active dislocation types. Detailed

analysis of the peak evolution reveals the stages of plastic deformation experienced by the sample, e.g. the transition from single slip to multiple slip associated with hardening. Figure 4.18 shows a (1 -1 7) peak of CMSX-4 alloy collected by scanning energy band 16250 eV to 16325 eV with 1 eV steps, where the intensity of detector frame pixels is summed up along the stacking axis z, which corresponds to the reciprocal space q_z axis. Such representation of Bragg peak accumulates the intensity along the q_z axis and gives a distributed peak of intensity in the q_x and q_y plane.

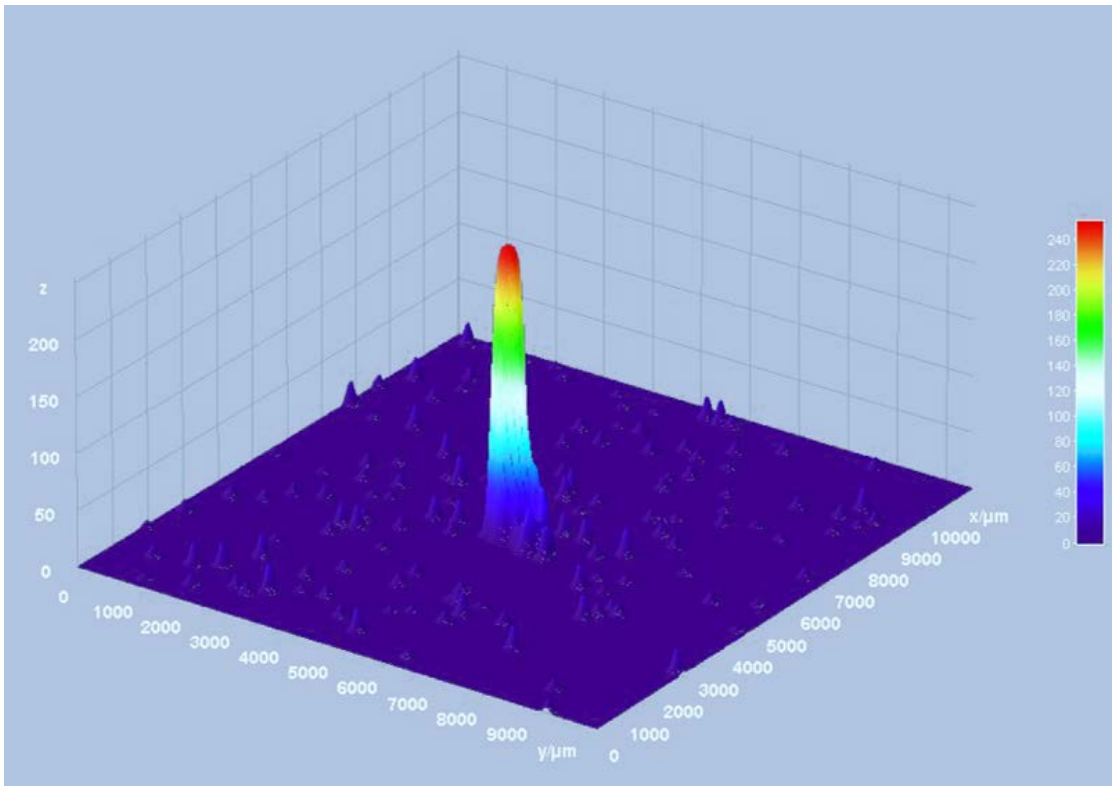

Figure 4.18 3D intensity map in reciprocal space of (1 -1 7) peak

Another way of representing the data in 3D in reciprocal space is to reconstruct the intensity sections obtained by monochromatic exposures, such as the one shown in Figure 4.19, into a 3D volume that represents the morphology of the

intensity distribution for pixels with intensity above a certain threshold. The threshold is calculated by the averaged detector dark field background level.

With such presentation, the local lattice misorientation Θ can be decomposed by in-plane transition (along q_x and q_y) terms and radial (q_z) terms, with associated lattice strain (d spacing) terms. The combined information on lattice strain and misorientation vectors with certain wavelength can help assess the overall distortion (strain and rotation) of the crystal within the probed volume.

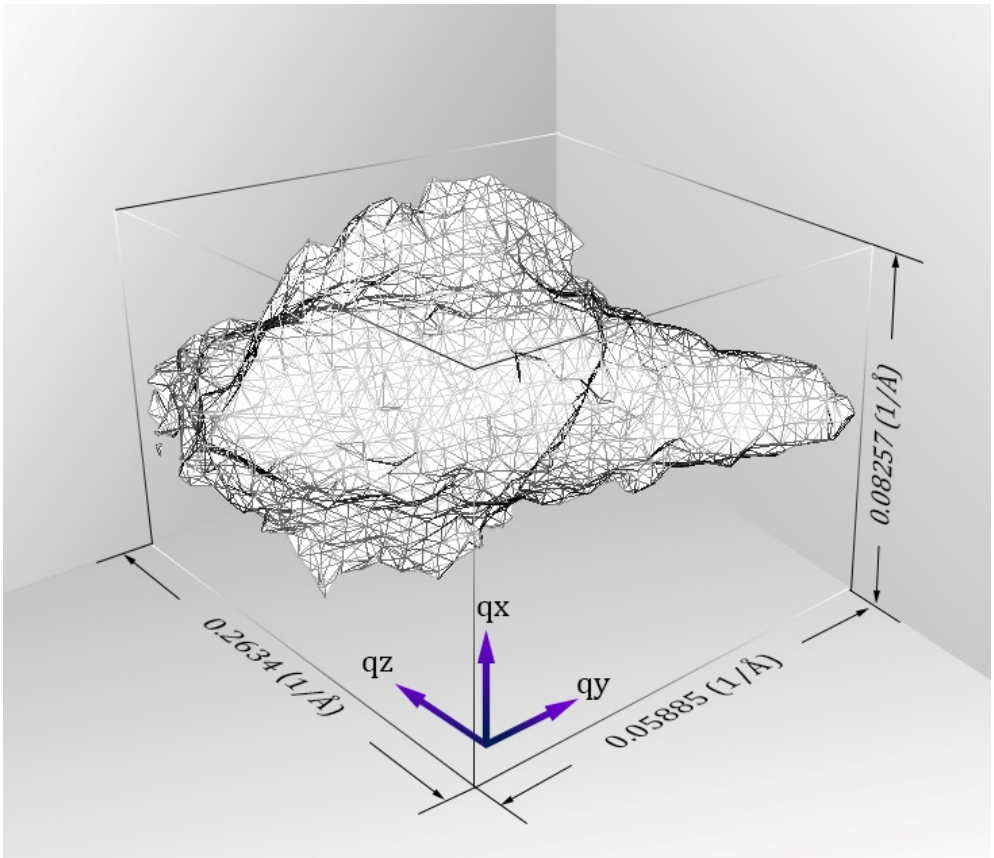

Figure 4.19 The 3D reconstruction of intensity map of a Laue spot (1 -1 7) streaks in reciprocal space.

The total deformation (displacement gradient) tensor is given by the sum:

$$\omega_{ij} = \omega_{ij}^{p} + \omega_{ij}^{e}, \tag{4.11}$$

which reflects the assumption of decomposition of rotation and strain fields into the elastic and plastic parts. As mentioned in the earlier sections, the elastic deformation tensor is given by the sum of the small rotation tensor (anti-symmetric part) and small strain tensor (symmetric part). The latter, in turn, can be decomposed into the *hydrostatic* part (with equal terms on the diagonal) responsible for uniform volume expansion or contraction, and the remaining *deviatoric* part that describes the distortion. In our case, in the presence of plastic strain, the elastic strain tensor needs to be calculated point-to-point with correction for the large rotation of the local cell induced by plasticity of the grain itself, and the surrounding regions.

4.7 Discussion

In situ loading experiments were performed on synchrotron beamline B16 (DLS) for two types of Ni-base superalloy single crystal samples. These sub-micron resolution X-ray micro-Laue diffraction microscopy experiments accurately measured *in situ* mechanical loading. In order to explore fully the capability of synchrotron-based X-ray analysis, a focusing system was designed and assembled. The KB-mirrors optics box was used to achieve a beam size of ~0.4μm by 0.3μm cross-section. Using this focused beam for sample characterisation required very high stability: movement of beam spot on the sample by less than 50 nm amplitude at frequencies below 1 Hz. The alloy crystals studied were subjected to different stress/loading histories; one was mechanically

polished and notched by focused ion beam milling, whilst the other experienced cyclic loading to initiate and propagate a crack at the tip of the notch.

Micro-Laue diffraction results were analysed and discussed in terms of intensity, lattice indexing, misorientation analysis, peak streaking and splitting, and reciprocal space mapping using monochromatic incident beam scanned over the relevant energy range. Each of aspect was analytically backed by theory and compared with the results.

However, some concerns prevail over the outcome of the study, and further improvements can be made in the future. The intensity interpretation can focus on the sum of integrated intensities for all diffracted peaks belonging to one grain, or for all grains indexed. These intensity interpretations can have results which vary from those calculated directly based on pixel intensity values, either by averaging or peak fitting. Indexation of the Laue patterns collected by CCD detector is done by searching and fitting peaks with pixel intensity over certain threshold value, and seeking convergence to the minimum deviation between the predicted and simulated peak positions, by tuning the orientation matrix. Such indexation process works efficiently working for Laue patterns with peaks that are sharp or mildly spread, e.g. those lying within the elastic region on the sample, or even for peaks showing splitting, yet maintaining well-defined peak shape (in the case of splitting, the pattern from the probed volume may be indexed as several contributing grains or cell blocks with different strain status and orientation). The indexed lattice parameters give the information on the lattice orientation and distortion, and hence on the elastic strain and stress states. However, the indexation mostly fails when it comes to severely distorted or streaked patterns (the missing part of the map in Figure 4.9 and Figure 4.11). Analysing such data

must rely on specific procedures for severely deformed crystals. Sections on streaking and split spot analysing have shown several methods that can be used to characterise plasticity, such as the analysis of the active slip system(s), geometrically necessary dislocation population evaluation, etc. However, no fully reliable method at present can give accurate quantitative statistics of the dislocation population. Although various simulations have been explored to compare the streaking or split Laue patterns, they don't lead to consistent numerical values for these parameters. The mapping of Laue spot in reciprocal space that was made possible *in situ* by scanning the energy of the monochromatic incident x-ray beam opened new interesting possibilities. The method helped reveal the distribution of X-ray intensity in reciprocal space. By choosing a threshold, the sections mapped in reciprocal space enable the reconstruction of the Laue spot 3D shape (for a given *hkl* reflection), providing the possibility to identify and confirm multiple GNDs slip systems and possible cross slip. There is no standard or convention for schematic representation of the results to quantify reciprocal space analysis results and their variation across the crystal structure, strain and stress status, active slip systems, dislocation kinds and distributions into boundaries or walls, especially for the dual-phase (yet coherent) single crystals such as the ones studied in the present work. The alternative approach to reciprocal stage analysis, namely, rocking the sample stage and using coherent illumination, can help reveal further detail of the inhomogeneous deformation state within the crystal, as will be explored and discussed in later chapters.

4.8 Conclusion

Sub-micron resolution X-ray Laue diffraction microscopy with *in situ* mechanical loading was made possible by devising, installing and exploiting bespoke experimental arrangements to study elastoplastic deformation and dislocation activity in dual-phase crystals of Ni-base superalloy samples with complex stress history. The experiment was novel in several respects, from sample preparation and pre-stressing of the crystals to experimental setup on the synchrotron beamline. The diffracted Laue patterns were examined in terms of intensity mapping, indexation, elastic strain/stress tensor analysis, misorientation, peak streaking and splitting, and reciprocal space mapping. The background theory was explained, results discussed, and limitations identified.

Future work is needed to develop robust schemes for plasticity description and comparison, along with simulations. Some further X-ray diffraction and simulation techniques, such as Bragg coherent x-ray diffraction imaging and discrete dislocation dynamics modelling will be discussed and presented in the separate chapters.

Chapter 5

Development of dual mode X-ray microscopy technique for *in situ* micropillar compression test

In previous chapters, the presentation of X-ray diffraction techniques was especially focused on the micro-Laue method that provides a non-destructive micro-probe of the crystal structure and stress state, revealing information about dislocation type, population and arrangement. Micro-mechanical testing techniques, such as micropillar compression tests have also been adapted to the study of Ni-base superalloy single crystal samples, and size effects in the mechanical response were observed and discussed with reference to novel mathematical models for the size-dependent trends in mechanical response. In order to reveal further the hierarchical development and organisation of internal structures related to plasticity (dislocation nucleation and propagation) within small material volumes, a dual mode X-ray microscopy and diffraction setup was devised to enable X-ray imaging of the specimen in transmission, and scattering analysis (diffraction). This was used during *in situ* experiments in October 2015, on the beamline B16, Diamond Light Source, UK. The present chapter discusses the technique, relevant theories, instrumentation and methods, with illustrations drawn from the results as necessary.

5.1 Introduction, motivation and background

The deformation of microscopic samples of metallic alloys displays features distinct from the response of larger, bulk samples in a number of significant respects. The increased fraction of near-surface grains and material volumes modifies the overall stress-strain behaviour, resulting in perceived changes in the trends of such properties, as stiffness, strength and toughness. These scaling transitions between occur around certain dimensions associated with characteristic length scales that are either associated with the underlying material structure or the 'cross-over' between power law scaling regimes of material strength.

It is well established [155,156] that the strength of a physical object whose deformation obeys a particular constitutive law must depend on the geometric dimension of this object according to a power law. Considering a series of identical physical objects that differ only in terms of their scale, now denote a measure of their strength by S, and the characteristic dimension of the object by *L.* If strength values S_0, S_1 and S were measured for objects of dimensions L_0, L_1 and L, respectively, then dependence of normalized strength on normalized size can be expressed as a universal function of the size ratio, $\lambda = L/L_0$:

$$\frac{S}{S_0} = f\left(\frac{L}{L_0}\right) = f(\lambda),\ \frac{S_1}{S_0} = f\left(\frac{L_1}{L_0}\right),\ \frac{S}{S_1} = f\left(\frac{L}{L_1}\right), \qquad (5.1)$$

Hence,

$$\frac{f\left(\frac{L}{L_0}\right)}{f\left(\frac{L_1}{L_0}\right)} = f\left(\frac{L}{L_1}\right) \ \ or\ f\left(\frac{L}{L_0}\right) = \ f\left(\frac{L}{L_1}\right) \cdot f\left(\frac{L_1}{L_0}\right) \qquad (5.2)$$

Differentiating with respect to L and substituting $L_1=L$ leads to differential equation giving,

$$\frac{L}{L_0} f'\left(\frac{L}{L_0}\right) = f'(1) \cdot f\left(\frac{L}{L_0}\right), or\ \lambda f'(\lambda) = f'(1) \cdot f(\lambda). \qquad (5.3)$$

Using notation $f'(1) = m$, separation of variable leads to $\frac{df}{f} = m\frac{d\lambda}{\lambda}$ and (subject to the initial condition f(1)=1) the power law solution:

$$f(\lambda) = \lambda^m, or\ S = S_0(\frac{L}{L_0})^m = CL^m; \qquad (5.4)$$

The strength of perfectly scaled physical objects depends on their dimension as a power law.

As a consequence of this universal scaling law, within the range of applicability of a particular physical deformation mechanism (and power-law exponent m), material property C can be introduced whose value remains constant. When sample strength is limited by plastic flow, the power law exponent m=0, and $C=\sigma_f$, flow stress. In contrast, if the sample strength is limited by cracking, as in the case of Linear Elastic Fracture Mechanics, a scaling law emerges when S is associated with the fracture stress, L with crack half-length, m=-1/2, and $C=K_{IC}/\pi^{0.5}$, where K_{IC} is the plane strain fracture toughness.

Now consider a situation when two different physical mechanisms govern the deformation depending on the size of the physical objects, so that for large sizes, as above, $S=CL^m$, whilst for small sizes $S=DL^n$ (where D is the value of C accordingly). Independently of whether strength S is considered intensive or extensive property, we define the “cross-over” system dimension as

$$CL_0^m = DL_0^n, L_0 = (C/D)^{1/(n-m)}\ . \qquad (5.5)$$

The above equation demonstrates that at intermediate dimensions $L \approx L_0$, the system displays transitional behaviour that is referred to as the size effect. In this regime, neither power law provides an adequate description of the deformation response. For the two cases considered above,

$$L_0 = (\sigma_f / K_{IC})^2, \quad (5.6)$$

a combination of properties that is often encountered in the description of size effects, e.g. in the expression for the plastic zone size, formulations of thresholds for fatigue crack initiation (the Kitagawa-Takahashi expression, El Haddad criterion, etc.).

Other manifestations of the above fundamental principles are encountered in the deformation behaviour of crystalline alloys. For example, for polycrystalline samples that are large compared to the typical grain size, there is a power law scaling of the contribution to material strength from grain interaction that is described by the well-known Hall-Petch law expressed as following,

$$\sigma = \sigma_0 + kd^{-n}, \quad (5.7)$$

where σ_0 denotes the (nominal) strength of a single crystal sample, *d* is the grain size, *k* is the scaling coefficient, and the power law exponent *n* is typically given as 1/2 in the 'classical' formulation, although a number of other values have been reported in the literature. It is interesting to note that with progressive grain refinement into the nanoscale, the trend of increasing strength is known to give way to the so-called 'reverse Hall-Petch' whereby the strength begins to decrease with further grain refinement. The reason for this observation is the onset of a different deformation mechanism that sets in when the grain size begins to

approach the typical length of a dislocation pile-up that is also similar to the characteristic length scale that arises in strain gradient plasticity formulations.

In the present work, our purpose was to observe size effect of strength at the micro-scale in FIB-milled micropillars of single crystal nickel-base superalloy CMSX-4. As already mentioned, the microstructure of this alloy is two-phase, consisting of the disordered FCC-structured γ matrix containing cuboidal inclusions of ordered γ' phase with the $L1_2$ structure (Figure 2.2). The strength of this alloy at room temperature is governed by crystal slip on the close-packed (111) planes that encounters stronger resistance in the gamma-prime inclusions, leading to dislocation pile-ups in gamma phase 'channels' against interphase boundaries, eventually leading to precipitate shearing, manifesting in the overall bulk deformation. In micro-scale samples, this effect leads to dislocations escaping at the sample boundaries, creating surface steps.

Since the typical precipitate size is of the order 100-200nm, a change in the deformation behaviour associated with the easy escape of dislocations to the sample surface is expected to occur as the sample size approaches the size of a few precipitates, i.e. $L \approx 1\mu m$. In fact, deviations from size-independent strength behaviour in single crystal samples emerge already in samples of a few microns in size [45,47,52,54,135]. However, to the best of our knowledge, no studies have been reported of the 'interaction' between sample size and the characteristic length scale of the phase structure in two-phase single crystal alloys, such as CMSX-4.

To study the phenomenon of size-dependent deformation behaviour of CMSX-4 micropillar samples machined by Focused Ion Beam milling were prepared and

subjected to continuously recording nanoindentation compression using a flat punch. Although *ex situ* work has been reported in Chapter 3, and discussed, in order to reveal the nature of lattice distortion that occurs within single crystal micropillars under compression, white beam synchrotron X-ray micro-Laue diffraction was employed to perform an *in situ* observation for the experiments.

Laue patterns were collected at several stages of loading process. The evolution of a low order reflection revealed the presence of initial 'blocky' lattice misorientation within the micropillar. In the course of pillar compression, this misorientation becomes homogenised and elongated in the <001> direction, which corresponds to the accumulations of geometrically necessary dislocations within the (-1 1 1)/<1 1 0> slip system that cause the observed lattice curvature. Further deformation leads to bulk slip mediated by dislocation motion and escape through the sample surface. However, the analysis of Laue reflection reveals further reduction in the overall intensity of reflection, revealing that further nucleation and accumulation of dislocations prevails. This phenomenon is associated with the presence of internal obstacles that are responsible for the persistence of strength in this particular alloy down to micron-sized volumes.

5.2 Material, specimen and experimental set-up

The CMSX-4 alloy specimen studied for the present experiment was cut out of cast bulk single crystal, the properties of which is well known and can be found in commercial material databases. A BUEHLER IsoMet slow cutter was used for cutting with a diamond and cubic boron nitride blade dressed in diamond particles, and the cutting process is lubricated and cooled by coolant, which helps to dissipate heat, remove swarf and thus maintain a minimally damaged cutting surface. The top surface of the cut-out piece is then polished to an EBSD ready standard, the detailed procedures and consumables utilized are listed in *Table 4.1 Grinding and polishing procedure for Ni-base superalloy* on page 101.

The crystallographic orientation was selected to be [001] being perpendicular to the top surface plane for better control on loading direction of the pillars fabricated out of it. The cut and polished crystal was then carefully chemically etched for to best degree removing the residual stress stored in the process of cutting and polishing. The etchant employed is freshly made Kalling's No. 2 solution, with the composition and concentration listed in the Table 5.1. The crystal was immersed in the etchant for 100-120 seconds with gentle swabbing of the solution. The sample surface showed clear indication of dual-phase (cuboidal γ' precipitates in γ matrix channels) as the different sensitivity or etching rate that each phase has, which also helped determine the two in-plane lattice axes and number of precipitates/ phase interfaces that are included while fabricating the pillar using focused ion beam (also shown in Figure 5.2).

Table 5.1 The composition and etching condition for Kalling's No. 2 etchant

Composition	Concentration	Etching condition
$CuCl_2$	5 grams	Immersion or swabbing etch at 20 degrees Celsius
Hydrochloric acid	100 ml	
Ethanol	100 ml	

The fabrication of the micropillars was done using TESCAN LYRA3 FIB-SEM system in MBLEM (Multi-Beam Laboratory for Engineering Microscopy) in the Department of Engineering Science, University of Oxford (Figure 5.1 a). The system combines a high-resolution field emission SEM column with a versatile FIB column intersecting the working point at 55° angle supplied with Ga ion source. Such dual beam system allows the *in situ* observation and highly accurate spatial controlling of the FIB milling process.

While there are normally two ways of pillar fabrication using FIB source, with the ion beam travelling perpendicular to the sample surface, or from a side, respectively. The first mode of ion beam-material interaction is employed for the present study. Multiple FIB pre-sets with ion beam current from 2 nA to 20 pA are used for various stages of ion milling process, as explained with illustrations in Table 5.2. The pillars are milled on the edges of prism sample with pathway of incident, transmitted and diffracted x-ray beam cleared for experiment purposes.

Table 5.2 Focused ion beam settings for micropillar fabrication

Fabricating procedure	Ion beam setting	Milling geometry
1. Surface and edge cleaning: Clean the roughness left from polishing and create perpendicular edges.	1 nA to 2 nA	Polygon top view of the prism 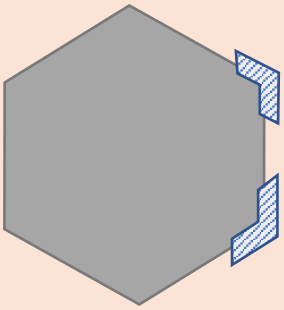
2. Trench milling: Mill firstly the triangular trenches to clean out the materials in the X-ray path; then the annular leaving inner radius of ~1μm.	200 pA to 350 pA	A corner of the polygon 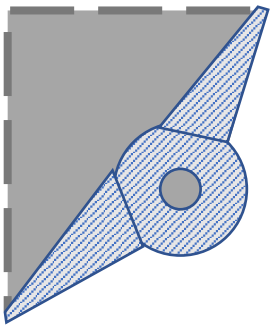
3. Pillar fine polishing: Polish with low current the left pillar into final diameter and height, and then fine polish with even low current to leave minimum ion affected layer.	20 pA to 50 pA	X-ray beam path indicated 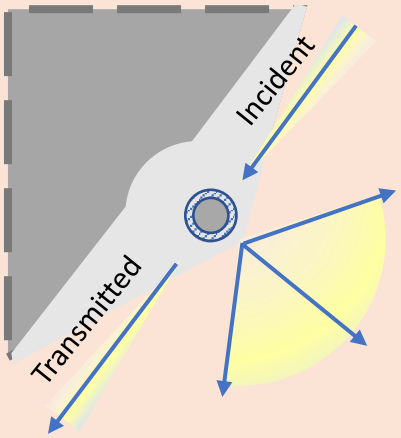

The process of pillar compression was performed using the ALEMNIS portable nanoindenter (shown in Figure 5.1,b) using a diamond flat punch tip. The ALEMNIS indenter offers the true displacement-control mode (as also mentioned and discussed in Chapter 3), allowing flow stress fluctuations to be captured with high accuracy.

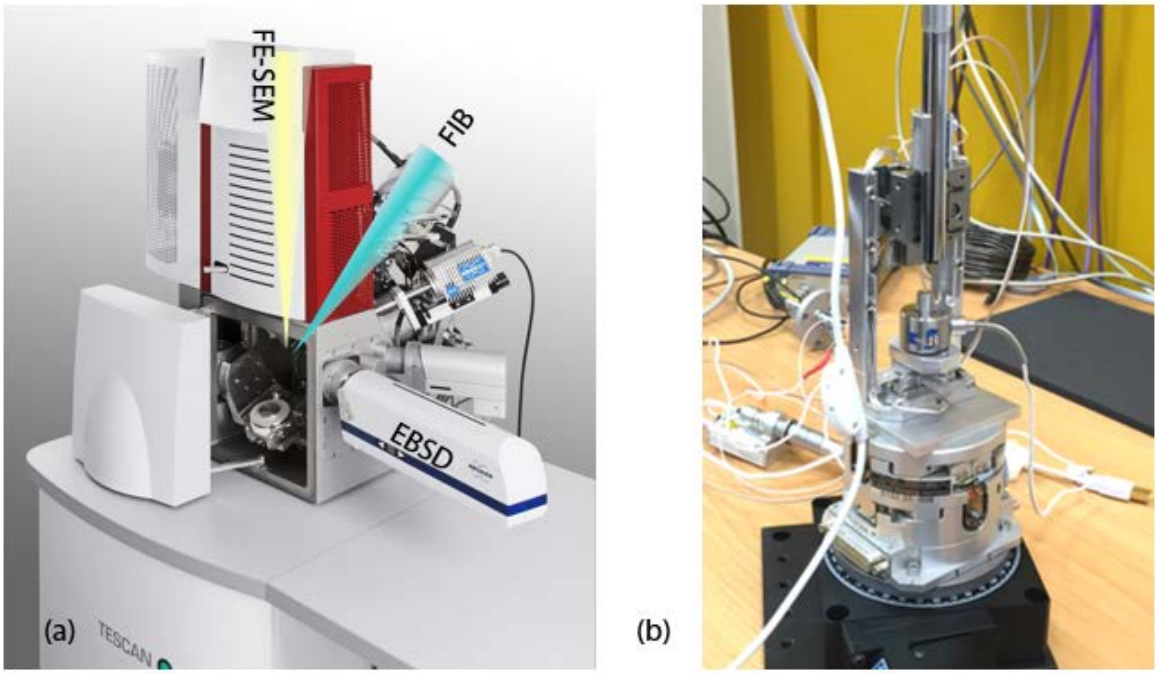

Figure 5.1 (a) TESCAN LYRA3 dual beam FE-SEM and FIB system at MBLEM, University of Oxford; (b) ALEMNIS in-chamber nanoindenter with high resolution optical microscope attached, mounted on rotation-enabled stage

For the synchrotron experiment setup, the specimen (crystal prism) was mounted on the SEM stub installed on the sample stage of the indenter which offers high resolution bi-axial movement. The indenter was mounted on a rotational stage of the beamline for aligning the incident beam and the FIB fabricated pillars at the crystal edges. A CCD area detector was mounted at 90° for collecting the diffracted beam, while the imaging detector was placed along the beam direction at a larger distance.

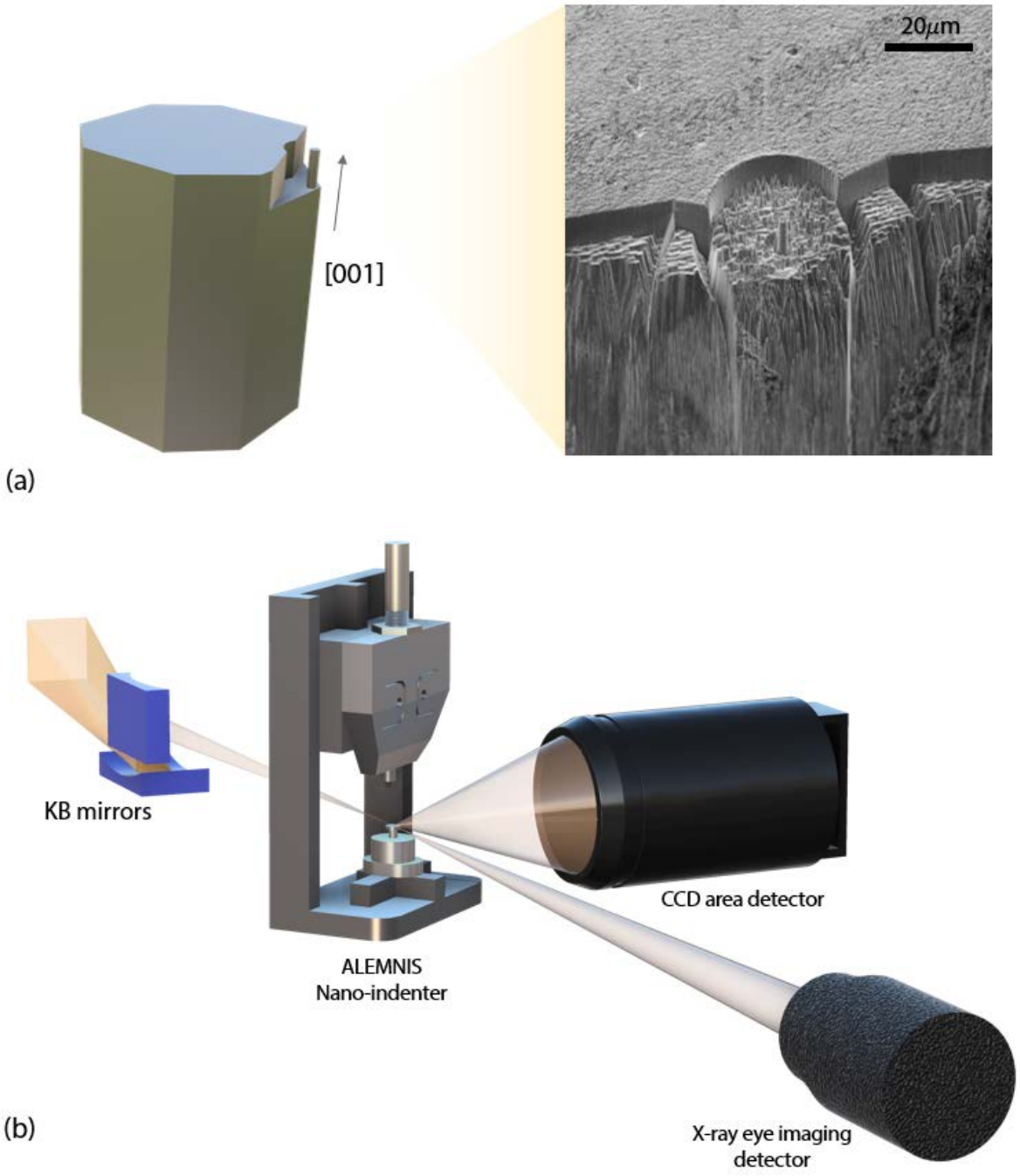

Figure 5.2 (a) Focused ion beam milled free standing micropillars on the edge of prism-shaped bulk crystal with the direction of the [001] axis indicated; (b) experimental setup schematic.

The schematic of the experimental setup on beamline B16 is also presented in Figure 5.2 (b). The beamline layout previously shown in Figure 4.1, and Figure 5.3 below shows further detail of the multiple microscope and detectors arrangement in the experiment hutch.

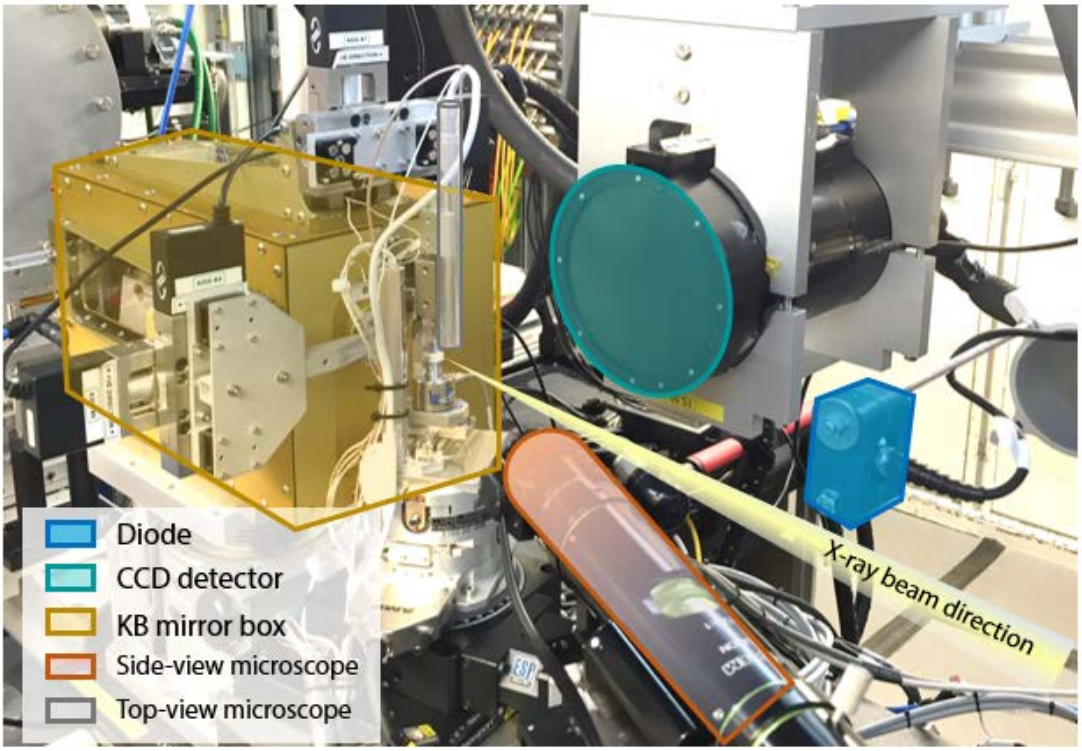

Figure 5.3 Multi-detector arrangement on the beam with CCD area detector, diode, side-view and top-view optical microscopes.

As shown, along the KB focusing mirrors and CCD area detector, a new signal detector (an avalanche photo-diode) was mounted to allow fast beam intensity scanning. Two optical microscopes, one mounted on the side (marked orange) and one (high resolution) mounted on the top (shown by the grey cylinder) were used for extra accuracy required to align the micropillar not only with the x-ray beam for probing, but also beneath the diamond flat punch for *in situ* compression nanoindentation test. The imaging detector for full-field imaging was placed

further downstream in the beam travel direction and is therefore not shown in the same picture.

5.3 Experimental procedures and methods

Since the indenter tip (plat punch) for the compression test is fixed on the nanoindenter frame already aligned with the rotational axes of the sample stage, it appeared sensible to use calibration samples with the same geometry as the samples to be tested. Therefore, micropillars were fabricated by the same method (shown in Table 5.2) on silicon wafer to be used as the calibration sample for the experimental setup, as shown in Figure 5.4. The dimensions of the silicon pillar were of the same order as those made from the superalloy samples, so that similar average diffraction intensity values were expected from the patterns.

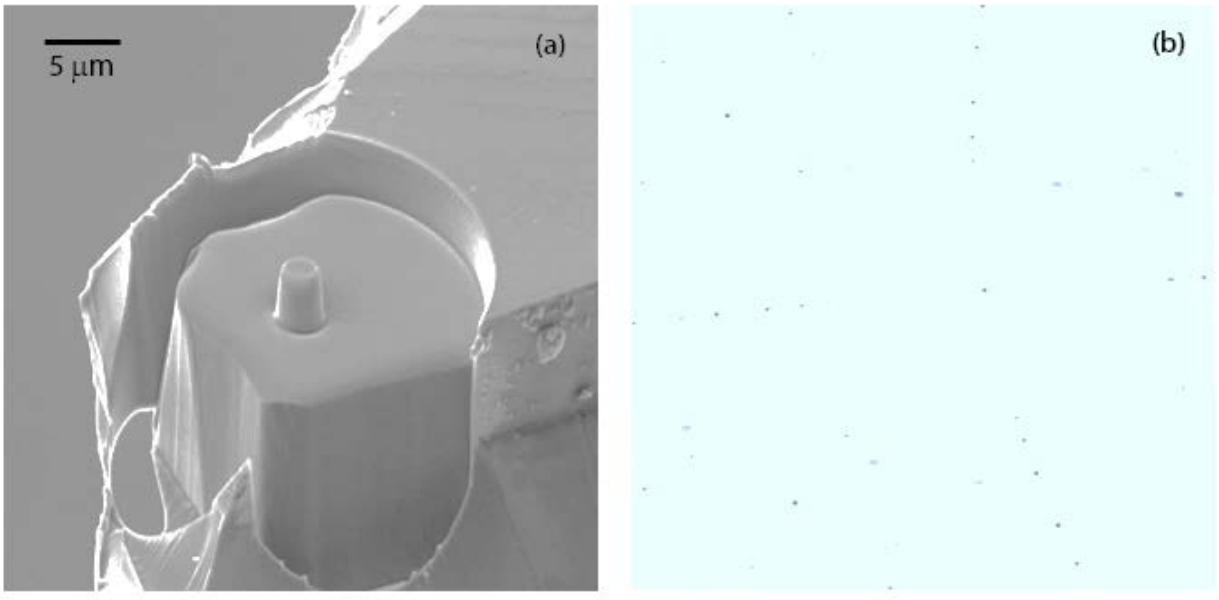

Figure 5.4 (a) 55° tilted SEM image of FIB fabricated micropillar on the surface of silicon wafer; (b) Diffraction pattern of the silicon micropillar collected by the CCD area detector.

5.3.1 Triangulation calibration

The diffraction patterns were collected at different sample-detector distances with known intervals ($dd_0 + n*\Delta d$), as shown in Figure 5.5. By the method of triangulation [91,136,157,158], it was possible to ray-trace the diffracted beams to their origins. Multiple parameters of the experimental setup can be determined by this approach, including sample-detector distance dd_0, the centre of signal position on the detector (x_c and y_c), etc. They are obtained by fitting various values for a convergence, where the deviation between detected peak positions and the calculated ones reach a minimum value.

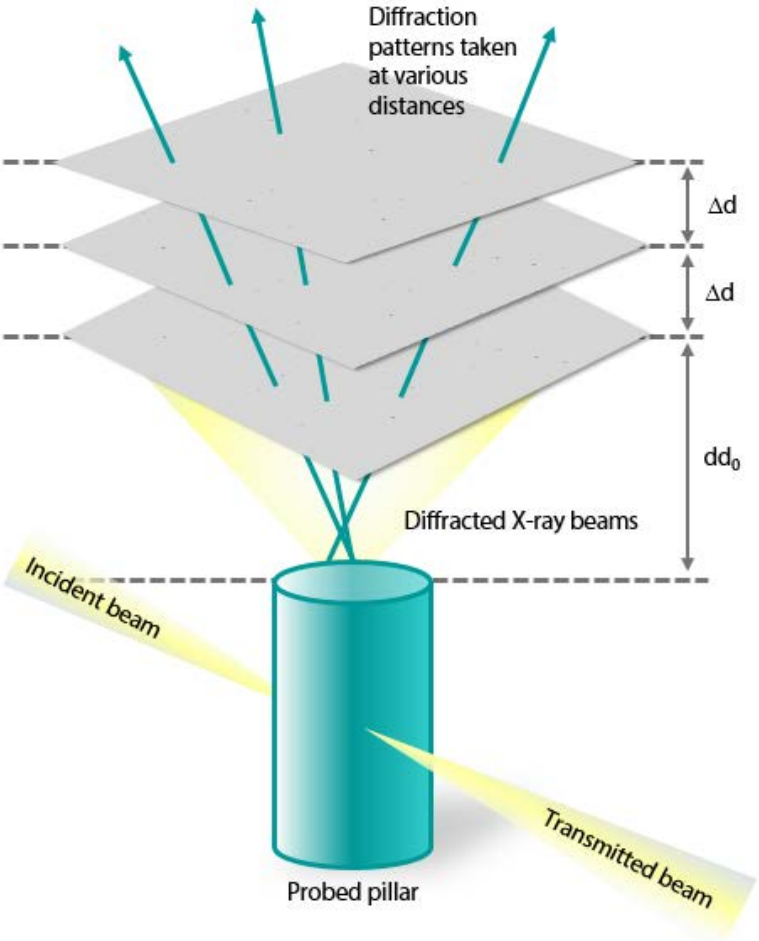

Figure 5.5 Schematic for triangulation distance calibration

After the sample-detector distance is determined for the sample with known lattice parameters (silicon crystal), the orientation and detector tilt angles can be refined for subsequent use in indexation and strain refinement.

5.3.2 Full-field imaging and Laue diffraction

As an important part of hard X-ray nanoprobe microscopy, full-field imaging capabilities have been continuously improving the resolution of transmission mode X-ray imaging, from micrometres down to less than fifty nanometres, with applications found in biology, materials science and condensed-matter physics [39,105,108,159–161]. The dual mode hard X-ray nanoprobe, designed and built for the present study, features simultaneous high resolution full-field imaging and the reflection mode Laue diffraction microscopy, both with high resolution 3D spatial and rotational positioning enabled.

High-resolution imaging is crucial for the success of the *in situ* micromechanical experiments. As mentioned in previous sections, micropillars for compression testing were fabricated by FIB below the bulk sample surface to prevent them from being damaged during transportation. Because of the nature of semi-hidden micropillars, it was challenging to align the indenter tip (diamond flat punch) with the pillar purely by optical microscopes, as is normally done inside the SEM chamber with high resolution imaging available (down to several nm).

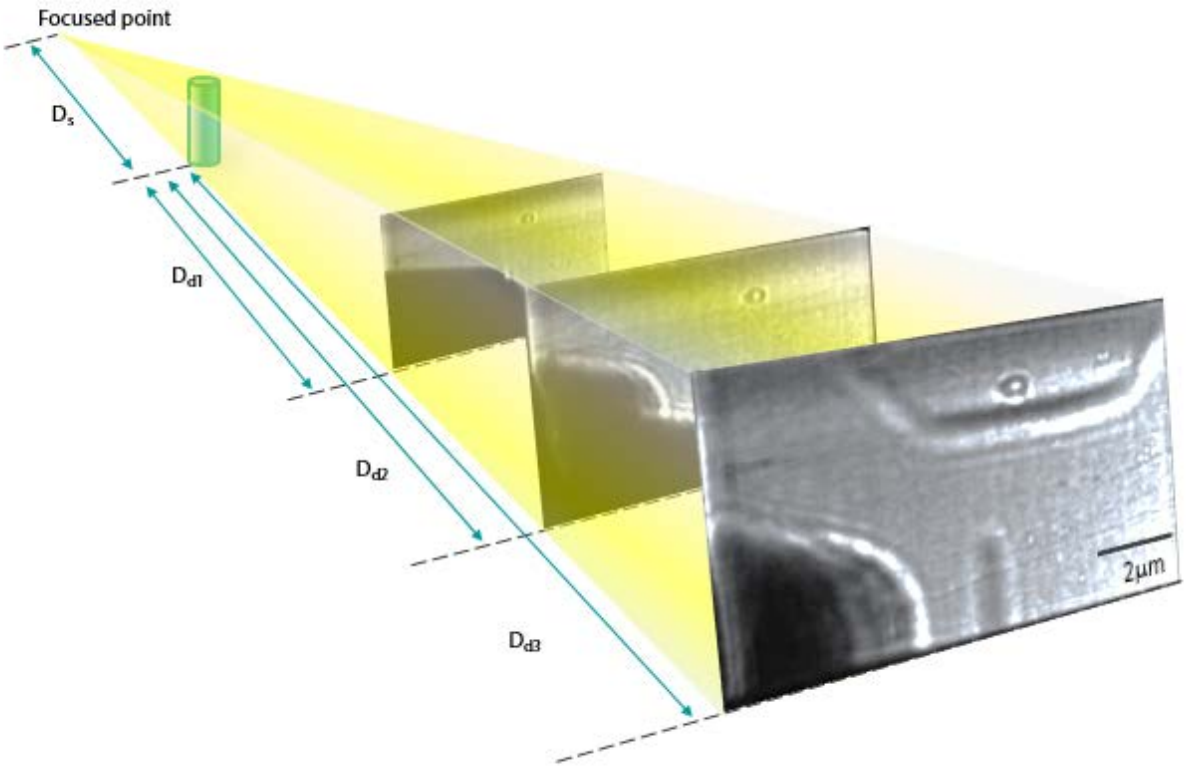

Figure 5.6 Schematic of full-field magnification imaging with images collected on X-ray EYE detector at various sample-detector distances

Figure 5.6 shows a schematic diagram of the full-field, variable magnification X-ray microscope with frames displayed collected at various sample-detector distances (D_d) using the "X-ray EYE" sCMOS imaging detector. The micropillar sample was placed at a certain distance downstream from the beam focus, and magnification of the illuminated part changed by translating it along the beam. The scale bar on the furthest frame (D_{d3}) shows the real space scale of the illuminated pillar sample, which is magnified by 230 times (D_{d3} / D_s) on the detector with pixel resolution of 6.5μm, yielding effective x-ray spatial resolution down to 25 nm.

Accurate location of the pillar and also of the diamond indentor flat punch tip were easily found at this high magnification. Once the nanoindenter punch tip and the pillar were aligned, the micropillar was moved upstream towards the focus point, so that the sample was placed at the focus to allow using the highest flux achievable for diffraction setup. By further adjusting the micropillar position, the diffraction pattern could be taken either of the whole pillar, or only of its part for higher resolution diffraction mapping.

5.3.3 Peak fitting and indexation

Bragg peaks on the diffracted Laue patterns can be fitted either manually or by several peak searching schemes. For fitting and indexing a sequence of patterns (frames), e.g. for Laue diffraction mapping, automated algorithms must be used. Firstly, a minimum threshold value is taken that eliminates the background noise on the CCD detector. Then a minimum peak size is defined (usually 2-4 pixels) for further clean out the high-intensity noise points, only leaving a finite number of discrete regions with certain average intensity value. From these regions recognized as peak accommodators, a mathematical peak fitting schemes are used, such as Centroid, Gaussian, Lorentzian, or Pearson peak types. To ensure the quality and accuracy of fitting results, other parameters such as maximum peak size, maximum fitting deviation, certain range for peak width and so on are also applied to the scheme. In the present study, due to the high flux of incident beam on the beamline B16, it was found that some of the Bragg peaks were

saturated (despite precautions taken, especially for the strong low order *hkl* reflections. Therefore, the peak fitting scheme was also set to tolerate saturated peaks with truncated peak shape. Figure 5.7 (a) shows a contour map of the [0 0 L] Bragg peak diffracted from the calibration sample (silicon pillar), and Figure 5.7 (b) shows the 3D intensity profile of the fitted shape of the same peak by the peak search and fitting scheme.

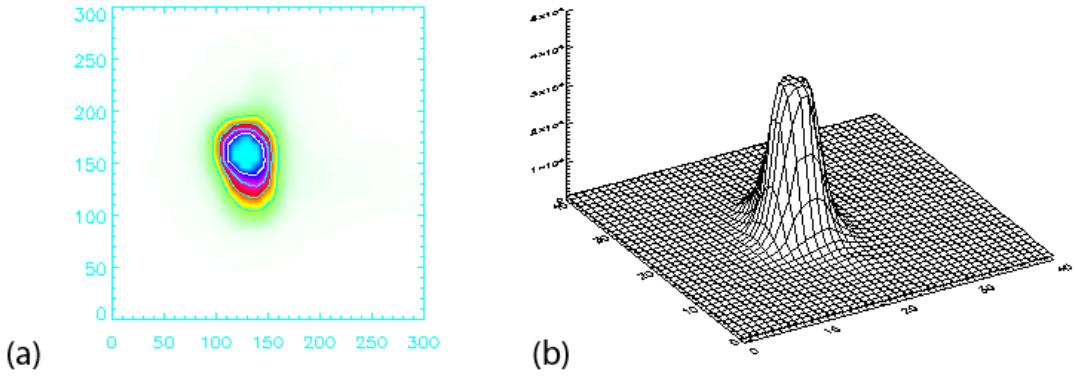

Figure 5.7 (a) contour map of the intensity of a [0 0 L] reflection spot of silicon; (b) fitted peak of the same reflection

Once the peaks are either manually or automatically found and listed, *hkl* index is sought for each, together with the lattice orientation of the probed volume of the crystal (micropillar in the present case). This is a numerical search-match procedure seeking minimum deviation (in pixels) between the predicted and actual peak positions. A tolerance allowance is normally given at the initial stage of indexation for an approximate approach before further refinements. The parameter to fit for the initial indexation is the orientation (rotation matrix) and, if needed, minor adjustments of the sample-detector distance and signal centre

position which are obtained by triangulation calibration previously. However, if some parameter, e.g. the previously determined sample-detector distance, reaches bigger error than what can be tolerated (defined as a certain range, e.g. 5 mm), then indexation fails.

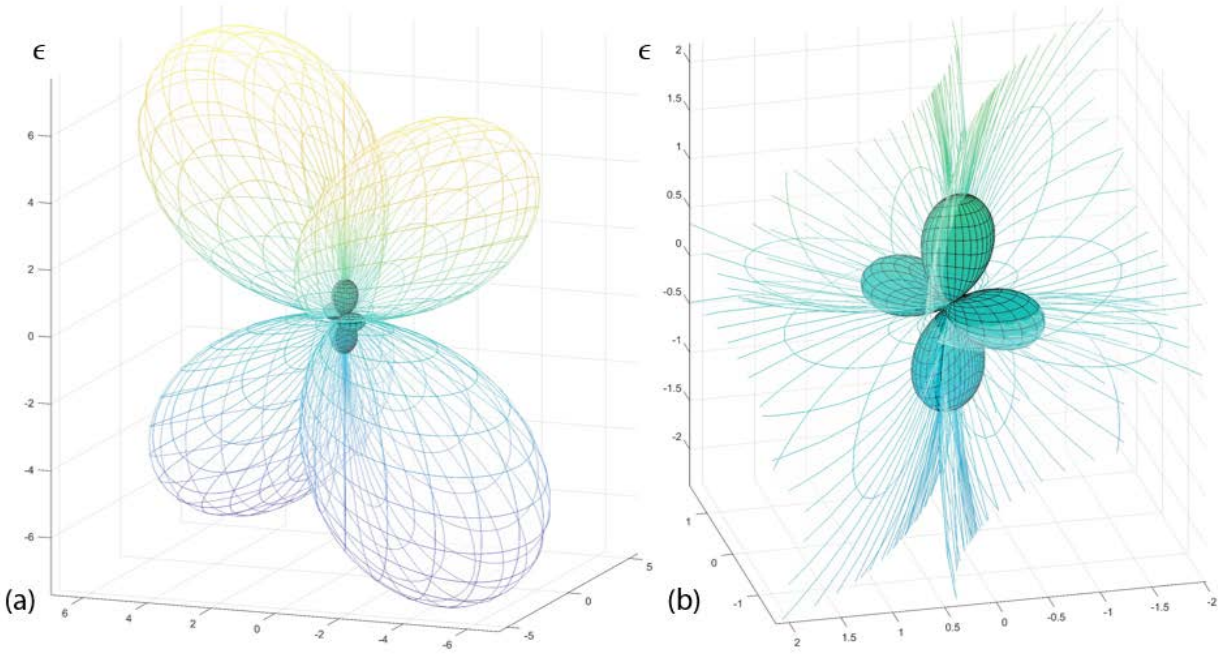

Figure 5.8 Comparison of strain tensor visualizations of indexed Laue pattern of Silicon pillar before (transparent mesh) and after (coloured surface) strain refinement process, where (b) is a zoom-in of frame (a).

Once the Laue pattern is indexed with experiment setup parameters (dd_0, x_c and y_c, *etc.*), refinements can be further done by fitting lattice parameters (a, b, c, α, β, γ), which was set to be standard values, to achieve minimum deviation. The fitting results give new values of lattice parameters for the probed crystal, and the difference between and the standard values give the strain information of the crystal. However, as calibration sample, the strain/stress stored is usually assumed to be at minimal values, which may work contrarily with maintaining

constant parameters (a = b = c, $\alpha = \beta = \gamma = 90°$). Figure 5.8 shows the visualization of the strain tensor from the indexation of Laue pattern of silicon pillars in the form of comparison of before (transparent mesh surface) and after (solid coloured surface) refitting the lattice parameters.

From the Figure, it can be seen that the magnitudes of strain were reduced to less than 10% by pure refining of lattice parameters. Furthermore, the parameters of the experimental setup are also adjusted to minimise the misfit (equals to 0.089 and 0.001, respectively, before and after refinement in the case shown in the Figure). After this refinement is completed, the experiment setup is considered calibrated. With the parameters calibrated by such scheme, Laue patterns diffracted from sample pillars (CMSX-4 alloy) can be also indexed easily. Figure 5.9 shows the final indexation results from (a) silicon and (b) CMSX-4 alloy pillars with *hkl* numbers labelled.

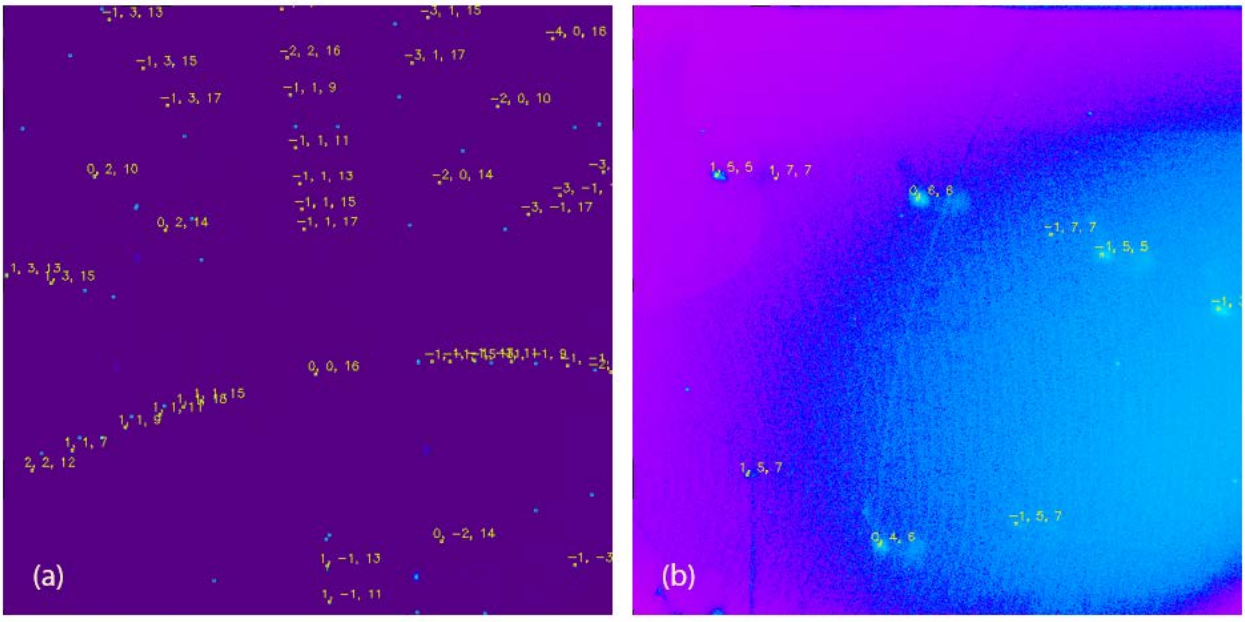

Figure 5.9 Indexed Laue pattern from (a) silicon pillar as calibration sample, and (b) CMSX-4 pillars with *hkl* peaks labelled.

5.4 Experiment results

5.4.1 Laue pattern and peak study

In the present study, a *in situ* compression test by diamond flat punch on a micropillar was conducted using reflection mode micro-Laue diffraction. The setup produced rather complex combination of multiple Laue patterns as a result of diffraction from multiple crystals, background reflection by trench side-walls and more interestingly, diffraction from the dual-phase structure of the CMSX-4 crystal. Figure 5.10 shows the Laue pattern collect by the CCD detector in the process of indentation when the indenter tip (diamond) is hovering very close to the micropillar. From frame (a) with longitude intensity value mapping, a higher intensity impression can be observed which covers a large area (shaded blue). This is due to the geometry of the one-side trenched sample surface which reflects some of the intensity of the incident beam.

Two sets of single crystal diffraction patterns are collected, one from the micropillar (CMSX-4 alloy) and one from the indenter tip (Diamond). The peaks diffracted from CMSX-4, compared to those seen in previous experiments (Figure 4.6), are much weaker and less well shaped. The maximum intensity of the peaks shown in the figure is around $2x10^4$ counts for 5-minute exposure, which is only 1/1800 as strong as those diffracted from bulk alloy beam (in Chapter 4).

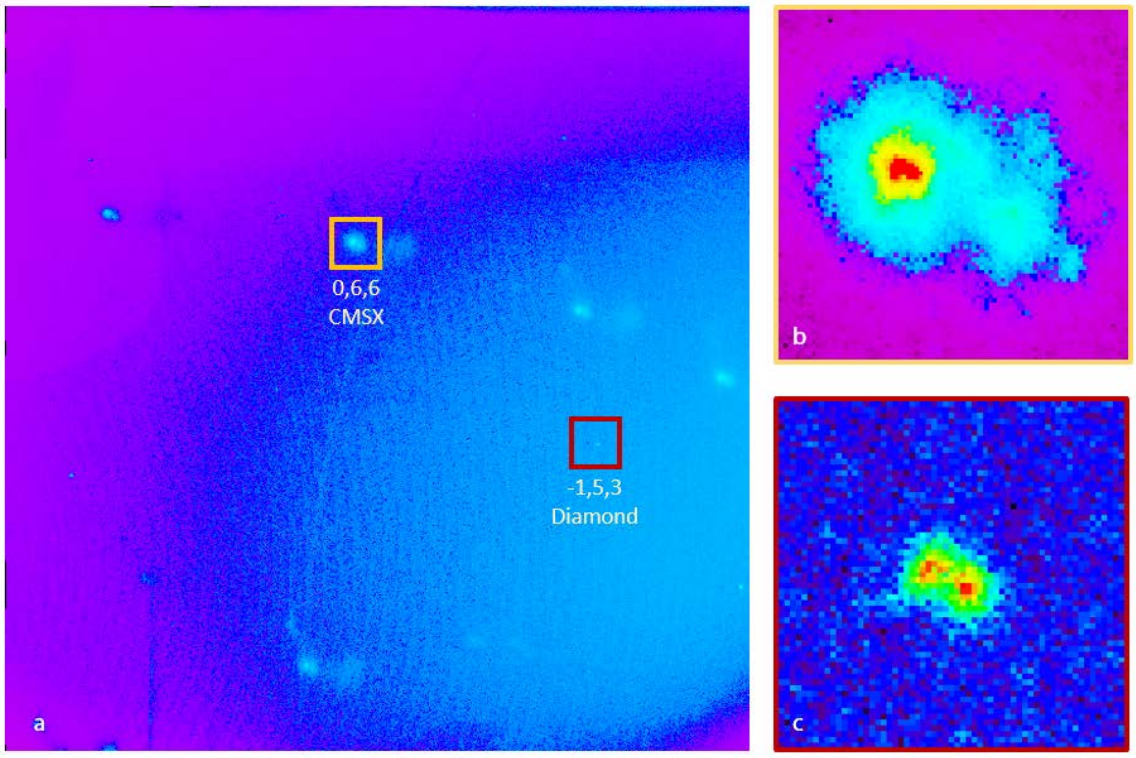

Figure 5.10 Laue pattern of the studied CMSX-4 alloy micropillar on the nanoindenter; (a) full frame collected on CCD detector; (b) zoom in of the [066] reflection of CMSX-4; (b) zoom in of the [-1,5,3] peak of the diamond indenter tip.

Given the fact that the white incident beam used for these experiments were of similar spectrum and flux, it is mainly due to reduction of diffracted flux. As pillars were only 1-2 microns in diameter, a significant amount of X-ray flux was transmitted (Figure 5.11, a). Diffraction from the diamond tip, though has similar intensity, shows a much sharper peak shape that reflects its high level of perfection.

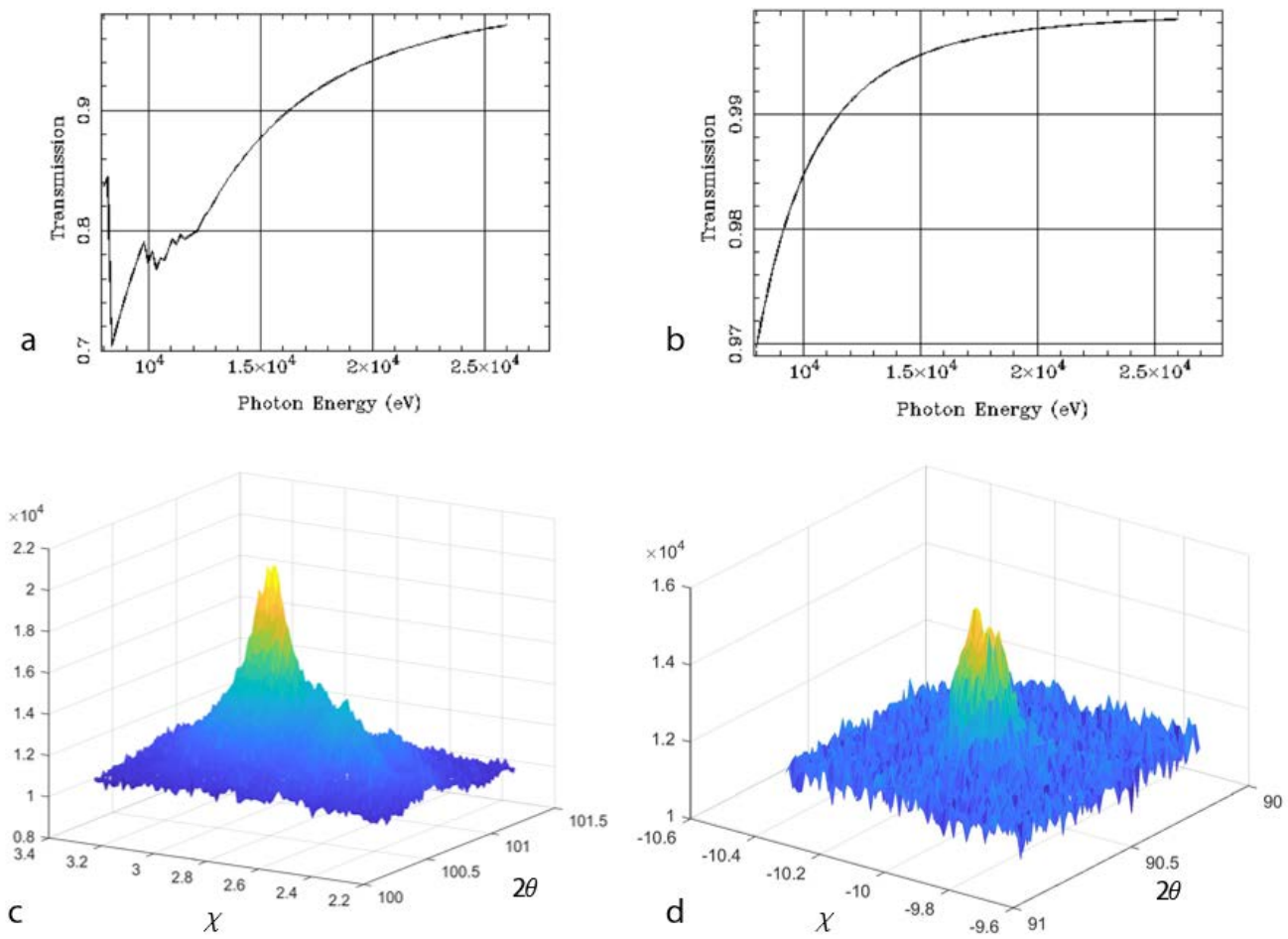

Figure 5.11 Plots of X-ray transmission through (a) 2-micron thick CMSX-4 alloy and (b) 20-micron diamond crystal across different photon energy (eV); 3D morphology of the intensity map of (c) [0 6 6] reflection of CMSX-4 and (d) [-1 5 3] reflection of the diamond.

Figure 5.11 (c) and (d) show the 3D shape of the two peaks in previous figure, from CMSX-4 and diamond respectively. The CMSX-4 peak is much broader and with higher intensity given the diameter of the diamond tip is around 20 microns. On top of which, the peak intensity of those diffracted from CMSX-4 is distributed into two major domains (shown in Figure 5.10, b) with higher intensity and several surrounded domains with relatively lower intensity. The relative distance and positions between these domains tend to show similar arrangements. Such

arrangement indicates the distribution of several block cells which are contained by the probed pillar, in our case, most likely the ordered γ' precipitates.

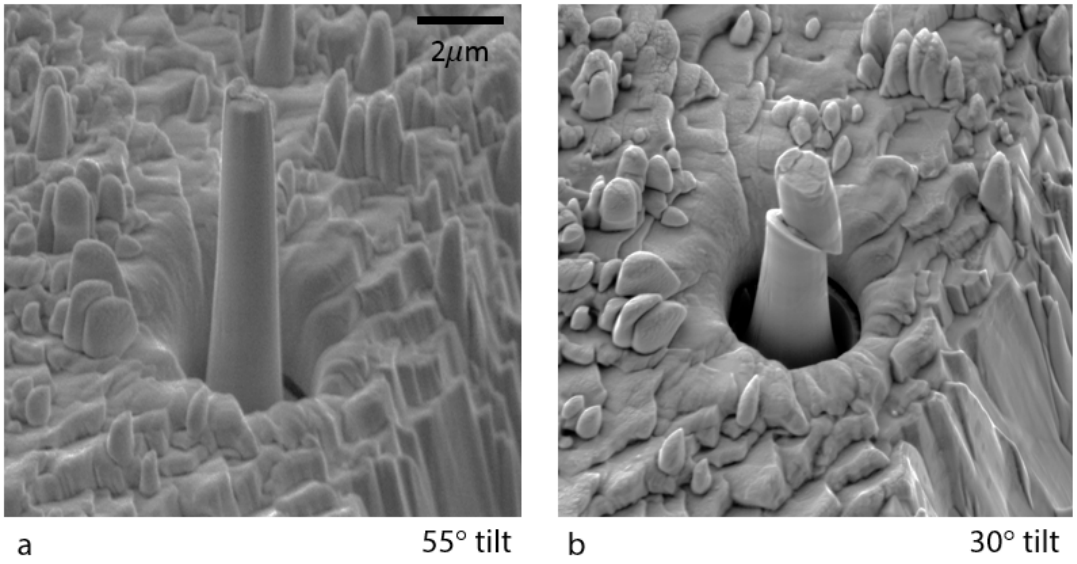

Figure 5.12 SEM image of the tested pillar (a) at 55° tilt angle before the experiment; and (b) at 30° tilt angle after the compression test.

Figure 5.12 shows SEM images of the same tested pillar that produced the diffraction patterns shown before. The pillar had the top diameter of 1.12μm, bottom diameter of 1.85μm, and height of 7.31μm. The precipitates were nominally cuboidal of lateral dimension from 200nm to 500nm. The scanning area of the incident beam was of size ~2μm by 2μm (perpendicular to the beam direction), which probed the upper 2μm of the micropillar. Therefore, the probed volume contained a limited number of precipitates. It is also supposed that dislocations are most likely stored in the γ matrix (before the indentation test), hence the diffraction Bragg peak is likely to split into several domains. Indexation on different sets of intensity domains (split peaks) gives more information about the misorientation and dislocations stored accordingly.

The indexed lattice orientation by two main sets of peak intensity domains are given as the following rotation matrix:

$$R1 = \begin{pmatrix} 0.28143 & 0.13340 & 0.17238 \\ -0.18424 & 0.28962 & 0.07885 \\ -0.10976 & -0.15108 & 0.29897 \end{pmatrix}$$

$$R2 = \begin{pmatrix} 0.28082 & 0.13243 & 0.17412 \\ -0.18426 & 0.28953 & 0.07912 \\ -0.11128 & -0.15209 & 0.29789 \end{pmatrix}$$

The misorientation indexed between them is smaller than 0.3 degree (along Euler axis), with ϕ=-0.217°, θ=0.257°, and ψ=0.067°.

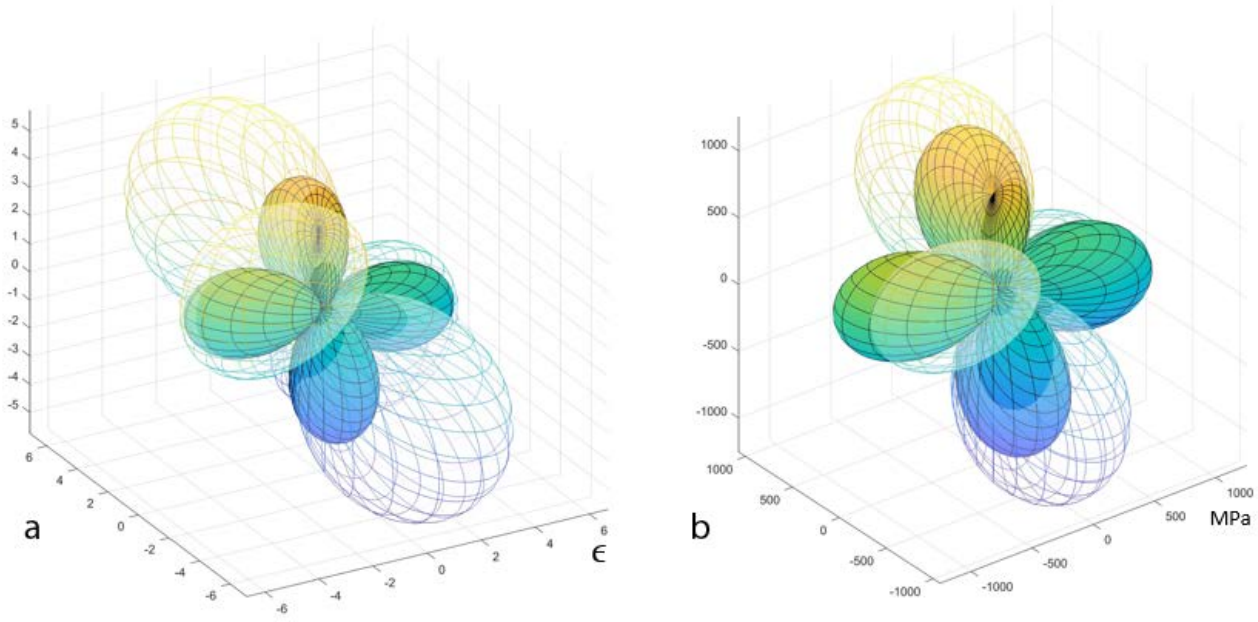

Figure 5.13 Comparison of two sets of split peaks in (a) strain tensor; (b) stress tensor; where the transparent mesh stands for primary peak and the solid coloured surface stands for secondary peaks.

Obvious difference is spotted when comparing the elastic strain and stress tensor calculated by indexation and strain refinement process, between the primary set of split peaks (with highest intensity) and the secondary set respectively, as shown in Figure 5.13. The primary set, shown in transparent mesh, gives higher magnitudes of strain and stress in each direction suggesting higher residual stress stored in the contributing phase. Such stress could be a result of the crystal solidification process taking place around precipitation cores, or the misfit stress between the γ and γ' phases. Given that precipitates take up over 70-80% volume fraction in the alloy, the primary contribution to the peak intensity is most likely made by the precipitates. Figure 5.14 shows the two fitted peaks by Gaussian in 2D plot and 3D surface.

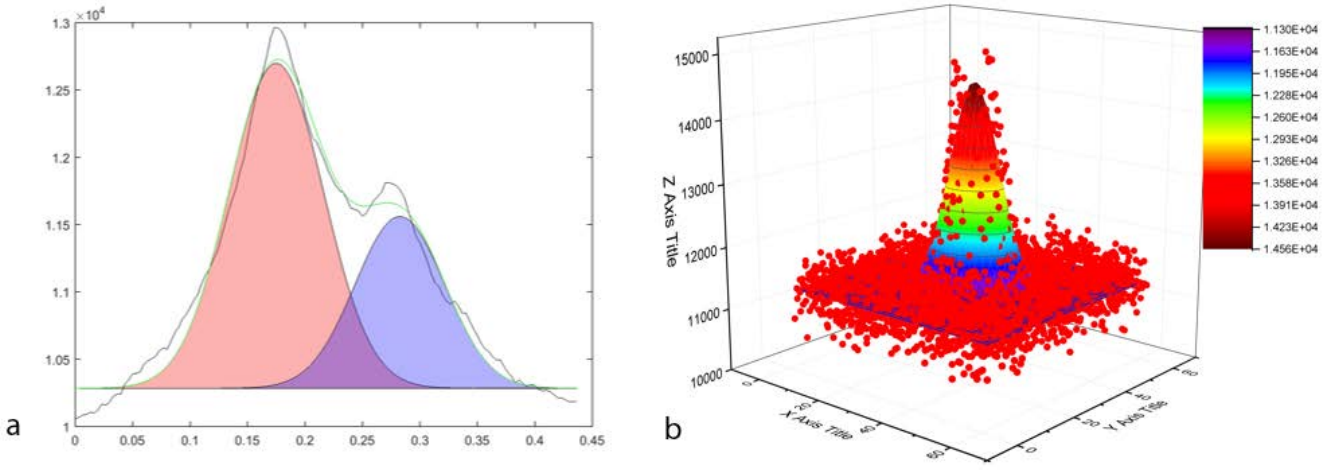

Figure 5.14 (a) 2D Gaussian fit of the peak intensity of [006] reflection; (b) 3D Gaussian surface fit of the peak intensity;

5.4.2 Laue spot sequence and mechanical annealing

Once the setup is calibrated and ready, the indenter tip was aligned with the pillar tip by full-field imaging (Figure 5.6). The alignment of the beam on the pillar can also be confirmed by the intensity of diffracted beams from the diamond tip (Figure 5.10). The exposure time was optimized to combine stability with sufficient intensity obtained by the CCD detector, and in the present experiment amounted to 5 minutes.

The compression test starts with the indenter calibration, and diamond punch 'cleaned' by indenting soft materials such as copper. The indenter tip finds the pillar surface by moving down at the speed of 5 nm/s and bouncing back when the load unit reads higher than 10-25 mN loading. The tip to sample surface distance is then determined. The incident beam is placed 2 micrometres below the pillar tip to monitor the scattering signal while the micropillar is compressed. The compression test is taken at true displacement control mode supported by the indenter, with tip downward velocity of 10 nm/s.

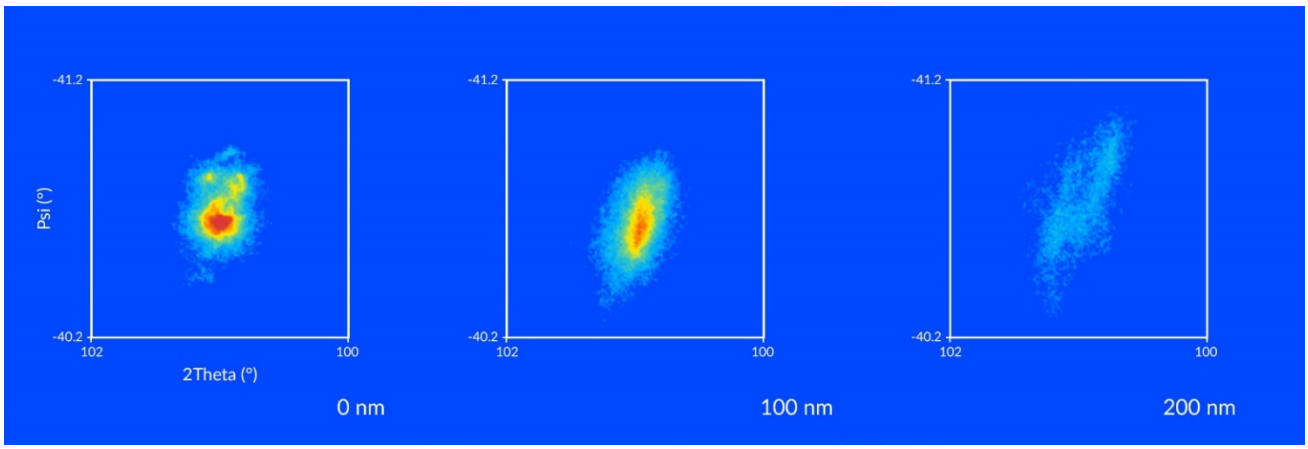

Figure 5.15 Bragg peak [006] of the CMSX-4 pillar under various loadings

The compression was paused after every 100-nm displacement step in order to take five-minute exposure of the diffraction beam. Figure 5.15 shows a sequence of the previously studied [006] peak collected when the pillar was under various stages of loading. It is observed that the intensity of the pattern was initially distributed in several domains before the test. As the value of loading was initially increased to 0.73 GPa (also see Figure 5.18, a), the intensity was redistributed into a single “streak” along one axis, before it became greatly reduced during further deformation. In other words, the dislocation density inside the pillar was reduced, and distribution changed from discontinuous to more uniform, during the first part of the compression test. This effect is often seen as the mechanical annealing [55] process or result of dislocation starvation, as the initially stored dislocations (SSDs giving the uniform intensity reduction and spreading, and GND’s in cell walls responsible for splitting) escape from the micropillar surface. As compression progresses, the dislocation population inside the micropillar is re-arranged into more uniformly distributed geometrically necessary dislocations of particular kind, leading to uni-directional streaking of the reflection. The domination of one type of dislocations inside the pillar is manifested by the Bragg peak elongation along the ξ axis (see also § 4.5.4), as observed in the second frame in Figure 5.15.

As the compression test continues, the pillar becomes severely deformed, and cross slip takes place. The deformed micropillar shape can be seen in the SEM images taken after the test (Figure 5.12, b). Figure 5.16 shows the intensity distribution in 2theta-chi coordinates of the Bragg peak [-1 5 5] when the pillar is under compression with various external stress applied. Frame a is collected before the compression, b and c are collected when the pillar is hardening with a

flow stress of 0.73 GPa and 1.40 GPa respectively, and frame d when the pillar is softening with flow stress 1.18 GPa.

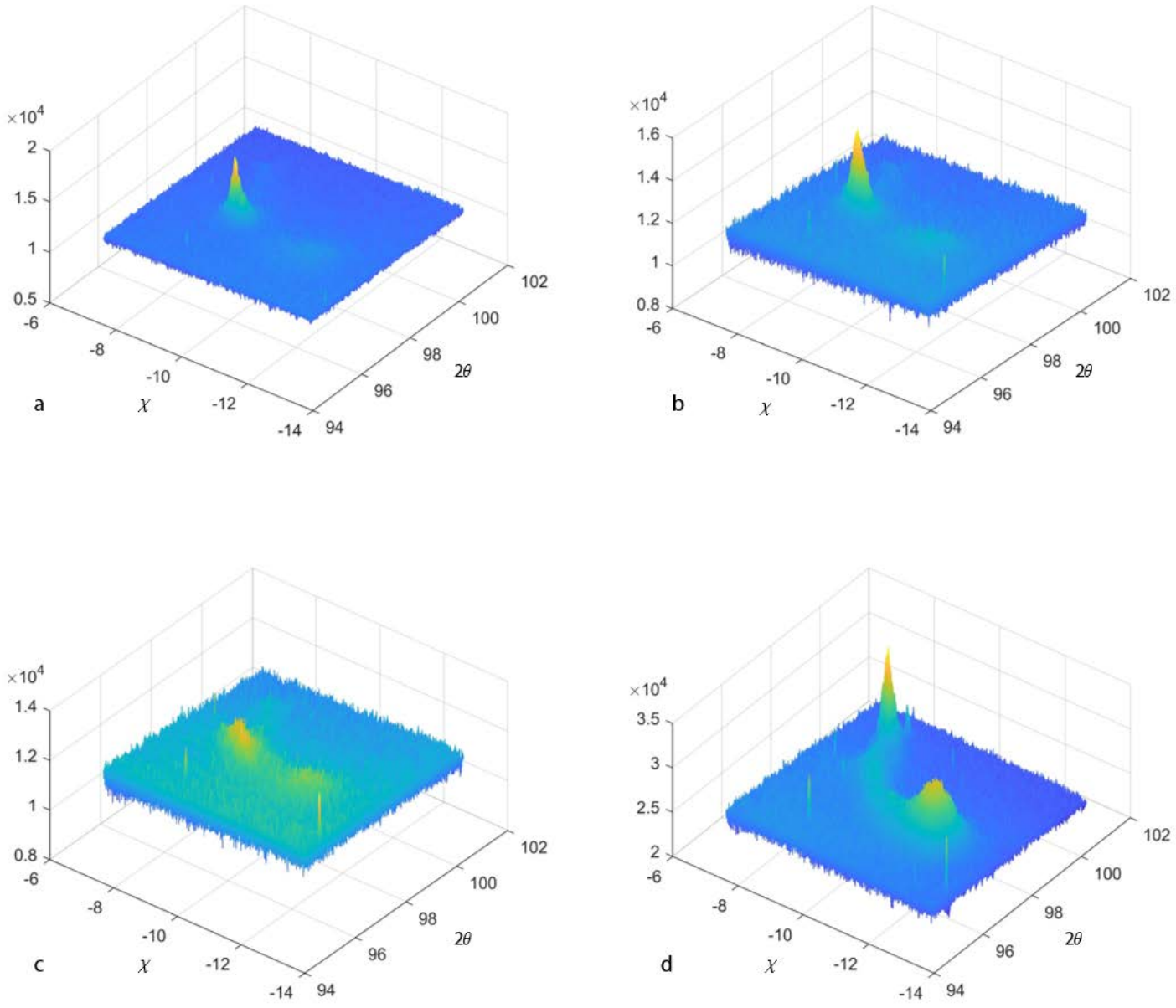

Figure 5.16 Peak intensity distribution map of the [-1 5 5] reflection of CMSX-4 alloy at (a) before compression; (b) 0.73 GPa loading; (c) 1.40 GPa loading; and (d) 1.18 GPa (softening stage);

The intensity re-distribution during compression reveals the major slip behaviour of the pillar, which effectively shears the pillar into two parts (upper and lower) with distinctive orientation shown by the diffracted X-ray beam. From frame d, continuous intensity distribution along a trace between the two separated peaks can be observed. Such streaking indicates the continuous stacking of slip planes with one type of dislocations (GNDs) which contribute to the major slip. The nucleation and aggregation of such dislocations distort and rotate the lattice continuously, hence change the d spacing and 2θ angle locally in the crystal. Such effect leads the displacement of the diffracted beam with different wavelength accordingly.

The difference in average lattice orientation indexed by the Laue pattern (Figure 5.16, d) between the upper and the lower of the slipped pillar is shown by Figure 5.17 (a). It is seen that after the major slip, the lower part (marked red) remains almost the same orientation as it is before the compression, and the upper part (marked blue) shows obvious misorientation compared to the original due to the cumulative effect of dislocations.

Figure 5.17 (b) shows the plot of the visualized elastic strain tensors of the upper (solid colour) and lower part (transparent mesh) of the slipped pillar. It is obvious that the strain tensor is aligned with the experimental axes for the lower part as few slipping incidents take place, and the strain remains aligned with the loading axis. While the upper part of the pillar shows misoriented strain tensor, due to the shear introduced by dislocations in the active slipping system.

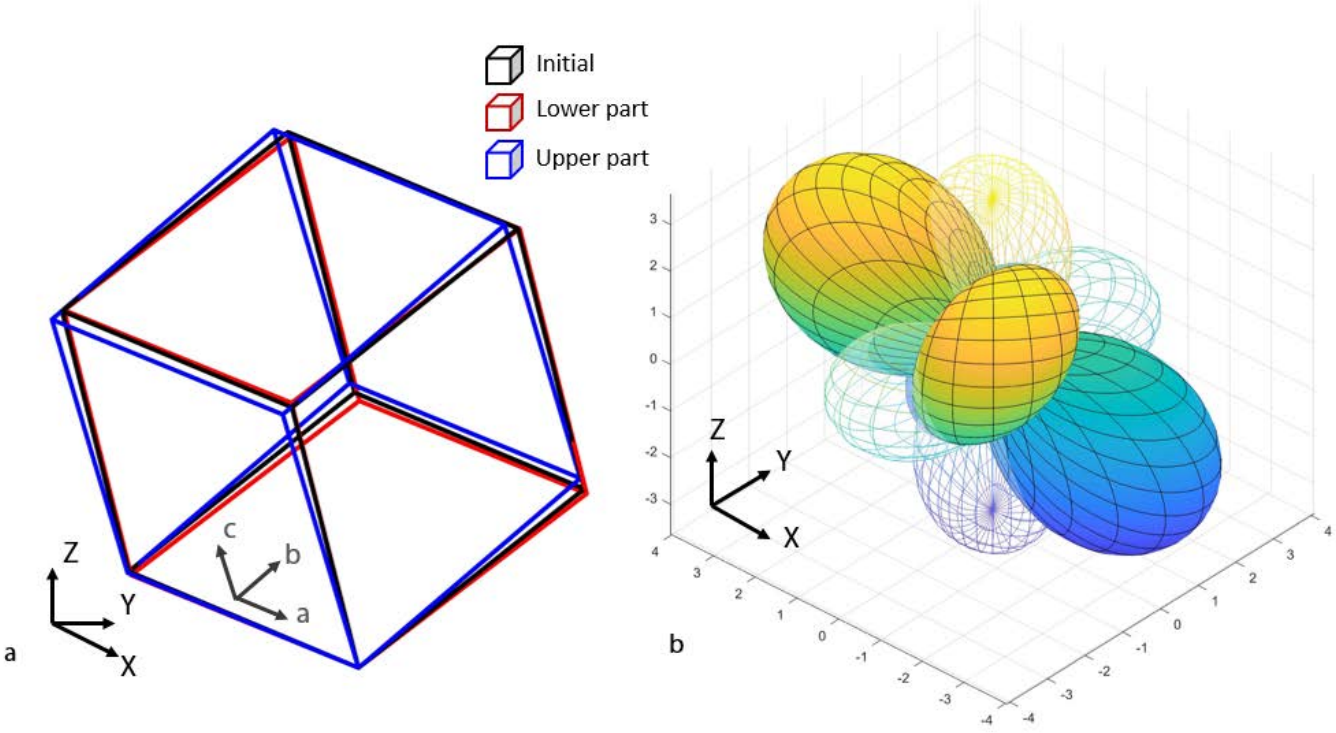

Figure 5.17 (a) Illustration of the indexed lattice orientation comparison, where the black cube represents the initial status and the blue and red represent the upper and lower part of the slipped pillar; (b) visualization of the strain tensor of the upper(solid colour) and the lower part(transparent mesh) of the pillar.

5.4.3 Loading response and size effect

As mentioned, the compression test is performed in true displacement control mode, by 100 nm displacement steps for the *in situ* diffraction purpose. Therefore, from the true stress and strain response curve of the pillar, as shown in Figure 5.18 (a), several pauses are shown with marked true displacement (after the indenter tip established the initial contact with the top surface of the pillar). Since the pause of the loading process which lasts for about 5 minutes, relaxation shows as the load reading drops with pausing time. As the loading continues, the flow

stress bounces back quickly, as the pillar hardens again. The general flow stress curve of the *in situ* compressed pillar shares the similarity with those results presented in Chapter 3 . The value reaches a maximum around 5% true strain before the response shows softening effect. The main significance of these results is that they confirm that the response of CMSX-4 alloy sample is unchanged during the *in situ* compression test comparing to the *ex situ* (in-SEM) experiment series reported previously.

Figure 5.18 (b) plots the data of the *in situ* test (marked by the red square) with the previously presented *ex situ* tests, for the flow stress at 5% true strain, as a function of top micropillar diameter. It can be seen that the result falls into the band consistent with the other data points, and the fitting curve by equation 3.6 still gives a good prediction. The red crosses shown in the same plot represent the predictions by the 2.5D discrete dislocation dynamics model that is presented and discussed in the following chapter.

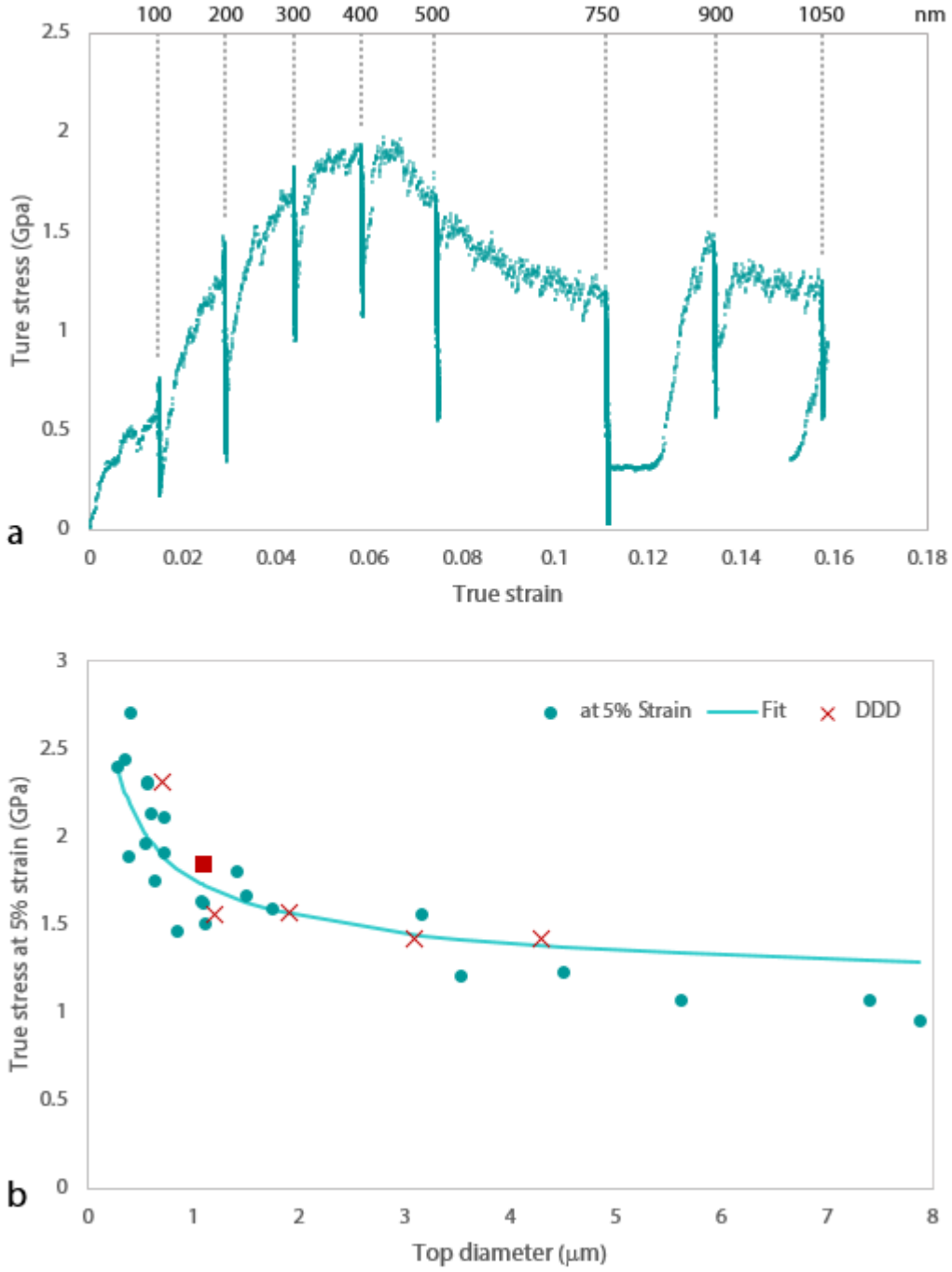

Figure 5.18 (a) The true stress and strain response curve of the pillar for the compression test, where pauses for Laue pattern collection is marked by true displacements; (b) true flow stress at 5% with various top diameters, with the tested pillar in the present work marked as red square.

5.5 Discussion and conclusion

Dual mode high resolution X-ray microscopy developed in the project and reported in this chapter allows simultaneous micro-Laue diffraction and full-field imaging. A set of challenging *in situ* micropillar compression tests were performed with a portable nanoindenter mounted on the beamline stage. The setup feasibility was proven in the present work, as it was capable of providing finer than 30 nm transmission imaging resolution, which was important for successful fine-scale movement and alignment of the nanoindenter tip to the micron-sized specimen features. With the micron-sized dual phase single crystal (CMSX-4) of ~1µm diameter illuminated with the focused white X-ray beam, micro-Laue diffraction method revealed the initial dislocation distribution and the 'mechanical annealing' effect during initial loading in the nanoindentation compression test. In most relevant publications on the subject, it is argued that the initially stored dislocations tend to escape from the sample surface as the size of the crystal studied gets smaller. Observation of the Bragg peak intensity aggregation presented in this work supports this theory. In addition, the dislocation type and population can be probed by this method *in situ* during the compression test, and their effect on the lattice distortion and rotation can be deduced from the Laue pattern indexation. As presented in the results, Laue diffraction captures the separated parts by major slipping incidents and identifies them by indexing the orientation and strain status.

The response of the compressed pillar is placed in the context of other data for *ex situ* compressed pillars by comparing the true stress – true strain traces. Both

mathematical fitting and the DDD model results (discussed below) give good agreement with the experimental data.

However, the limitation of the present method for revealing the strain state of the probed crystal with complex microstructure is also obvious. The resolution of the mapped strain distribution inside the crystal is relying on the indexation of distinctive single peaks, which are the projections of diffracted X-rays with different wavelength onto one section of q space. In order to resolve the information per wavelength and improve the resolution of strain status inside the crystal, reciprocal mapping by scanning beam energy or rocking the probed crystal is necessary. With that said, the breadth of material information which can be derived from probed volume is vast, with the need to improve not only the data acquisition, but also analysis techniques we have so far.

Overall, the work presented in this chapter demonstrated that the setup for high resolution imaging combined with micro-Laue diffraction delivered a method for *in situ* mechanical testing, theory validation and refinement, and data interpretation schemes. It also shed light on how this setup can be a practical tool for probing mesoscale plasticity in crystals with complex structure under mechanical deformation.

Chapter 6

Dislocation-based modelling for mesoscale plasticity and the development of advanced X-ray diffractive imaging techniques

6.1 Dislocation Dynamics and Modelling

Dislocations along with other types of defects in crystals (such as vacancies and grain boundaries, etc.) nucleate, interact and form complex structures that contribute to crystals mechanical properties spanning across various scales and length of time, of which, however, a fundamental understanding and precise description is lacking. In previous works presented, different types of dislocations and its network or distribution (so-called microstructure) inside the crystal is always discussed associated with the plasticity it causes. Although it is recognized as an important fact that material's overall mechanical properties depend on a collective contribution of all different types of defect. This section is going to review discrete dislocations, whose dynamics (dislocation dynamics) defines the physics of interest at mesoscale plasticity (Table 6.1).

Table 6.1 The terms and scales used to describe mechanics [162]

Unit structure	Length scale	Timescale	Mechanics of interest
Complex Structure	10^{3} m	10^{6} s	Structural mechanics
Simple structure	10 m	10^{3} s	Fracture mechanics
Component/object	10^{-1} m	1 s	Continuum mechanics
Grain microstructure	10^{-3} m	10^{-3} s	Crystal plasticity
Dislocation microstructure	10^{-5} m	10^{-6} s	Micromechanics
Discrete dislocation	10^{-7} m	10^{-9} s	Dislocation dynamics
Atoms	10^{-9} m	10^{-12} s	Molecular dynamics
Electron orbitals	10^{-11} m	10^{-15} s	Quantum mechanics

In X-ray studies presented in Chapter 4 and Chapter 5 dislocation behaviour and its contribution to plasticity is studied by the intensity distribution, broadening or streaking, of the diffracted peaks from a crystal. There are also published works which have successfully observed dislocation and its structure via TEM [69,98,100,112,163], dislocation electron tomography [164–168], micro-Laue [151,169] etc. Although advances in electron and X-ray microscopic techniques have in great deal helped observe and characterize the dislocations in crystals, how and why organised and structured dislocations emerge during plastic flow is never persuasively answered with a commonly accepted theory. Almost inevitably, computational modelling is mostly relied on for developing a solid theory until it is firmly settled between the mechanical physicists, material scientists and mathematicians someday.

This section is going to give a brief review on dislocations, its properties and how they contribute to the plasticity inside the crystals. This is followed by the presentation of a 2.5-dimensional discrete dislocation model with its applications.

6.1.1 Dislocation properties, force and dynamics

Dislocations are firstly described topologically in French by Volterra in 1907 [170] before edge dislocations [171–173] and screw dislocations are discovered and discussed as a type of defects later. Figure 6.1 (a) illustrates an edge dislocation with the line direction along the z-axis (perpendicular to the paper plane), indicated by symbol ⊥. As shown, edge dislocations can be described as an extra half plane inserted into the crystal lattice, causing distortions. They are characterized by the line direction and the Burgers vector, ***b***, which is determined

by drawing a Burgers circuit. Two sample type edge dislocation of opposite directions (two half planes with the same line direction) will be able to annihilate each other when they are close enough. Figure 6.1 (b) illustrates two opposite screw type dislocations.

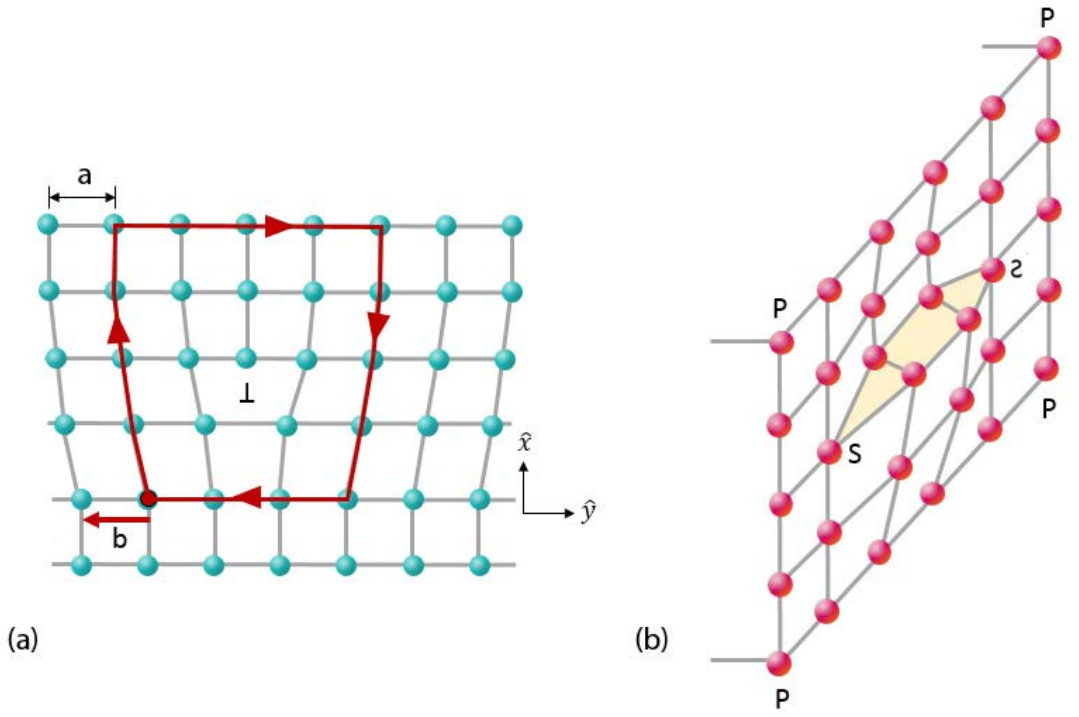

Figure 6.1 (a) Illustration of an edge dislocation with line direction along z-axis (perpendicular to the plane of paper), where b is the Burgers vector; (b) illustration of a screw type dislocation on the plane indexed P.

The plasticity that a single dislocation introduces can be described as the plastic distortion tensor, $\beta_{ij}^{p}(x)$ [174], where *i* indicates the normal to the dislocation plane and *j* indicates the Burgers vector, gives,

$$\beta_{ij}^{p}(x) = b\delta(x_i)\Theta(x_j), \tag{6.20}$$

Where $\Theta(x)=1$ when $x<0$, and $\Theta(x)=0$ when $x>0$, and $\delta(x_i)$ is the Dirac delta function that restricts the dislocation to the plane where $x_i=0$. Therefore, the plastic strain can be described as following for $\beta_{ij}^{p}(x)$,

$$\epsilon_{ij}^{p}(x) = \frac{1}{2}(\beta_{ij}^{p} + \beta_{ji}^{p}). \tag{6.21}$$

The strain or plasticity certainly shifts its location as the dislocation moves easily within the crystals. The easiest movement an edge dislocation can perform is towards the direction of its Burgers vector by shifting the extra half plane by every single lattice position, so-called slip or glide, which requires it to overcome a minimum stress value. Such stress is called Peierls-Nabarro (ranges 10^{-6} to 10^{-5} times of the shear modulus for FCC structures [175]). In most cases, edge dislocations are strictly moving along the gliding or slipping plane, while under certain conditions they tend to climb and cross-slip off the slipping plane [14,18,72,139,176,177] as a pair of activated mechanisms. The movement along the axis perpendicular to its slip planes is called climb, which requires material to diffuse in and out the dislocation core hence often thermally activated. And cross slip happens when screw type dislocation shifts its plane from one to another, enabling the edge dislocation to move off the slip plane as well.

When dislocations glide due to the application of external stress, along certain slip plane, the Orowan equation can be used to describe the collective plastic strain they introduce to the crystal as,

$$\Delta\epsilon^{p} = b\rho\langle\Delta x\rangle \tag{6.23}$$

Where b is the Burgers vector's magnitude, ρ stands for the dislocation density, and <Δx> presents the average travel of each dislocation along the slip plane. Which can be divided by time and rewrite as strain rate equation as,

$$\dot{\epsilon}^p = b\rho\langle \mathrm{v} \rangle \tag{6.24}$$

Notably only moving dislocations are counted for the dislocation density factor, whereas the pinned, escaped or interlocked populations are not. If we introduce the elastic constants matrix c_{ijkl} and rewrite the strain into crystallographic direction tensor along the elastic component, we get the following,

$$\epsilon_{ij} = \epsilon_{ij}{}^e + \epsilon_{ij}{}^p,\ \sigma_{ij} = c_{ijkl}\epsilon_{kl}^e. \tag{6.25}$$

This equation is used to link the external stress and the total strain response of the crystal when dislocations are counted as the majority of the defects that contribute to the plastic strain.

On top of the statistics of the stress-strain response with the collective contribution due to dislocations, the dynamics and forces are also important for studying them as discrete objects. The Peach-Koehler relation [68,95,178,179] (also termed force) is used to describe the dislocation movement response to stress as,

$$\mathbf{F} = (\boldsymbol{b} \cdot \boldsymbol{\sigma}) \times \hat{\xi}\ ,\ \text{or}\ \ F_i = \epsilon_{ijk} b_l \sigma_{jl} \hat{\xi}_k \tag{6.26}$$

Where $\boldsymbol{b}$ stands for the Burgers vector, $\hat{\xi}$ stands for the line direction of the dislocation, and σ is the total stress tensor, ϵ_{ijk} is the components of the Levi-Civita tensor [180]. The total stress felt by one dislocation is often described as a sum of the applied external stress σ_{app}, stress field introduced by other dislocations $\sigma_{\perp}$, and stress introduced by other types of defects σ_{other}. Assuming

the isotropic elasticity of the dislocations [181,182], the stress tensor component arising from a dislocation loop L can be written as,

$$\sigma_{ij}^{L} = \frac{\mu b_n^L}{8\pi} \oint [R_{,mpp}(\epsilon_{jmn} d\ell_i + \epsilon_{imn} d\ell_i) + \frac{2}{1-\nu} \epsilon_{kmm} (R_{,ijm} - \delta_{ij} R_{,ppm}) d\ell_k] \qquad (6.27)$$

Where $R_{,i}$ stands for a derivative of R with respect to axis x_i, R=||, stands for the distance between the stress evaluated position and the dislocation point (along the integration of the dislocation curve), $d\ell$ is the differential line element; μ stands for the shear modulus, ν stands for Poisson's ratio.

The self-energy of dislocation is regarded as proportional to the dislocation length and the square of Burgers vector, given as,

$$T = E_{dis} \propto \mu b^2 \qquad (6.28)$$

Where T is the line tension equal to the self-energy E_{dis}. Self-energy is also contributed by another term describing dislocation self-stress/self-Peach-Koehler-force that affect themselves.

In addition, there is also a frictional force used as a term that describes the damping effect while dislocation is in motion due to lattice shifting or other defects, $\gamma\mathbf{v}$, where **v** is the velocity of the dislocation and γ is the damping term. The damping can also be described as mobility factor, *m*, as,

$$\boldsymbol{v} = \frac{1}{\nu} \boldsymbol{F} = m\boldsymbol{F}. \qquad (6.29)$$

The combined force, stress, and damping is the full description that most models will employ for the motions of the discrete dislocations. Energy expressions associated with dislocations are not going to be reviewed here.

Another important topic here to discuss is, how and where do dislocations nucleate, interact and annihilate with each other. As mentioned above, two edge dislocations with opposite sign moving along the same slip plane annihilate each other and leave no plasticity behind, hence affect the total population and density of the dislocations. It is also possible for dislocations to combine and form new dislocation meeting the criterium of Burgers vectors, that $\boldsymbol{b}_a + \boldsymbol{b}_b = \boldsymbol{b}_c$. When dislocations of different types collide in short-range, it is also possible for them to form intersections or junctions. Intersection happens when two nonparallel dislocations slip into each other and junctions refers to long-range interaction which form relatively stable structure. There are also special cases, such as Lomer-Cottrell locks. These interactions are the main concern which impede the free motion of the dislocations.

Dislocations are nucleated at many places, such as surface, grain boundaries and so-called dislocation sources. The most well-known dislocation source of all is called the Frank-Read source [183], where one dislocation segment is pinned at each end of it and bow out at certain stress value and direction. This pair of dislocations bow out and back forming a close dislocation loop when annihilating each other, which mechanism allows the source to produce multiple dislocation pairs.

6.1.2 Discrete dislocation simulations

Due to the major difficulty caused by the multiplicity and complexity of the mechanisms of dislocation motion and interactions, it is almost not possible to develop a quantitative analytical approach, thus methods to the corresponding scale are needed that take dislocations as discrete simulating entities. Therefore, in the field of mesoscale material researches, two main simulation methods have been proposed. One is phase-field methods which is an energy-driven method that counts the elastic energy of dislocations [65,182,184,185], the other is the discrete dislocation dynamics (DDD) model which is force-driven that solves motion equations for dislocations [15,62,63,68–72,75–78,80,82–85,186]. Both are to a certain degree helpful to reveal the underlying mechanisms linking the mesoscale plasticity (unobservable or hardly observable structures) and the larger scale behaviour of the materials, however, the present work focuses on the DDD models.

One of the earliest work is a model on dislocation interacting with obstacles [187], however, the most contributing model which is later adopted by many is the one by Needleman and van der Giessen [15,62,68,75,80]. Such models are 2D based and have successfully helped discover dislocation structures and dynamics such as cellular-like, hamming, creep dynamics, Andrade creep, etc. And this method has been extended to 3D [188] for studying advanced or more complex dislocation structures and networks inside crystals, which, of course, become more computationally expensive.

The events and models inside DDD models have so far developed a big variety serving different purposes, from simple time-free interactions and annihilations to

thermally activated cross slip and climb. However, the key problem or question for mesoscale plasticity modelling is rather now which behaviour or activities to be included for certain modelling occasions.

The setup of boundary conditions in dislocation dynamics models is also a crucial factor. For finite geometries at small scale (several micrometre size), it is most straightforward to set either a free or an un-penetrable boundaries where dislocations easily escape, escape with an effort or get pinned. Periodic boundary conditions (also found in the later model presented) are more often found for bulk material modelling where the computational resource is saved for solving cases with enormous sizes. However, the problem of periodic boundary conditions falls in the realisticity and reliability of the dislocation structures developed through such interactions. With that said, the biggest challenge that DDD models face is computational, by which the utility is still limited. In order to control the practicality and to reduce the computation cost of DDD models, simplifications are more or less made such as ignoring the lattice rotation that dislocations may introduce to the slip plane, etc.

6.1.3 A versatile 2.5-D discrete dislocation dynamics model

With the significant demand that three-dimensional DDD models place on the computing cost, we propose a '2.5-D' DDD model that requires minimum computing resources while maintaining an excellent means of capturing the fundamental trends of material behaviour. The early work of this model with multiple applications has been published and discussed [15,73].

6.1.3.1 Model setup

The present model simulates a projection of the crystal at a variable orientation where the dislocation population belongs to different types and slip systems are all visible. Figure 6.2 shows two simulation planes with different orientation hence different traces for various slip systems can be observed, as the dislocations in motion.

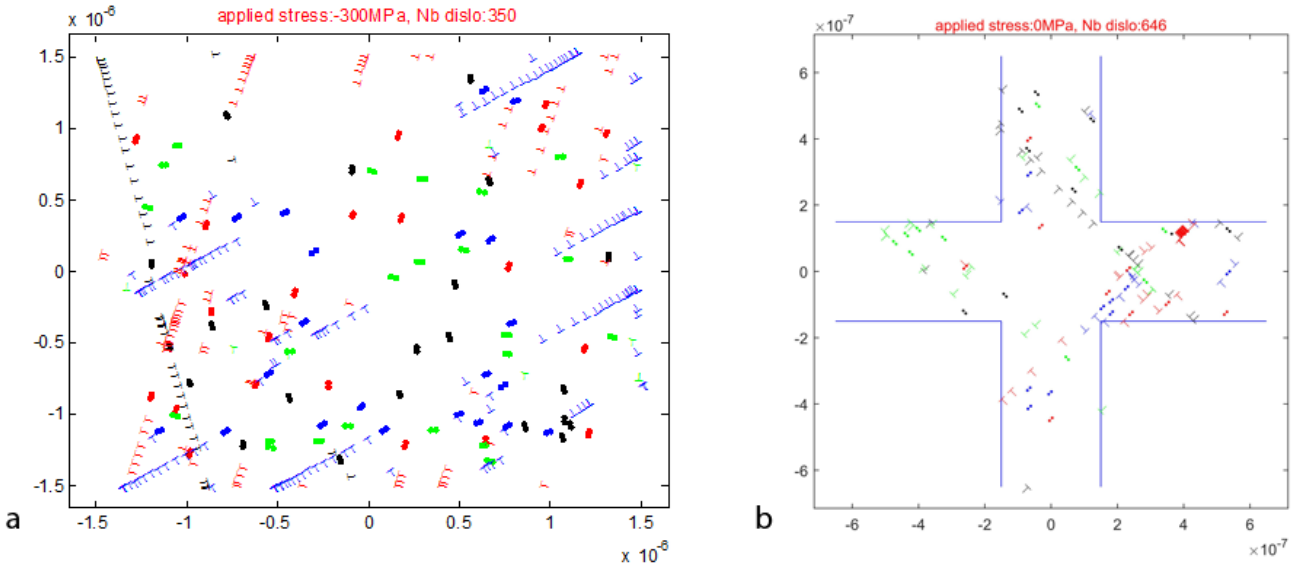

Figure 6.2 simulation plane of the model (a) close boundary grain at 300 MPa compressive external stress with simulation plane at an angle off the [001] direction; (b) periodic two boundary two-phase single crystal with simulation plane at [001] direction.

At the setup, the simulation session can be assigned with certain crystal structure (eg. FCC) orientation, and available slip systems. And then at the initial state, a given number of Frank-Read sources are assigned to different slip systems and randomly distributed, or deliberately one of the phases, in the simulation plane. A pair of edge dislocations is nucleated from the sources when the local stress exceeds a critical stress, τ_{nu}. Once nucleated, dislocations feel the local shear as a collective effect of numerous forces, including locally resolved external stress, dislocation-dislocation interaction force, drag force, dislocation self-force, image force, and osmotic force in the case of climb or thermal force arising from thermal fluctuations. The motion of the dislocation is thus controlled by motion equation according to the resultant of the forces, F_r, given as,

$$m_s \dot{\boldsymbol{v}} + \frac{1}{M_s(T,p)} \boldsymbol{v} = \boldsymbol{F}_r \quad , \; m_s = \frac{1}{v}\left(\frac{dW}{dv}\right) \tag{6.30}$$

Where M_s stands for dislocation mobility depending on temperature, T, and pressure, p, and W is total energy per unit length of a moving dislocation.

6.1.3.2 Stress and force fields

The stress induced by the dislocations in the simulation system at an arbitrary field position is often given as Peach-Koehler integral equation [178], given as,

$$\sigma_{ij}^{d}(P) = \sum_{l=1}^{N_l} \sum_{s=1}^{N_s^{(l)}} \left\{ -\frac{\mu}{8\pi} \oint b_p \epsilon_{mpi} \frac{\partial}{\partial {x'}_m} \nabla'^2 R d{x'}_j - \frac{\mu}{8\pi} \oint b_p \epsilon_{mpj} \frac{\partial}{\partial {x'}_m} \nabla'^2 R d{x'}_i \right.$$
$$\left. - \frac{\mu}{4\pi(1-\upsilon)} \oint b_p \epsilon_{mpi} \left(\frac{\partial^3 R}{\partial {x'}_m \partial {x'}_i \partial {x'}_j} - \delta_{ij} \frac{\partial}{\partial {x'}_m} \nabla'^2 R \right) d{x'}_k \right\} \tag{6.31}$$

Where N_l is total dislocation number, $N_s^{(l)}$stands for number of segments per loop l, ϵ_{mpi} is the permutation symbol, R is the magnitude of the vector difference between the position P and the line segment on the dislocation. The stress field can thus be calculated, and Figure 6.3 shows the stress field induced by single edge dislocation in an infinite plane (no boundary). And such stress field distribution is used for simulation sessions reflecting bulk response, such as those with periodic boundary conditions.

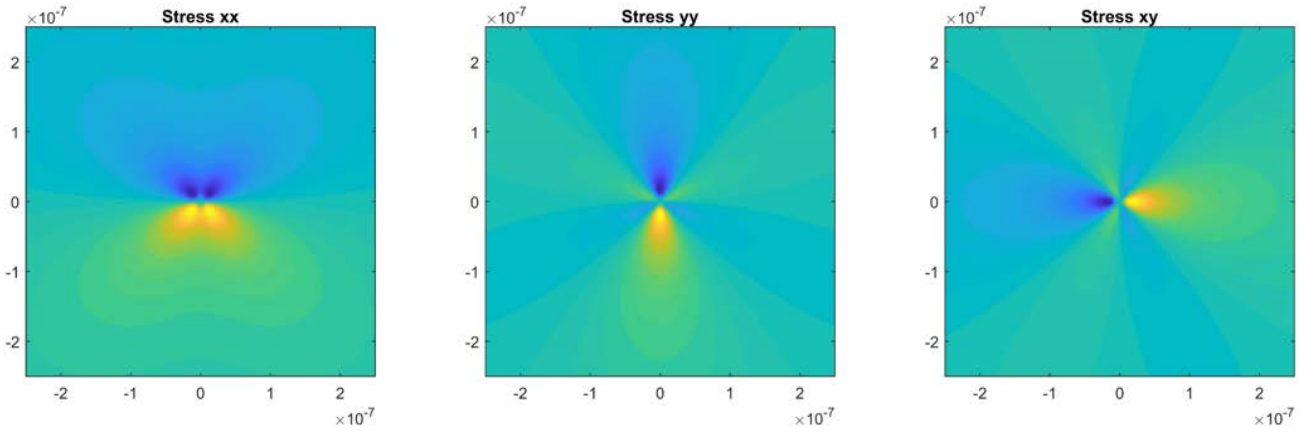

Figure 6.3 visualization of the stress field by an edge dislocation in an infinite plane

For dislocations near edges, holes or free surfaces, the expression is altered according to Hills et al [189] who developed a concise and readable expression for a dislocation near free surface, given as,

$$\sigma_{xx}^{i} = \frac{2\mu_1}{\pi(\kappa_1+1)}\left[b_x G_{xxx}^{i} + b_y G_{yxx}^{i}\right]$$

$$\sigma_{yy}^{i} = \frac{2\mu_1}{\pi(\kappa_1+1)}\left[b_x G_{xyy}^{i} + b_y G_{yyy}^{i}\right]$$

$$\sigma_{xy}^{i} = \frac{2\mu_1}{\pi(\kappa_1+1)}\left[b_x G_{xxy}^{i} + b_y G_{yxy}^{i}\right] \quad (6.32)$$

Where μ denotes the shear modulus of the phase, κ is the Kolosov's constant ($\kappa = 3 - 4\upsilon$ in plane strain where ν stands for the Poisson's ratio), b_x and b_y stand for resolved Burgers vector components, notation '1' and 'i' stand for phase and region index for multiple phases and interfaces, and G^i_{lmn} represents the so-called 'influence functions' which is as following for single dislocation near free surface/edge:

$$G_{xxx} = y\left\{-\frac{1}{r_1^2} - \frac{2x_1^2}{r_1^4} + \frac{1}{r_2^2} + \frac{2x_2^2}{r_2^4} - \frac{4\xi x_2}{r_2^4} + \frac{4\xi^2}{r_2^4} + \frac{16\xi x_2^3}{r_2^6} - \frac{16\xi^2 x_2^2}{r_2^6}\right\}$$

$$G_{xyy} = y\left\{-\frac{1}{r_1^2} + \frac{2x_1^2}{r_1^4} + \frac{1}{r_2^2} - \frac{2x_2^2}{r_2^4} + \frac{12\xi x_2}{r_2^4} - \frac{4\xi^2}{r_2^4} - \frac{16\xi x_2^3}{r_2^6} + \frac{16\xi^2 x_2^2}{r_2^6}\right\}$$

$$G_{xxy} = -\frac{x_1}{r_1^2} + \frac{2x_1^3}{r_1^4} + \frac{x_2}{r_2^2} - \frac{2\xi}{r_2^2} - \frac{2x_2^3}{r_2^4} + \frac{16\xi x_2^2}{r_2^4} - \frac{12\xi^2 x_2}{r_2^4} - \frac{16\xi x_2^4}{r_2^6} + \frac{16\xi^2 x_2^3}{r_2^6}$$

$$G_{yxx} = -\frac{x_1}{r_1^2} + \frac{2x_1^3}{r_1^4} + \frac{x_2}{r_2^2} - \frac{2\xi}{r_2^2} - \frac{2x_2^3}{r_2^4} - \frac{8\xi x_2^2}{r_2^4} + \frac{12\xi^2 x_2}{r_2^4} + \frac{16\xi x_2^4}{r_2^6} - \frac{16\xi^2 x_2^3}{r_2^6}$$

$$G_{yyy} = +\frac{3x_1}{r_1^2} - \frac{2x_1^3}{r_1^4} - \frac{3x_2}{r_2^2} - \frac{2\xi}{r_2^2} + \frac{2x_2^3}{r_2^4} + \frac{16\xi x_2^2}{r_2^4} - \frac{12\xi^2 x_2}{r_2^4} - \frac{16\xi x_2^4}{r_2^6} + \frac{16\xi^2 x_2^3}{r_2^6}$$

$$G_{yyy} = y\left\{-\frac{1}{r_1^2} + \frac{2x_1^2}{r_1^4} + \frac{1}{r_2^2} - \frac{2x_2^2}{r_2^4} - \frac{4\xi x_2}{r_2^4} + \frac{4\xi^2}{r_2^4} + \frac{16\xi x_2^3}{r_2^6} - \frac{16\xi^2 x_2^2}{r_2^6}\right\} \qquad (6.33)$$

Where r_1, r_2 describe the position of the arbitrary point, and ξ is the distance of the dislocation off the edge or a surface, as illustrated in Figure 6.4. And Figure 6.5 shows the distribution of the stress field due to a single edge dislocation near free surface after implanting equation 6.32 and equation 6.33. Such equations can also be modified for dislocations near phase interfaces by replacing the free-

space on the left by a second material phase with different values employed for material properties such as Poisson's ratio, shear modulus and Burgers vectors.

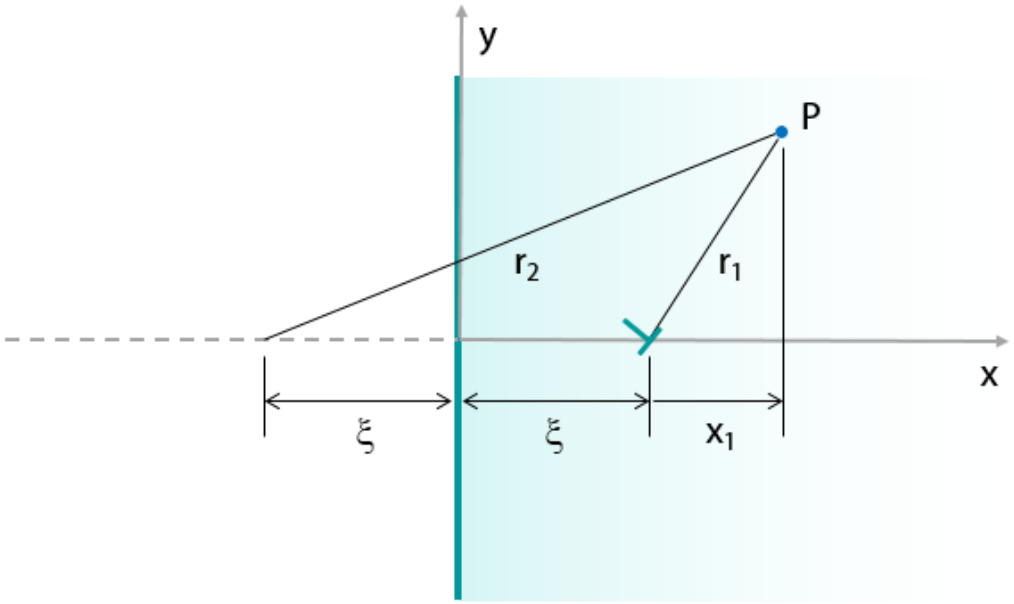

Figure 6.4 Illustration of a single dislocation at (ξ,0) near a half-plane with an arbitrary point P described by r_1 and r_2.

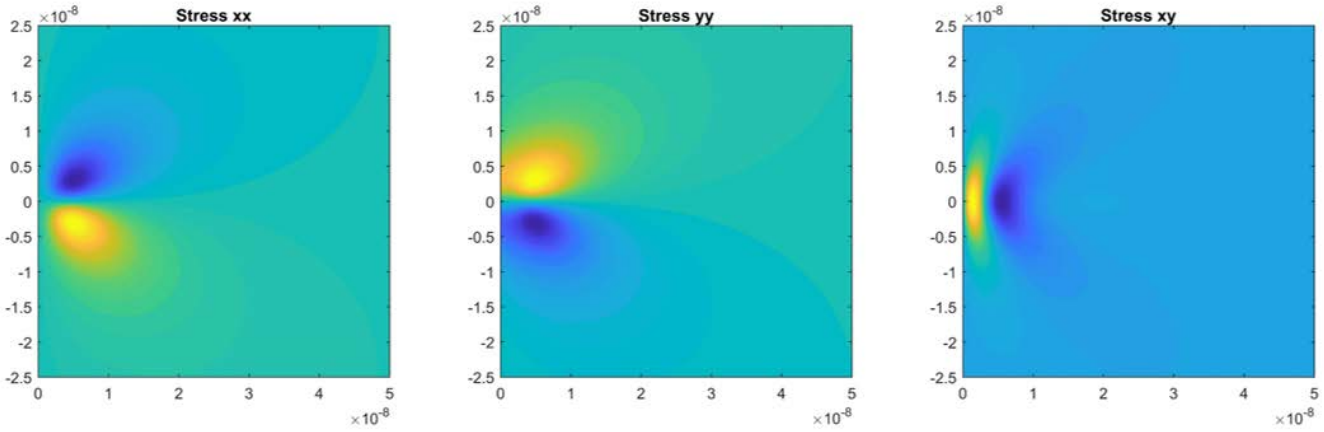

Figure 6.5 Visualization of the stress field by an edge dislocation near free surface (to the left).

6.1.3.3 Evaluation of plastic strain

The plastic strain induced by dislocation motion can be separately described as plastic strain rate tensor $\dot{\varepsilon}^p$ and the plastic spin tensor W^p given by,

$$\dot{\varepsilon}^p = \sum_{s=1}^{N_s} \frac{l_s v_{gs}}{2V} (\boldsymbol{n}_s \otimes \boldsymbol{b}_s + \boldsymbol{b}_s \otimes \boldsymbol{n}_s)$$

$$W^p = \sum_{s=1}^{N_s} \frac{l_s v_{gs}}{2V} (\boldsymbol{n}_s \otimes \boldsymbol{b}_s - \boldsymbol{b}_s \otimes \boldsymbol{n}_s) \quad (6.34)$$

Where $\boldsymbol{n}_s$ stands for a unit normal the slip plane, v_{gs} stands for the magnitude of the gliding velocity of segment s, and capital V is the volume of the RVE (representative volume element). The dislocation density tensor is given as,

$$\boldsymbol{\rho} = \sum_{s=1}^{N_s} \frac{l_s}{V} \boldsymbol{b}_s \otimes \boldsymbol{\xi}_s \quad (6.35)$$

6.1.3.4 Periodic boundary conditions and application

Many of the parameters and mechanisms of the present model can be modified for various applications. In the first case [15], the model is modified to work as an RVE of two-phase Ni-base superalloy bulk single crystal under cyclic loading, where periodic boundary conditions are applied. This is shown in Figure 6.2 (b). The dislocation sources are Frank-Read sources for edge locations which are distributed randomly in the γ matrix channels and 12 FCC <110> {111} slip systems are activated for the case. The orientation of the projected simulation plane can be modified in order to evaluate different response of the crystal due to misorientations implanted in the process of material growing.

As shown in Figure 6.6 (b), as the applied stress increases, dislocation pairs are nucleated and driven in the opposite directions by the action of forces experienced by them, and blocked at precipitate boundaries, leading to the formation of

dislocation pile-ups. During unloading some of these dislocations remain pinned, whilst others undergo reverse glide. When two dislocations with opposite Burgers vector signs approach each other travelling along the same slip trace, annihilation takes place, if the distance between the dislocations becomes smaller than the critical distance.

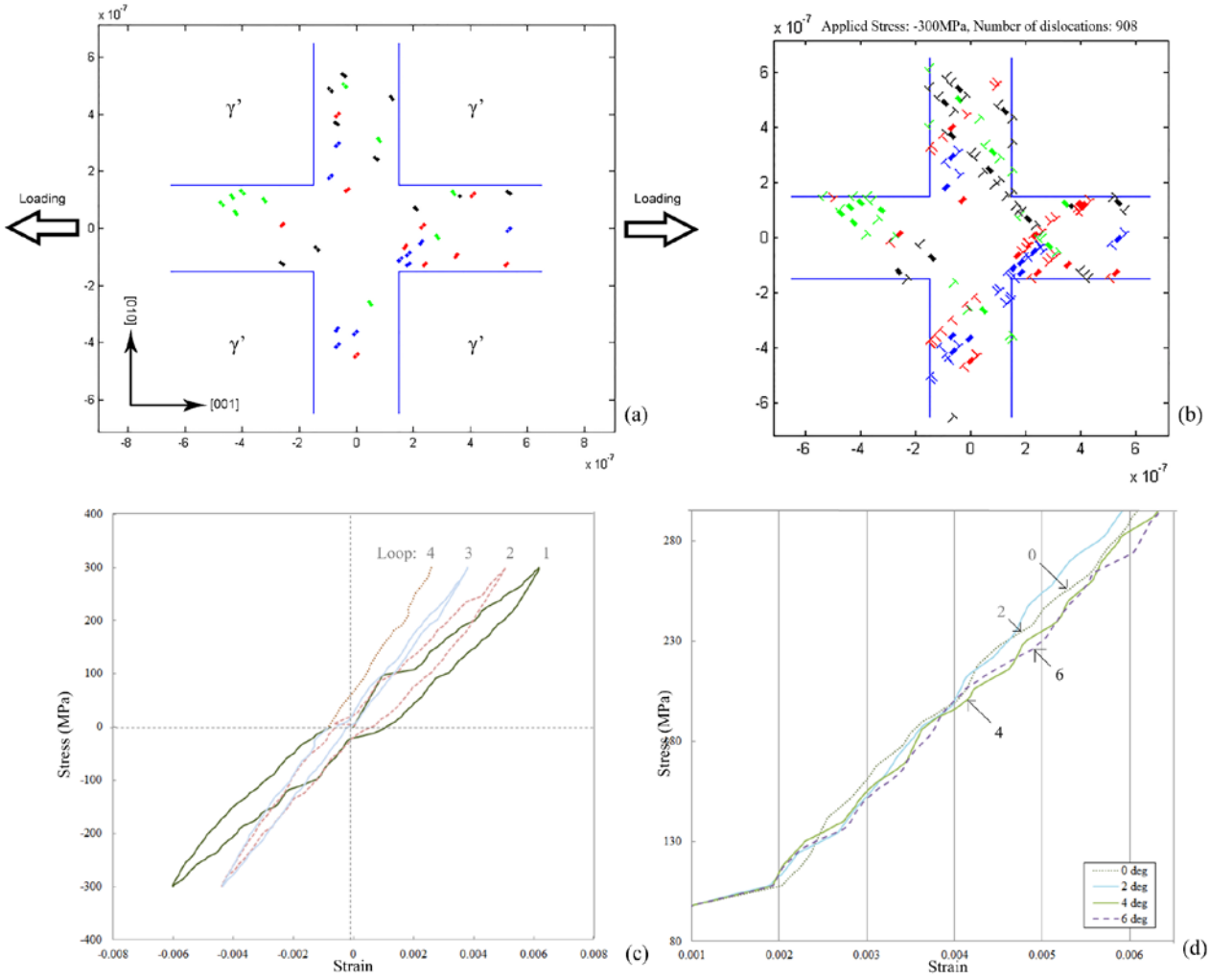

Figure 6.6 (a) Model setup for the Ni-base superalloy unit cell RVE. (b) The simulation plane snapshot of the discrete dislocation distribution within the ductile γ-phase under the maximum compressive stress of 300MPa, in the second fatigue half-loop; (c) The cyclic stress-strain curves for the RVE under cyclic loading. (d) The monotonic tensile loading curves for the RVE with different crystallographic orientations (α values).

In the present case, we consider cyclic loading at the temperature of ~700℃. The value of Young’s modulus of the γ and γ’ phase is taken to be about 100 GPa. The critical resolved shear stress (CRSS) required for the nucleation of a dislocation pair from a Frank-Read source was taken to be 50 MPa. No source hardening was assumed i.e. CRSS remained unchanged in the course of deformation. However, the multiplication and interaction of dislocations between themselves and with the obstacles created by the precipitate boundaries, resulted in apparent hardening of the system response. Figure 6.6 (c) illustrates the cyclic strain hardening observed under load-controlled fully reversed stressing (corresponding to R = -1) along the [001] direction. The amplitude of the cyclic stress applied was set to 300MPa. It is worth noting the variation of flow stress in compression after the first load reversal, which is the manifestation of the Bauschinger effect and in the context of continuum plasticity is referred to as kinematic hardening. This effect can be ascribed to dislocation interaction that causes them to become pinned within the pile-ups in so-called self-locked configurations, meaning that by the fourth cycle, no plastic deformation takes place during load reversal.

The model was used to investigate the difference in plastic deformation response, due to difference in the lattice orientation with respect to the load application direction. The monotonic response of the RVE for different α values is shown in Figure 6.6 (d). Given even the small difference in lattice orientation, the stress-strain curves appear to show some difference. Tentatively it can be reasoned that larger misorientations appear to correspond to less overall hardening at large strains.

6.1.3.5 Micropillar models

The model is later modified to a MATLAB based code with a graphic user interface (GUI) dedicated for modelling pillar compression for dual-phase crystal cases, as shown in Figure 6.7. In the revised code, the parameter of the material by phase can be specified along with the phase geometry, volume fraction value and the overall geometry and orientation of the pillar to be compressed. The model works swiftly for nano- to micropillar sizes with low computation cost and predicts precisely when compared to the experimental data.

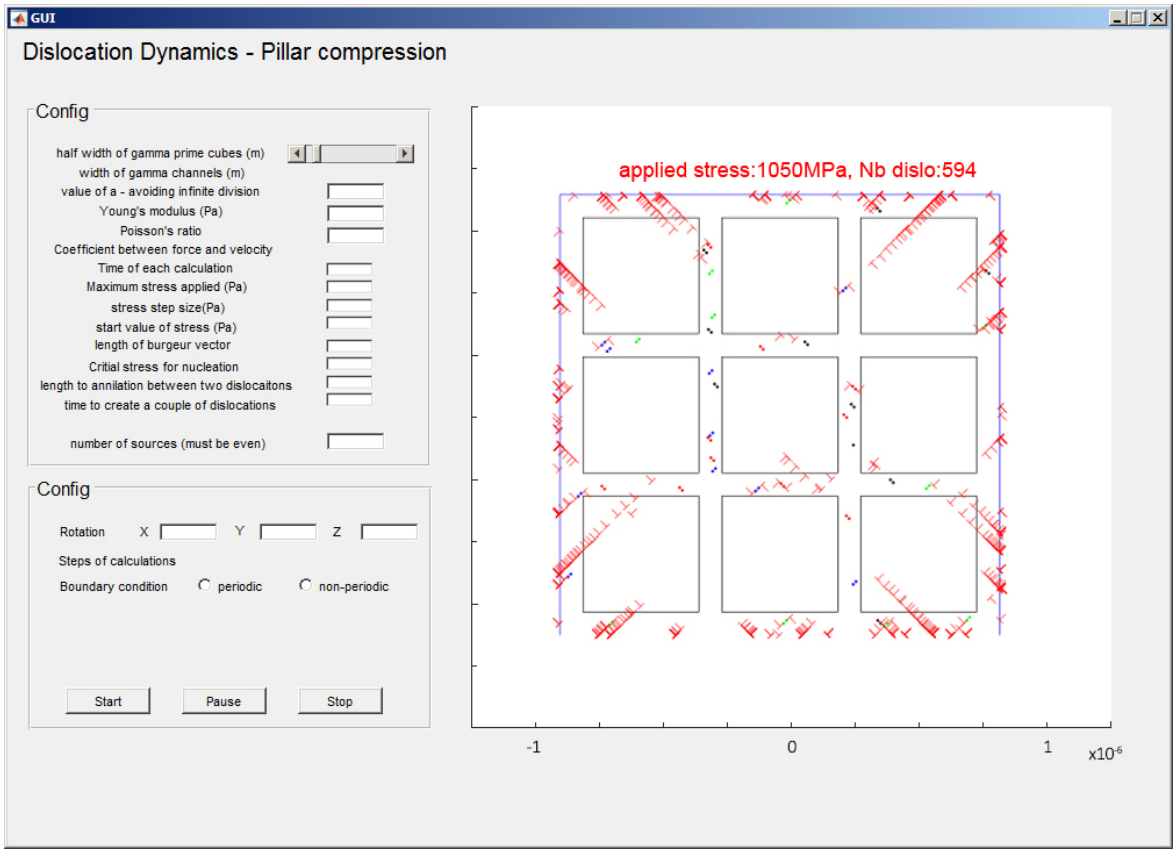

Figure 6.7 The graphic user interface (GUI) of the model code for dual-phase crystal micropillar compression tests

Notably in this version, dislocations are allowed to penetrate phase interfaces at given drag and stress trust values, and the motion of them is under adjusted law inside different phases. The upper and lower boundaries are impenetrable due to

the existence of the indenter punch and the bulk crystal, and a thin layer of interface modelling the Ga+ contaminated layer is applied to the left and right boundaries for impede the dislocations from escaping freely.

The geometry of the pillar can be altered by diameter (left-to-right span width for the simulation plane), precipitate geometry (number, size and distribution) and pillar crystallographic orientation.

Selected results comparing to the experimental data can be found in the Figure 5.18 (b) (shown as red crosses).

6.1.4 Conclusions

A computationally economical 2.5-D discrete dislocation dynamics model is presented for the simulation of a particular projection plane with all slip systems in an FCC-structured crystal. In the results presented, the model is adapted to the simulation of dual-phase Ni-base superalloy single crystals. Due to the model's flexibility, both finite small crystal geometries or bulk crystal behaviour can be simulated (the latter using periodic boundary conditions). Satisfying model results were obtained in application to Ni-base superalloys in terms of successful capturing the slip behaviour and interaction between dislocations and boundaries, and to some dependence of the plastic response on the lattice orientation. Modelling micropillar compression shows very good agreement with the experimental data points and the overall fit to them. With further development the model will be able to capture further advanced aspects of the complex material behaviour, such as larger scale dislocation structures and thermally activated dislocation cross-slip with associated crystal rotation.

6.2 Bragg coherent X-ray diffractive imaging of dual-phase Ni-base superalloy single crystals

As reviewed in §2.4.5, coherent X-ray imaging, especially combined with Bragg peak analysis (as opposed to transmission imaging), has extended the application of X-ray microscopy by providing the ability to reconstruct the phase and lattice distortion (hence full strain tensor) of the probed crystal with a resolution falling much below the probe size. It is for this reason that the method is sometimes referred to as “lenseless microscopy”. Ni-base superalloys, such as CMSX-4, which combine multi-phase structure with stored lattice strain misfit, provide a great benchmarking object for studying BCDI technique with its application to revealing mesoscale plasticity inside single crystals. This Chapter covers the background theory of the coherent X-ray diffraction method, experimental design, and a synchrotron-based BCDI experiment performed on beamline I13, Diamond Light Source, UK.

6.2.1 Fundamentals of the coherent diffractive method

6.2.1.1 Basic concepts of coherent sources

It is desired to focus radiation to a smallest spot, to minimize its divergence while maximizing its propagating distance, and to generate interference patterns, which means its phase and amplitude variation of the fields need to be well defined. However, in real life, radiation with short wavelength (such as X-ray) is only with

well-defined phase relationships over limited spatial and temporal scales, which is technically measured by its so-called coherence.

The emerging accelerator-based X-ray sources such as synchrotron, energy-recovery linacs, free-electron lasers, high-harmonic light created from intense laser pulses, etc [190–195] all, in general, emits X-ray as a coherent or partially coherent beam with low divergence. In other words, photons emitted by such techniques (sources) propagate at small angles (θ, between beam direction and propagation direction) even after scattering, which allows the adoption of paraxial approximation ($\sin\theta \approx \theta$) and the scalar formulation of diffraction theory neglecting the polarization effects.

Consider an electromagnetic field with the electric field, $E(\rho,t)$, varying with time and space expressed by a mutual coherence function (MCF),

$$\Gamma(\rho_1, \rho_2, \tau) = \langle E(\rho_1, t) E^*(\rho_2, t+\tau) \rangle \tag{6.1}$$

Where ρ is the spatial position coordinates and *t* stands for time, τ describes the time delay between the arrival of photon from ρ_1 *and* ρ_2, and the MCF as an ensemble average over the realization of the field, which is expendable to higher order with thermal, Gaussian, character, etc. To express the degree of coherence, the MCF is normalized as,

$$\gamma^1(\rho_1, \rho_2, \tau) = \frac{\Gamma(\rho_1,\rho_2,\tau)}{\sqrt{\Gamma(\rho_1,\rho_2,0)\Gamma(\rho_1,\rho_2,0)}} \tag{6.2}$$

Which can be rewritten as,

$$\gamma^1(\rho_1, \rho_2, \tau) = \frac{\langle E(\rho_1,t) E^*(\rho_2,t+\tau) \rangle}{\sqrt{\langle I(\rho_1,t)\rangle \langle I(\rho_2,t)\rangle}} \tag{6.3}$$

Hanbury-Brown and Twiss proposed an intensity correlation based coherence measurement via fourth-order field correlations (second-order intensity correlations), given as,

$$\gamma^1(\rho_1, \rho_2, \tau) = \frac{\langle E(\rho_1,t)E^*(\rho_2,t+\tau)\rangle}{\sqrt{\langle I(\rho_1,t)\rangle\langle I(\rho_2,t)\rangle}} \tag{6.4}$$

Assuming the fluctuation in the electric fields holds a Gaussian distribution, the expression is then simplified into,

$$\gamma^2(\rho, \rho, \tau) = 1 + \beta|\gamma^1(\rho, \rho, \tau)|^2 \tag{6.5}$$

Which allows the coherence measurements to be done by intensity-correlation measurement, also known as the Siegert relation, where β is a correction factor. In the case of X-ray, the experiment is measured by intensity on the detector by self-correlation of the field which is given as,

$$I(\rho) = \Gamma(\rho, \rho, 0) \tag{6.6}$$

And in the form of the cross-spectral density function as

$$W(\rho_1, \rho_2, \omega) = \int \Gamma(\rho_1, \rho_2, \tau)\exp[i\omega\tau]d\tau \tag{6.7}$$

So far, for an X-ray source which obeys Gaussian statistics, the coherence properties can be determined by the 1st order MCF (equation 6.5) and temporal coherence properties by spectral properties (equation 6.7). Nonetheless, experimental variations may also affect the accuracy of the measurement. For most practical cases, the integral is limited in a certain bandwidth of electromagnetic field, which is called quasi-monochromatic approximation giving,

$$\Gamma(\rho_1, \rho_2, \tau) \approx J(\rho_1, \rho_2,)\exp[-i\omega_0\tau] \tag{6.8}$$

Where ω_0 stands for the central angular frequency of the distribution, and *J* is the mutual optical intensity (MOI). This equation assumes a harmonic variation in time for the electric fields in the wave, and the density W can be thus rewritten as,

$$W(\rho_1, \rho_2, \omega) \approx J(\rho_1, \rho_2,)\delta(\omega - \omega_0) \tag{6.9}$$

Which assume the beam (or source) consists of only single effective frequency (or wavelength), as most of the experimental setup tried to achieve.

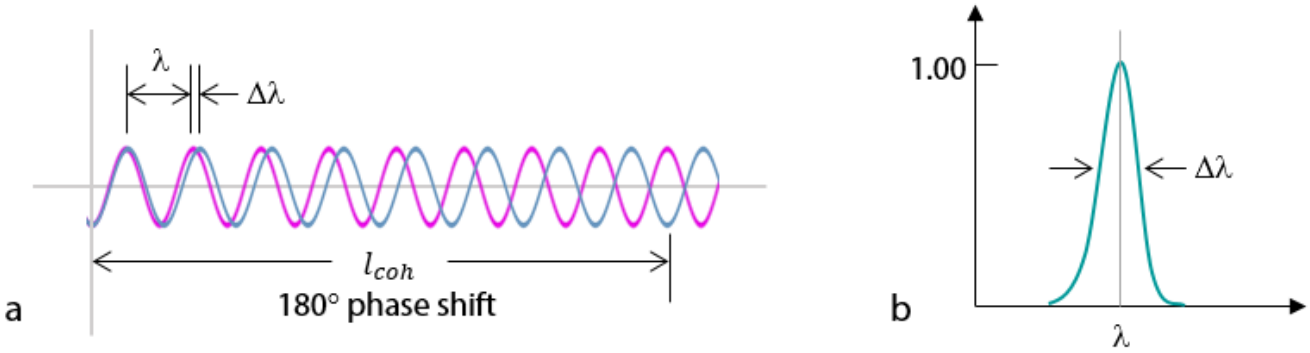

Figure 6.8 Coherence length defined by half width at half maximum (HWFM) (a) Spectral bandwidth; (b) coherence length defined as destructive interference due to finite spectral bandwidth for radiation of wavelength λ and spectral bandwidth Δλ.

To simply the definition and properties for the coherent source, the concept of coherent length is introduced as the distance over which the correlations are reduced to a certain level, which is also determined with a certain distribution of correlations. With coherent length as a parameter, we can rewrite equation 6.2 as,

$$\gamma^1(\mathrm{r}_1 - \mathrm{r}_2) = \exp[-{|\mathrm{r}_1 - \mathrm{r}_2|^2}/{l_{coh}^2}] \tag{6.10}$$

In terms of equation 6.10, the coherence length is given as the interval of spatial positions where the correlation is below the value of e^{-1}[118]. However, other definition exist such as using half width at half maximum[195], or simply 0.88 for visible lights. However, for X-ray, FWHM for the frequency distribution is mostly used which derives the longitudinal coherence length as the following,

$$\ell_c^{long} = \frac{\sqrt{\ln(2)}}{\Delta\omega} = \frac{\sqrt{\ln(2)}}{2\pi}\frac{\lambda^2}{\Delta\lambda} \tag{6.11-1}$$

More specifically for X-ray, the coherence length is given by [118] as,

$$\ell_c = \frac{2\lambda z}{\pi D} \tag{6.11-2}$$

Suppose that we measure the diffraction pattern with distribution *T(r)*, and the measured pattern recovers the complex field σ(s) somehow, given as,

$$\sigma(\boldsymbol{s}) = \int T(\boldsymbol{r})\exp[-ik\boldsymbol{s}\cdot\boldsymbol{r}]d\boldsymbol{r} \tag{6.12}$$

The mutual optical intensity (MOI) for partially coherent diffraction on a thin two-dimensional probed object can be described using equation 6.1 as,

$$J_o(r_1, r_2) = J_i(r_1, r_2,)T(r_1)T^*(r_2) \tag{6.13}$$

The propagation as transforming from object position z1 to detector position z2 at a distance of Z can thus be expressed as,

$$E(r, z_2) = -i\frac{k}{2\pi Z}\int E(r', z_1)\exp[\frac{ik}{2Z}|r' - r|^2]dr' \tag{6.14}$$

Which yields the function for the MOI for the partially coherent diffraction by thin 2d object (via equation 6.13 and 6.14) as,

$$\mathrm{J}(r_1, r_2, \mathrm{Z}) = \frac{k^2}{4\pi^2 Z^2}\int \begin{matrix} J_{in}(r_1', r_2', 0)T(r_1')T^*(r_2') \\ \times \exp[\frac{ik}{2Z}(|r_1' - r_1|^2 - |r_2' - r_2|^2)] \end{matrix} dr_1' dr_2' \tag{6.15}$$

And he measured intensity on the detector can be described as,

$$\mathrm{I}(r,\mathrm{Z}) = \frac{k^2}{4\pi^2 Z^2}\int \begin{matrix} J_{in}(r_1', r_2', 0)T(r_1')T^*(r_2') \\ \times \exp[\frac{ik}{2Z}(r_1'^2 - r_2'^2 - 2(r_1' - r_2')\cdot r] \end{matrix} dr_1' dr_2' \qquad (6.16)$$

Taking the far-zone approximation (where Z is big enough), the propagation of MOI can be simplified to,

$$J_\infty(r_1\mathbf{s}_1, r_2\mathbf{s}_2) = \frac{1}{\rho_1\rho_2}\exp[ik(\rho_2 - \rho_1)]L(\mathbf{s}_1, \mathbf{s}_2) \qquad (6.16)$$

Where L is the radiant cross intensity, $\mathbf{s_1}$ and $\mathbf{s_2}$ are the unit vectors on the direction from object to detector.

Finally, Born or Rytov approximation[196,197] is normally taken to neglect the multiple scattering effects as X-ray is mostly considered penetrating and only leave single scattering. Therefore, the far-zone intensity distribution by scattering via a 3D object can be described as a function of angle by,

$$I_{far}(\boldsymbol{s}) = \int J_{inc}(\boldsymbol{r_1}, \boldsymbol{r_2})S_3(\boldsymbol{r_1}, \boldsymbol{r_2})\exp[-ik\boldsymbol{s}\cdot(\boldsymbol{r_2} - \boldsymbol{r_1})]d\boldsymbol{r_1}d\boldsymbol{r_2} \qquad (6.17)$$

In many experiments based on the coherent methods, other approximations such as the projection approximation are used on top of equation 6.17, reviewing of which is not going to be expanded here.

6.2.1.2 Coherent diffractive imaging reconstructing algorithm

As the diffractive method of X-ray probing has expended the resolution from limited by physical optical lens to maximum diffraction angle ($\theta_{\max}$), Sayre (1952 [198]) firstly proposed the possibility that twice sampling (or oversampling) the diffraction spots can potentially reveal the complete 3D reconstruction of the probed crystal structure. Such proposal then become in practice (20 years later)

with soft X-ray for biological object in a region where there is absorption contrast between carbon and oxygen [199,200]. The Gerchberg-Saxton algorithm [201] for phase reconstruction is used since then, which is a iterative method where a consistency of the phase distribution in the probed object is found in intensity imaging and far-field diffraction image. The fitting begins by assigning a set of random phases to the support and evaluating using a fast Fourier transform as a 'first guess' of diffraction pattern in reciprocal space. The iteration then begins by overwriting the guess by measured amplitude and back transforming it to real space density, followed by real space boundary conditions such as positive value of density and transform the result to reciprocal again. Based on this so-called 'error reduction' method, which is later modified by Fienup [202–204] where only support information is used at the object plane (also known as 'input/output methods'). Later work by Miao [119,205] has taken the first practice of these ideas on X-ray diffractive imaging experiments and circumvented the deliberately missed direct beam information (by beam stopper to protect the detector) by recreating the low spatial frequency data using an electron microscope image. In general, the key fact for these algorithms is that there is a consistent object distribution with the support and the measured diffraction pattern.

Figure 6.9 shows a general outline of the reconstructing algorithm, where the error reduction method simply imposes the known support while the input/output introduce a relaxation parameter into the object-update stage making it less possible to stagnate before convergence [206]. Application of these algorithms is straight-forward and has been presented by various works [207–210]. However, the success and accurate output through such algorithms is significantly relying on skills and experiences.

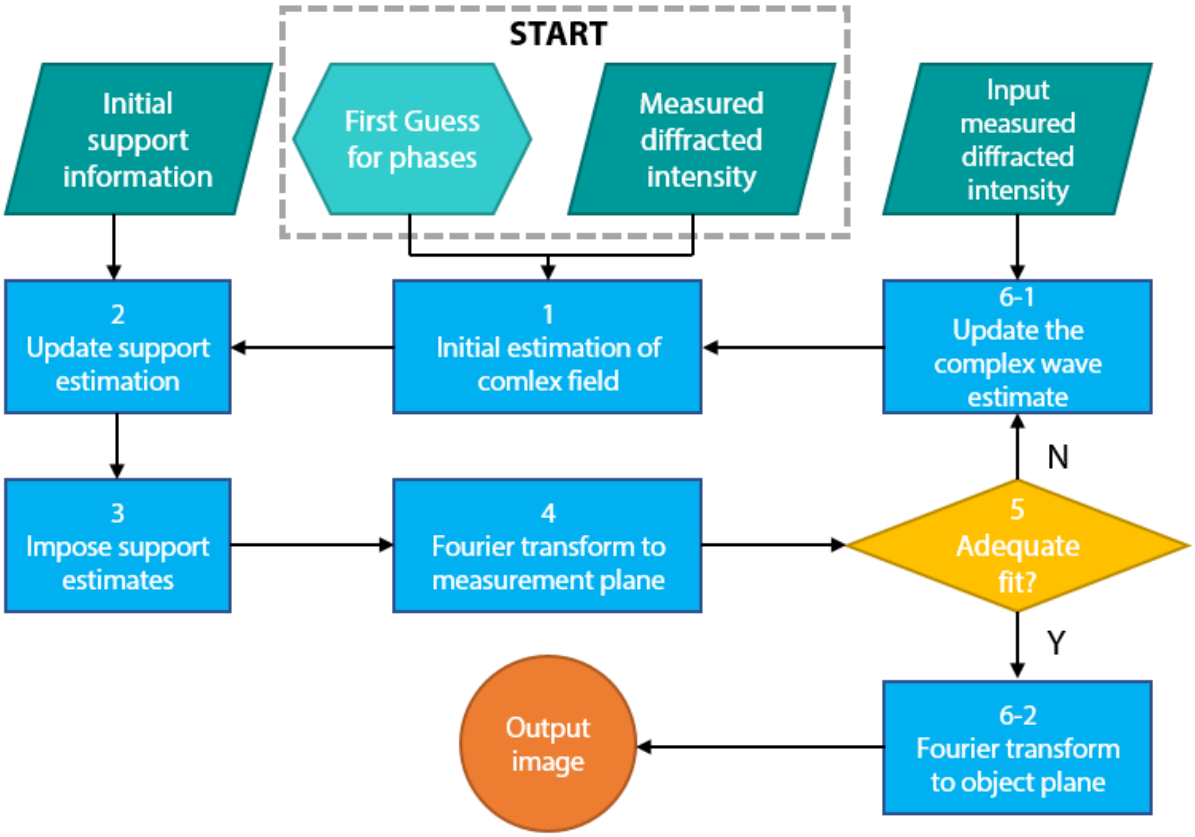

Figure 6.9 the general outline of the reconstructing algorithm

6.2.2 Experimental practices and solutions

Since early experimental work by Miao [119], a significant number of relevant works have shown interests and practices of the coherent diffractive imaging on high-resolution imaging for small biological molecules, which later works extending the simulation and reconstruction into three-dimensional objects [120,121,211,212]. Until Robinson and Vartanyants [213,214] firstly propose the idea (with partial coherence analysis) that diffraction pattern from a finite crystal

will be described as the convolution of the diffraction pattern from an infinite crystal with a shape function, which can be decomposed from each of the Bragg peaks. Three-dimensional imaging works have been presented [215] following such idea, where phase of the complex shape function reveals strain inside the crystal. Later works have developed matured techniques involving rocking the sample to obtain full 3D information of the Bragg peak in reciprocal space [116,125,126,128]. The recent development [115] of such method has reported a finest resolution as low as 5 nm. There are also variations on the coherence diffraction imaging such as keyhole diffraction imaging, with applications on bio-materials, and sources based on laser, etc, are not considered relevant to the present work hence will not be reviewed.

In almost any practice of the coherent diffraction imaging experiments, the algorithms employed is not guaranteed to converge a certain solution. Since the propagation process utilized by all the algorithms for reconstructing uses Fourier transform, which assumes that the optical field is fully coherent. Such property does normally fit with the beam generated by X-ray free-electron laser, yet rather not by 3rd generation synchrotron sources. Spence [216] published an analysis claiming that coherent patch of the light/beam needs to be twice of the width of the probed object, which gives,

$$X_c = \frac{\lambda}{\theta_c} > 2W \tag{6.18}$$

Where X_C stands for the transverse coherence width at the sample by Van-Cittert-Zernike theorem, and θ_c is the angle where the incoherently filled sources subtending angle at the sample. However, coherent length is still needed for defining the coherent patch, which is, as mentioned previously, a measurement

based on the width of the Gaussian distribution of the light field. As the far-zone intensity distribution in equation 6.17 can be rewritten according to Williams [217,218] as,

$$I_{far}(\boldsymbol{s}) = I_0 \int\int T(\boldsymbol{r} - \tfrac{\boldsymbol{x}}{2}) T^*(\boldsymbol{r} + \tfrac{\boldsymbol{x}}{2}) d\boldsymbol{r} \exp[-ik_0 \boldsymbol{s} \cdot \boldsymbol{x} - \tfrac{|\boldsymbol{x}|^2}{2\ell_c^2}] d\boldsymbol{x} \qquad (6.19)$$

From equation 6.19 it can be concluded that when coherence length is infinite ($\ell_c \to \infty$), the intensity distribution of the diffraction pattern is the Fourier transform of the autocorrelation function of the scattering distribution. And when coherence length is finite for most cases, equation 6.19 gives a convolution over intensity. This equation leads to a conclusion that even small degree of partial coherence, where the coherence length is still much greater than the object dimensions, shall make the algorithm fail to converge. Therefore, in the scenario where a zone plate is used for focusing, the spatial coherence length is required to be bigger than the zone plate, so that it is fully coherently illuminated; and the temporal coherence length should exceed path differences, meaning the monochromaticity, $\lambda/\Delta\lambda$, needs to be greater than the number of the zones in the plate. Overall requirement for the coherent method is thus a sufficient small source or at sufficient distance. With that said, most recent advances have improve the algorithm along with high-harmonic generation sources, or curved beams [127,219–221].

6.2.3 Experiment design and performance

Multi-beam Bragg coherence diffraction imaging, as reviewed, has the potential to enable the three-dimensional resolved measurement of the full lattice strain tensor, non-destructively, in micro-sized single crystals. The success of such

method, however, relies on the data collection of 3D coherent X-ray diffraction pattern and the phase-retrieval algorithm used, which iteratively invert it towards a convergent phase in real space. Such method has been used for weakly strained crystals by growth or lattice mismatch [128,129,213], and for dislocation based strain with improved algorithm [113,127]. Such applications make it curious to study Ni-base superalloy single crystals, which features a coherent dual-phase microstructure with dislocation and phase-boundary misfit induced strain distributed accordingly. The Bragg coherent diffraction imaging experiment presented in this section was proposed, designed and performed for focused ion beam fabricated micropillars out of CMSX-4 Ni-base superalloy single crystals.

6.2.3.1 Sample preparation

The samples studied in this experiment are freestanding micropillars fabricated by focused ion beam at MBLEM, University of Oxford. The pillars are allocated at the top of a sharp wedge of the bulk crystal, which is cut by Isomet cutter and polished to a EBSD ready standard with the residual stress and strain kept to a minimum. The process of sample cutting, polishing and FIB milling is similar to what has been described in previous chapters of this thesis (please refer to Table 4.1 for grinding and polishing, and Table 5.2 for FIB milling).

6.2.3.2 Experimental setup and procedures

The experiment was carried out in August 2016 on the beamline I13 of the Diamond Light Source, UK, which consists of two 250-metre long branchlines. Figure 6.10 shows the schematic for the beamline I13 with the coherence branchline (I13-1, coloured in the figure). A quadruple crystal monochromator was employed to select a monochromatic beam of energy 14.81 KeV, with the horizontal spatial coherence tuned by slits located at insertion device. The beam is thus condensed to 10 μm via a blazed zoneplate. A two-metre-long fly tube is placed in the pathway between detector and sample in order to reduce vibrational effects and allowing the long travel distance needed.

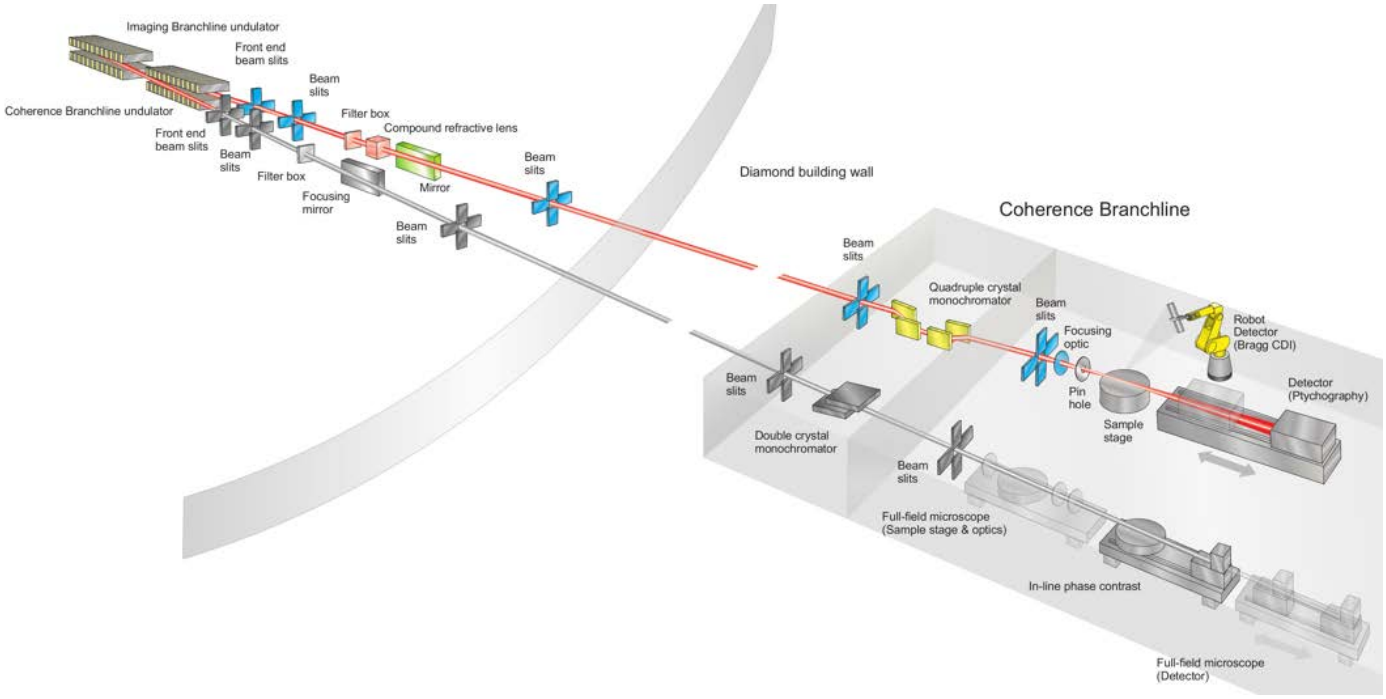

Figure 6.10 Beamline schematic for I13-1 (coloured) at Diamond Light Source [222]

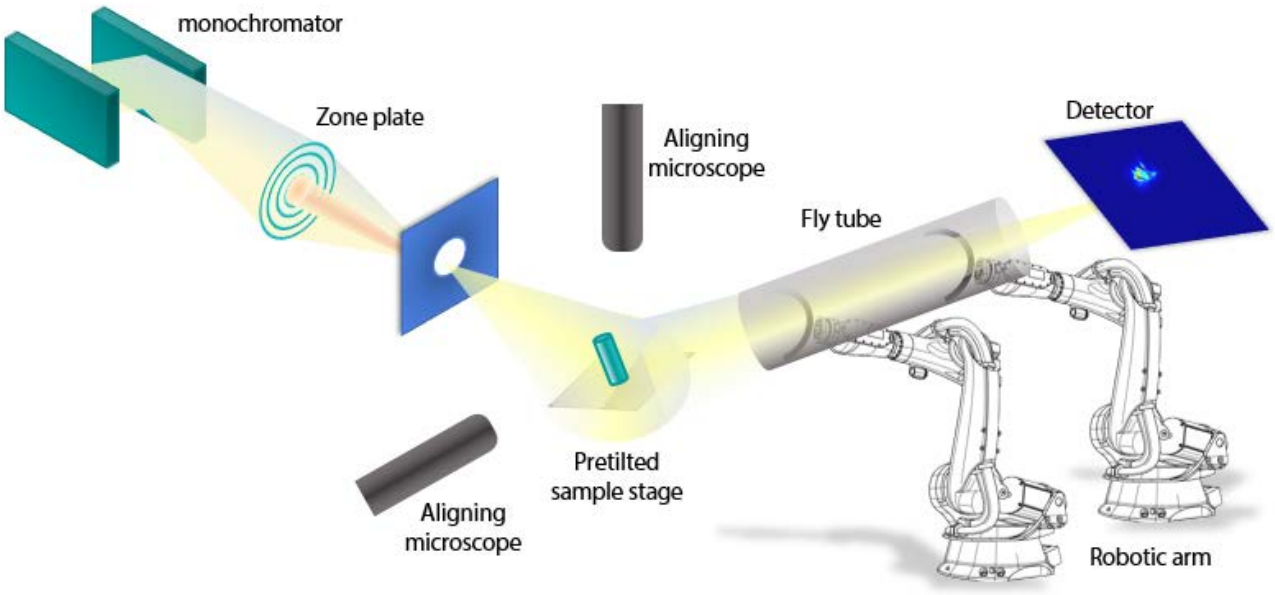

Figure 6.11 Illustration of the experimental setup of BCDI on beamline I13 at DLS.

The fly tube is grabbed both ends by two industrial robotic arms, which are programmed to perform combinational spatial positioning according to the 2θ angle of the reflection needed.

The detector used for the experiment is the Quad (512 x 512) system which consists of four (256 x 256) MERLIN Medipix3 detector chips in a two by two matrix, which is suitable for 5-17 KeV energy band and has a detector pixel size of 55 μm. The sample is glued on a SEM stub mounted on the sample goniometer and is aligned to the X-ray via optical microscopes on the side and a PCO CCD camera located downstream facing the beam.

Diffracted beam is captured by an X-ray luminescence paper taped downstream, and found by Bragg law calculations in the far field on the detector. The full information of Bragg peak in 3D is then obtain by rocking the sample stage (θ or

χ angle) by 0.05-degree angle steps and take 60 seconds exposure frame per step. The Bragg peak in reciprocal space is thus reconstructed by staking the frames and reconstructing into 3D.

6.2.4 Results and discussion

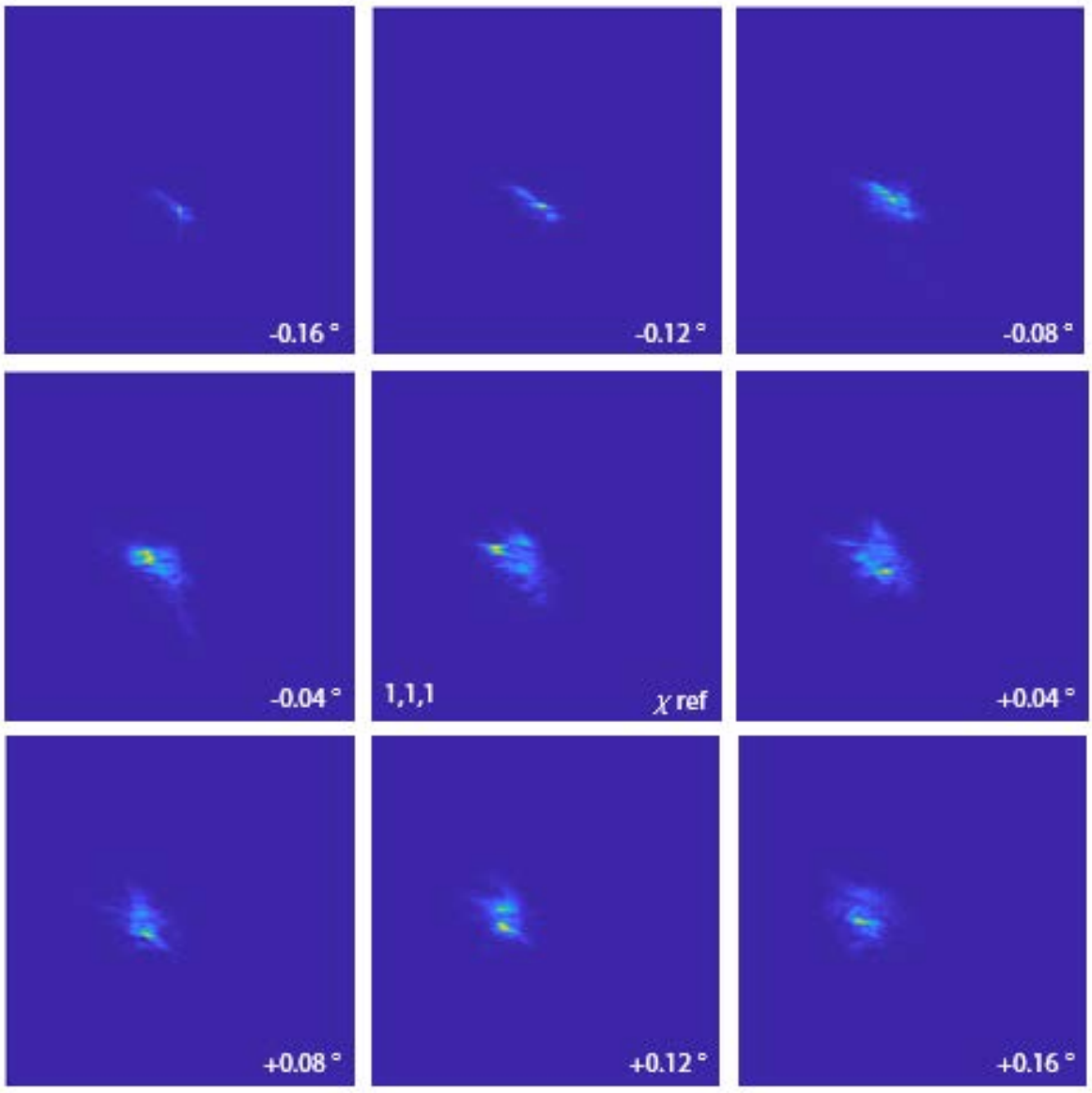

Figure 6.12 Coherent Bragg peak for <111> planes collected by rocking χ at 0.04-degree steps

Once certain reflections are collected by detector, intensity sections are taken at every 0.02-degree step rocking the χ (Figure 6.12) or θ (Figure 6.13) angle. The

angular coverage is from 0.8° (±0.4° with respect to the reflection centre) to 1.6° (±0.8°) according to the morphology (elastic or streaking) of the reflection. Multiple scans are also taken and aligned [223] for each reflection for the purpose to reduce the signal to noise level. Reflections are also collected from multiple pillars with various dimensions and stress status (compressed or not compressed).

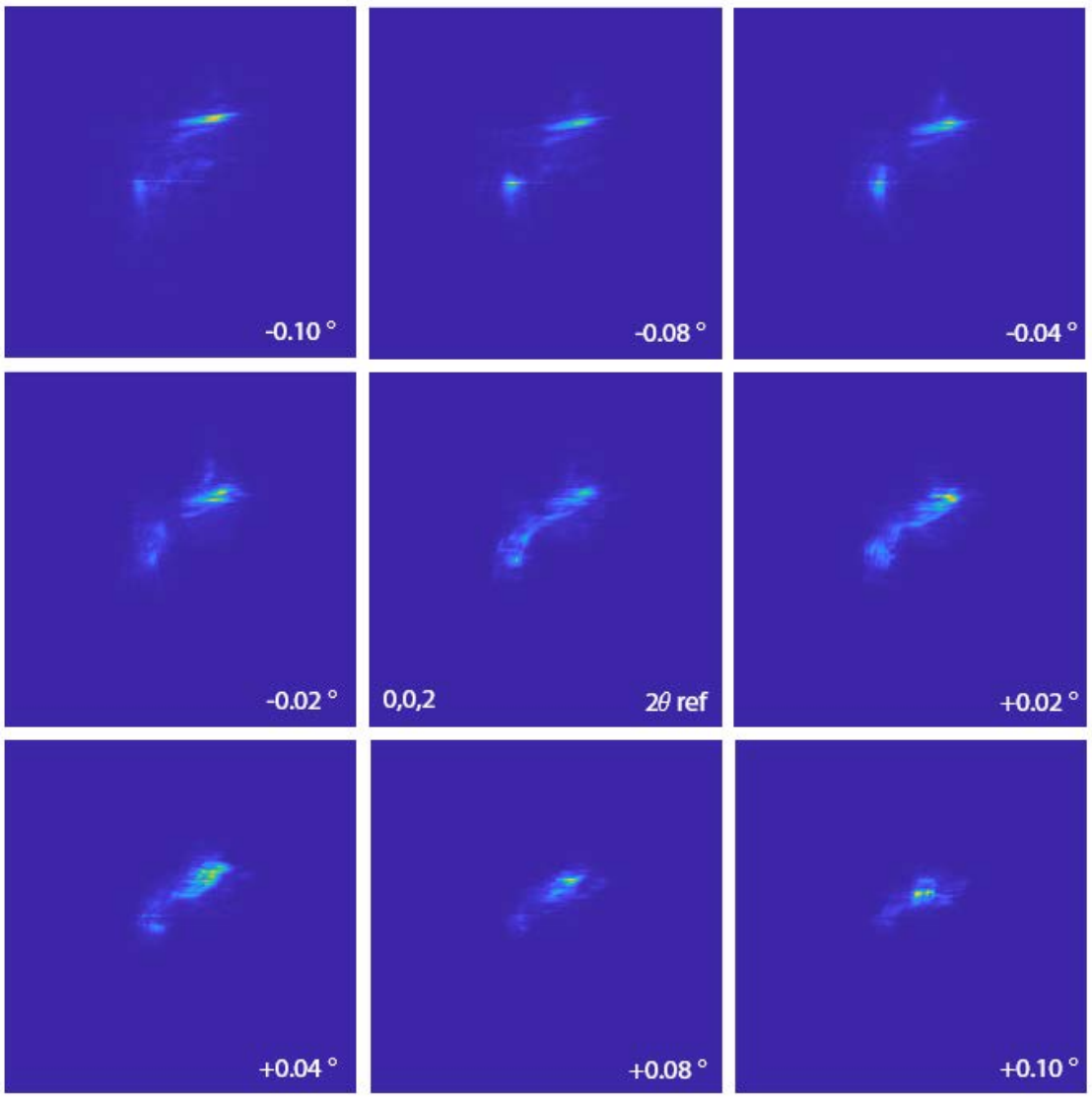

Figure 6.13 Coherent Bragg peak for <0 0 2> planes collected by rocking θ at 0.04-degree steps

The data was then processed to reduce noise and ported into Numpy [224] format for phase-retrieval algorithm application. 3D visualization of the treated coherent

diffraction Bragg peaks of different pillars and *hkl* index are as shown in Figure 6.14.

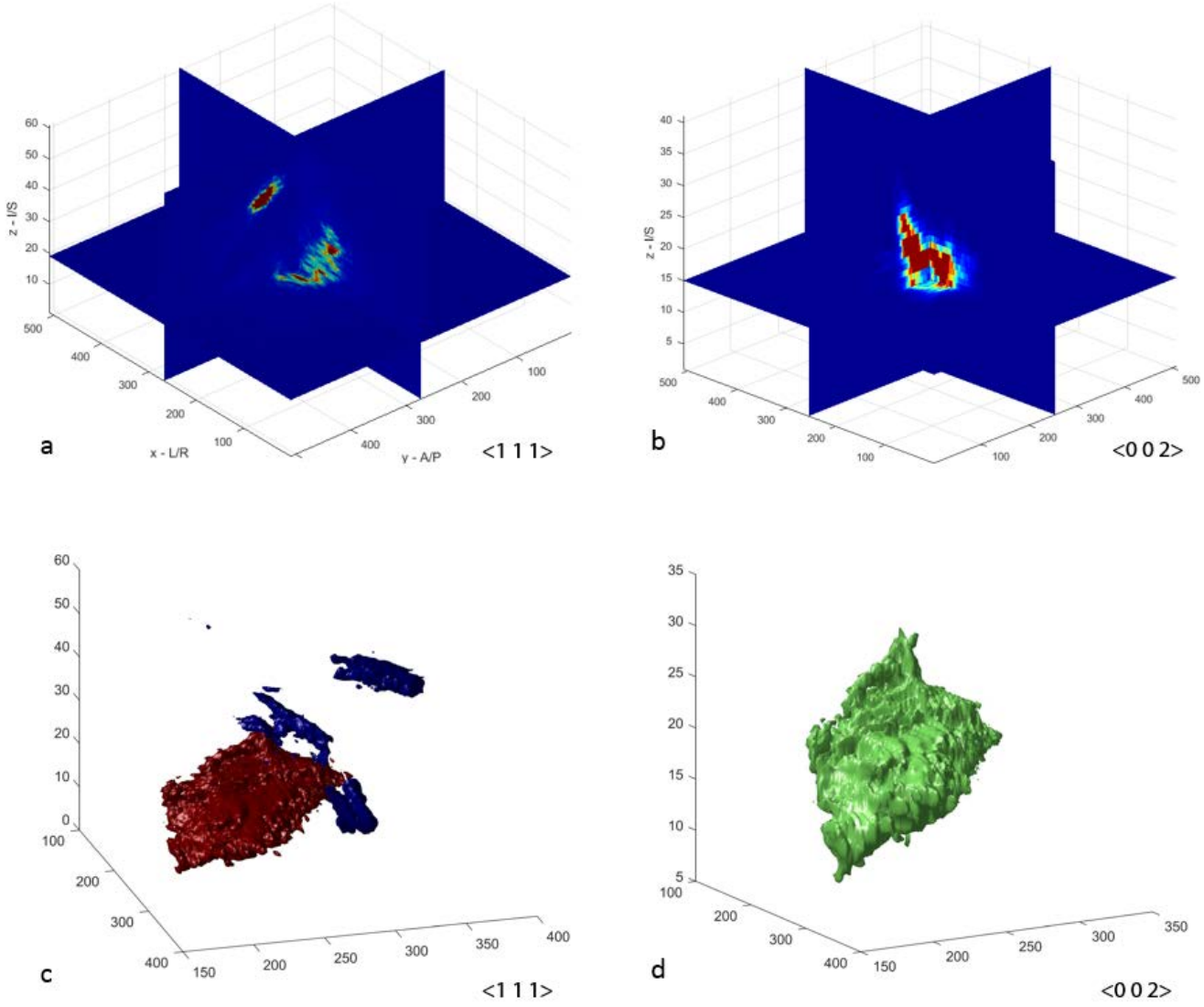

Figure 6.14 3D visualisation of the treated data. Cross sectional intensity view for (a) reflection <111> (b) reflection <002> and (c) and (d) isosurfaces, respectively.

Clear differences can be observed as frame a and c belong to the same reflection of a compressed tip of one pillar, and frame b and d belong to an uncompressed pillar. As the former one covers a larger reciprocal space volume and show at least two discrete coherent reflection centres (coloured differently) which belong to the same group of crystal planes. This is an indication that the pillar has

suffered major slips after the compression test, and the lattice parameters of the crystal planes fell into finite number of groups (indication of GNDs and GNBs distributed in the probed crystal). However, on the other reflection which belong to an uncompressed pillar, the peak is less streaked and only shows single coherent reflection centre.

6.2.5 Discussion and future work

Fundamentals of the coherent diffractive imaging method were reviewed and applied in the context of a Bragg coherent X-ray diffractive imaging experiment designed and performed to study the internal strain distribution inside FIB fabricated Ni-base superalloy single crystal micropillars.

The results obtained reveal that the experimental approach developed in the present study provides a suitable foundation platform for the study of the structure and deformation in samples with complex hierarchical internal arrangement of features. Nevertheless, although the visualisation of the Bragg peak intensity distribution in reciprocal space was successful, the data did not possess sufficient quality to allow real space interpretation required. The reasons for this outcome are multiple. Firstly, the object of investigation (two-phase Ni-base superalloy micropillar) possessed much greater complexity than the near-perfect nano-sized single crystals placed on dissimilar substrates that were chosen as objects for study in the vast majority of experiments reported in the literature (as reviewed). The internal lattice distortion fields in the present case are expected to be much more complex, creating additional challenges to interpretation. Furthermore, unlike the simple shape faceted polyhedral crystals considered elsewhere, the

FIB-milled micropillars considered in the present study were extended in the axial direction, meaning that they were not completely embedded in the incident beam. As a consequence, coherent scattering patterns did not show the characteristic fringe patterns associated with sample surface facets which greatly aid in the interpretation and result analysis. Additional limitations arose due to the complex nature of beam alignment and data collection, which demanded considerable time to be devoted to preparing the final quality data collection. Nevertheless, the results demonstrate the feasibility of this approach for the analysis of internal structure and deformation fields in complex objects such as Ni-base superalloy micropillars. With concerted effort directed at developing the experimental and interpretation procedures, the results of the present study allow confident expression of the view that further work in this direction is likely to lead to major advances in understanding in this field.

Chapter 7

Conclusions and future work

The present thesis presented the investigations of the micromechanical properties and mesoscale plasticity in Ni-base superalloy single crystals. The highlights of the results presented concern the achievements in the development of advanced electron microscopy and synchrotron-based X-ray methods and techniques. The direction of these efforts needs to be viewed in the context of theoretical analyses of the dislocation-induced size effect in two-phase single crystals, probed mechanically in the form of micropillar samples, and simulated using discrete dislocation dynamics computer models.

Advanced electron microscopy techniques utilised in this project included high resolution SEM imaging, EDS mapping, TEM imaging, and FIB milling. These were adopted as the key tools for observing and characterizing the complex multi-scale structure of Ni-base superalloy single crystal samples, as well as for finely controlled fabrication of miniature samples, such as TEM lamella and micropillars. Advances in the development and application of these techniques provided the basis for subsequent development of X-ray experimental set-ups, the results of which could be compared with the predictions of dislocation-based models.

Standardized procedures for FIB assisted micropillar fabrication and in-chamber compression testing were developed and applied for the study of CMSX-4 alloy samples. The size effect was observed for the micropillars of diameter ranging from ~200 nm up to several micrometres. Flow stress response was recorded, together with anomalies directly linked to slip activity, such as dislocation bursts.

Based on a model explicitly incorporating the finite size effect that considers both extrinsic and intrinsic length scales, a modified Hall-Petch equation (equation 3.6) was proposed for fitting the observed size effect in the flow stress. Satisfactory agreement was achieved between the fit and experimental results.

The capabilities of the micro-Laue method were studied via synchrotron-based *in situ* three-point bending tests on Ni-base superalloy beam samples. The experiments were designed to allow sub-micron X-ray probe to investigate the stress concentration around FIB-milled notch or fatigue-induced crack within the sample. The diffraction patterns were analysed in terms of the intensity distribution, and streaking and splitting of Bragg peaks to characterise the local misorientation and lattice distortions. Bragg peak morphology was also examined in 3D in reciprocal space by scanning the monochromatic beam energy of the incident X-ray beam. The result of this experimental study shows that the micro-Laue technique allows revealing the local lattice information of the probed crystal volume, and with the use of beamlines based on a modern synchrotron-based source can perform large area mapping with fine resolution.

In order to align the results from the micro-Laue with micromechanical testing, a novel dual mode X-ray microscopy and scattering setup was designed and developed for *in situ* micropillar compression testing on synchrotron beamline that enables full field X-ray transmission imaging and reflection mode micro-Laue diffraction using micro-focused X-ray beam. In this experiment, the capability of conventional X-ray illumination (not using beam coherence properties) was exploited fully. The evolution of the dislocation density, dislocation type and structure was observed during micropillar compression. The phenomenon of mechanical annealing was observed and discussed.

With the recent development of coherent diffractive imaging techniques, and the desire to push the limit of X-ray probing further, a Bragg coherent X-ray diffractive imaging experiment was designed for Ni-base superalloy pillars. The experiment was carried out on the coherent branch of beamline I13 at Diamond Light Source, UK. The coherent source was finely focused via a Fresnel zone plate, and the Ni-base superalloy single crystal micropillars were probed. Bragg peaks of different reflections were collected in 3-D in reciprocal space, treated and reconstructed via appropriate algorithms. As a first trial of the BCDI method on single crystals with complex microstructure and strain state, no existing phase-retrieval algorithm was suitable for reconstructing the strain information back to real space.

For comparing and guiding the understanding of dislocation induced plasticity inside crystals, a 2.5-D discrete dislocation dynamics model was introduced. By manipulating the boundary conditions and loading fields applied, the model benefited from the reduced dimension of analysis, whilst was still able to capture the mechanical behaviour of materials with complex microstructures in versatile applications. Simulation results produced by this model aligned well with the experimental results.

The results presented in this thesis cover several advanced experimental and modelling techniques. They reveal interesting aspects of dislocation behaviour and interaction on mesoscale plasticity inside single crystals with complex microstructure. However, due to the extremely complicated nature of the material studied, further insights into mesoscale mechanics must be sought. Therefore, the author proposes some directions for future studies, as follows:

1. Due to the limit of information resolved via the current state-of-art synchrotron-based X-ray Laue method, development of methods that can retrieve crystal structure and strain information with higher spatial resolution should be found for better understanding of the mesoscale dislocation plasticity inside crystals using advanced X-ray sources.
2. The method of diffractive imaging using X-ray sources still has its limitations since the lack of a standardized experimental setup and a widely applicable phase-retrieval algorithm. Further work needs to be invested in improving the procedures for techniques such as BCDI, to transform it from an ‘art’ experience to a well-studied and standardized microscopy tool.
3. Discrete dislocation dynamics models are useful for examining the nature of plastic flow and comparison with the experimental phenomena. With that said, there remains much to be done towards the convergence of the development of the fundamental theories and phenomenological approaches and observations.

Publications by the Author

Work presented in this thesis are also included in the publications listed below, some of which may still be under review.

1. Siqi Ying, A. M. Korsunksy, et al. On the nanostructural origins of the size effect in the compression response of single crystal Ni-base superalloy micropillars. Under review.
2. Siqi Ying, A. M. Korsunsky, et al. *In situ* micro-Laue diffraction studies on the three-point bending of a notched single crystal. Under review.
3. Siqi Ying, A. M. Korsunsky, et al. Development of dual mode X-ray experiment on micropillar compression, and advances on Bragg coherent X-ray diffraction imaging techniques. Under review.
4. S. Ying, T. Sui, et al. On the cyclic deformation and residual stress in Ni-base single crystal superalloys. Proceedings of the World Congress on Engineering 2. 2014.

Work listed below are published.

Development of synchrotron-based X-ray diffraction techniques applied on advanced engineering materials:

5. E. Salvati, AJG. Lunt, S. Ying, et al. Eigenstrain reconstruction of residual strains in an additively manufactured and shot peened nickel superalloy compressor blade. Computer Methods in Applied Mechanics and Engineering 320, 335-351, 2017.
6. RMN Fleury, D Nowell, T Sui, S Ying, et al. Characterisation of handling and service surface damage on Nickel alloys caused by low velocity impacts of blunt hard objects. Mechanics of Materials 107, 45-55, 2017.
7. T Sui, E Salvati, S Ying, et al. Strain softening of nano-scale fuzzy interfaces causes Mullins effect in thermoplastic polyurethane. Scientific Reports 7 (1), 916, 2017.

8. T Sui, K Titov, S Ying, et al. Probing the nano-scale architecture of diamond-patterned electrospun fibre mats by synchrotron small angle X-ray scattering. RSC Advances 7 (14), 8200-8204, 2017.
9. T Sui, S Ying, et al. Operando observation of the Taylor cone during electrospinning by multiple synchrotron X-ray techniques. Materials & Design 110, 933-934, 2016.
10. H Zhang, KS Fong, X Song, S Ying, et al. Synchrotron X-ray Diffraction Analysis of Bending Strains in Magnesium Alloy AZ31B Processed by Severe Plastic Deformation. Proceedings of the International MultiConference of Engineers and Computer Scientists. 2016.

Advances on X-ray microscopy and electron microscopy techniques with the applications on biomaterials and medical materials:

11. T. Sui, S. Ying, A. M. Korsunsky, G. Landini. X-ray study of human dental tissues affected by erythroblastosis fetalis. Journal of dental research 94(7), 1004-1010, 2015.
12. T. Sui, S. Ying et al, In Situ X-ray Diffraction Measurements of the Apparent Modulus of Human Dental Tissue in the Vicinity of the Dentine-Enamel Junction (DEJ). Applied Mechanics and Materials 798, 339-343, 2015.
13. T. Sui, S. Ying et al, High resolution ultrastructure imaging of fractures in human dental tissues. Theoretical and Applied Mechanics Letters 4 (4), 2014.
14. O Roberts, AJG Lunt, S Ying et al, A study of phase transformation at the surface of a zirconia ceramic. Proceedings of the world congress on engineering 2, 2014.
15. AJG Lunt, G Mohanty, S Ying et al. A comparative transmission electron microscopy, energy dispersive x-ray spectroscopy and spatially resolved micropillar compression study of the yttria partially stabilised zirconia-porcelain interface in dental prosthesis. Thin Solid Films 596, 222-232, 2015.
16. A Lunt, A Terry, S Ying, et al. Characterisation of nanovoiding in dental porcelain using small angle neutron scattering and transmission electron microscopy. Dental Materials 33 (5), 486-497, 2017.

Advances in electron microscopy techniques for the research on novel materials:

17. B. Song, T. Sui, S. Ying, L. Li, L. Lu, A. M. Korsunsky. Nano-structural changes in Li-ion battery cathodes during cycling revealed by FIB-SEM serial sectioning tomography. Journal of Materials Chemistry A 3 (35), 18171-18179, 2015.
18. Y. Sheng, X. Wang, K. Fujisawa, S. Ying, et al. Photoluminescence segmentation within individual hexagonal monolayer tungsten disulphide domains grown by chemical vapor deposition. ACS Applied Materials & Interfaces 9 (17), 15005-15014, 2017.
19. NW Khun, EM Mahdi, S. Ying, et al. Fine-scale tribological performance of zeolitic imidazolate framework (ZIF-8) based polymer nanocomposite membranes. APL Materials 2 (12), 124101, 2014.
20. L. R. Brandt, E. Salvati, C Papadaki, H Zhang, S Ying, et al. Probing the deformation and fracture properties of Cu/W nano-multilayers by in situ SEM and synchrotron XRD strain microscopy. Surface and Coatings Technology 320, 158-167, 2017.
21. T. Sui, H. Zhang, S. Ying et al. FIB-SEM serial sectioning nano- tomography of flax fibres. Proceedings of the International Multi-Conference of Engineers and Computer Science. 2015.

Development of Multi-beam engineering microscopy for material research:

22. AJG Lunt, N Baimpas, E Salvati, IP Dolbnya, T Sui, S Ying, et al. A state-of-the-art review of micron-scale spatially resolved residual stress analysis by FIB-DIC ring-core milling and other techniques. The Journal of Strain Analysis for Engineering Design 50 (7), 426-444, 2015.
23. E Salvati, T Sui, S Ying, et al. On the accuracy of residual stress evaluation from Focused Ion Beam DIC (FIB-DIC) ring-core milling experiments. Proceedings of the 5th international conference on nanotechnology: fundamentals and applications. 2014.
24. AM Korsunsky, T Sui, J Dluhoš, S Ying, et al. Multi-beam engineering microscopy-a versatile tool for optimal materials design. Proc IMCECS 2, 2015.

25. H Zhang, E Salvati, S Ying, et al. Effect of Pt Deposition on Digital Image Correlation Analysis for Residual Stress Measurement Using FIB-DIC Ringcore Method. Proceedings of the World Congress on Engineering 2. 2016.
26. H Zhang, M Senn, T Sui, A Lunt, LR Brandt, C Papadaki, S Ying, et al. On the Upper and Lower Bounds of Correlation Window Size in Digital Image Correlation Analysis. Proceedings of the World Congress on Engineering 1, 2017.

References

[1] R.C. Reed, The Superalloy Fundamentals and Applications, Cambridge University Press, 2006.

[2] M. Segersäll, Nickel-Based Single-Crystal Superalloys temperature properties, 2013.

[3] D. Leidermark, Crystal plasticity and crack initiation in a single-crystal nickel-base superalloy Modelling , evaluation and applications, 2011.

[4] A. Sato, Nickel-based single crystal superalloys for industrial gas turbines, Mater. Res. (2011).

[5] MTU Aero Engines, PurePower ® PW1000G Engine, (2017). http://www.mtu.de/fileadmin/EN/7_News_Media/2_Media/Brochures/Engines/PW1000G.pdf (accessed October 3, 2017).

[6] K. Harris, J.B. Wahl, Improved single crystal superalloys, CMSX-4 (SLS) [La+Y] and CMSX-486, Superalloys 2004 (Tenth Int. Symp. (2004) 45–52.

[7] A.K. Jena, M.C. Chaturvedi, Review The role of alloying elements in the design of nickel-base superalloys, J. Mater. Sci. 19 (1984) 3121–3139.

[8] R.C. Reed, T. Tao, N. Warnken, Alloys-By-Design: Application to nickel-based single crystal superalloys, Acta Mater. 57 (2009) 5898–5913. doi:10.1016/j.actamat.2009.08.018.

[9] P. Li, B.M. Zhou, Y.Z. Zhou, J.G. Li, T. Jin, X.F. Sun, Z.F. Zhang, Effect of orientations on in situ tensile deformation and fracture behaviours of nickel-base single-crystal superalloys, Philos. Mag. 94 (2014) 2426–2446. doi:10.1080/14786435.2014.914261.

[10] T.P. Gabb, J. Gayda, R. V Miner, Orientation and Temperature Dependence of Some Mechanical Properties of the Single-Crystal Nickel-Base Superalloy Ren6 N4 : Part I1 . Low Cycle Fatigue Behavior, Metall. Trans. A. 17 (1986) 491–496.

[11] R.P. Dalal, C.R. 'ihcmas, L.E. Dardi, The effect of crystallographic orientation on the physical and mechanical properties of an investment cast single crystal nickel-base superalloy, (n.d.).

[12] R.L. Amaro, S.D. Antolovich, R.W. Neu, A. Staroselsky, On thermo-mechanical fatigue in single crystal Ni-base superalloys, Procedia Eng. 2 (2010) 815–824. doi:10.1016/j.proeng.2010.03.088.

[13] A. Scholz, Y. Wang, S. Linn, C. Berger, R. Znajda, Modeling of mechanical properties of alloy CMSX-4, Mater. Sci. Eng. A. 510511 (2009) 278–283. doi:10.1016/j.msea.2008.04.103.

[14] N. Matan, D.. C. Cox, M.. A. Rist, C.M.. M.F. Rae, R.. Reed, N. Matan, D.. C. Cox, M.. A. Rist, C.M.. M.F. Rae, Creep of CMSX-4 superalloy single crystals: effects of rafting at high temperature, Acta Mater. 47 (1999) 3367–

3381. doi:10.1016/S1359-6454(99)00217-7.

[15] S. Ying, T. Sui, A.J.G. Lunt, R.C. Reed, A.M. Korsunsky, On the Clyclic Deformation and Residual Stress in Ni-base Single Crystal Superalloys, in: Proc. World Congr. Eng., 2014.

[16] P.H. Thornton, Cross slip in phases having the L12 structure, Metall. Trans. 3 (1972) 291–300. doi:10.1007/BF02680608.

[17] S.-J. Liang, D.P. Pope, The yield stress of L12 ordered alloys, Acta Metall. 25 (1977) 485–493. doi:10.1016/0001-6160(77)90188-2.

[18] T. Tsuno, S. Shimabayashi, K. Kakehi, C.M.F. Rae, R.C. Reed, Tensile/compression asymmetry in yield and creep strengths of Ni-base superalloys, in: Superalloys, TMS, 2008: pp. 433–442.

[19] T. Saburi, T. Hamana, S. Nenno, H. Pak, Temperature and Orientation Dependence of the Yield Strength of Ni3 (Al, W), Jpn. J. Appl. Phys. 16 (1977) 267–272.

[20] G. Saada, P. VeyssiÈre, Kear-Wilsdorf Locks and Mechanical Properties of L12 Alloys, MRS Proc. 288 (1992) 411. doi:10.1557/PROC-288-411.

[21] B. Song, T. Sui, S. Ying, L. Li, L.L. Lu, A.M.A.M.A.M. Korsunsky, Nano-structural changes in Li-ion battery cathodes during cycling revealed by FIB-SEM serial sectioning tomography, J. Mater. Chem. A. 3 (2015). doi:10.1039/c5ta04151a.

[22] A. Lunt, A. Terry, S. Ying, N. Baimpas, T. Sui, S. Kabra, J. Kelleher, S. King, N.T. Khin, A.M. Korsunsky, Characterisation of nanovoiding in dental porcelain using small angle neutron scattering and transmission electron microscopy, Dent. Mater. (2016). doi:10.1016/j.dental.2017.02.005.

[23] A.J.G. Lunt, G. Mohanty, S. Ying, J. Dluhoš, T. Sui, T.K. Neo, J. Michler, A.M. Korsunsky, A comparative transmission electron microscopy, energy dispersive x-ray spectroscopy and spatially resolved micropillar compression study of the yttria partially stabilised zirconia - Porcelain interface in dental prosthesis, Thin Solid Films. 596 (2015). doi:10.1016/j.tsf.2015.07.070.

[24] L. Romano Brandt, E. Salvati, C. Papadaki, H. Zhang, S. Ying, E. Le Bourhis, I. Dolbnya, T. Sui, A.M. Korsunsky, Probing the deformation and fracture properties of Cu/W nano-multilayers by in situ SEM and synchrotron XRD strain microscopy, Surf. Coatings Technol. (2016). doi:10.1016/j.surfcoat.2017.01.065.

[25] A.M. Korsunsky, T. Sui, J. Dluhoš, S. Ying, A.J.G. Lunt, B. Song, E. Salvati, H. Zhang, T. Kim, S.M. Kreynin, Multi-beam engineering microscopy - A versatile tool for optimal materials design, in: Lect. Notes Eng. Comput. Sci., 2015.

[26] A. Lunt, A. Terry, S. Ying, N. Baimpas, T. Sui, S. Kabra, J. Kelleher, S. King, N.T. Khin, A.M. Korsunsky, Characterisation of nanovoiding in dental porcelain using small angle neutron scattering and transmission electron microscopy, Detntal Mater. (2017) 486–497.

doi:10.1016/j.dental.2017.02.005.

[27] T. Sui, S. Ying, G. Landini, A.M. Korsunsky, High resolution ultrastructure imaging of fractures in human dental tissues, Theor. Appl. Mech. Lett. 4 (2014). doi:10.1063/2.1404107.

[28] K.D. Vernon-Parry, Scanning Electron Microscopy: an introduction, III-Vs Rev. 13 (2000).

[29] A. Rother, K. Scheerschmidt, Relativistic effects in elastic scattering of electrons in TEM, Ultramicroscopy. 109 (2009) 154–160. doi:10.1016/j.ultramic.2008.08.008.

[30] J.J. Friel, X-ray and Image Analysis in Electron Microscopy, 2nd ed., Princeton Gamma-Tech, 2003.

[31] Y. Sheng, X. Wang, K. Fujisawa, S. Ying, A. Laura Elias, Z. Lin, W. Xu, Y. Zhou, A.M. Korsunsky, H. Bhaskaran, M. Terrones, J.H. Warner, A.L. Elias, Z. Lin, W. Xu, Y. Zhou, A.M. Korsunsky, H. Bhaskaran, M. Terrones, J.H. Warner, Photoluminescence Segmentation within Individual Hexagonal Monolayer Tungsten Disulfide Domains Grown by Chemical Vapor Deposition, ACS Appl. Mater. Interfaces. 9 (2017) 15005–15014. doi:10.1021/acsami.6b16287.

[32] J. Melngailis, Focused ion beam technology and applications, J. Vac. Sci. Technol. B Microelectron. Process. Phenom. 5 (1987) 469–495. doi:10.1116/1.2366617.

[33] L.A. Giannuzzi, F.A. Stevie, Introduction to focused ion beams : instrumentation, theory, techniques, and practice, Springer, 2005.

[34] S. Reyntjens, R. Puers, A review of focused ion beam applications in microsystem technology, J. Micromechanics Microengineering. 11 (2001) 287–300.

[35] A.J.. Lunt, N. Baimpas, E. Salvati, I.P. Dolbnya, T. Sui, S. Ying, H. Zhang, A.K. Kleppe, J. Dluhoš, A.M. Korsunsky, A state-of-the-art review of micron-scale spatially resolved residual stress analysis by FIB-DIC ring-core milling and other techniques, J. Strain Anal. Eng. Des. 50 (2015). doi:10.1177/0309324715596700.

[36] E. Salvati, T. Sui, A.J.G.G. Lunt, A.M. Korsunsky, The effect of eigenstrain induced by ion beam damage on the apparent strain relief in FIB-DIC residual stress evaluation, Mater. Des. 92 (n.d.) 649–658. doi:10.1016/j.matdes.2015.12.015.

[37] T. Sui, H. Zhang, S. Ying, P. O'Brien, A.M. Korsunsky, FIB-SEM serial sectioning nanotomography of flax fibres, in: Lect. Notes Eng. Comput. Sci., 2015.

[38] A.M. Korsunsky, M. Sebastiani, E. Bemporad, Focused ion beam ring drilling for residual stress evaluation, Mater. Lett. 63 (2009) 1961–1963. doi:10.1016/j.matlet.2009.06.020.

[39] A.M. Korsunsky, M. Sebastiani, E. Bemporad, Residual stress evaluation at the micrometer scale: Analysis of thin coatings by FIB milling and digital

image correlation, Surf. Coatings Technol. 205 (2010) 2393–2403. doi:10.1016/j.surfcoat.2010.09.033.

[40] H. Zhang, E. Salvati, S. Ying, A. Lunt, T. Sui, A.M. Korsunsky, Effect of Pt deposition on digital image correlation analysis for residual stress measurement using FIB-DIC ringcore method, in: Lect. Notes Eng. Comput. Sci., 2016.

[41] E. Bemporad, M. Brisotto, L.E. Depero, M. Gelfi, A.M. Korsunsky, A.J.G. Lunt, M. Sebastiani, A critical comparison between XRD and FIB residual stress measurement techniques in thin films, Thin Solid Films. 572 (2014) 224–231. doi:10.1016/j.tsf.2014.09.053.

[42] A.M. Korsunsky, Residual elastic strain due to laser shock peening: modelling by eigenstrain distribution, J. Strain Anal. Eng. Des. 41 (2006). doi:10.1243/03093247JSA141.

[43] M. Sebastiani, K.E. Johanns, E.G. Herbert, F. Carassiti, G.M. Pharr, A novel pillar indentation splitting test for measuring fracture toughness of thin ceramic coatings, Philos. Mag. 95 (2015) 1928–1944. doi:10.1080/14786435.2014.913110.

[44] M.D. Uchic, D.M. Dimiduk, J.N. Florando, W.D. Nix, Sample Dimensions Influence Strength and Crystal Plasticity, Science. 305 (2004). doi:10.1126/science.1098993.

[45] H. Fei, A. Abraham, N. Chawla, H. Jiang, Evaluation of Micro-Pillar Compression Tests for Accurate Determination of Elastic-Plastic Constitutive Relations, J. Appl. Mech. 79 (2012) 61011. doi:10.1115/1.4006767.

[46] C.P.P. Frick, B.G.G. Clark, S. Orso, A.S.S. Schneider, E. Arzt, Size effect on strength and strain hardening of small-scale [1 1 1] nickel compression pillars, Mater. Sci. Eng. A. 489 (2008) 319–329. doi:10.1016/j.msea.2007.12.038.

[47] J.R. Greer, W.C. Oliver, W.D. Nix, Size dependence of mechanical properties of gold at the micron scale in the absence of strain gradients, Acta Mater. 53 (2005) 1821–1830. doi:10.1016/j.actamat.2004.12.031.

[48] M.D. Uchic, P.A. Shade, D.M. Dimiduk, Plasticity of Micrometer-Scale Single Crystals in Compression, Annu. Rev. Mater. Res. 39 (2009) 361–386. doi:10.1146/annurev-matsci-082908-145422.

[49] S. Il Baik, X. Yin, D.N. Seidman, Correlative atom-probe tomography and transmission electron microscope study of a chemical transition in a spinel on an oxidized nickel-based superalloy, Scr. Mater. 68 (2013) 909–912. doi:10.1016/j.scriptamat.2013.02.025.

[50] A. Lunt, G. Mohanty, S. Ying, J. Dluhoš, T. Sui, T. Neo, A Correlative Microscopy Study of the Zirconia-Porcelain Interface in Dental Prostheses: TEM, EDS and Micro-pillar Compression, Surf Coat Tech,. (2015).

[51] J.R. Greer, W.D. Nix, Nanoscale gold pillars strengthened through dislocation starvation, Phys. Rev. B - Condens. Matter Mater. Phys. 73

(2006) 1–6. doi:10.1103/PhysRevB.73.245410.

[52] J.R. Greer, C.R. Weinberger, W. Cai, Comparing the strength of f.c.c. and b.c.c. sub-micrometer pillars: Compression experiments and dislocation dynamics simulations, Mater. Sci. Eng. A. 493 (2008) 21–25. doi:10.1016/j.msea.2007.08.093.

[53] S. Brinckmann, J.Y. Kim, J.R. Greer, Fundamental differences in mechanical behavior between two types of crystals at the nanoscale, Phys. Rev. Lett. 100 (2008) 1–4. doi:10.1103/PhysRevLett.100.155502.

[54] Q. Sun, Q. Guo, X. Yao, L. Xiao, J.R. Greer, J. Sun, Size effects in strength and plasticity of single-crystalline titanium micropillars with prismatic slip orientation, Scr. Mater. 65 (2011) 473–476. doi:10.1016/j.scriptamat.2011.05.033.

[55] Z.W. Shan, R.K. Mishra, S.A. Syed Asif, O.L. Warren, A.M. Minor, Mechanical annealing and source-limited deformation in submicrometre-diameter Ni crystals., Nat. Mater. 7 (2008) 115–119. doi:10.1038/nmat2085.

[56] K.S. Ng, A.H.W. Ngan, Stochastic nature of plasticity of aluminum micro-pillars, Acta Mater. (2008). doi:10.1016/j.actamat.2007.12.016.

[57] D.M. Dimiduk, T.A.T. Parthasarathy, M.D. Uchic, T.A.T. Parthasarathy, Size-affected single-slip behavior of pure nickel microcrystals, Acta Mater. 53 (2005) 4065–4077. doi:10.1016/j.actamat.2005.05.023.

[58] E.O. Hall, The Deformation and Ageing of Mild Steel: III Discussion of Results, Proc. Phys. Soc. Sect. B. 64 (1951) 747–753. doi:10.1088/0370-1301/64/9/303.

[59] N.J. Petch, The Cleavage Strength of Polycrystals, J. Iron Steel Inst. 173 (1953) 25–28.

[60] S.S. Brenner, Plastic Deformation of Copper and Silver Whiskers, J. Appl. Phys. . 28 (1957) 1023–9. doi:10.1063/1.1722294.

[61] S.S. Brenner, Tensile Strength of Whiskers, J. Appl. Phys. 27 (1956) 1484–41301. doi:10.1063/1.1992666.

[62] L. Nicola, E. Van Der Giessen, A. Needleman, 2D dislocation dynamics in thin metal layers, Mater. Sci. Eng. A. 309–310 (2001) 274–277. doi:10.1016/S0921-5093(00)01690-7.

[63] B. von Blanckenhagen, P. Gumbsch, E. Arzt, Dislocation sources and the flow stress of polycrystalline thin metal films, Philos. Mag. Lett. 83 (2003) 1–8. doi:10.1080/0950083021000050287.

[64] D.J. Dunstan, A.J. Bushby, The scaling exponent in the size effect of small scale plastic deformation, Int. J. Plast. 40 (2013) 152–162. doi:10.1016/j.ijplas.2012.08.002.

[65] A. Hunter, H. Kavuri, M. Koslowski, A continuum plasticity model that accounts for hardening and size effects in thin films, Model. Simul. Mater. Sci. Eng. 18 (2010). doi:10.1088/0965-0393/18/4/045012.

[66] O. Torrents Abad, J.M. Wheeler, J. Michler, A.S. Schneider, E. Arzt, Temperature-dependent size effects on the strength of Ta and W micropillars, Acta Mater. 103 (2016) 483–494. doi:10.1016/j.actamat.2015.10.016.

[67] E. Arzt, SIZE EFFECTS IN MATERIALS DUE TO MICROSTRUCTURAL AND DIMENSIONAL CONSTRAINTS: A COMPARATIVE REVIEW, Acta Mater. 46 (1999). doi:10.1016/S0957-5820(99)70836-0.

[68] E. Van der Giessen, A. Needleman, Discrete dislocation plasticity: a simple planar model, Model. Simul. Mater. Sci. Eng. 3 (1995) 689–735. doi:10.1088/0965-0393/3/5/008.

[69] R.J. Arnodeo, N.M. Ghoniem, Dislocation dynamics. I. A proposed methodology for deformation micromechanics, Phys. Rev. B. 41 (1990).

[70] J. Ldpinoux, L.P. Kubin, The dynamic organization of dislocation structures: A simulation, Scr. Metall. . 21 (1987) 833–838.

[71] Kobe University Repository : Kernel Discrete Dislocation Dynamics Simulation of Interfacial Dislocation Network in, 11 (2016) 73–80.

[72] S.M. Hafez Haghighat, G. Eggeler, D. Raabe, Effect of climb on dislocation mechanisms and creep rates in γ′-strengthened Ni base superalloy single crystals: A discrete dislocation dynamics study, Acta Mater. 61 (2013) 3709–3723. doi:10.1016/j.actamat.2013.03.003.

[73] G. Gaucherin, F. Hofmann, J.P. Belnoue, A.M. Korsunsky, Crystal plasticity and hardening: A dislocation dynamics study, Procedia Eng. 1 (2009) 241–244. doi:10.1016/j.proeng.2009.06.057.

[74] J.A. El-Awady, Unravelling the physics of size-dependent dislocation-mediated plasticity., Nat. Commun. 6 (2015) 5926. doi:10.1038/ncomms6926.

[75] A.A. Benzerga, Y. Brechet, A. Needleman, E. Van Der Giessen, Incorporating three-dimensional mechanisms into two-dimensional dislocation dynamics, Model. Simul. Mater. Sci. Eng. 12 (2004) 159–196. doi:10.1088/0965-0393/12/1/014.

[76] M. Verdier, M. Fivel, I. Groma, Mesoscopic scale simulation of dislocation dynamics in fcc metals: Principles and applications, Model. Simul. Mater. Sci. Eng. 6 (1999) 755–770. doi:10.1088/0965-0393/6/6/007.

[77] K.W. Schwarz, Simulation of dislocations on the mesoscopic scale. I. Methods and examples, J. Appl. Phys. 85 (1999) 108–119. doi:10.1063/1.369429.

[78] a Arsenlis, W. Cai, M. Tang, M. Rhee, T. Oppelstrup, G. Hommes, T.G. Pierce, V. V Bulatov, Enabling strain hardening simulations with dislocation dynamics, Model. Simul. Mater. Sci. Eng. 15 (2007) 553–595. doi:10.1088/0965-0393/15/6/001.

[79] A.A. Benzerga, N.F. Shaver, Scale dependence of mechanical properties of single crystals under uniform deformation, Scr. Mater. 54 (2006) 1937–1941. doi:10.1016/j.scriptamat.2006.02.003.

[80] V.S. Deshpande, A. Needleman, E. Van Der Giessen, Plasticity size effects in tension and compression of single crystals, J. Mech. Phys. Solids. 53 (2005) 2661–2691. doi:10.1016/j.jmps.2005.07.005.

[81] J.A. El-Awady, M. Wen, N.M. Ghoniem, The role of the weakest-link mechanism in controlling the plasticity of micropillars, J. Mech. Phys. Solids. 57 (2009) 32–50. doi:10.1016/j.jmps.2008.10.004.

[82] S.I. Rao, D.M. Dimiduk, T.A. Parthasarathy, M.D. Uchic, M. Tang, C. Woodward, Athermal Mechanisms of Size-Dependent Crystal Flow Gleaned from Three-Dimensional Discrete Dislocation Simulations, (2008).

[83] J. Senger, D. Weygand, P. Gumbsch, O. Kraft, Discrete dislocation simulations of the plasticity of micro-pillars under uniaxial loading, Scr. Mater. 58 (2008) 587–590. doi:10.1016/j.scriptamat.2007.11.031.

[84] D. Weygand, M. Poignant, P. Gumbsch, O. Kraft, Three-dimensional dislocation dynamics simulation of the influence of sample size on the stress-strain behavior of fcc single-crystalline pillars, Mater. Sci. Eng. A. 483–484 (2008) 188–190. doi:10.1016/j.msea.2006.09.183.

[85] Y. Cui, G. Po, N. Ghoniem, Temperature insensitivity of the flow stress in body-centered cubic micropillar crystals, Acta Mater. 108 (2016) 128–137. doi:10.1016/j.actamat.2016.02.008.

[86] W.L. Bragg, The structure of some crystals as indicated by their diffraction of X-rays, Proc. R. Soc. A Math. Phys. Eng. Sci. 89 (1913) 248–277. doi:10.1098/rspa.1913.0083.

[87] W. Friedrich, P. Knipping, M. Laue, Interferenzerscheinungen bei Röntgenstrahlen, Ann. Phys. 346 (1913) 971–988. doi:10.1002/andp.19133461004.

[88] C. Hammond, J. Bernstein, G.R. Desiraju, J.R. Helliwell, T. Mak, P. Muller, P. Paufler, H. Schenk, P. Spadon, D. Viterbo, The Basics of Crystallography and Diffraction, 3rd ed., Oxford University Press, 2009. doi:10.1088/0957-0233/13/2/708.

[89] V. Sass, U. Glatzel, Anisotropic creep properties of the nickel-base superalloy CMSX-4, 44 (1996) 1967–1977.

[90] J.-S. Chung, G.E. Ice, Automated indexing for texture and strain measurement with broad-bandpass x-ray microbeams, J. Appl. Phys. Appl. Phys. Lett. J. Appl. Phys. 86 (1999). doi:10.1063/1.3625316.

[91] G.E. Ice, J.W.L. Pang, Tutorial on x-ray microLaue diffraction, Mater. Charact. 60 (2009) 1191–1201. doi:10.1016/j.matchar.2009.07.006.

[92] M.A. Krivoglaz, Theory of x-ray and thermal neutron scattering by real crystals., Springer, 1969.

[93] R.I. Barabash, G.E. Ice, F.J. Walker, Quantitative microdiffraction from deformed crystals with unpaired dislocations and dislocation walls, J. Appl. Phys. 93 (2003) 1457–3173. doi:10.1063/1.1534378.

[94] G.E. Ice, R.I. Barabash, Chapter 79 White Beam Microdiffraction and

Dislocations Gradients, Dislocations in Solids. 13 (2007) 499–601. doi:10.1016/S1572-4859(07)80011-8.

[95] F.R.N. Nabarro, J.P. Hirth, Dislocation in Solids, 2007. doi:10.1017/CBO9781107415324.004.

[96] O.M. Barabash, S.S. Babu, J.M. Vitek, S.A. David, G.E. Ice, R.I. Barabash, Unusual Dislocation Density Oscillations after Local Melting and, TMS Lett. (2005).

[97] O.M. Barabash, S.S. Babu, S.A. David, J.M. Vitek, R.I. Barabash, Deformation in the heat affected zone during spot welding of a nickel-based single crystal, J. Appl. Phys. 94 (2003) 738–742. doi:10.1063/1.1579863.

[98] B.C. Larson, A. El-Azabz, W. Yangx, J.Z. Tischlery, W. Liu{, G.E. Icey, Experimental characterization of the mesoscale dislocation density tensor, Philos. Mag. 87 (2007) 8–9. doi:10.1080/14786430600943930.

[99] M. Wilkens, The Determination of Density and Distribution of DisIocations in Deformed Single Crystals from Broadened X-Ray Diffraction Profiles, Phys. Stat. Sol. 2 (1970) 359–370.

[100] W. Pantleon, N. Hansen, Dislocation boundaries - The distribution function of disorientation angles, Acta Mater. 49 (2001) 1479–1493. doi:10.1016/S1359-6454(01)00027-1.

[101] W. Pantleon, Disorientations in dislocation structures: Formation and spatial correlation, J. Mater. Res. 17 (2002) 2433–2441. doi:10.1557/JMR.2002.0355.

[102] R. Madec, B. Devincre, L.P. Kubin, From Dislocation Junctions to Forest Hardening, Phys. Rev. Lett. 89 (2002) 255508. doi:10.1103/PhysRevLett.89.255508.

[103] B.J. Claessens, S.B. van der Geer, G. Taban, E.J.D. Vredenbregt, O.J. Luiten, Ultracold Electron Source, Phys. Rev. Lett. 95 (2005) 164801. doi:10.1103/PhysRevLett.95.164801.

[104] W.A. de Heer, A. Ch telain, D. Ugarte, A Carbon Nanotube Field-Emission Electron Source, Science. 270 (1995) 1179–1180. doi:10.1126/science.270.5239.1179.

[105] R.P. Winarski, M. V. Holt, V. Rose, P. Fuesz, D. Carbaugh, C. Benson, D. Shu, D. Kline, G. Brian Stephenson, I. McNulty, J. Maser, A hard X-ray nanoprobe beamline for nanoscale microscopy, J. Synchrotron Radiat. 19 (2012) 1056–1060. doi:10.1107/S0909049512036783.

[106] G.E. Ice, J.D. Budai, J.W.L. Pang, The Race to X-ray Microbeam and Nanobeam Science, Science. 334 (2011) 1234–1239. doi:10.1126/science.1202366.

[107] M. Holt, R. Harder, R. Winarski, V. Rose, Nanoscale Hard X-Ray Microscopy Methods for Materials Studies *, Annu. Rev. Mater. Res. 43 (2013) 183–211. doi:10.1146/annurev-matsci-071312-121654.

[108] J. Kirz, C. Jacobsen, The history and future of X-ray microscopy, J. Phys.

Conf. Ser. 186 (2009) 12001. doi:10.1088/1742-6596/186/1/012001.

[109] C.G. Schroer, O. Kurapova, J. Patommel, P. Boye, J. Feldkamp, B. Lengeler, M. Burghammer, C. Riekel, L. Vincze, A. Van Der Hart, M. Küchler, Hard X-ray nanoprobe based on refractive X-ray lenses, in: AIP Conf. Proc., 2007: pp. 1295–1298. doi:10.1063/1.2436301.

[110] H. Mimura, S. Handa, T. Kimura, H. Yumoto, D. Yamakawa, H. Yokoyama, S. Matsuyama, K. Inagaki, K. Yamamura, Y. Sano, K. Tamasaku, Y. Nishino, M. Yabashi, T. Ishikawa, K. Yamauchi, Breaking the 10 nm barrier in hard-X-ray focusing, Nat. Phys. 6 (2010) 122–125. doi:10.1038/nphys1457.

[111] R.L. Sandberg, A. Paul, D.A. Raymondson, S. Hädrich, D.M. Gaudiosi, J. Holtsnider, R.I. Tobey, O. Cohen, M.M. Murnane, H.C. Kapteyn, C. Song, J. Miao, Y. Liu, F. Salmassi, Lensless diffractive imaging using tabletop coherent high-harmonic soft-X-ray beams, Phys. Rev. Lett. 99 (2007) 1–4. doi:10.1103/PhysRevLett.99.098103.

[112] P. Thibault, V. Elser, X-Ray Diffraction Microscopy, Annu. Rev. Condens. Matter Phys. 1 (2010) 237–55. doi:10.1146/annurev-conmatphys-070909-104034.

[113] J. Clark, X. Huang, R. Harder, I. Robinson, High-resolution three-dimensional partially coherent diffraction imaging, Nat. Commun. 3 (2012). doi:10.1038/ncomms1994.

[114] S.J.L. Billinge, I. Levin, The Problem with Determining Atomic Structure at the Nanoscale, 561 (2007). doi:10.1126/science.1135080.

[115] C.G. Schroer, P. Boye, J.M. Feldkamp, J. Patommel, A. Schropp, A. Schwab, S. Stephan, M. Burghammer, S. Schöder, C. Riekel, Coherent X-Ray Diffraction Imaging with Nanofocused Illumination, Phys. Rev. Lett. 101 (2008). doi:10.1103/PhysRevLett.101.090801.

[116] Huang X, Harder R, Xiong G, Shi X, Robinson I, Propagation uniqueness in three-dimensional coherent diffractive imaging, Phys. Rev. B. 83 (2011).

[117] R. Harder, M. Liang, Y. Sun, Y. Xia, I.K. Robinson, Imaging of complex density in silver nanocubes by coherent x-ray diffraction, New J. Phys. 12 (2010).

[118] K.A. Nugent, Coherent methods in the X-ray sciences, Adv. Phys. 59 (2009) 1–99. doi:10.1080/00018730903270926.

[119] J. Miao, P. Charalambous, J. Kirz, D. Sayre, Extending the methodology of X-ray crystallography to allow imaging of micrometre-sized non-crystalline specimens, Nature. 400 (1999) 342–344.

[120] J. Miao, T. Ishikawa, B. Johnson, E.H. Anderson, B. Lai, K.O. Hodgson, High resolution 3D x-ray diffraction microscopy, Phys. Rev. Lett. 89 (2002) 88303. doi:10.1103/PhysRevLett.89.088303.

[121] H.N. Chapman, A. Barty, S. Marchesini, A. Noy, S.P. Hau-Riege, C. Cui, M.R. Howells, R. Rosen, H. He, J.C.H. Spence, U. Weierstall, T. Beetz, C. Jacobsen, D. Shapiro, High-resolution ab initio three-dimensional x-ray

diffraction microscopy, J. Opt. Soc. Am. A. 23 (2006) 1179. doi:10.1364/JOSAA.23.001179.

[122] Y. Takahashi, N. Zettsu, Y. Nishino, R. Tsutsumi, E. Matsubara, T. Ishikawa, K. Yamauchi, Three-dimensional electron density mapping of shape-controlled nanoparticle by focused hard X-ray diffraction microscopy, Nano Lett. 10 (2010) 1922–1926. doi:10.1021/nl100891n.

[123] S.O. Hruszkewycz, M. V. Holt, C.E. Murray, J. Bruley, J. Holt, A. Tripathi, O.G. Shpyrko, I. Mcnulty, M.J. Highland, P.H. Fuoss, A. Tripathi, O.G. Shpyrko, I. McNulty, M.J. Highland, P.H. Fuoss, Quantitative nanoscale imaging of lattice distortions in epitaxial semiconductor heterostructures using nanofocused X-ray Bragg projection ptychography, Nano Lett. 12 (2012) 5148–5154. doi:10.1021/nl303201w.

[124] M. Dierolf, A. Menzel, P. Thibault, P. Schneider, C.M. Kewish, R. Wepf, O. Bunk, F. Pfeiffer, Ptychographic X-ray computed tomography at the nanoscale, Nature. 467 (2010) 436–439. doi:10.1038/nature09419.

[125] G.J. Williams, M.A. Pfeifer, I.A. Vartanyants, I.K. Robinson, Three-Dimensional Imaging of Microstructure in Au Nanocrystals, (n.d.). doi:10.1103/PhysRevLett.90.175501.

[126] M.C. Newton, S.J. Leake, R. Harder, I.K. Robinson, Three-dimensional imaging of strain in a single ZnO nanorod, Nat. Mater. 9 (2009). doi:10.1038/NMAT2607.

[127] J.N. Clark, J. Ihli, A.S. Schenk, Y.-Y. Kim, A.N. Kulak, J.M. Campbell, G. Nisbet, F.C. Meldrum, I.K. Robinson, Three-dimensional imaging of dislocation propagation during crystal growth and dissolution, Nat. Mater. 14 (2015) 780–784.

[128] M.A. Pfeifer, G.J. Williams, I.A. Vartanyants, R. Harder, I.K. Robinson, Three-dimensional mapping of a deformation field inside a nanocrystal, Nature. 442 (2006). doi:10.1038/nature04867.

[129] R. Harder, M.A. Pfeifer, G.J. Williams, I.A. Vartaniants, I.K. Robinson, Orientation variation of surface strain, Phys. Rev. B. 76 (2007). doi:10.1103/PhysRevB.76.115425.

[130] A.S. Schneider, D. Kiener, C.M. Yakacki, H.J. Maier, P.A. Gruber, N. Tamura, M. Kunz, A.M. Minor, C.P. Frick, Influence of bulk pre-straining on the size effect in nickel compression pillars, Mater. Sci. Eng. A. 559 (2013) 147–158. doi:10.1016/j.msea.2012.08.055.

[131] W.D. Nix, H. Gao, Indentation size effects in crystalline materials: A law for strain gradient plasticity, J. Mech. Phys. Solids. 46 (1998) 411–425. doi:10.1016/S0022-5096(97)00086-0.

[132] E.P. Busso, F.T. Meissonnier, N.P. O'Dowd, Gradient-dependent deformation of two-phase single crystals, J. Mech. Phys. Solids. 48 (2000) 2333–2361. doi:10.1016/S0022-5096(00)00006-5.

[133] D.J. Dunstan, Validation of a phenomenological strain-gradient plasticity theory, 839 (2016). doi:10.1080/09500839.2016.1215605.

[134] J. Hütsch, E.T. Lilleodden, The influence of focused-ion beam preparation technique on microcompression investigations: Lathe vs. annular milling, Scr. Mater. 77 (2014) 49–51. doi:10.1016/j.scriptamat.2014.01.016.

[135] B. Girault, A.S. Schneider, C.P. Prick, E. Arzt, Strength effects in micropillars of a dispersion strengthened superalloy, Adv. Eng. Mater. 12 (2010) 385–388. doi:10.1002/adem.201000089.

[136] R. Maaß, M.D. Uchic, In-situ characterization of the dislocation-structure evolution in Ni micro-pillars, Acta Mater. 60 (2012) 1027–1037. doi:10.1016/j.actamat.2011.11.007.

[137] A.M. Korsunsky, J. Guénolé, E. Salvati, T. Sui, M. Mousavi, A. Prakash, E. Bitzek, Quantifying eigenstrain distributions induced by focused ion beam damage in silicon, 2016. doi:10.1016/j.matlet.2016.08.111.

[138] N.A. Protasova, I.L. Svetlov, M.B. Bronfin, N. V. Petrushin, Lattice-parameter misfits between the γ and γ′ phases in single crystals of nickel superalloys, Phys. Met. Metallogr. 106 (2008) 495–502. doi:10.1134/S0031918X08110094.

[139] J.X. Zhang, T. Murakumo, Y. Koizumi, T. Kobayashi, H. Harada, S. Masaki, Interfacial dislocation networks strengthening a fourth-generation single-crystal TMS-138 superalloy, Metall. Mater. Trans. A. 33 (2002) 3741–3746. doi:10.1007/s11661-002-0246-7.

[140] C.A. Volkert, E.T. Lilleodden, Size effects in the deformation of sub-micron Au columns, Philos. Mag. 86 (2006) 5567–5579. doi:10.1080/14786430600567739.

[141] T.L. Li, Y.F. Gao, H. Bei, E.P. George, Indentation Schmid factor and orientation dependence of nanoindentation pop-in behavior of NiAl single crystals, J. Mech. Phys. Solids. 59 (2011) 1147–1162. doi:10.1016/j.jmps.2011.04.003.

[142] M. Zhang, F. Li, L. Wang, S. Wang, Investigations of inhomogeneous mechanical properties and plastic deformations in HIPed P/M nickel-base superalloy FGH96 by using micro-indentation methods, Mater. Sci. Eng. A. 556 (2012) 233–245. doi:10.1016/j.msea.2012.06.081.

[143] T. Hiroshi, A note on the finite width corrections to the stress intensity factor, Eng. Fract. Mech. 3 (1971) 345–347. doi:10.1016/0013-7944(71)90043-9.

[144] T.T. Zhu, B. Ehrler, X.D. Hou, A.J. Bushby, Analysis of the inverse square-root size effect in the plasticity of metals, (n.d.).

[145] D.J. Dunstan, A.J. Bushby, Grain size dependence of the strength of metals: The Hall-Petch effect does not scale as the inverse square root of grain size, Int. J. Plast. 53 (2014) 56–65. doi:10.1016/j.ijplas.2013.07.004.

[146] Y. Li, A.J. Bushby, D.J. Dunstan, The Hall–Petch effect as a manifestation of the general size effect, Proc. R. Soc. London A Math. Phys. Eng. Sci. 472 (2016).

[147] J. Petit, M. Bornert, F. Hofmann, O. Robach, J.S. Micha, O. Ulrich, C. Le Bourlot, D. Faurie, A.M. Korsunsky, O. Castelnau, Combining Laue

microdiffraction and digital image correlation for improved measurements of the elastic strain field with micrometer spatial resolution, in: Procedia IUTAM, 2012: pp. 133–143. doi:10.1016/j.piutam.2012.05.015.

[148] F. Hofmann, B. Abbey, W. Liu, R. Xu, B.F. Usher, E. Balaur, Y. Liu, X-ray micro-beam characterization of lattice rotations and distortions due to an individual dislocation., Nat. Commun. 4 (2013) 2774. doi:10.1038/ncomms3774.

[149] F. Hofmann, B. Abbey, X. Song, I. Dolbnya, A.M. Korsunsky, Intragranular Lattice Misorientation Mapping By Synchrotron X-Ray Micro-Beams: Laue Vs Energy-Resolved Laue Vs Monochromatic Reciprocal Space Analysis, Int. J. Mod. Phys. B. 24 (2010) 279–287. doi:10.1142/S0217979210064216.

[150] I.A. Treninkov, A.A. Alekseev, D. V. Zaitsev, Structure of Reciprocal Lattice Sites of a Single-Crystal Ni-Based Superalloy, Phys. Met. Metallogr. 113 (2012) 938–946. doi:10.1134/S0031918X12100146.

[151] X. Song, F. Hofmann, A.M. Korsunsky, Dislocation-based plasticity model and micro-beam Laue diffraction analysis of polycrystalline Ni foil: A forward prediction, Philos. Mag. 90 (2010) 3999–4011. doi:10.1080/14786435.2010.502149.

[152] D.L. Source, Beamline Schematic - Materials - Diamond Light Source, (n.d.). http://www.diamond.ac.uk/Beamlines/Materials/B16/schematic.html (accessed August 30, 2017).

[153] DEBEN, In-situ Tensile & Compression stages for SEM - Deben UK – SEM accessories & tensile testing, (n.d.). http://deben.co.uk/tensile-testing/sem/ (accessed August 30, 2017).

[154] R. Jenkins, R.L. Snyder, Diffraction Theory, in: Introd. to X-Ray Powder Diffractometry, John Wiley & Sons, Inc., Hoboken, NJ, USA, 1996: pp. 47–95. doi:10.1002/9781118520994.ch3.

[155] Z.P. Bažant, Scaling of Structural Strength, 2005. doi:10.1016/B978-0-7506-6849-1.X5000-7.

[156] Z.P. Baz Ïant, Z.P. Bažant, Size effect on structural strength: a review, Arch. Appl. Mech. 69 (1999) 703–725. doi:10.1007/s004190050252.

[157] F. Hofmann, S. Eve, J. Belnoue, J.-S. Bastien Micha, A.M. Korsunsky, Analysis of strain error sources in micro-beam Laue diffraction, Nucl. Inst. Methods Phys. Res. A. 660 (2011) 130–137. doi:10.1016/j.nima.2011.09.009.

[158] B.C. Valek, N. Tamura, A.L. Source, L.B. National, XMAS Tutorial v.1, Inf. Disp. (1975). (n.d.).

[159] F. Schotte, M. Lim, T.A. Jackson, A. V Smirnov, J. Soman, J.S. Olson, G.N. Phillips, M. Wulff, P.A. Anfinrud, Watching a protein as it functions with 150-ps time-resolved x-ray crystallography., Science. 300 (2003) 1944–7. doi:10.1126/science.1078797.

[160] T. Sui, K. Titov, S. Ying, H. Zhang, I.P. Dolbnya, J.-C. Tan, A. Korsunsky, Probing the nano-scale architecture of diamond-patterned electrospun fibre

mats by synchrotron small angle X-ray scattering, RSC Adv. 7 (2017). doi:10.1039/c6ra25770d.

[161] G. Srajer, L.H. Lewis, S.D. Bader, A.J. Epstein, C.S. Fadley, E.E. Fullerton, A. Hoffmann, J.B. Kortright, K.M. Krishnan, S.A. Majetich, T.S. Rahman, C.A. Ross, M.B. Salamon, I.K. Schuller, T.C. Schulthess, J.Z. Sun, Advances in nanomagnetism via X-ray techniques, J. Magn. Magn. Mater. 307 (2006) 1–31. doi:10.1016/j.jmmm.2006.06.033.

[162] J. Fish, Bridging the scales in nano engineering and science, J. Nanoparticle Res. 8 (2006) 577–594. doi:10.1007/s11051-006-9090-9.

[163] N. Matan, D.C. Cox, P. Carter, M.A. Rist, C.M.F. Rae, R.C. Reed, CREEP OF CMSX-4 SUPERALLOY SINGLE CRYSTALS : EFFECTS OF MISORIENTATION AND TEMPERATURE, 47 (1999).

[164] Z. Wang, R.J. McCabe, N.M. Ghoniem, R. LeSar, A. Misra, T.E. Mitchell, Dislocation motion in thin Cu foils: A comparison between computer simulations and experiment, Acta Mater. 52 (2004) 1535–1542. doi:10.1016/j.actamat.2003.12.005.

[165] S. Hata, H. Miyazaki, S. Miyazaki, M. Mitsuhara, M. Tanaka, K. Kaneko, K. Higashida, K. Ikeda, H. Nakashima, S. Matsumura, J.S. Barnard, J.H. Sharp, P.A. Midgley, High-angle triple-axis specimen holder for three-dimensional diffraction contrast imaging in transmission electron microscopy, Ultramicroscopy. 111 (2011) 1168–1175. doi:10.1016/j.ultramic.2011.03.021.

[166] J.S. Barnard, A.S. Eggeman, J. Sharp, T.A. White, P.A. Midgley, Dislocation electron tomography and precession electron diffraction - Minimising the effects of dynamical interactions in real and reciprocal space, in: Philos. Mag., 2010: pp. 4711–4730. doi:10.1080/14786430903581338.

[167] A. Mussi, P. Cordier, S. Demouchy, Characterization of dislocation interactions in olivine using electron tomography, Philos. Mag. 95 (2015) 335–345. doi:10.1080/14786435.2014.1000996.

[168] G.S. Liu, S.D. House, J. Kacher, M. Tanaka, K. Higashida, I.M. Robertson, Electron tomography of dislocation structures, Mater. Charact. 87 (2014) 1–11. doi:10.1016/j.matchar.2013.09.016.

[169] F. Hofmann, S. Ad Keegan, A.M. Korsunsky, Diffraction post-processing of 3D dislocation dynamics simulations for direct comparison with micro-beam Laue experiments, Mater. Lett. 89 (2012) 66–69. doi:10.1016/j.matlet.2012.08.052.

[170] V. Volterra, Annales scientifiques de l'École normale supérieure., Ann. Sci. l'École Norm. Supérieure. 24 (1907) 401–517.

[171] G.I. Taylor, The Mechanism of Plastic Deformation of Crystals. Part I. Theoretical, Proc. R. Soc. A Math. Phys. Eng. Sci. 145 (1934) 362–387. doi:10.1098/rspa.1934.0106.

[172] M. Polanyi, Uber eine Art Gitterstorung, die einen Kristall plastisch machen konnte, Zeitschrift Fur Phys. 89 (1934) 660–664. doi:10.1007/BF01341481.

[173] E. Orowan, Zur Kristallplastizitat. III, Zeitschrift Fur Phys. 89 (1934) 634–659. doi:10.1007/BF01341480.

[174] T. Mura, Micromechanics of defects in solids, 2nd ed., Martinus Nijhoff Publishers, Boston, 1987.

[175] D. Hull, D.J. Bacon, Introduction to Dislocations, 5TH ed., ELSEVIER, 2011. doi:10.1016/C2009-0-64358-0.

[176] Z. Zhu, H. Basoalto, N. Warnken, R.C.C. Reed, A model for the creep deformation behaviour of nickel-based single crystal superalloys, Acta Mater. 60 (2012) 4888–4900. doi:10.1016/j.actamat.2012.05.023.

[177] J.X. Zhang, J.C. Wang, H. Harada, Y. Koizumi, The effect of lattice misfit on the dislocation motion in superalloys during high-temperature low-stress creep, Acta Mater. 53 (2005) 4623–4633. doi:10.1016/j.actamat.2005.06.013.

[178] J.P. Hirth, J. Lothe, Theory of dislocations, 2nd ed., Krieger Publishing Company, 1982.

[179] M. Peach, J.S. Koehler, The Forces Exerted on Dislocations and the Stress Fields Produced by Them, Phys. Rev. 80 (1950) 436.

[180] G.B. Arfken, H.J. Weber, F.E. Harris, Mathematical Methods for Physicists, 2013. doi:10.1016/C2009-0-30629-7.

[181] R. de Wit, The Continuum Theory of Stationary Dislocations, Solid State Phys. 10 (1960) 249–292. doi:10.1016/S0081-1947(08)60703-1.

[182] R. Lesar, Simulations of Dislocation Structure and Response, Annu. Rev. Condens. Matter Phys. 5 (2014) 375–407. doi:10.1146/annurev-conmatphys-031113-133858.

[183] W.T. Read, Dislocations In Crystals, McGraw Hill Book Company Inc., 1953.

[184] Y.U. Wang, Y.M. Jin, A.G. Khachaturyan, Phase field microelasticity theory and modeling of elastically and structurally inhomogeneous solid, J. Appl. Phys. 92 (2002) 1351–1360. doi:10.1063/1.1492859.

[185] Y.U. Wang, Y.M. Jin, A.G. Khachaturyan †, Mesoscale modelling of mobile crystal defects—dislocations, cracks and surface roughening: phase field microelasticity approach, Philos. Mag. 85 (2005) 261–277. doi:10.1080/14786430412331315699.

[186] B. von Blanckenhagen, P. Gumbsch, E. Arzt, Dislocation sources in discrete dislocation simulations of thin-film plasticity and the Hall-Petch relation, Model. Simul. Mater. Sci. Eng. 9 (2001) 157–169. doi:10.1088/0965-0393/9/3/303.

[187] A.J.E. Foreman, M.J. Makin, Dislocation Movement Through Random Arrays of Obstacles, Philos. Mag. 14 (1966) 911–924. doi:10.1080/14786436608244762.

[188] L.P. Kubin, G. Canova, The modelling of dislocation patterns, Scr. Metall. Mater. 27 (1992) 957–962.

[189] D.A. Hills, P.A. Kelly, D.N. Dai, A.M. Korsunsky, Solution of Crack Problems: The distributed dislocation technique, Springer, 1996.

[190] D.H. Bilderback, P. Elleaume, E. Weckert, Review of third and next generation synchrotron light sources, J. Phys. B At. Mol. Opt. Phys. 38 (2005) S773–S797. doi:10.1088/0953-4075/38/9/022.

[191] S.M. Gruner, D. Bilderback, I. Bazarov, K. Finkelstein, G. Krafft, L. Merminga, H. Padamsee, Q. Shen, C. Sinclair, M. Tigner, Energy recovery linacs as synchrotron radiation sources (invited), in: Rev. Sci. Instrum., 2002: p. 1402. doi:10.1063/1.1420754.

[192] G.R. Neil, C.L. Bohn, S. V. Benson, G. Biallas, D. Douglas, H.F. Dylla, R. Evans, J. Fugitt, A. Grippo, J. Gubeli, R. Hill, K. Jordan, R. Li, L. Merminga, P. Piot, J. Preble, M. Shinn, T. Siggins, R. Walker, B. Yunn, Sustained Kilowatt Lasing in a Free-Electron Laser with Same-Cell Energy Recovery, Phys. Rev. Lett. 84 (2000) 662–665. doi:10.1103/PhysRevLett.84.662.

[193] K.-J. Kim, Rf and space-charge effects in laser-driven rf electron guns, Nucl. Instruments Methods Phys. Res. 275 (1989) 201–218.

[194] T. Popmintchev, M.-C. Chen, P. Arpin, M.M. Murnane, H.C. Kapteyn, The attosecond nonlinear optics of bright coherent X-ray generation, Nat. Photonics. 4 (2010). doi:10.1038/nphoton.2010.256.

[195] D. Attwood, Soft X-Rays and Extreme Ultraviolet Radiation : Principles and Applications, Cambridge University Press, 1999.

[196] E. Wigner, On the Quantum Correction For Thermodynamic Equilibrium, Phys. Rev. 40 (1932) 749–759.

[197] W.P. Brown, Validity of the Rytov Approximation in Optical Propagation Calculations*, J. Opt. Soc. Am. 56 (1966) 1045–1052.

[198] D. Sayre, Some implications of a theorem due to Shannon, Acta Crystallogr. 5 (1952) 843–843. doi:10.1107/S0365110X52002276.

[199] D. Sayre, J. Kirz, R. Feder, D. Kim, E. Spiller, Transmission microscropy of unmodified biological materials: comparative radiation dosages with …, Ultramicroscopy. 2 (1977) 337–349. doi:10.1016/S0304-3991(76)91997-5.

[200] D. Sayre, J. Kirz, R. Feder, D.M. Kim, E. Spiller, Potential operating region for ultrasoft x-ray microscopy of biological materials., Science. 196 (1977) 1339–1340. doi:10.1126/science.867033.

[201] R.W. Gerchberg, W.O. Saxton, A practical algorithm for the determination of phase from image and diffraction plane pictures, Optik (Stuttg). 35 (1972) 237–246. doi:10.1070/QE2009v039n06ABEH013642.

[202] J.R. Fienup, Phase retrieval algorithms: a personal tour [Invited], Appl. Opt. 52 (2013) 45–56.

[203] J.R. Fienup, Phase retrieval for undersampled broadband images, J. Opt. Soc. Am. A. 16 (1999) 1831. doi:10.1364/JOSAA.16.001831.

[204] J.R. Fienup, Phase retrieval algorithms: a comparison., Appl. Opt. 21 (1982)

2758–69. doi:10.1364/AO.21.002758.

[205] J. Miao, D. Sayre, H.N. Chapman, Phase retrieval from the magnitude of the Fourier transforms of nonperiodic objects, J. Opt. Soc. Am. A. 15 (1998) 1662.

[206] S. Marchesini, Invited Article: A unified evaluation of iterative projection algorithms for phase retrieval, Rev. Sci. Instrum. 78 (2007). doi:10.1063/1.2403783.

[207] V. Elser, I. Rankenburg, P. Thibault, Searching with iterated maps, Proc. Natl. Acad. Sci. 104 (2007) 418–423. doi:10.1073/pnas.0606359104.

[208] S. Marchesini, H. He, H.N. Chapman, S.P. Hau-Riege, A. Noy, M.R. Howells, U. Weierstall, J.C.H. Spence, X-ray image reconstruction from a diffraction pattern alone, Phys. Rev. B. 68 (2003) 140101. doi:10.1103/PhysRevB.68.140101.

[209] H.H. Bauschke, P.L. Combettes, D.R. Luke, Phase retrieval, error reduction algorithm, and Fienup variants: a view from convex optimization, J. Opt. Soc. Am. A. 19 (2002).

[210] G. Oszlányi, A. Süto, Ab initio structure solution by charge flipping. II. Use of weak reflections, Acta Crystallogr. Sect. A Found. Crystallogr. 61 (2005) 147–152. doi:10.1107/S0108767304027746.

[211] H.D. Jiang, D. Ramunno-Johnson, C. Song, B. Amirbekian, Y. Kohmura, Y. Nishino, Y. Takahashi, T. Ishikawa, J.W. Miao, Nanoscale imaging of mineral crystals inside biological composite materials using x-ray diffraction microscopy, Phys. Rev. Lett. 1 (2008) 4. doi:038103\r10.1103/PhysRevLett.100.038103.

[212] J. Miao, C.-C. Chen, C. Song, Y. Nishino, Y. Kohmura, T. Ishikawa, D. Ramunno-Johnson, T.-K. Lee, S.H. Risbud, Three-dimensional GaN-Ga2O3 core shell structure revealed by x-ray diffraction microscopy., Phys. Rev. Lett. 97 (2006) 215503. doi:10.1103/PhysRevLett.97.215503.

[213] I.K. Robinson, I.A. Vartanyants, G.J. Williams, M.A. Pfeifer, J.A. Pitney, Reconstruction of the Shapes of Gold Nanocrystals Using Coherent X-Ray Diffraction, Phys. Rev. Lett. 87 (2001). doi:10.1103/PhysRevLett.87.195505.

[214] I.A. Vartanyants, I.K. Robinson, Partial coherence effects on the imaging of small crystals using coherent x-ray diffraction, J. Phys. Condens. Matter. 13 (2001) 10593–10611.

[215] I.K. Robinson, I.A. Vartanyants, Use of coherent X-ray diffraction to map strain fields in nanocrystals, Appl. Surf. Sci. 182 (2001) 186–191.

[216] J.C.H. Spence, U. Weierstall, M. Howells, Coherence and sampling requirements for diffractive imaging, Ultramicroscopy. 101 (2004) 149–152. doi:10.1016/j.ultramic.2004.05.005.

[217] G.J. Williams, H.M. Quiney, A.G. Peele, K.A. Nugent, Coherent diffractive imaging and partial coherence, Phys. Rev. B - Condens. Matter Mater. Phys. 75 (2007). doi:10.1103/PhysRevB.75.104102.

[218] G. Williams, H. Quiney, B. Dhal, C. Tran, K. Nugent, a. Peele, D. Paterson, M. de Jonge, Fresnel Coherent Diffractive Imaging, Phys. Rev. Lett. 97 (2006) 1–4. doi:10.1103/PhysRevLett.97.025506.

[219] J.N. Clark, L. Beitra, G. Xiong, A. Higginbotham, D.M. Fritz, H.T. Lemke, D. Zhu, M. Chollet, G.J. Williams, M. Messerschmidt, B. Abbey, R.J. Harder, A.M. Korsunsky, J.S. Wark, I.K. Robinson, Ultrafast Three-Dimensional Imaging of Lattice Dynamics in Individual Gold Nanocrystals, 341 (2013). doi:10.1126/science.1236034.

[220] B. Chen, R.A. Dilanian, S. Teichmann, B. Abbey, A.G. Peele, G.J. Williams, P. Hannaford, L. Van Dao, H.M. Quiney, K.A. Nugent, Multiple wavelength diffractive imaging, Phyrical Rev. A. 79 (2009). doi:10.1103/PhysRevA.79.023809.

[221] L.W. Whitehead, G.J. Williams, H.M. Quiney, K.A. Nugent, A.G. Peele, D. Paterson, M.D. De Jonge, I. Mcnulty, Fresnel diffractive imaging: Experimental study of coherence and curvature, Phys. Rev. B. 77 (2008). doi:10.1103/PhysRevB.77.104112.

[222] Diamond Light Source, I13 - X-Ray Imaging and Coherence - Materials - Diamond Light Source, (n.d.). http://www.diamond.ac.uk/Beamlines/Materials/I13.html (accessed September 25, 2017).

[223] M. Guizar-Sicairos, S.T. Thurman, J.R. Fienup, Efficient subpixel image registration algorithms, Optcis Lett. 33 (2008).

[224] M.C. Newton, Y. Nishino, I.K. Robinson, Bonsu: the interactive phase retrieval suite, J. Appl. Cryst. 45 (2012) 840–843. doi:10.1107/S0021889812026751.